Multimodal vibration damping of structures coupled to their analogous piezoelectric networks

Boris Lossouarn

CONSERVATOIRE NATIONAL DES ARTS ET MÉTIERS | le cnam

École Doctorale "Sciences des Métiers de l'Ingénieur" (SMI)

Laboratoire de Mécanique des Structures et des Systèmes Couplés (LMSSC)

THÈSE DE DOCTORAT

présentée par : **Boris LOSSOUARN**

soutenue le : **16 septembre 2016**

pour obtenir le grade de : **Docteur du Conservatoire National des Arts et Métiers**

Spécialité : **Mécanique**

Multimodal vibration damping of structures coupled to their analogous piezoelectric networks

THÈSE dirigée par

M. DEÜ Jean-François — *Professeur, LMSSC, Cnam (Paris)*

CO-ENCADRANT

M. AUCEJO Mathieu — *Maître de conférence, LMSSC, Cnam (Paris)*

RAPPORTEURS

M. MAURINI Corrado — *Professeur, ∂'Alembert, UPMC (Paris)*
M. LEFEUVRE Elie — *Professeur, IEF, Université Paris Sud (Orsay)*

EXAMINATEURS

M. ALLIX Olivier — *Professeur, LMT, ENS Cachan (Cachan)*
M. BERGAMINI Andrea — *Docteur, EMPA (Dübendorf)*
M. MULTON Bernard — *Professeur, SATIE, ENS Rennes (Bruz)*
M. CUNEFARE Kenneth A. — *Professeur, IAL, Georgia Institute of Technology (Atlanta)*

Acknowledgments

This work was funded by the French Ministry of National Education, Higher Education and Research through a three-year scholarship for doctoral studies within the Structural Mechanics and Coupled Systems Laboratory (LMSSC) at Cnam in Paris.

I first want to express my most sincere gratitude to Jean-François Deü for giving me the opportunity to work on a research topic that could not have better fulfilled my expectations. His guidance was a perfect balance between helpful suggestions and freedom to explore various research directions. Jean-François advised me in scientific matters as well as personal projects, and this is one of the numerous reasons why I owe him so much. I also would like to acknowledge my second advisor, Mathieu Aucejo, who awed me with his availability and his ability to answer my numerous questions. He was always there to give me invaluable advice and comments, whether it concerned scientific issues or teaching methods.

I am very grateful to all the members of my PhD Committee. I wish to thank Corrado Maurini and Elie Lefeuvre for accepting to review my thesis and Olivier Allix for acting as President of the Committee. My thanks also go to Andrea Bergamini and Bernard Multon for sharing their strong expertise with me, and I hope that this only represents the beginning of a larger collaboration. I want to express my most sincere acknowledgments to Kenneth A. Cunefare, not only for being part of the jury but also for inviting me to his lab, the Integrated Acoustics Laboratory, for a nine-month visit. I learned so much from his efficient pragmatic approach to potentially complicated theoretical concepts.

My research visit to the Georgia Institute of Technology would probably not have been possible without the Fulbright Program, which gave me a truly unique opportunity to discover the United States. This has been an amazing experience, and I will not forget the memories I made with all the American people, Fulbright scholars and other international grantees I have met through my journey. Special thanks go to Louise and Stephen for showing me what hospitality means in the US, and to David and Giuli for making my time in Atlanta so enjoyable. I also would like to thank the PhD students who were my labmates for nine months: Ellen, Elliott, Fabio, David, Tarcisio... More specifically, I am

very thankful to Stephen Leadenham for helping me with the bonding of the piezoelectric plates and for the interesting discussions we had about that. Thanks also to Bradley Argauer for the manufacturing of the clamping frame.

Moreover, I am very thankful to my labmates at the Structural Mechanics and Coupled Systems Laboratory for the moments we spent together in this lively office talking about science or any other topic. To those who already graduated like Yassine, Luciano, Quentin, Stéphanie; and those who are next, Benjamin, Olivier, Pierre, Guillaume, Martin, Aro, Christophe... Thanks also to Roger for brightening our mornings with discussions full of precious advice. I wish to thank Philippe and Fred for their everyday assistance implementing experimental setups. Lastly, my thanks goes to members of the SATIE laboratory; to Laurent Prévond who showed me how to design my first inductors and to Sylvain who helped me to get access to the winding machine in Cachan.

Time flew by, and I owe my family and friends an apology for not having spent more time with them during the past three years. Still, they always supported me through this journey and helped me take my mind off of research when I needed it. To my parents and my sisters who contribute to the growth of our wonderful family. Finally, I cannot thank Florence enough for her inestimable support. I keep remembering all the good times we already had together and I look forward to the ones which are awaiting us.

Abstract

Structural vibrations can be reduced by benefiting from the electromechanical coupling that is offered by piezoelectric materials. In terms of passive damping, piezoelectric shunts allow converting the vibration energy into electrical energy. Adding an inductor in the circuit creates an electrical resonance due to the charge exchanges with the piezoelectric capacitance. By tuning the resonance of the shunt to the natural frequency of the mechanical structure, the equivalent of a tuned mass damper is implemented. This strategy is extended to the control of a multimodal structure by increasing the number of piezoelectric patches. These are interconnected through an electrical network offering modal properties that approximate the behavior of the structure to control. This multi-resonant network allows the simultaneous control of multiple mechanical modes. An adequate electrical topology is obtained by discretizing the mechanical structure and applying the direct electromechanical analogy. The analogous network shows inductors and transformers, whose numbers and values are chosen according to the frequency band of interest. After focusing on the design of suitable magnetic components, the passive control strategy is applied to the damping of one-dimensional structures as bars or beams. It is then extended to the control of thin plates by implementing a two-dimensional analogous network.

Keywords : Vibration control, Multimodal damping, Passive control, Piezoelectric coupling, Resonant shunt, Periodic array, Analogous electrical network, Design of magnetic components

Résumé court en français

L'amplitude vibratoire d'une structure mince peut être réduite grâce au couplage électromécanique qu'offrent les matériaux piézoélectriques. En termes d'amortissement passif, les shunts piézoélectriques permettent une conversion de l'énergie vibratoire en énergie électrique. La présence d'une inductance dans le circuit crée une résonance électrique due à l'échange de charges avec la capacité piézoélectrique. Ainsi, l'ajustement de la fréquence propre de ce shunt résonant à celle de la structure mécanique équivaut à la mise en œuvre d'un amortisseur à masse accordée. Cette stratégie est étendue au contrôle d'une structure multimodale par multiplication du nombre de patchs piézoélectriques. Ceux-ci sont interconnectés via un réseau électrique ayant un comportement modal approximant celui de la structure à contrôler. Ce réseau multi-résonant permet donc le contrôle simultané de plusieurs modes mécaniques. La topologie électrique adéquate est obtenue par discrétisation de la structure mécanique puis par analogie électromécanique directe. Le réseau analogue fait apparaître des inductances et des transformateurs dont le nombre et les valeurs sont choisis en fonction de la bande de fréquences à contrôler. Après s'être penché sur la conception de composants magnétique adaptés, la solution de contrôle passif est appliquée à l'amortissement de structures unidimensionnelles de type barres ou poutres. La stratégie est ensuite étendue au contrôle de plaques minces par mise en œuvre d'un réseau électrique bidimensionnel.

Mots clés : Contrôle vibratoire, Amortissement multimodal, Contrôle passif, Couplage piézoélectrique, Shunt résonant, Structure périodique, Réseau électrique analogue, Conception de composants magnétiques

Résumé étendu en français

I Introduction

Le shunt résonant [2], constitué d'une inductance et d'un patch piézoélectrique collé sur la structure à contrôler, peut être vu comme l'analogue électrique d'un amortisseur à masse accordée. En effet, lorsque la fréquence de résonance électrique est réglée sur une résonance mécanique, un transfert énergétique génère une réduction de l'amplitude vibratoire. L'utilisation d'un réseau de patchs périodiques multiplie le nombre de shunts nécessaires, mais a l'avantage de limiter les problèmes d'annulation de charges qui pourraient se produire avec des patchs aux dimensions proches des longueurs d'onde considérées. Cette solution a été appliquée au contrôle de barres [4], de poutres [46] ou encore de plaques [50]. Cependant, chaque shunt résonant n'est efficace que sur une bande de fréquences étroite et, même en considérant des composants magnétiques à haute perméabilité, les valeurs d'inductance nécessaires peuvent s'avérer trop élevées pour permettre une mise en œuvre purement passive. Il est pourtant possible de réduire les spécifications d'inductance et de proposer un contrôle large bande en considérant une interconnexion des patchs piézoélectriques plutôt que des shunts indépendants. Cette stratégie fut explorée par Maurini et al. qui ont comparé plusieurs architectures de réseaux périodiques [17]. Il est finalement observé qu'un amortissement multimodal nécessite le couplage de la structure à contrôler à son analogue électrique. Des solutions de contrôle piézoélectrique par réseau analogue passif ont ainsi été proposées pour des poutres [21] et des plaques [24]. Malgré tout, les résultats présentés restent théoriques et prennent en compte un réseau électrique homogénéisé, ce qui s'éloigne des applications pratiques pour lesquelles le nombre de composants électriques est limité.

Ce résumé étendu synthétise la démarche théorique ainsi que les principaux résultats expérimentaux de l'application de la stratégie d'amortissement piézoélectrique analogue à des cas de barres, poutres et plaques. L'élaboration d'un modèle discret approximant la structure continue à contrôler rend possible l'utilisation de l'analogie électromécanique directe qui conduit au réseau électrique analogue [30, 74]. Ce réseau électrique est synthétisé expérimentalement à partir de composants magnétiques passifs puis couplé à la struc-

ture mécanique par l'intermédiaire d'un ensemble de patchs piézoélectriques. Ceci permet d'observer des réductions de l'amplitude vibratoire dues au transfert d'énergie vers le réseau électrique analogue. On obtient finalement l'équivalent d'un amortisseur à masse accordée multimodal qui fonctionne de façon totalement autonome.

II Contrôle vibratoire par shunt piézoélectrique résonant

L'analyse du shunt piézoélectrique résonant nous montre que sa mise en œuvre nécessite la conception d'inductances de grandes valeurs. Celles-ci peuvent être réalisées avec des composants magnétiques à haute perméabilité comme des pots en ferrites ou des tores nanocristallins afin de générer un dispositif d'amortissement vibratoire purement passif.

II.1 Optimisation du shunt résonant

La Figure 1(a) représente une structure munie d'une paire de patchs piézoélectriques connectés à un shunt résonant. Ce shunt est constitué d'une inductance L qui, associée à la capacité piézoélectrique, génère une résonance électrique. Une résistance R est également présente afin d'apporter la dissipation énergétique nécessaire à l'amortissement vibratoire. En première approximation, la structure continue peut être modélisée par un système masse-ressort de masse m et de raideur K^E quand les patchs sont court-circuités. La force appliquée à la structure est notée F et le déplacement est représenté par la variable U. Les équations relatives au couplage piézoélectrique permettent de représenter le système électromécanique selon le modèle de la Figure 1(b). Ici, le shunt est modélisé par son équivalent mécanique faisant apparaître l'analogie avec un système de type amortisseur à masse accordée. La capacité piézoélectrique sans déformation C^ε se retrouve dans la raideur e^2/C^ε où e représente le coefficient de couplage piézoélectrique. On note également le lien entre la résistance et l'amortisseur e^2R, ainsi qu'entre l'inductance et la masse e^2L dont le déplacement est associé à q, le déplacement de charges électriques dans le shunt.

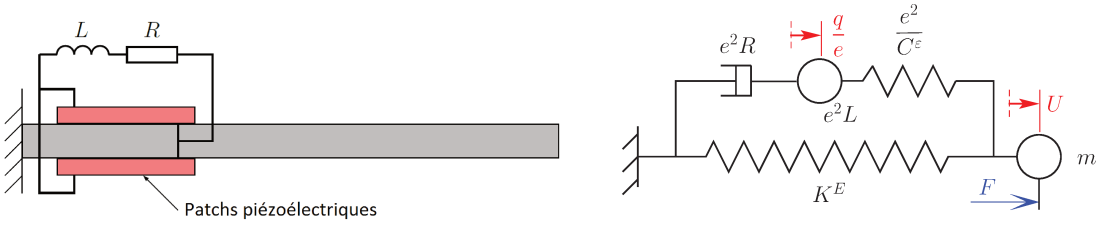

Figure 1: Contrôle par dispositif piézoélectrique résonant: (a) Structure munie de patchs piézoélectriques connectés à un shunt résonant. (b) Modèle mécanique équivalent.

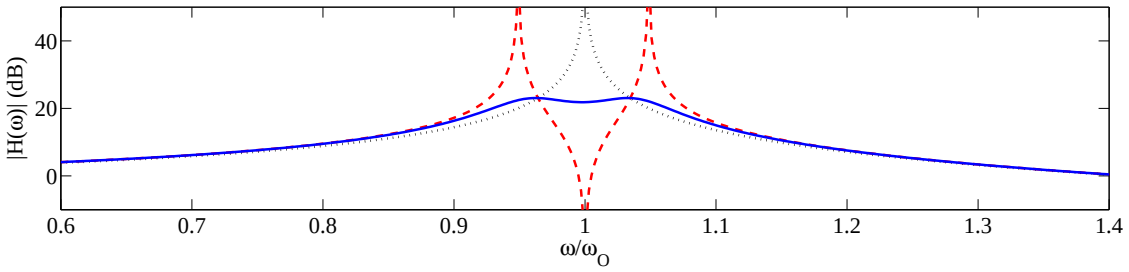

Figure 2: Module de la fonction de transfert $H(\omega)$ - $(\cdots)$ en circuit ouvert (résistance infinie), (- -) avec l'inductance optimale et une résistance nulle, (—) avec l'inductance optimale et la résistance optimale.

À partir du modèle de la Figure 1(b), il est possible de définir la fonction de transfert

$$H(\omega) = \frac{U}{F/K^D} = \frac{1 - \dfrac{\omega^2}{\omega_e^2} + 2\mathrm{j}\xi_e \dfrac{\omega}{\omega_e}}{\dfrac{\omega_S^2}{\omega_O^2} - \left(\dfrac{1}{\omega_O^2} + \dfrac{1}{\omega_e^2}\right)\omega^2 + \dfrac{\omega^4}{\omega_O^2\omega_e^2} + 2\mathrm{j}\xi_e \dfrac{\omega}{\omega_e}\left(1 - \dfrac{\omega^2}{\omega_O^2}\right)}, \tag{1}$$

où K^D est la raideur de la structure en circuit ouvert, $\omega_e = 1/\sqrt{LC^\varepsilon}$ représente la pulsation de résonance électrique, $\xi_e = \dfrac{R}{2}\sqrt{\dfrac{C^\varepsilon}{L}}$ est le coefficient d'amortissement et $\omega_O = \sqrt{\dfrac{K^D}{m}}$ est la pulsation de résonance de la structure mécanique en circuit ouvert. Une optimisation de type $\mathcal{H}_\infty$ qui consiste à minimiser le maximum du module de la fonction de transfert selon le critère $\min\limits_{L,R}\left(\max\limits_{\omega}|H(\omega, L, R)|\right)$ permet de définir des valeurs optimales pour les composants du shunt électrique [43]:

$$L = \frac{1}{C^\varepsilon \omega_O^2} \quad \text{and} \quad R = \sqrt{\frac{3}{2}}\frac{k_c}{C^\varepsilon \omega_O}, \tag{2}$$

où $k_c = \sqrt{\dfrac{\omega_O^2 - \omega_S^2}{\omega_S^2}}$ avec $\omega_S = \sqrt{\dfrac{K^E}{m}}$ la pulsation de résonance de la structure quand les patchs sont court-circuités. Le tracé du module de la fonction de transfert de l'Eq. (1) permet d'observer l'effet du shunt résonant sur la dynamique vibratoire. Ceci est représenté sur la Figure 2 où l'on remarque que l'ajout d'une inductance dédouble la résonance initiale mais que la résistance permet ensuite de réduire simultanément l'amplitude vibratoire des deux maxima.

II.2 Limites de mise en œuvre pratique

Les limites de la technique du shunt résonant apparaissent lors de sa mise en application pratique. En effet, pour un contrôle vibratoire basse fréquence, les valeurs d'inductances nécessaires sont souvent bien supérieures à celles proposées dans les gammes de composants

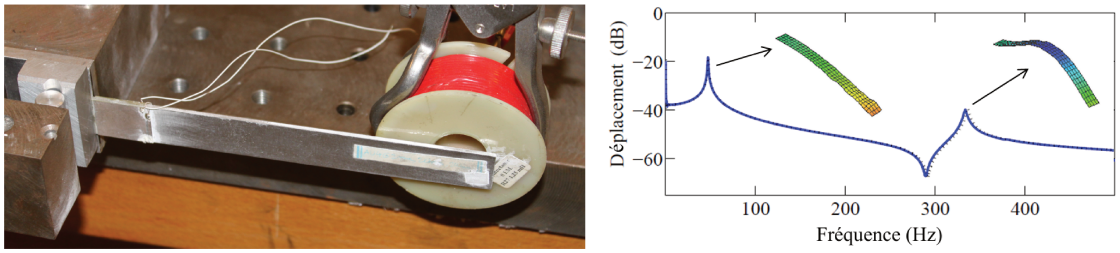

(a) (b)

Figure 3: Mise en œuvre expérimentale: (a) Poutre encastrée-libre munie d'une paire de patchs piézoélectriques près de l'encastrement. (b) Fonctions de réponse en fréquence en bout de poutre et déformées modales opérationnelles obtenues expérimentalement (en court-circuit).

Table 1: Fréquences de résonances, coefficients de couplage et caractéristiques du shunt résonant pour un contrôle optimal des deux premiers modes de flexion.

	f_S (Hz)	f_O (Hz)	k_c	L (H)	R (Ω)
Mode 1	47.07	47.46	0.129	330	15 000
Mode 2	333.6	336.1	0.123	6.5	2 100

électriques standards. Ceci est illustré par un dispositif expérimental constituée d'une poutre encastrée-libre de 170 mm de long munie d'une paire de patchs piézoélectriques disposés près de l'encastrement. L'extrémité libre est excitée par le système bobine-aimant visible sur la Figure 3(a). On mesure alors la fonction de réponse en fréquence pour le déplacement en bout de poutre. La Figure 3(b) montre les deux premiers modes de vibration en flexion dont les fréquences de résonance en court-circuit sont 47.07 Hz et 333.6 Hz. Sachant que la capacité piézoélectrique est évaluée à $C^{\varepsilon} = 35.4$ nF pour une connexion parallèle, les valeurs d'inductances et de résistance optimales du Tableau 1 sont calculées à partir de l'Eq. (2). Les inductances requises sont nettement supérieures à 0.5 H qui représente la limite supérieure de la plupart des gammes d'inductances standards. De plus, les spécifications en matière de résistance conduisent à des composants à haut facteur de qualité, qui nécessitent une conception spécifique.

II.3 Conception d'inductances de fortes valeurs

Pour le dispositif expérimental considéré, aucun composant standard comme celui représenté sur la Figure 4(a) ne permet de satisfaire à la fois les valeurs d'inductance et de résistance optimales pour le contrôle d'un des deux premiers modes de flexion. Il est

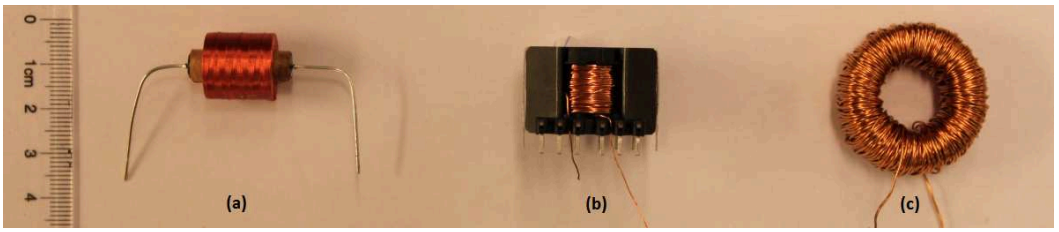

Figure 4: Trois types d'inductance: (a) Composant standard bobiné sur un cylindre en ferrite. (b) Inductance bobinée sur pot en ferrite RM. (c) Inductance bobinée sur tore nanocristallin.

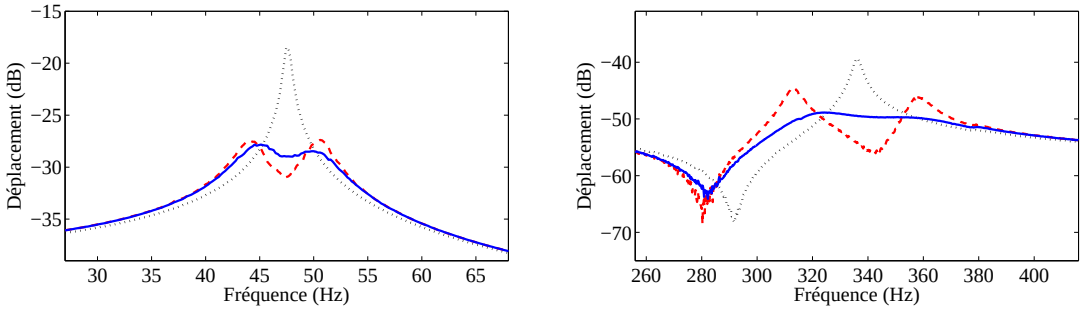

Figure 5: Résultats expérimentaux: (a) Amortissement du premier mode de flexion avec le tore nanocristallin (1800 tours) - (· · ·) circuit ouvert, (- -) avec inductance mais pas de résistance additionnelle, (—) avec inductance et résistance additionnelle de 6.7 kΩ. (b) Amortissement du deuxième mode de flexion avec le pot en ferrite (613 tours) - (· · ·) circuit ouvert, (- -) avec inductance mais pas de résistance additionnelle, (—) avec inductance et résistance additionnelle de 1.8 kΩ.

donc nécessaire de se tourner vers des circuits magnétiques à haute perméabilité qui permettent d'atteindre des valeurs d'inductance élevées avec un bobinage à nombre de tours limité. Deux circuits magnétiques fermés sont considérés: un pot en ferrite de type RM10 et un tore nanocristallin. Le premier, représenté sur la Figure 4(b) permet d'atteindre les 6.5 H requis pour le contrôle du second mode en bobinant 613 tours de fil. Pour le premier mode, un tore nanocristallin avec 1800 tours devient nécessaire et permet d'atteindre une valeur d'inductance de 330 H.

La conception de ces composants passifs est validée par une mise en œuvre au sein du shunt piézoélectrique contrôlant la poutre (Figure 3(a)). Un amortissement significatif est observé sur la Figure 5 pour les deux premiers modes de flexion. Ceci montre que malgré les contraintes pratiques associées aux valeurs optimales pour les constituants d'un shunt résonant, il est possible de concevoir des composants dédiés qui permettre une mise en application de la stratégie de contrôle avec un dispositif purement passif.

III Amortissement multimodal d'une barre

Le contrôle vibratoire par shunt résonant est étendu à l'amortissement multimodal par couplage analogue. L'analogue électrique d'une barre est obtenu par discrétisation d'un milieu de propagation longitudinal puis application de l'analogie électromécanique directe. Le réseau électrique obtenu vient ensuite interconnecter un ensemble de patchs piézoélectriques de manière à réduire l'amplitude vibratoire de la barre à contrôler sur une large plage de fréquences.

III.1 Discrétisation du milieu mécanique

Un milieu mécanique de type barre soumis à une propagation longitudinale est caractérisé par une équation différentielle qui s'écrit sous la forme

$$\rho \frac{\partial^2 u(x,t)}{\partial t^2} = Y \frac{\partial^2 u(x,t)}{\partial x^2}, \tag{3}$$

où x représente la variable d'espace, t la variable de temps et $u(x,t) = U(x)g(t)$ est le déplacement longitudinal, $g(t)$ représentant une évolution harmonique. Les constantes ρ et Y sont respectivement la densité du milieu propagatif et son module de Young. Avec S l'aire de la section de la barre, N définit l'effort normal selon

$$\begin{array}{l} N(x) = YSU'(x) \\ -\rho S\omega^2 U(x) = N'(x) \end{array}. \tag{4}$$

Ainsi, une méthode des différences finies permet de définir le système d'équations

$$\begin{array}{l} N_{\mathrm{I}} = K(U_{\mathrm{R}} - U_{\mathrm{L}}) \\ -\frac{m}{2}\omega^2 U_{\mathrm{L}} = N_{\mathrm{I}} - N_{\mathrm{L}} \\ -\frac{m}{2}\omega^2 U_{\mathrm{R}} = N_{\mathrm{R}} - N_{\mathrm{I}} \end{array}, \tag{5}$$

où $m = \rho Sa$ et $K = YS/a$ quand a est la longueur de la portion de barre discrétisée. Ce système peut être représenté par le modèle discret de la Figure 6(a) en considérant que N_{I} correspond à l'effort dans le ressort de raideur K. Ce modèle correspond finalement

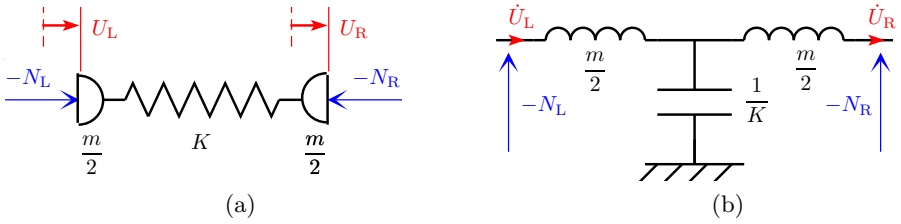

Figure 6: Cellules élémentaires pour la propagation longitudinale: (a) Portion de barre discrétisée. (b) Analogue électrique d'une portion de barre.

à l'approximation discrète d'une portion de barre en traction-compression. La succession de n cellules élémentaires de ce type offre donc un modèle discrétisé pour une barre de longueur $l = na$. Ce modèle est valide tant que la longueur d'onde considérée est grande devant la longueur a d'une cellule élémentaire. Pour des problèmes d'analyse vibratoire, une limite peut être fixée à un minimum de dix cellules par longueur d'onde.

III.2 Réseau électrique analogue

À partir de la cellule élémentaire discrétisée présentée sur la Figure 6(a), il devient possible de définir l'analogue électrique d'une barre en traction-compression. Nous utilisons ici l'analogie électromécanique directe [74] qui considère une équivalence entre une force et une tension, ainsi qu'entre une vitesse et un courant électrique. Par conséquent, une masse est équivalente à une inductance et une raideur est équivalente à l'inverse d'une capacité électrique. L'analogue de la portion de barre discrétisée est donc représenté par la Figure 6(b) qui montre une ligne d'inductances $m/2$ avec une connexion à la masse par l'intermédiaire d'un condensateur de valeur $1/K$.

Afin de faire apparaître un couplage multimodal destiné à l'amortissement large bande d'une barre, celle-ci est couplée à son réseau électrique analogue par l'intermédiaire d'une distribution périodique de patchs piézoélectriques. Le guide d'onde électromécanique qui en résulte est représenté sur la Figure 7 où l'on peut observer que les patchs piézoélectriques prennent le rôle du condensateur représenté sur la Figure 6(b). Il n'est donc nécessaire d'ajouter qu'une ligne d'inductances L interconnectant les patchs successifs. La succession d'un nombre suffisant de cette cellule élémentaire permet de tendre vers un continuum électrique qui représente l'analogue d'une barre en traction-compression. En ce qui concerne les conditions aux limites électriques, une condition de bord libre impose la mise à la masse d'une extrémité du réseau afin d'assurer l'analogie entre la structure mécanique et le réseau électrique. De même, une condition de blocage revient à laisser un port ouvert de façon à empêcher le passage du courant.

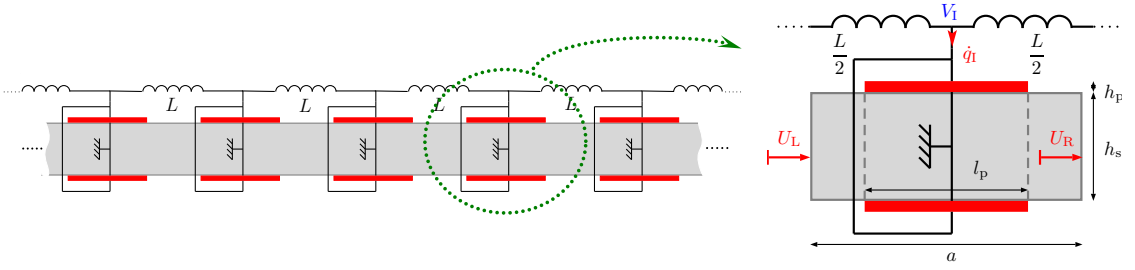

Figure 7: Barre couplée à son réseau électrique analogue par l'intermédiaire d'une distribution périodique de patchs piézoélectriques et cellule élémentaire associée.

III.3 Conditions de couplage modal

L'objectif du couplage analogue est de synthétiser un milieu secondaire étant capable d'approximer les modes de la structure à contrôler. Dans notre cas, le milieu secondaire est le réseau électrique qui doit donc présenter les mêmes fréquences de résonance et les mêmes formes modales que la barre considérée. Pour ce faire, une première condition est d'imposer des connections électriques en bouts de réseau qui sont analogues aux conditions aux limites mécaniques. Ensuite, la relation de dispersion du milieu électrique doit approximer la relation de dispersion de la barre. Cette condition est vérifiée si le rapport de la raideur sur la masse est égal dans les deux milieux propagatifs. Le milieu secondaire étant un réseau électrique, on obtient

$$\frac{1}{LC^{\varepsilon}} = \frac{K^E}{m}, \tag{6}$$

où K^E représente la raideur d'une portion de barre quand les patchs sont court-circuités et m est la masse de cette même portion de barre. La capacité piézoélectrique C^{ε} est imposée par la géométrie et le matériau des patchs et de la cellule élémentaire. C'est donc l'inductance L qui est choisie, en fonction de la masse et de la raideur de la cellule élémentaire, de façon à satisfaire le couplage modal.

III.4 Modélisation du système électromécanique

La condition de couplage modal de l'Eq. (6) se base sur un modèle discrétisé du problème électromécanique. En effet, la cellule élémentaire de la Figure 7 peut être représentée par le circuit électrique de la Figure 8 où le transformateur représente le couplage piézoélectrique. Ici, l'analogie entre les domaines mécanique et électrique est évidente car un couplage nul engendre deux lignes de propagation distinctes mais possédant la même topologie. Pourtant, le milieu mécanique est en réalité continu et l'approximation discrète ne peut se faire que pour des longueurs d'onde importantes devant la longueur de la cellule

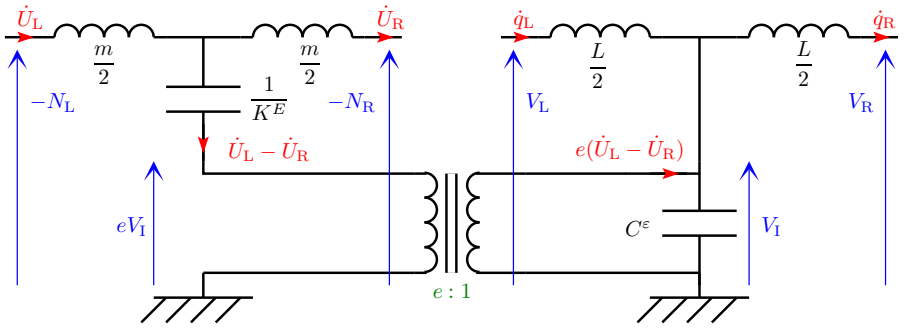

Figure 8: Modèle discret de la cellule élémentaire électromécanique.

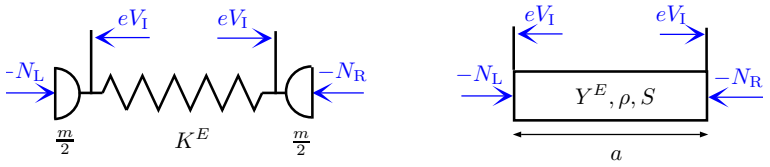

(a) (b)

Figure 9: Modélisation de la partie mécanique du problème couplé: (a) Modèle discret. (b) Modèle homogénéisé.

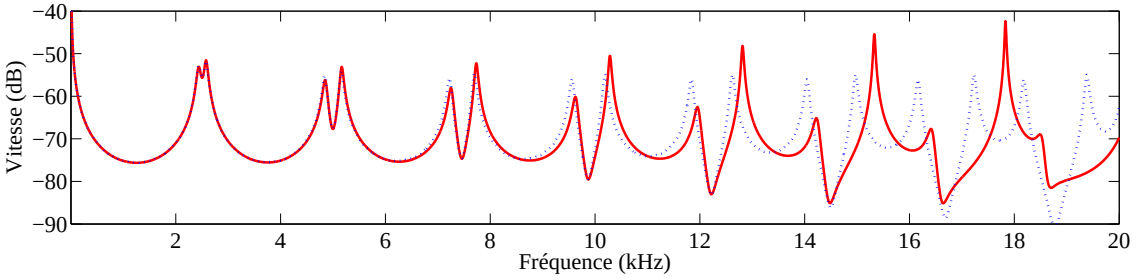

Figure 10: Fonctions de réponse en fréquence pour une barre libre-libre constituée de 20 cellules élémentaires - (· · ·) pour le modèle discret, (—) pour le modèle homogénéisé.

élémentaire. La validité du modèle discret représenté sur la Figure 9(a) peut donc être remise en question. Un modèle semi-continu est alors proposé pour prendre en compte le couplage d'un réseau électrique discret à une structure mécanique continue.

Le modèle homogénéisé de la Figure 9(b) est comparé au modèle discret. L'exemple considéré se base sur une succession de 20 cellules élémentaires identiques à celle représentée sur la Figure 7. La structure est excitée longitudinalement à l'une de ses extrémités et on mesure la vitesse de l'autre extrémité, celle-ci n'étant soumise à aucune force extérieure. Le rapport entre la vitesse longitudinale et la force d'excitation permet de tracer la fonction de réponse en fréquence de la Figure 10. Au-delà de 10 kHz, on y observe une nette différence entre les deux modèles considérés. Pour des conditions aux limites libre-libre, cette fréquence correspond à une longueur d'onde approchant 10 fois la longueur de la cellule élémentaire. On remarque ainsi que le modèle discret ne permet pas de prendre en compte le phénomène de désaccordage entre les résonances du réseau électrique discret et celles de la structure mécanique continue. Par conséquent, le modèle semi-continu qui se base sur un milieu mécanique homogénéisé est nécessaire quand la longueur d'onde considérée approche ou devient inférieure à 10 cellules élémentaires. Ceci justifie le choix du modèle semi-continu pour les comparaisons entre simulations et résultats expérimentaux qui s'étendent jusqu'au quatrième mode longitudinal.

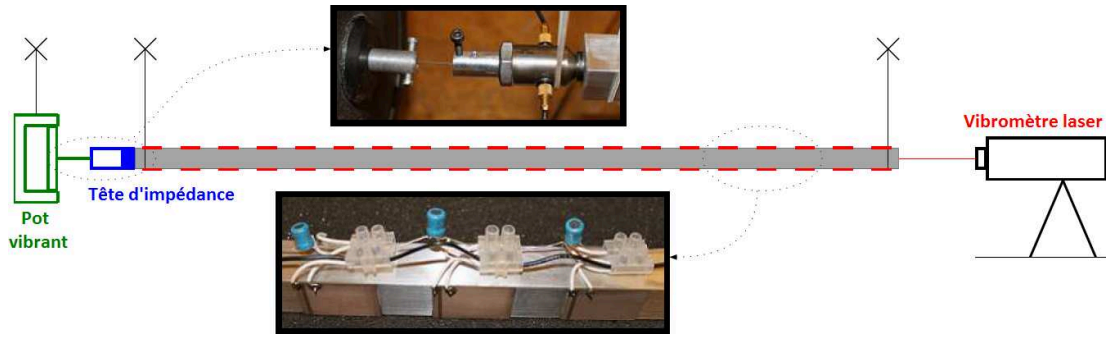

Figure 11: Dispositif expérimental pour l'analyse de l'amortissement vibratoire longitudinal: barre suspendue couplée à son réseau électrique analogue.

III.5 Validation expérimentale

Une barre en duraluminium d'un mètre de long et de section carré de 2 cm de côté est munie de 20 paires de patchs piézoélectriques. Une paire de patchs offrant une capacité électrique $C^{\varepsilon} = 35$ nF, des inductances $L = 2.8$ mH sont choisies afin de satisfaire l'Eq. (6). Comme illustré sur la Figure 11, la barre est suspendue par des câbles élastiques et excitée par un pot vibrant à l'une de ses extrémités. Afin de respecter l'analogie avec une barre en conditions libre-libre, la ligne d'inductance doit être connectée à la masse à chacune de ses extrémités. Une tête d'impédance mesure la force du côté de l'excitation et un vibromètre laser donne accès à la vitesse de déplacement de l'autre extrémité.

La fonction de réponse en fréquence, présentée sur la Figure 12, prouve l'efficacité du dispositif en matière d'amortissement vibratoire multimodal. En effet, des réductions d'amplitude supérieures à 20 dB sont observées pour les 4 premiers modes de traction-compression. Ces performances pourraient même être améliorées en augmentant la dissipation dans le réseau par ajout de résistances électriques. L'apparition de minima locaux marqués traduit, en effet, un comportement de type amortisseur à masse accordée nette-

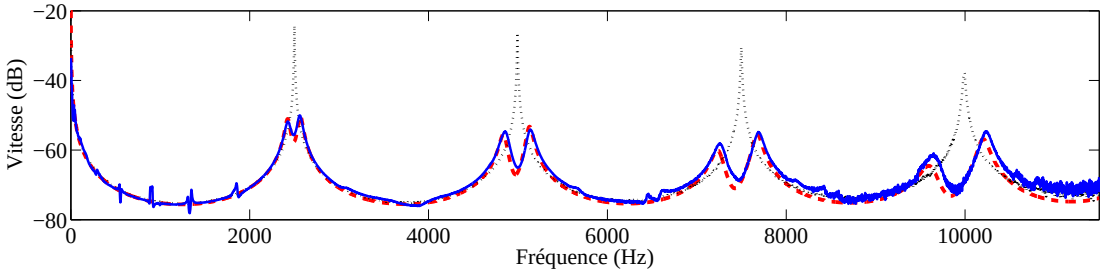

Figure 12: Fonctions de réponse en fréquence pour la vitesse longitudinale en bout de barre - (· · ·) réponse expérimentale sans contrôle, (—) réponse expérimentale avec contrôle analogue, (– –) réponse simulée avec contrôle analogue.

ment sous-amorti. Enfin, on remarque que le système électromécanique peut être modélisé de façon adéquate car les simulations numériques, basées sur une approche par matrice de transfert, concordent avec les résultats expérimentaux.

IV Amortissement multimodal d'une poutre

La stratégie de contrôle vibratoire par couplage piézoélectrique analogue est appliquée à une structure de type poutre. Comme dans le cas d'une barre, le modèle discret d'une poutre permet de définir son analogue électrique. Celui-ci est assemblé avec des composants passifs puis couplé à une poutre afin de réduire son amplitude vibratoire.

IV.1 Discrétisation du milieu mécanique

En considérant les hypothèses d'Euler-Bernoulli, la propagation transversale dans un milieu de type poutre s'exprime de la façon suivante:

$$\rho S \frac{\partial^2 w(x,t)}{\partial t^2} = -YI \frac{\partial^4 w(x,t)}{\partial x^4}, \tag{7}$$

où $w(x,t) = W(x)g(t)$ représente le déplacement transversal alors que I est le moment quadratique de la poutre considérée. L'Equation (7) peut être développée sous la forme d'un système faisant intervenir les variables internes Q, M et θ représentant respectivement l'effort tranchant, le moment fléchissant et le déplacement angulaire:

$$\begin{array}{ll} Q'(x) = -\rho S\omega^2 W(x) & \\ Q(x) = -M'(x) & \end{array} \quad \text{et} \quad \begin{array}{ll} M(x) = YI\theta'(x) & \\ \theta(x) = W'(x) & \end{array} \quad . \tag{8}$$

De la même manière que pour la détermination du modèle de barre discrétisé, une méthode des différences finies appliquée à l'Eq. (8) conduit au modèle discret d'une portion de poutre:

$$\begin{array}{ll} Q_{\mathrm{R}} - Q_{\mathrm{L}} = -m\omega^2 W_{\mathrm{I}} & \\ Q_{\mathrm{L}} = -\dfrac{M_{\mathrm{I}} - M_{\mathrm{L}}}{a/2} & \\ Q_{\mathrm{R}} = -\dfrac{M_{\mathrm{R}} - M_{\mathrm{I}}}{a/2} & \end{array} \quad \text{et} \quad \begin{array}{ll} M_{\mathrm{I}} = K_\theta(\theta_{\mathrm{R}} - \theta_{\mathrm{L}}) & \\ \theta_{\mathrm{L}} = \dfrac{W_{\mathrm{I}} - W_{\mathrm{L}}}{a/2} & \\ \theta_{\mathrm{R}} = \dfrac{W_{\mathrm{R}} - W_{\mathrm{I}}}{a/2} & \end{array} \quad . \tag{9}$$

Ce modèle est illustré par la Figure 13(a), où la masse $m = \rho Sa$ est égale à la masse de la portion de poutre et $K_\theta = YI/a$ correspond à sa raideur de flexion. Comme précédemment pour la barre, la succession d'un nombre suffisant de cette cellule élémentaire offre un modèle discret approximant le comportement dynamique d'une poutre en flexion.

IV.2 Réseau électrique analogue

L'analogie électromécanique directe appliquée au modèle discret de la Figure 13(a) conduit à la cellule élémentaire électrique de la Figure 13(b). La masse de la cellule est de

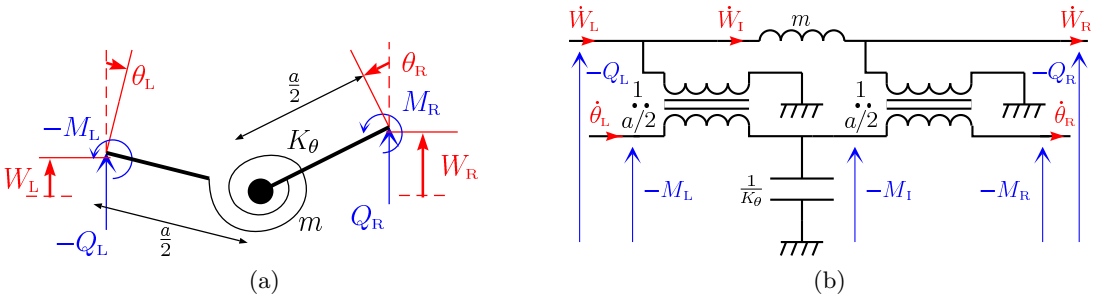

Figure 13: Cellules élémentaires pour la propagation transversale: (a) Portion de poutre discrétisée. (b) Analogue électrique d'une portion de poutre.

nouveau représentée par une inductance et sa raideur intervient au niveau d'un condensateur. Cette portion de réseau est tout de même plus complexe car elle présente deux lignes électriques séparées par des transformateurs de rapport $a/2$. Ceux-ci sont les analogues des bras de levier de longueur $a/2$ qui traduisent les conditions de proportionnalité entre les angles et les déplacements, ainsi qu'entre les moments et les efforts.

Le couplage d'une poutre à son réseau électrique analogue est représenté sur la Figure 14. Deux transformateurs de rapport $\hat{a}/2$ peuvent être remplacés par un seul transformateur de rapport $\hat{a}$ et comme précédemment, aucun condensateur ne doit être ajouté car on peut bénéficier de la capacité piézoélectrique. Une condition de bord libre à l'extrémité d'une poutre impose à son analogue électrique une connexion à la masse du bout de la ligne associée au moment fléchissant ($M = 0$) ainsi qu'à celle associée à l'effort tranchant ($Q = 0$). D'autres conditions aux limites sont naturellement réalisables comme, par exemple, une condition simplement appuyée qui nécessite une connexion à la masse de la ligne associée au moment fléchissant ($M = 0$) et une ligne associée à l'effort tranchant laissée ouverte ($W = 0$).

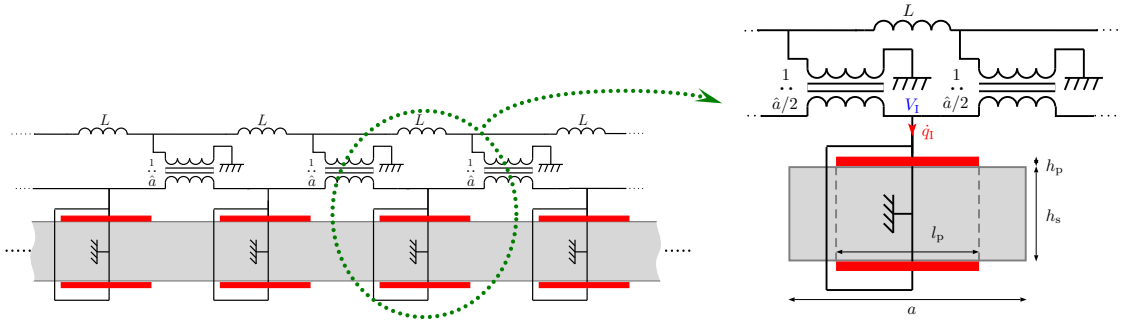

Figure 14: Poutre couplée à son réseau électrique analogue par l'intermédiaire d'une distribution périodique de patchs piézoélectriques et cellule élémentaire associée.

IV.3 Conditions de couplage modal

Comme pour la barre, le réseau électrique relatif à la propagation transversale doit offrir des conditions aux limites analogues et une relation de dispersion similaire à celle de la poutre à contrôler. Cette dernière condition revient à respecter l'égalité

$$\frac{1}{\hat{a}^2}\frac{1}{LC^{\varepsilon}} = \frac{1}{a^2}\frac{K_{\theta}^{E}}{m}, \tag{10}$$

où $\hat{a}$ est le rapport de transformation des transformateurs du réseau électrique. La raideur en flexion en court-circuit K_{θ}^{E}, la masse m et la longueur a étant imposés par les caractéristiques de la poutre et C^{ε} étant la capacité piézoélectrique, le réglage du réseau se fait à travers le choix de l'inductance L et du rapport de transformation $\hat{a}$.

IV.4 Validation expérimentale

L'analyse expérimentale de l'amortissement des vibrations transversales se base sur la même structure que celle utilisée pour l'étude longitudinale. Cependant, l'excitation et la mesure de vitesse sont ici transversales et le réseau est constitué d'une succession de cellules élémentaires électriques telles que celle illustrée sur la Figure 14. Le dispositif expérimental est présenté sur les Figures 15(a) et 15(b). Il fait apparaître la poutre en conditions libre-libre ainsi que le réseau constitué de composants magnétiques passifs, inductances et transformateurs, spécialement conçus pour l'application proposée. Le rapport de transformation choisi étant $\hat{a} = 1$, les inductances doivent être proches de $L = 120$ mH. Pour ce faire, des ferrites RM à haute perméabilité permettent d'atteindre des facteurs de qualité satisfaisants.

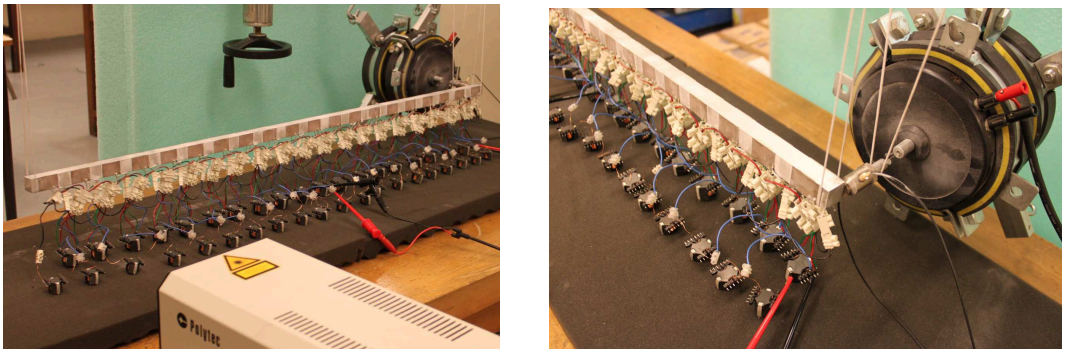

(a) (b)

Figure 15: Dispositif expérimental pour l'analyse de l'amortissement vibratoire transversal: (a) Poutre suspendue couplée à son réseau électrique analogue. (b) Excitation transversale exercée par un pot vibrant suspendu.

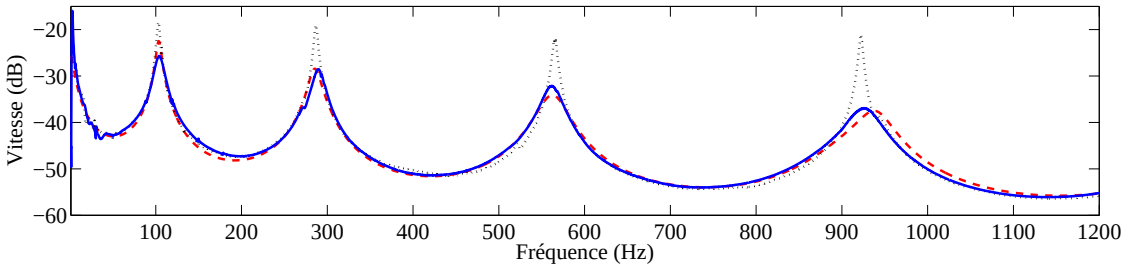

Figure 16: Fonctions de réponse en fréquence pour la vitesse transversale en bout de poutre - $(\cdots)$ réponse expérimentale sans contrôle, (—) réponse expérimentale avec contrôle analogue, $(--)$ réponse simulée avec contrôle analogue.

La réponse fréquentielle de la Figure 16 montre que les résultats expérimentaux concordent avec le modèle basé sur une formulation par matrice de transfert. De plus, une réduction de l'amplitude vibratoire est observée sur une large bande de fréquences. Contrairement aux résultats de la Figure 12, aucun minimum local n'est présent au niveau des résonances de la réponse vibratoire. Ceci s'explique par le fait que les résistances internes des transformateurs utilisés dans le réseau électrique sont non-négligeables et conduisent à un système de contrôle légèrement sur-amorti.

V Amortissement multimodal d'une plaque mince

L'analogue électrique d'une poutre en flexion est étendu à un réseau bidimensionnel pour le contrôle vibratoire d'une plaque mince. Le réseau obtenu est validé numériquement puis expérimentalement avant d'être connecté à un ensemble de patchs piézoélectriques. La mise en œuvre expérimentale montre le potentiel de cette stratégie de contrôle passif en matière d'amortissement multimodal.

V.1 Modèle discret d'une portion de plaque carrée

Le comportement d'une plaque mince peut être décrit par la théorie de Kirchhoff-Love qui conduit à

$$-D\left(\frac{\partial^4 w}{\partial x^4}+2\frac{\partial^4 w}{\partial x^2\partial y^2}+\frac{\partial^4 w}{\partial y^4}\right)=\rho h\frac{\partial^2 w}{\partial t^2}, \tag{11}$$

où x et y sont les deux variables d'espace, t la variable de temps et $w = W(x,y)g(t)$ le déplacement transversal. Pour une plaque de module de Young Y, de coefficient de Poisson ν et d'épaisseur h, $D = \frac{Yh^3}{12(1-\nu^2)}$ représente sa raideur en flexion. À partir de l'Eq. (11), l'extension du cas de flexion unidimensionnelle conduit à un système d'équations

faisant intervenir les variables internes Q, M et θ:

$$\begin{aligned} &\frac{\partial Q_x}{\partial x} + \frac{\partial Q_y}{\partial y} = -\rho h a \omega^2 W && M = aD\left(\frac{\partial \theta_x}{\partial x} + \frac{\partial \theta_y}{\partial y}\right) \\ &Q_x = -\frac{\partial M}{\partial x} && \theta_x = \frac{\partial W}{\partial x} \\ &Q_y = -\frac{\partial M}{\partial y} && \theta_y = \frac{\partial W}{\partial y} \end{aligned} \quad \text{et} \quad . \tag{12}$$

L'application de la méthode des différences finies à l'Eq. (12) permet ensuite d'obtenir un ensemble d'équations discrètes qui définissent le modèle différences finies d'un élément de plaque carré de côté a:

$$\begin{aligned} &Q_\mathrm{R} - Q_\mathrm{L} + Q_\mathrm{T} - Q_\mathrm{B} = -m\omega^2 W_\mathrm{I} && M_\mathrm{I} = D\left(\theta_\mathrm{R} - \theta_\mathrm{L} + \theta_\mathrm{T} - \theta_\mathrm{B}\right) \\ &Q_\mathrm{L} = -\frac{M_\mathrm{I} - M_\mathrm{L}}{a/2} && \theta_\mathrm{L} = \frac{W_\mathrm{I} - W_\mathrm{L}}{a/2} \\ &Q_\mathrm{R} = -\frac{M_\mathrm{R} - M_\mathrm{I}}{a/2} && \theta_\mathrm{R} = \frac{W_\mathrm{R} - W_\mathrm{I}}{a/2} \\ &Q_\mathrm{B} = -\frac{M_\mathrm{I} - M_\mathrm{B}}{a/2} && \theta_\mathrm{B} = \frac{W_\mathrm{I} - W_\mathrm{B}}{a/2} \\ &Q_\mathrm{T} = -\frac{M_\mathrm{T} - M_\mathrm{I}}{a/2} && \theta_\mathrm{T} = \frac{W_\mathrm{T} - W_\mathrm{I}}{a/2} \end{aligned} \quad \text{et} \quad , \tag{13}$$

où 'I' correspond au centre de l'élément de plaque et 'L', 'R', 'B' et 'T' représentent respectivement ses côtés gauche, droit, bas et haut.

V.2 Analogue électrique bidimensionnel

À partir du modèle différences finies d'un élément de plaque représenté par l'Eq. (13), l'analogie électromécanique directe mène à la cellule élémentaire électrique présentée sur la Figure 17. Cette portion de réseau est finalement une extension bidimensionnelle de l'analogue électrique de la Figure 13(b). En effet, $m = \rho h a^2$ représente la masse de la portion de plaque et D est sa raideur en flexion. Quatre transformateurs de rapport $a/2$ assurent l'analogie avec le bras de levier de longueur $a/2$ et un cinquième transformateur de rapport 1 est ajouté pour assurer l'unicité du déplacement au centre de la cellule.

Le choix de conditions aux limites électriques analogues aux conditions aux limites mécaniques devient malheureusement plus difficile à traiter dans un cas bidimensionnel. Bien que les conditions cinématiques de type déplacement nul ou rotation nulle imposent de laisser simplement ouvertes les lignes électriques correspondante, des conditions de type bord libre ne sont pas directement associées à des tensions nulles en bord de la cellule électrique de la Figure 17. Malgré tout, les plaques encastrées ou simplement appuyées n'offrant pas de bord libre, leur analogue électrique peut être directement mis en œuvre avec le réseau passif proposé.

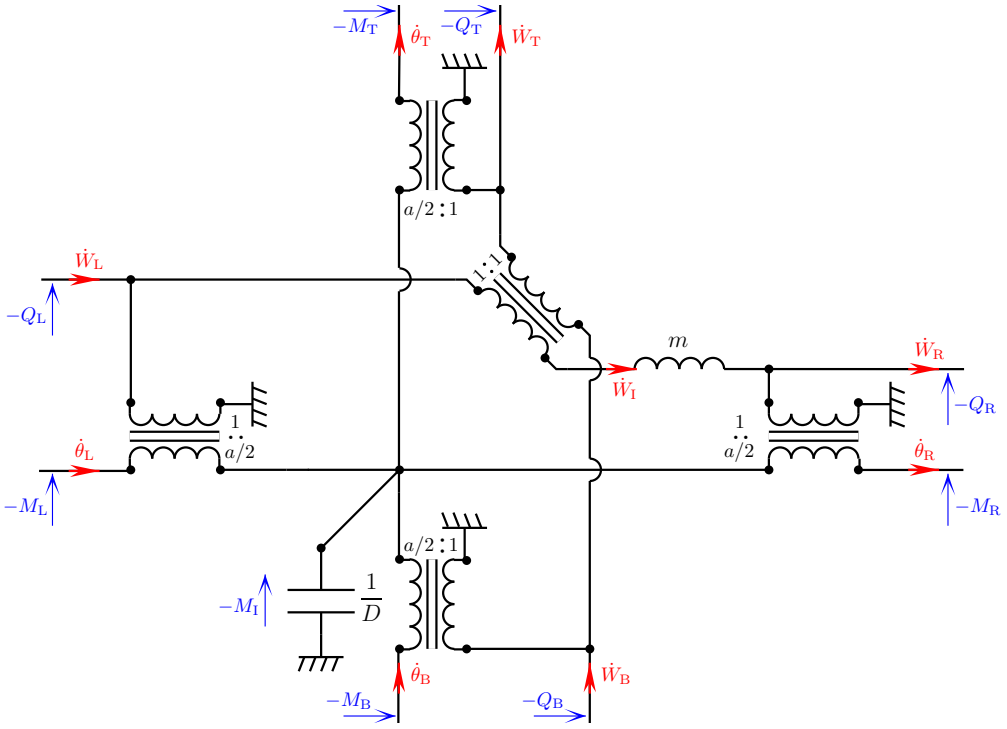

Figure 17: Analogue électrique d'un élément de plaque carré discrétisé.

V.3 Conditions de couplage modal

Le réseau dédié aux plaques est une extension de celui obtenu pour le contrôle d'une poutre. Ainsi, on retrouve la même condition traduisant l'égalisation des relations de dispersion dans les milieux électriques et mécaniques:

$$\frac{1}{\hat{a}^2}\frac{1}{LC} = \frac{1}{a^2}\frac{D}{m}. \tag{14}$$

Associée à des conditions aux limites électriques analogues à celles de la plaque considérée et en utilisant un nombre suffisant de cellules élémentaires, l'Eq. (14) permet de générer des modes électriques qui ont les mêmes fréquences propres et les mêmes formes modales que les modes de plaque.

Pour la modélisation du réseau, connaissant les équations électriques caractérisant la cellule élémentaire de la Figure 17, il devient possible de définir l'équivalent d'une matrice de raideur élémentaire $\boldsymbol{K}^{\mathrm{e}}$ et d'une matrice de masse élémentaire $\boldsymbol{M}^{\mathrm{e}}$. Ces matrices proviennent de la relation entre le vecteur $\boldsymbol{F}^{\mathrm{e}}$ contenant les tensions sur les bords de la cellule et le vecteur $\boldsymbol{q}^{\mathrm{e}}$ associé aux déplacements de charges électriques:

$$\boldsymbol{F}^{\mathrm{e}} = \left(\boldsymbol{K}^{\mathrm{e}} - \omega^2 \boldsymbol{M}^{\mathrm{e}}\right) \boldsymbol{q}^{\mathrm{e}}. \tag{15}$$

L'analogue électrique d'une plaque est construit par assemblage d'un nombre suffisant d'éléments bidimensionnels discrets de façon à approximer la continuité du milieu. De la même façon, le réseau est modélisé par un assemblage de matrices élémentaires. Une analyse modale peut ensuite être appliquée aux matrices globales afin de vérifier la validité de la topologie du réseau et les conditions de couplage modal. L'exemple considéré est l'analogue électrique d'une plaque d'aluminium de 1.9 mm d'épaisseur, 400 mm de longueur et 320 mm de côté en conditions simplement appuyées. Lorsque l'Eq. (14) est respectée, on observe sur la Figure 18(a) que l'augmentation du nombre de cellules élémentaires de l'analogue électrique fait tendre les fréquences propres du réseau discret vers celles de la plaque continue, représentées par des lignes horizontales. De plus, les distributions spatiales du courant électrique représentées sur la Figure 18(b) montrent l'équivalent de déformées modales d'une plaque simplement appuyée. Les simulations numériques valident donc bien l'analogue électrique proposé.

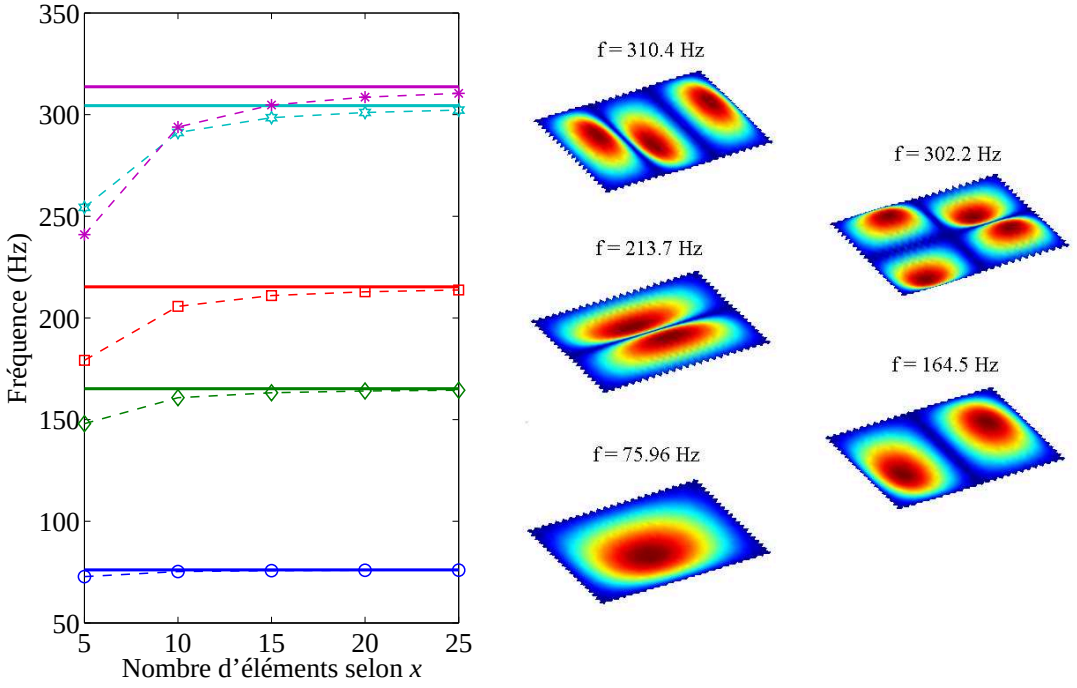

(a) (b)

Figure 18: Analyse modale d'un réseau électrique analogue: (a) Convergence vers les fréquences propres théoriques. (b) Distributions de courant pour un réseau constitué de 25×20 cellules élémentaires.

V.4 Validation expérimentale du réseau analogue

Un réseau bidimensionnel est assemblé afin de valider expérimentalement l'analogue électrique d'une structure de type plaque. Pour des raisons pratiques liées au nombre de composants, l'analyse se limite à un réseau constitué de 5×4 cellules élémentaires. Le réseau électrique étant par la suite destiné au contrôle vibratoire d'une plaque encastrée, des conditions aux limites analogues doivent être respectées en laissant ouvertes toutes les lignes électriques sur les bords du réseau. L'analogue électrique peut donc être assemblé avec 16 condensateurs, 23 transformateurs et 6 inductances. L'organisation spatiale du réseau respecte la topologie périodique imposée par la succession bidimensionnelle de la cellule élémentaire, comme le montrent les Figures 19(a) et 19(b).

Par analogie avec l'analyse vibratoire d'une structure mécanique où l'on applique généralement une force tout en mesurant des champs de vitesse, on applique ici une tension et on mesure les distributions de courant dans le réseau d'inductance. Sur la Figure 20, six résonances sont observées et associées à des distributions de courant équivalentes à des modes de plaque encastrée. Le réseau électrique est donc capable de reproduire la dynamique d'une plaque mince, ce qui valide sa topologie. De plus, la corrélation entre les mesures expérimentales et la simulation valide le modèle basé sur un assemblage de matrices élémentaires.

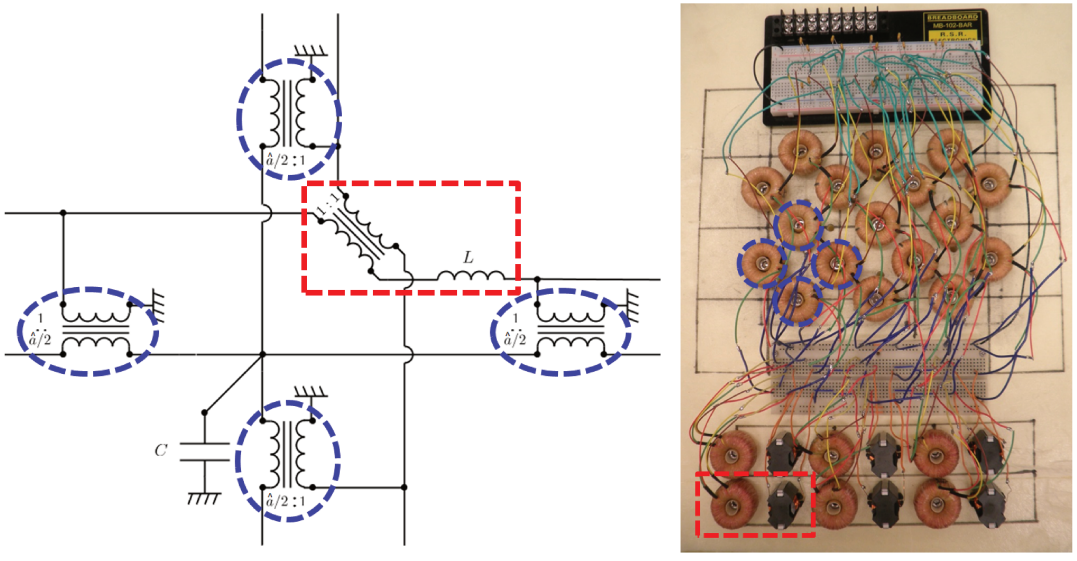

(a) (b)

Figure 19: Fabrication du réseau électrique analogue: (a) Cellule électrique élémentaire. (b) Réseau périodique constitué de 5×4 cellules élémentaires.

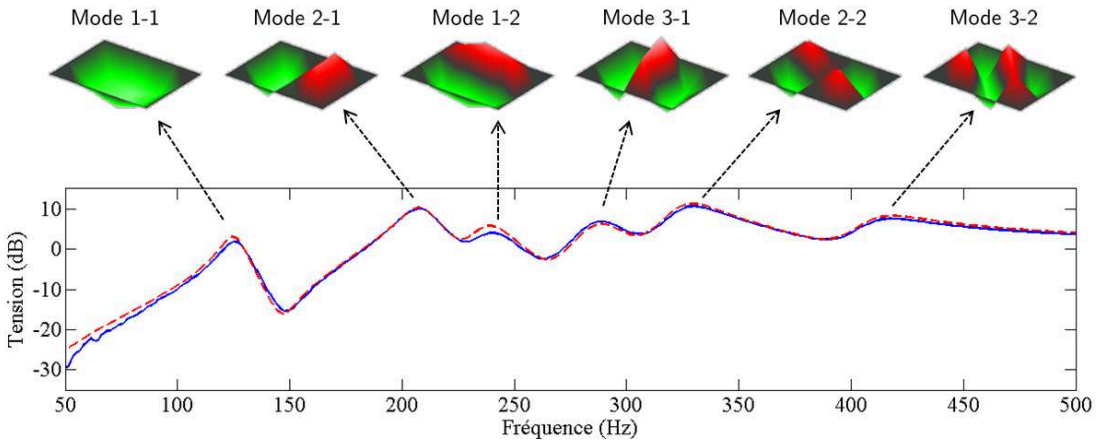

Figure 20: Distributions spatiales du courant et fonctions de réponse en fréquence pour la tension aux bornes d'une inductance avec $L = 0.9$ H et $C = 470$ nF - (—) réponse expérimentale, (– –) réponse simulée.

V.5 Réduction vibratoire d'une plaque encastrée

Dans un objectif d'amortissement vibratoire large bande, vingt patchs piézoélectriques carrés recouvrent une plaque d'aluminium encastrée sur les quatre côtés, comme présenté sur les Figures 21(a) et 21(b). La plaque fait 400 mm de long, 320 mm de hauteur et 1.9 mm d'épaisseur. Les patchs, d'épaisseur 0.27 mm, sont connectés au réseau électrique analogue, lui-même constitué de 20 cellules élémentaires. Des transformateurs électriques de rapport $\hat{a} = 4$ sont utilisés, ce qui conduit à une valeur d'inductance $L = 0.9$ H. Comme pour les analyses unidimensionnelles, un pot vibrant applique un effort en un point de la plaque et un vibromètre laser mesure la vitesse de déplacement transversal. Le couplage du réseau analogue à la plaque encastrée modifie fortement sa réponse fréquentielle. Le

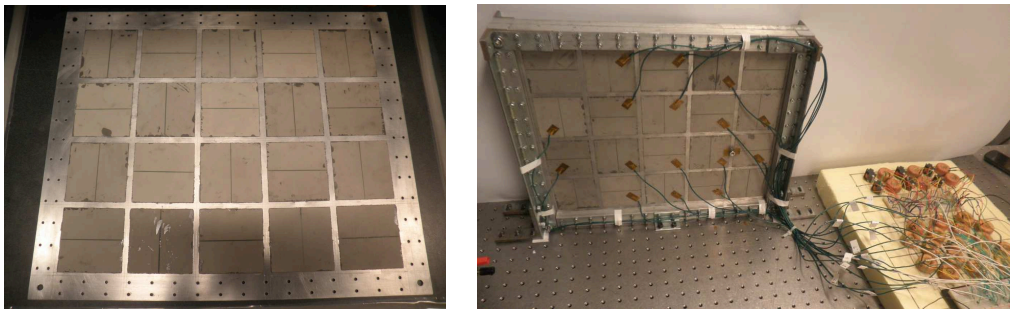

(a) (b)

Figure 21: Dispositif expérimental pour l'amortissement multimodal d'une structure bidimensionnelle: (a) Plaque d'aluminium recouverte de vingt patchs carrés. (b) Encastrement sur les bords et couplage au réseau électrique analogue.

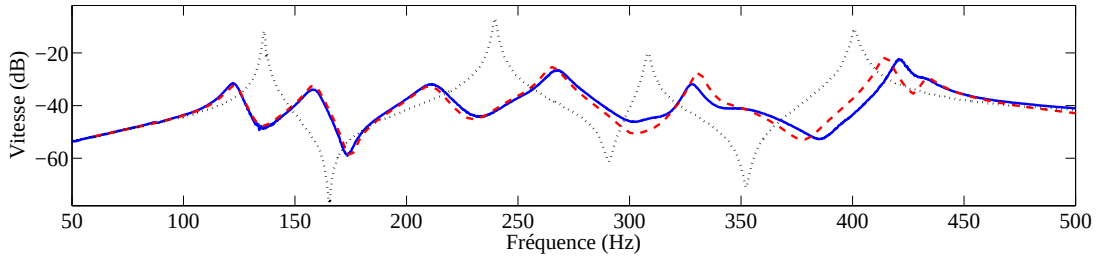

Figure 22: Effet du couplage au réseau analogue sur la réponse vibratoire de la plaque - (· · ·) réponse expérimentale en court-circuit, (—) réponse expérimentale pour $L = 0.9$ H et $R_s^+ = 0\ \Omega$, (– –) réponse simulée pour $L = 0.9$ H et $R_s^+ = 0\ \Omega$.

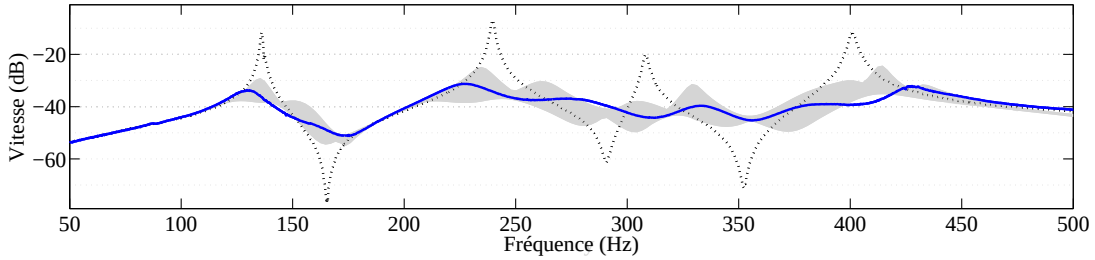

Figure 23: Influence de la valeur des inductances sur l'amortissement vibratoire - (· · ·) réponse expérimentale en court-circuit, (—) réponse expérimentale avec le réseau analogue pour $L = 0.7$ H et $R_s^+ = 180\ \Omega$, ( ) simulation d'une variation de $\pm 30\%$ sur L.

réseau multi-résonant crée l'équivalent d'un amortisseur à masse accordée multimodal comme l'indiquent, sur la Figure 22, les antirésonances bien visibles au niveau des premier et second modes de plaque.

Un modèle numérique a également été développé à partir d'un assemblage d'éléments de plaque couplés au réseau analogue. Ce modèle est validé par les résultats expérimentaux et il offre donc des perspectives intéressantes pour l'optimisation d'un réseau discret couplé à une structure continue. En effet, le réseau analogue est constitué d'un nombre limité de cellules élémentaires ce qui l'éloigne du modèle continu. Dans le cas présent, l'inductance L doit être ajustée à une valeur de 0.7 H afin de mieux positionner les résonances électriques sur la plage de fréquences considérée allant de 50 à 500 Hz. Des résistances $R_s^+ = 180\ \Omega$ sont ensuite ajoutées dans le réseau pour optimiser la réduction vibratoire. Considérant ce réglage du réseau électrique, la Figure 23 montre des réductions de plus de 20 dB sur l'ensemble des modes de plaque considérés, ce qui valide la stratégie d'amortissement par couplage analogue dans un cas bidimensionnel. Enfin, la Figure 23 montre l'effet d'une variation d'inductance sur la dynamique du système couplé. Même avec une variation de l'ordre de $\pm 30\%$ on observe toujours un net amortissement vibratoire ce qui met en avant la robustesse du système de contrôle.

VI Conclusion

Ce résumé étendu offre une description de la stratégie d'amortissement vibratoire de structures mécaniques par couplage piézoélectrique à un réseau électrique analogue. Pour des structures de type barres, poutres ou plaques, une discrétisation du milieu mécanique suivie d'une analogie électromécanique directe a permis de proposer des analogues électriques passifs. Des conditions de réglage des réseaux électriques sont également présentées de façon à assurer une interaction entre les modes électriques et les modes mécaniques sur une large bande de fréquences. Même si la quantité de matériau piézoélectrique ajoutée reste relativement limitée, les validations expérimentales montrent une nette réduction de l'amplitude vibratoire des structures considérées. De nature intrinsèquement passive, cette stratégie d'amortissement vibratoire multimodal semble donc prometteuse, en particulier pour des applications de contrôle embarqué.

Contents

List of Tables

List of Figures

Chapter 1

Introduction

1.1 Motivations

The mass of any vehicle or embedded system is a key factor that strongly influences the global costs in terms of energy consumption. However, reducing the mass of a system is often related to the use of thinner structural elements. Those might generate undesired vibrations when subjected to dynamic loading. Structural vibrations then results in a degradation of the user's convenience through noise or oscillations and more dramatically it can lead to a ruin of the system. In order to reduce vibration, classical solutions are based on local control devices placed between the considered structural element and a reference point. One can mention passive or magnetorheological dampers, as well as cylinder actuators requiring active control strategies. When no fixed point is available, we may consider dynamic vibration absorbers that are placed directly on the structure to control. For instance, the tuned mass dampers [1] can reduce the vibration amplitude around its natural frequency, without any mechanical connection to a reference point. Yet, those local solutions only allow controlling the displacement of a single point of the structure. This is certainly sufficient for rigid bodies but when considering flexible structures, fixing a single point might simply modify the boundary conditions, which would not lead to a global vibration reduction. Distributed solutions are thus considered to generate a vibration control over broader spatial and frequency domains. A strategy consists in distributing highly dissipative material all over the structure. For instance, cyclic deformation of viscoelastic layers generates a dissipation of the mechanical energy into heat. Unfortunately, the damping properties of classical viscoelastic materials decrease significantly at low frequencies and high temperatures.

Piezoelectric materials are capable of converting mechanical energy over wider ranges of frequency and temperature. They also offer a high power density, which explains why they have been used in various industrial applications. Piezoelectric sensors are based on

the direct piezoelectric effect that generates an electric field when the material is subjected to a mechanical strain. Conversely, a strain is observed when applying an electric field across the piezoelectric material. This shows that a distributed control strategy can be implemented by combining arrays of piezoelectric sensors and actuators. The control yet becomes active, which usually requires external instrumentation and power supply. Still, it has been shown that a single piezoelectric patch behaves simultaneously as sensor and actuator when it is connected to an electrical shunt [2, 3]. The piezoelectric element acts as an electromechanical transducer able to convert the mechanical energy into electrical energy, which is then dissipated into a resistor. This solution allows the synthesis of a so-called "smart material" with substantial damping properties. Considering passive electrical shunts, the control does not require any power supply, it is thus completely autonomous and inherently stable.

Hagood and von Flotow [2] have shown that the resonant piezoelectric shunt made of an inductor and a resistor is equivalent to a tuned mass damper. Compared to the purely resistive shunt which is equivalent to a single damper, the resonant shunt offers a significant vibration reduction when the electrical resonance is tuned to a natural frequency of the considered structure. Then, the solution can be distributed all over the structure through an array of piezoelectric patches [4–6]. One of the main limits is that the required inductance values are usually very large [7]. It is still possible to generate synthetic inductors with operational amplifiers [8] but the system then requires a power supply. Another drawback of the resonant shunt strategy is certainly its robustness as a small variation of the inductance can lead to a significant decrease of the damping performance [9]. In the low frequency range, the narrow bandwidth of classical resonant shunt also means that two modes cannot be controlled simultaneously. Multi-resonant shunts have been proposed for this purpose [8, 10, 11] but the number of electrical components makes the practical implementation difficult when considering a large array of piezoelectric patches. Nevertheless, a solution has been given by dell'Isola and his coworkers, who worked actively on interconnected arrays of piezoelectric patches between 1997 and 2005 [12–14]. Interconnecting successive patches creates a multi-resonant network but it also increases the robustness of the control [15, 16] and reduces the inductance requirements [17, 18]. It has been noticed that an optimal eletromechanical coupling can be achieved by implementing an electrical network which is the analogue of the structure to control [19, 20]. From this conclusion, research has been conducted on multimodal damping of beams [21, 22] or plates [23, 24] with passive analogous networks.

Although very promising, damping solutions based on analogous piezoelectric networks have not been implemented into any real application. This is most likely due to the fact that no experimental setup has been developed to validate the theoretical concepts.

A line of inductors has been coupled to an array of piezoelectric patches on a beam [25, 26] but it cannot generate a real multimodal coupling. To this end, an adequate electrical network would be the analogue of a beam [16, 21]. Paschero at al. decided to synthetize this electrical network with operational amplifiers [27, 28]. Electrical circuits solving stability issues were proposed [29] but it seems that they have not been integrated into a complete piezoelectric array. The use of synthetic components had been decided because the passive transformers involved in the beam electrical analogue are difficult to manufacture for broadband and low frequency applications [18]. It was yet proven in the 40's that such analogous electrical network can be implemented with passive components. At that time, no powerful digital computers were available and the analogous electrical networks were used to simulate various mechanical problems [30]. Electrical analogues were first proposed for truss bridges [31] or assembly of beam structures [32, 33]. Then, Kron extended the analysis to numerous differential equations as the compressible fluid flow equations, the electromagnetic field equations of Maxwell or the wave equations of Schrödinger [34, 35]. Concerning the theory of elasticity, 3D models were introduced [35, 36] but real implementations of analogous networks were usually restrained to simpler cases involving one- or two-dimensional structural members. Simulations involving "analog computers" were performed for beams [30, 37], plates [30, 38], stiffened shells [39] and even a whole airplane [40]. We note that this branch of the scientific literature has not been fully exploited since the advent of the modern digital computers in the 60's. Even if it was not the original purpose of the authors, the previous references finally represent an important resource when considering the implementation of multimodal damping with a passive piezoelectric network.

1.2 Objectives

The main objective of this thesis is to develop a passive control of structural vibrations based on piezoelectric coupling to an analogous network. In this work, passive means that no power supply or synthetic electrical components are required. The structures under consideration are rods, beams or plates that are covered with a periodic array of piezoelectric patches. The array is distributed all over the structures, therefore no optimization of the patch positioning is considered. The coupling to an electrical analogue means that the resulting control is based on multi-resonant networks, which necessarily involves inductors. Furthermore, as the electrical analogues are obtained from classical mechanical models that have a limited range of validity, we restrain the analysis to linear vibrations in the low-frequency range. When considering the existing literature focusing on interconnected array of piezoelectric patches, it has not been found any experimental validation of a multimodal damping with an analogous electrical network. This might

be explained by the fact that the practical implementation of a proper electrical network requires further analysis. Moreover, it has been remarked that most of the proposed models focuses on an electrical continuum, which does not offer an adequate comparison with a real system involving a finite number of piezoelectric patches. Considering the previous comments, the objectives of the thesis are detailed as follows:

- Propose adequate topologies and practical designs for electrical analogous networks made of passive electrical components;
- Develop electromechanical models for periodic structures involving a finite number of interconnected piezoelectric patches;
- Build experimental setups to prove the practical feasibility of a multimodal damping through a piezoelectric analogous network for the control of rods, beams and plates.

1.3 Outline

The present thesis is organized into four main chapters that can be read one by one. Yet, for a better understanding and as some references to previous chapters appears from time to time, it is advised to follow the conventional order of the manuscript. This offers a gradual increase in the complexity of the models and related concepts. Indeed, Chap. 2 starts with classical resonant shunts for the control of a single mode. The passive piezoelectric control is then applied to multimodal structures through multi-resonant networks. One-dimensional structures such as rods and beams are treated in Chaps. 3 and 4 respectively. At last, Chap. 5 extends the control strategy to the damping of a plate with a two-dimensional analogous electrical network.

- Chapter 2 gives an introduction to piezoelectric transducers. The 3D linear piezoelectricity theory is reduced to the case of a one-dimensional transducer. It is observed that electrical shunts modify the equivalent stiffness of the piezoelectric element. Then, focusing on resonant piezoelectric control, the electromechanical analogy shows that the resonant shunt is equivalent to a tuned mass damper. Its natural frequency and damping coefficient have to be optimized to reduce the vibration amplitude. However, it is noticed that the optimal inductance and resistance values can usually not be satisfied with standard electrical components. This is the reason why we propose a design of suitable inductors with closed magnetic cores made of high permeability materials.
- Chapter 3 deals with the damping of a rod through a periodic array of piezoelectric patches. A solution involving identical resonant shunts is compared to the use

of a multi-resonant network approximating the modal properties of the rod. This last control solution is equivalent to a multimodal tuned mass damper whose purely mechanical model is also given to illustrate the electromechanical analogy. Actually, there is a coupling of two periodic waveguides, which can be analyzed with a transfer matrix method. A unit cell involving both mechanical and electrical contributions is first defined through a fully discrete model. The model is then improved by ensuring the continuity of the mechanical part of the unit cell but maintaining the discrete nature of the electrical network. Discrete and semi-continuous models are then compared to determine their respective ranges of validity. In the end, an experimental setup allows the validation of the numerical model but, above all, it proves the feasibility of the multimodal damping of a rod with an analogous piezoelectric network.

- Chapter 4 is rather similar to Chap. 3 in terms of global layout because the same methods are applied to the case of a beam. The main difference is that independent resonant shunts are no more considered as we only focus on multimodal control with an analogous electrical network whose advantages have been illustrated for a rod. Here, the analogous network is obtained from a finite difference method applied to the Euler-Bernoulli equation of motion. The periodic electromechanical structure made of an interconnected array of piezoelectric patches on a beam is still modeled with a transfer matrix method. As in Chap. 3, discrete and semi-continuous models are compared in order to determine the most appropriate over the considered frequency range. The models are also used to design an experimental setup involving the electrical analogue of a beam. The electrical network requires transformers whose practical design is detailed. Once the network is coupled to the beam, we get a significant multimodal damping, which validates the strategy for the control of bending waves.

- Chapter 5 extends the use of an analogous electrical network to the control of a plate. Here, a finite difference model obtained from the Kirchhoff-Love plate theory is used to define an analogous electrical unit cell. The complete electrical network is then modeled by following an assembly process similar to what is classically performed through finite element methods. The plate electrical analogue is implemented experimentally and electrical plate-like mode shapes are observed. Over a second phase, an electromechanical model is proposed for a piezoelectric laminate connected to an electrical network. This model is validated through experiments when the analogous electrical network is coupled to a piezoelectric plate. A broadband vibration reduction is obtained from a suitable tuning of the electrical network. Moreover, the robustness of the control strategy is evaluated.

Chapter 2

Passive vibration damping with resonant piezoelectric shunts

Abstract: *Considering piezoelectric damping, a resonant shunt can lead to a significant vibration reduction when tuned to the mechanical mode to control. This requires specific inductance and resistance whose values are defined from the optimization of a theoretical transfer function. However, limits appear when looking at practical applications in a low frequency range: the required inductance is often too high to be satisfied with standard passive components. Suitable inductors can yet be designed for applications requiring high inductance and low resistance values. Indeed, the permeance of a magnetic circuit can be significantly increased with closed cores made of high permeability materials. Three designs are described and compared: an inductor from standard series and two handmade inductors involving a ferrite core and a nanocrystalline toroid. The components are successively integrated into a piezoelectric shunt dedicated to the vibration control of a cantilever beam. It is shown that custom designs can definitely extend the application of passive resonant shunt strategies to lower frequency.*

Contents

2.1 Introduction

Structural damping occurs when shunting piezoelectric material with passive electrical circuits as the resistive and resonant shunts that were described by Hagood and von Flotow [2]. The mechanical energy of a vibrating structure is converted by a piezoelectric patch into electrical energy, which is then dissipated into a resistor. The resonant shunt requires an inductor that is combined to the piezoelectric capacitance in order to generate an electrical resonance. Similarly to what is observed with a tuned mass damper [1, 41], the electrical resonance enhances the energy transfer when tuned to the mechanical mode to control. Consequently, a passive and potentially lightweight solution can provide significant vibration reduction without strong modification of the mechanical structure. This control strategy was first applied through single-mode shunts [2, 42–45] and then extended to multi-mode shunts [8, 10, 11, 46].

A drawback of the resonant shunt technique is that practical applications generally require large inductance values. The notion of "large inductance" is not clearly defined in the shunt damping literature because, depending on the authors, it can be in a range of 0.1 H, 10 H or even 1000 H [7, 43, 46]. In any case, the standard inductor series are usually limited to 0.5 H, which cannot satisfy most of the resonant shunt applications. Fleming et al. [7] proposed to use additional capacitance across the electrodes of the piezoelectric patches in order to decrease the required inductance. However, they also show that this solution induces a reduction of the damping performance. Another solution was proposed by Mokrani et al. [47], who focused on an array of patches for the control of a rotationally periodic structure. The piezoelectric capacitance of the shunt is actually increased by suitable parallel connections. The main limit is that the whole piezoelectric network is designed for the control of a single pair of modes. Even if the inductance requirement can eventually be reduced, standard inductors present another limit that is rarely highlighted. Indeed, they offer an internal resistance which is usually too large for resonant shunt applications [48]. The challenging inductance and resistance requirements explain why most of the experimental validations involving resonant shunts are performed with synthetic inductors [8, 28, 43, 46, 48–51]. The use of those active circuits pushes back the limits of physical inductors but it questions the implementation of a purely passive resonant shunt damping.

A passive inductor is commonly made of a coil of conductive wire wound around a magnetic circuit. Contrary to what has been sometimes stated [7, 47], passive inductors above 1 H are easily feasible with closed magnetic cores [52, 53]. Moreover, the direct equivalence between large inductance and large weight or volume [48, 50, 51] is unfunded because the selection of a magnetic core depends on the energy stored in the component.

Ferrite cores are easily available and give access to large inductance values [53, 54]. Furthermore, numerous magnetic materials with larger permeabilities are also available. For example, nanocrystalline alloys exhibit permeabilities up to ten times the highest ferrite permeabilities. The required inductance can then be obtained with a fewer number of turns, which reduces the internal resistance of the component. The use of closed magnetic circuits with high permeability materials thus enables the design of inductors with large inductance values and high quality factors [54]. This allows the application of piezoelectric damping strategies with purely passive components.

The first objective of this chapter is to introduce the theoretical concepts related the analysis of piezoelectric shunts. From the 3D linear theory of piezoelectricity, one defines a one-dimensional model for a piezoelectric transducer connected to an electrical circuit. It is then focused on the case of a resonant shunt made of an inductor and a resistor. An optimal tuning of the electrical component is defined by minimizing the displacement of the structure to control. Yet, we note that practical applications can lead to very high inductance values that cannot be satisfied with standard inductors. A last section thus shows that closed core inductors can be of great interest for resonant piezoelectric damping. The main characteristics of passive inductors are described and it is explained how to select a suitable magnetic core from resonant shunt specifications. Suitable electrical models are also given in order to better understand the frequency dependence that is observed with passive components. The end of the chapter is then devoted to the design of inductors for the control of a cantilever beam with a pair of piezoelectric patches. A ferrite core and a nanocrystalline toroid are selected and the resulting components are compared to standard inductors. The limits of the three designs are observed by considering their ability to damp the first three bending modes of the example cantilever beam.

2.2 Piezoelectric transducers

Several applications based on piezoelectric systems are illustrated through a brief history of piezoelectricity. Afterward, the 3D linear theory is reduced to the case of a one-dimensional piezoelectric transducer that is modeled by an electrical circuit or a discrete mechanical structure. The influence of an electrical shunt connected to the piezoelectric transducer is presented through the definition of an equivalent Young's modulus, which depends on the considered electrical impedance.

2.2.1 A brief history of piezoelectric materials and applications

In 1880, Pierre and Jacques Curie measured electric charges on surface of crystals stressed by a mechanical load. This was the first experimental demonstration of the

direct piezoelectric effect, which means the generation of electricity resulting from pressure. Actually, they found that crystals, such as tourmaline, quartz, topaz, Rochelle salt or even cane sugar, are able to generate an electric charge displacement when their asymmetric crystallographic structures are subjected to deformation. The converse piezoelectric effect was then predicted through the thermodynamical theory proposed by Gabriel Lippmann in 1881. This converse effect was validated by the Curie brothers, who were able to observe a mechanical stress when applying an electric field on piezoelectric crystals. This experiment proved the reversibility of piezoelectric materials that can act as transducers between mechanical and electrical domains. About 30 years later, in 1910, Woldemar Voigt published his "Lehrbuch der Kristallphysik" [55], which became a reference work defining the tensor analysis of piezoelectric crystals.

Several applications quickly appeared but they were first dedicated to laboratory instrumentation. One can mention the microbalance, based on the direct piezoelectric effect, and high voltage generators benefiting from the converse effect. The first industrial applications came with World War I when the ultrasonic submarine detector was introduced by Paul Langevin as a precursor of the modern sonar. Then, Walter Cady built the first quartz crystal oscillator in 1921, which had a great impact on the development of the quartz clock. Other consumer applications grew with the improvement of piezoelectric materials: new type of phonograph, acoustic transducers, accelerometers, microphones, pressure sensors...

The growth of piezoelectric applications speeded up after World War II with the discovery of synthetic ceramic materials, as barium titanate and lead zirconate titanate (PZT), offering piezoelectric constants considerably higher than natural crystals. Furthermore, the fact that those new materials can be manufactured allows choosing their properties for specific applications. A strong development of piezoelectric systems was observed in Japan, where the piezoelectric industry was less subjected to patents or classified applications compared to the US market. Initiated by Issac Koga, the Japanese research led to a large amount of modern consumer systems such as filters for radio and television, piezo igniters or remote control systems.

Nowadays, the research on piezoelectricity is even more active with the improvement of the industrial process, which offers an easier access to high quality piezoelectric materials. Several research applications consider the use of polymers, as the polyvinylidene fluorides (PVDF), whose piezoelectric properties were discovered by Kawai in 1969 [56]. Its flexibility and low density makes it a serious candidate for robotics and biomedical systems [57, 58]. Recently, energy harvesting has also become a very active research area. The idea is to benefit from the direct piezoelectric effect in order to generate electrical power from ambient vibrations [59–63]. This solution allows using embedded electronics without any

need of external power supply or heavy energy storage system. Finally, one actual interest in piezoelectricity still concerns vibration damping. Based on the converse piezoelectric effect, active solutions give a way to control a structure from a suitable voltage applied to piezoelectric elements [64–67]. Another strategy benefiting simultaneously from both direct and converse piezoelectric effects relies on electrical shunts connected to piezoelectric patches. A strong coupling between the mechanical and the electrical domains can offer significant damping performances with purely passive circuits. The piezoelectric shunt solution was first considered by Forward [42] in 1979 and then formalized by Hagood and von Flotow [2] in 1991. This last paper has certainly been the starting point of numerous studies and it is still a reference work in the today's active area of piezoelectric shunt damping.

2.2.2 3D linear piezoelectricity

According to the IEEE Standards on piezoelectricity [68], the constitutive equations for 3D linear piezoelectricity can be written as

$$\begin{array}{l} \varepsilon_{ij} = s^E_{ijkl}\sigma_{kl} + d_{kij}E_k \\ D_i = d_{ikl}\sigma_{kl} + \epsilon^\sigma_{ik}E_k \end{array} , \tag{2.1}$$

where ε_{ij}, σ_{ij}, D_i and E_k represent respectively the strain, stress, electric displacement and electric field components. The constants s^E_{ijkl} refer to the elastic compliance at constant electric field, d_{kij} represents the piezoelectric constants and ϵ^σ_{ik} is the permittivity at constant stress. One then focuses on the case of a transverse isotropic PZT, meaning that the ceramic is isotropic in the plane perpendicular to the direction of polarization [69]. Using the Voigt notation defined in Tab. 2.1, Eq. (2.1) is written under a matrix form, which simplifies as

$$\begin{bmatrix} \varepsilon_1 \\ \varepsilon_2 \\ \varepsilon_3 \\ \varepsilon_4 \\ \varepsilon_5 \\ \varepsilon_6 \\ D_1 \\ D_2 \\ D_3 \end{bmatrix} = \left[\begin{array}{cccccc|ccc} s^E_{11} & s^E_{12} & s^E_{13} & 0 & 0 & 0 & 0 & 0 & d_{31} \\ s^E_{12} & s^E_{11} & s^E_{13} & 0 & 0 & 0 & 0 & 0 & d_{31} \\ s^E_{13} & s^E_{13} & s^E_{33} & 0 & 0 & 0 & 0 & 0 & d_{33} \\ 0 & 0 & 0 & s^E_{44} & 0 & 0 & 0 & d_{15} & 0 \\ 0 & 0 & 0 & 0 & s^E_{44} & 0 & d_{15} & 0 & 0 \\ 0 & 0 & 0 & 0 & 0 & s^E_{66} & 0 & 0 & 0 \\ \hline 0 & 0 & 0 & 0 & d_{15} & 0 & \epsilon^\sigma_{11} & 0 & 0 \\ 0 & 0 & 0 & d_{15} & 0 & 0 & 0 & \epsilon^\sigma_{11} & 0 \\ d_{31} & d_{31} & d_{33} & 0 & 0 & 0 & 0 & 0 & \epsilon^\sigma_{33} \end{array}\right] \begin{bmatrix} \sigma_1 \\ \sigma_2 \\ \sigma_3 \\ \sigma_4 \\ \sigma_5 \\ \sigma_6 \\ E_1 \\ E_2 \\ E_3 \end{bmatrix} \tag{2.2}$$

when the PZT ceramic is polarized along the direction '3'.

Considering that the only non-zero electric field component is along '3' and that the PZT is free along '2' and '3', i.e. $\sigma_2 = \sigma_3 = 0$, then

$$\begin{array}{l} \varepsilon_1 = s^E_{11}\sigma_1 + d_{31}E_3 \\ D_3 = d_{31}\sigma_1 + \epsilon^\sigma_{33}E_3 \end{array} , \tag{2.3}$$

Table 2.1: Tensor notation and Voigt notation.

	Stress						Strain					
Tensor	σ_{11}	σ_{22}	σ_{33}	σ_{23}	σ_{13}	σ_{12}	ε_{11}	ε_{22}	ε_{33}	$2\varepsilon_{23}$	$2\varepsilon_{13}$	$2\varepsilon_{12}$
Voigt	σ_1	σ_2	σ_3	σ_4	σ_5	σ_6	ε_1	ε_2	ε_3	ε_4	ε_5	ε_6

which is equivalent to

$$\begin{aligned} \sigma_1 &= \frac{1}{s_{11}^E}\varepsilon_1 - \frac{d_{31}}{s_{11}^E}E_3, \\ D_3 &= \frac{d_{31}}{s_{11}^E}\varepsilon_1 + \left(\epsilon_{33}^\sigma - \frac{d_{31}^2}{s_{11}^E}\right)E_3 \end{aligned} . \tag{2.4}$$

The material constants s_{11}^E, d_{31} and ϵ_{33}^σ are here highlighted because they are commonly given by the piezoelectric material manufacturers.

2.2.3 One-dimensional model for a thin piezoelectric patch

A thin piezoelectric patch under plane stress assumption and longitudinal excitation satisfies the one-dimensional stress-charge form in Eq. (2.4) when '1' refers to the longitudinal direction and '3' to the direction of polarization [70]. So,

$$\begin{aligned} \sigma_1 &= \bar{c}_{11}^E\varepsilon_1 - \bar{e}_{31}E_3 \\ D_3 &= \bar{e}_{31}\varepsilon_1 + \bar{\epsilon}_{33}^\varepsilon E_3 \end{aligned} , \tag{2.5}$$

where $\bar{c}_{11}^E = 1/s_{11}^E$, $\bar{e}_{31} = d_{31}/s_{11}^E$ and $\bar{\epsilon}_{33}^\varepsilon = \epsilon_{33}^\sigma - d_{31}^2/s_{11}^E$. σ_1 and ε_1 represent the longitudinal stress and strain, D_3 is the transverse electric displacement and E_3 is the transverse electric field. The longitudinal stress is considered uniform along the cross-section and it is thus given by $\sigma_1 = N_\mathrm{p}/S_\mathrm{p}$, where N_p is the normal force applied to the patch and S_p is its cross-sectional area. The considered piezoelectric patch has a length l_p, a width b_p and a thickness h_p, which gives $S_\mathrm{p} = b_\mathrm{p}h_\mathrm{p}$. Still assuming a thin patch, the electric field E_3 is also considered constant along the thickness [70]. So, $E_3 = -V_\mathrm{p}/h_\mathrm{p}$, where V_p is the voltage between the two electrodes of the piezoelectric patch. At last, the electric charge q_p on an electrode of surface area $A_\mathrm{p} = b_\mathrm{p}l_\mathrm{p}$ is related to the electric displacement through $q_\mathrm{p} = -\int D_3 dA_\mathrm{p}$. Consequently, the local piezoelectric formulation (2.5) can be recast into the global system

$$\begin{aligned} N_\mathrm{p} &= Y_\mathrm{p}^E S_\mathrm{p}\varepsilon_1 - e_\mathrm{p}V_\mathrm{p} \\ q_\mathrm{p} &= e_\mathrm{p}\Delta U_\mathrm{p} + C_\mathrm{p}^\varepsilon V_\mathrm{p} \end{aligned} , \tag{2.6}$$

where $\Delta U_\mathrm{p} = U_{\mathrm{pR}} - U_{\mathrm{pL}}$ is the difference between the longitudinal displacements at both right and left ends of the piezoelectric patch. Furthermore, $Y_\mathrm{p}^E = \bar{c}_{11}^E$ is the short-circuited Young's modulus, $e_\mathrm{p} = -b_\mathrm{p}\bar{e}_{31}$ is the longitudinal coupling coefficient and $C_\mathrm{p}^\varepsilon = \bar{\epsilon}_{33}^\varepsilon A_\mathrm{p}/h_\mathrm{p}$ is the blocked capacitance, which is obtained when $\Delta U_\mathrm{p} = 0$.

Note that the global constants appearing in Eq. (2.6) are valid only if the considered piezoelectric patch is free along the direction '2', i.e. $\sigma_2 = 0$. This is not true if the patch is glued onto a substrate because it would be constrained along both principal directions. For instance, a very stiff substrate would induce $\varepsilon_1 = \varepsilon_2 = 0$, and the direct measurement of the piezoelectric capacitance would not give C_p^ε but a significantly lower value [17, 71], later defined in Chap.5. In any case, the general form used to described the 1D piezoelectric coupling in Eq. (2.6) is still valid and the global constants can eventually be updated depending on the considered case of application.

2.2.4 Equivalent circuit model of a piezoelectric transducer

Regarding a thin piezoelectric patch stressed along its longitudinal direction, if its length l_p is sufficiently small compared to the considered wavelength, the strain ε_1 can be seen as uniform over l_p. Consequently, ε_1 can be defined as the engineering strain, from a difference between the positions at the left and right ends of the element: $\varepsilon_1 = (U_{\mathrm{pR}} - U_{\mathrm{pL}})/l_\mathrm{p}$. Equation (2.6) thus gives

$$\begin{array}{l} N_\mathrm{p} = K_\mathrm{p}^E(U_{\mathrm{pR}} - U_{\mathrm{pL}}) - e_\mathrm{p}V_\mathrm{p} \\ q_\mathrm{p} = e_\mathrm{p}(U_{\mathrm{pR}} - U_{\mathrm{pL}}) + C_\mathrm{p}^\varepsilon V_\mathrm{p} \end{array} , \tag{2.7}$$

where $K_\mathrm{p}^E = \bar{c}_{11}^E S_\mathrm{p}/l_\mathrm{p}$ is the stiffness of the patch at constant electric field, i.e. when the patch is short-circuited ($V_\mathrm{p} = 0$). In order to show the analogy with a problem involving electrical components under harmonic excitation, the global formulation in Eq. (2.7) is written as

$$\begin{array}{l} -N_\mathrm{p} = \frac{K_\mathrm{p}^E}{\mathrm{j}\omega}(\dot{U}_{\mathrm{p_L}} - \dot{U}_{\mathrm{p_R}}) + e_\mathrm{p}V_\mathrm{p} \\ V_\mathrm{p} = \dfrac{1}{\mathrm{j}\omega C_\mathrm{p}^\varepsilon}\left(\dot{q}_\mathrm{p} + e_\mathrm{p}(\dot{U}_{\mathrm{p_L}} - \dot{U}_{\mathrm{p_R}})\right) \end{array} , \tag{2.8}$$

where j is the imaginary unit. Equation (2.8) is then illustrated by the electric circuit in Fig. 2.1(a) representing a piezoelectric transducer, i.e. a device based on electrostatic coupling capable of converting mechanical energy into electrical energy and reciprocally. The transformer representing the coupling is between the left and right branches, which refers respectively to the mechanical and electrical domains [72, 73]. The whole electromechanical system can thus be represented by an electrical circuit involving passive components. This is made possible by the use of the direct electromechanical analogy which establishes an equivalence between a velocity and a current as well as between a force and a voltage [74], as it is observed in the left branch of Fig. 2.1(a). An alternative might have been to consider velocity-voltage and force-current equivalences through the so-called indirect or inverse analogy [75]. However, Bloch showed that only the direct analogy allows representing an electrostatic coupling with a transformer [74]. So, it is chosen to consider the direct

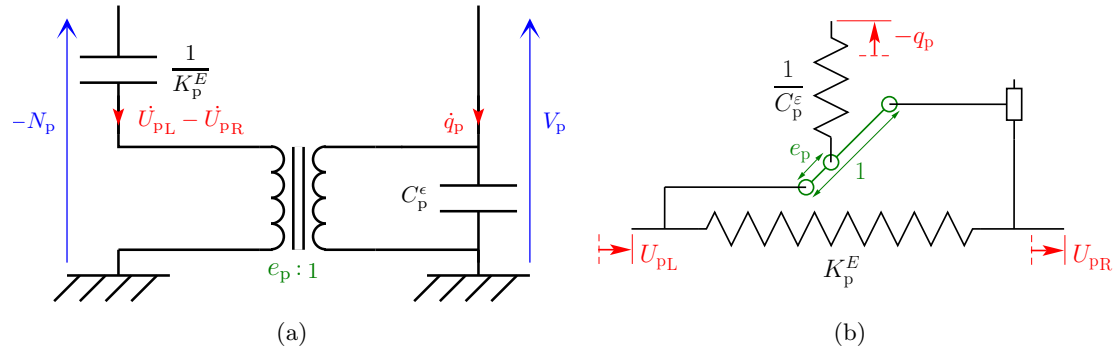

Figure 2.1: Discrete model for a piezoelectric transducer: (a) Equivalent electrical circuit. (b) Mechanical model.

analogy in all the following developments focusing on the representation of piezoelectric coupling with passive electrical circuits.

The piezoelectric transducer has been illustrated by an electrical circuit in Fig. 2.1(a) but a purely mechanical representation is also possible. Indeed, Eq. (2.7) can be written

$$\begin{aligned} N_\mathrm{p} &= K_\mathrm{p}^E (U_\mathrm{pR} - U_\mathrm{pL}) - e_\mathrm{p} V_\mathrm{p} \\ -V_\mathrm{p} &= \frac{1}{C_\mathrm{p}^\varepsilon} \left(-q_\mathrm{p} + e_\mathrm{p} (U_{\mathrm{p}_\mathrm{R}} - U_{\mathrm{p}_\mathrm{L}}) \right) \end{aligned} , \tag{2.9}$$

which shows that the total force N_p applied between both ends of the transducer is the sum of a purely elastic contribution involving a stiffness K_p^E and an additional force $-e_\mathrm{p} V_\mathrm{p}$, which depends on q_p. This can be represented by the mechanical model in Fig. 2.1(b), where $-V_\mathrm{p}$ represents the force applied by the spring of stiffness $1/C_\mathrm{p}^\varepsilon$ to the lever. Its elongation is equal to $-q_\mathrm{p} + e_\mathrm{p}(U_{\mathrm{p}_\mathrm{R}} - U_{\mathrm{p}_\mathrm{L}})$, which is the result of the lever placed at 45 degrees from both vertical and horizontal axis. This lever of ratio e_p is finally the exact analogue of the e_p:1 transformer represented in Fig. 2.1(a).

2.2.5 Electrical shunt on a piezoelectric transducer

Connecting an electrical shunt of impedance $Z(\omega)$ on a piezoelectric transducer leads to the electrical circuit in Fig. 2.2. The piezoelectric voltage V_p and the charge displacement q_p are no more independent because

$$V_\mathrm{p} = -Z(\omega) \dot{q}_\mathrm{p}. \tag{2.10}$$

By substituting Eq. (2.10) into Eq. (2.7), one obtains

$$N_\mathrm{p} = \left[K_\mathrm{p}^E + \frac{e_\mathrm{p}^2}{C_\mathrm{p}^\varepsilon + \dfrac{1}{\mathrm{j}\omega Z(\omega)}} \right] \Delta U_\mathrm{p}, \tag{2.11}$$

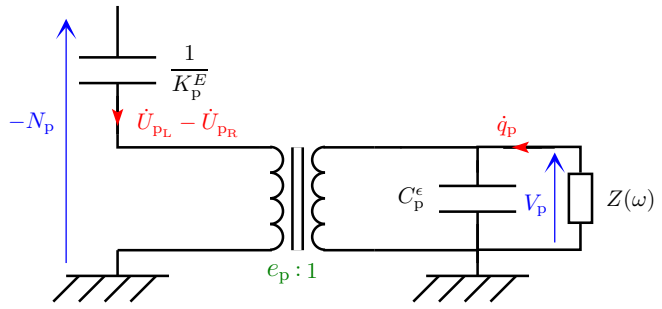

Figure 2.2: Electrical shunt of impedance $Z(\omega)$ on a piezoelectric transducer.

which defines an equivalent stiffness depending on the impedance of the electrical shunt. If we rather focus on an equivalent Young's modulus $Y_{\mathrm{p}}(\omega)$ satisfying $N_{\mathrm{p}} = Y_{\mathrm{p}}(\omega) S_{\mathrm{p}} \Delta U_{\mathrm{p}} / l_{\mathrm{p}}$, Eq. (2.11) gives

$$Y_{\mathrm{p}}(\omega) = \bar{c}_{11}^E \left[1 + \frac{k_{31}^2}{1 + \dfrac{1}{\mathrm{j}\omega C_p^{\varepsilon} Z(\omega)}} \right], \quad \text{where} \quad k_{31} = \sqrt{\frac{\bar{e}_{31}^2}{\bar{c}_{11}^E \bar{\epsilon}_{33}^{\varepsilon}}}. \tag{2.12}$$

From this equivalent Young's modulus of the shunted piezoelectric material, one can define an equivalent Young's modulus in open-circuit obtained when $Z(\omega)$ goes to infinity:

$$Y_{\mathrm{p}}^D = \bar{c}_{11}^E + \frac{\bar{e}_{31}^2}{\bar{\epsilon}_{33}^{\varepsilon}} = \frac{1}{s_{11}^E - \dfrac{d_{31}^2}{\epsilon_{33}^{\sigma}}}. \tag{2.13}$$

Note that the equivalent Young's modulus has a physical meaning only when considering large wavelength compared to the length of the piezoelectric element, that is ε_1 can be approximated by $(U_{\mathrm{pR}} - U_{\mathrm{pL}})/l_{\mathrm{p}}$. If this is not true, Eq. (2.11) is not valid and the actual normal force is found from Eqs. (2.6) and (2.10):

$$N_{\mathrm{p}} = Y_{\mathrm{p}}^E S_{\mathrm{p}} \varepsilon_1 + \frac{e_{\mathrm{p}}^2}{C_{\mathrm{p}}^{\varepsilon} + \dfrac{1}{\mathrm{j}\omega Z(\omega)}} \Delta U_{\mathrm{p}}. \tag{2.14}$$

Considering a case where a piezoelectric patch is subjected to a strain whose typical wavelength is equal to the length of the patch, we have $U_{\mathrm{pL}} = U_{\mathrm{pR}}$ therefore $\Delta U_{\mathrm{p}} = 0$, which means that the normal force N_{p} does not depend on the impedance $Z(\omega)$ anymore. The equivalent Young's modulus is then equal to Y_{p}^E whatever the electrical shunt, even with an open-circuited patch. This illustrates the charge cancellation phenomenon that ruins the piezoelectric effect for short wavelength compared to the length of the piezoelectric element.

Under large wavelength condition, we remark from Eq. (2.12) that the equivalent Young's modulus of a shunted piezoelectric transducer tends to infinity when

$$Z(\omega) = -\frac{1}{\mathrm{j}\omega C_{\mathrm{p}}^{\varepsilon}}. \tag{2.15}$$

Two simple electrical shunts can satisfy Eq. (2.15). The first solution is

$$Z(\omega) = \frac{1}{\mathrm{j}\omega C} \quad \text{where} \quad C = -C_{\mathrm{p}}^{\varepsilon}, \tag{2.16}$$

which corresponds to a negative capacitance whose value counterbalances the piezoelectric capacitance. A limit of this solution is that it is subjected to stability issues [76]. Furthermore, a negative capacitance cannot be implemented passively and thus requires an external power source. Yet, an "infinite" Young's modulus Y_{p} can also be obtained with

$$Z(\omega) = \mathrm{j}\omega L \quad \text{where} \quad L = \frac{1}{\omega_e^2 C_{\mathrm{p}}^{\varepsilon}}, \tag{2.17}$$

which corresponds to a shunt involving an inductor. Here, the condition in Eq. (2.15) is only satisfied at one specific angular frequency $\omega = \omega_e$. On the other hand, the shunt can be implemented with a purely passive component, which induces inherent stability and self-sufficiency of the control system. A piezoelectric shunt involving an inductor is usually called a resonant shunt because of the electrical resonance generated at $\omega_e = 1/\sqrt{LC_{\mathrm{p}}^{\varepsilon}}$. The eventual addition of a resistor does not enable reaching an equivalent infinite stiffness of the transducer because Eq. (2.15) cannot be satisfied anymore. However, a suitable choice of the resistance offers a significant broadband damping as will be seen in the next section.

2.3 Resonant shunt damping

The resonant piezoelectric control is modeled by purely mechanical systems and their analogous electrical circuits. Optimal inductance and resistance values are found from a minimization of the displacement to control. The maximum current flowing through the shunt is also quantified for later design of the electrical components. However, an example experimental setup shows that the required inductance values cannot be satisfied with standard passive components.

2.3.1 Coupled model involving a single mechanical degree of freedom

The effect of a resonant piezoelectric shunt is first illustrated through the control of a unimodal structure represented by a spring mass system. As shown in Fig. 2.3, a shunted

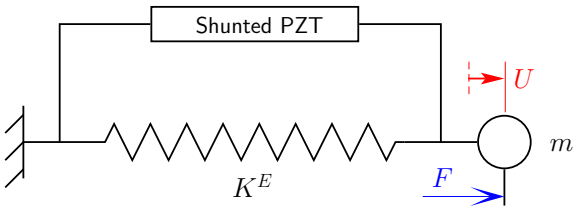

Figure 2.3: Spring-mass model illustrating control with shunted piezoelectric ceramics.

PZT is connected in parallel with a spring of stiffness K^E, representing the stiffness of the whole structure when the piezoelectric transducer is short-circuited. The piezoelectric coupling is defined from an extension of Eq. (2.7) to the present case as

$$\begin{aligned} N &= K^E U - eV \\ q &= eU + C^\varepsilon V \end{aligned} . \tag{2.18}$$

The subscript 'p' is not used because we focus on the global constants for the whole structure, eventually controlled by several piezoelectric elements. If the total moving mass is equal to m, it is found from Fig. 2.3 that $m\ddot{U} = F - N$ and Eq. (2.18) gives

$$\begin{aligned} m\ddot{U} &= F - K^E U + eV \\ q &= eU + C^\varepsilon V \end{aligned} . \tag{2.19}$$

One can then define a natural frequency in short circuit: $\omega_S = \sqrt{K^E/m}$. This refers to the resonance of the mechanical structure when the piezoelectric element is short-circuited ($V = 0$). If the shunt is made of an inductor L in series with a resistor R, the impedance $Z(\omega) = R + \mathrm{j}\omega L$ leads to

$$V = -R\dot{q} - L\ddot{q}. \tag{2.20}$$

Substituting Eq. (2.20) into Eq. (2.19) gives

$$\begin{aligned} m\ddot{U} &= F - K^E U + \frac{e}{C^\varepsilon}(q - eU) \\ -L\ddot{q} &= R\dot{q} + \frac{1}{C^\varepsilon}(q - eU) \end{aligned} , \tag{2.21}$$

which can be illustrated by the mechanical model in Fig. 2.4(a). The shunted PZT in Fig. 2.3 is thus represented by a mechanical system similar to the one in Fig. 2.1(b) with addition of a mass L and a damper R representing the inductance and the resistance of the shunt. Note the mass-inductor, damper-resistor and spring-capacitor equivalences, which refer to the direct electromechanical analogy [74]. Alternatively, Eq. (2.21) can be written

$$\begin{aligned} m\ddot{U} &= F - K^E U - \frac{e^2}{C^\varepsilon}(U - \frac{q}{e}) \\ e^2 L\frac{\ddot{q}}{e} &= -e^2 R\frac{\dot{q}}{e} + \frac{e^2}{C^\varepsilon}(U - \frac{q}{e}) \end{aligned} , \tag{2.22}$$

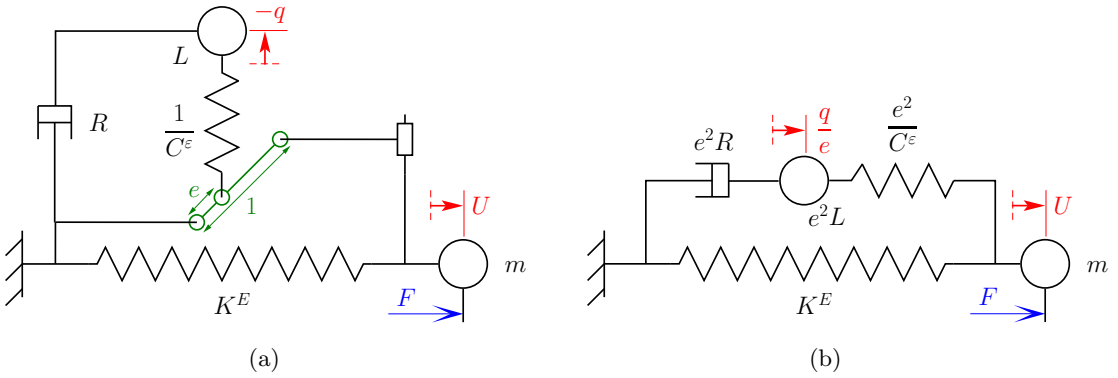

Figure 2.4: Mechanical analogues of a resonant piezoelectric shunt: (a) Complete model. (b) Simplified model.

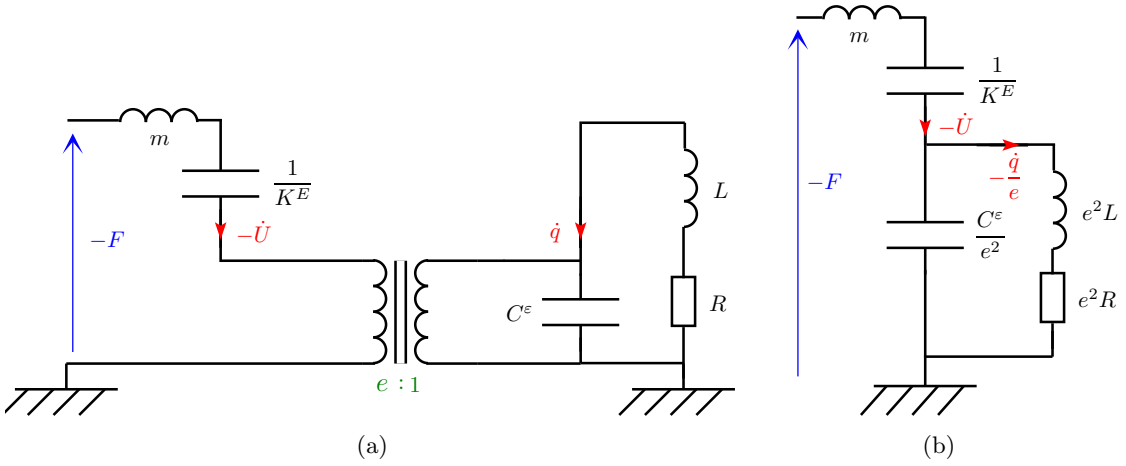

Figure 2.5: Electrical circuits as analogues of the mechanical models: (a) Complete model. (b) Simplified model.

whose mechanical model is shown in Fig. 2.4(b). It is found a simplified model that directly shows the analogy of the resonant shunt with a tuned mass damper [1, 41]. Remark that the damper is not between the two moving mass but between the added mass and the ground, so that an infinite damping is equivalent to an open-circuit case.

Both mechanical models in Figs. 2.4(a) and 2.4(b) can be converted into their electrical analogues by employing the direct electromechanical analogy. Equation (2.21) is reformulated as

$$\begin{aligned} -F &= -\mathrm{j}\omega m\dot{U} - \frac{K^E}{\mathrm{j}\omega}\dot{U} + \frac{e}{\mathrm{j}\omega C^\varepsilon}(\dot{q} - e\dot{U}) \\ -\mathrm{j}\omega L\dot{q} - R\dot{q} &= \frac{1}{\mathrm{j}\omega C^\varepsilon}(\dot{q} - e\dot{U}) \end{aligned} , \tag{2.23}$$

in order to highlight the correlation with the electrical circuit in Figs. 2.5(a). The RL

shunt is directly represented in the electrical branch, meaning that this model is finally similar to Fig. 2.2 after addition of an inductor m representing the mass of the mechanical structure. Furthermore, Eq. (2.22) leads to

$$\begin{aligned} -F &= -\mathrm{j}\omega m\dot{U} - \frac{K^E}{\mathrm{j}\omega}\dot{U} + \frac{e^2}{\mathrm{j}\omega C^\varepsilon}(\frac{\dot{q}}{e} - \dot{U}) \\ -\mathrm{j}\omega e^2 L\frac{\dot{q}}{e} - e^2 R\frac{\dot{q}}{e} &= \frac{e^2}{\mathrm{j}\omega C^\varepsilon}(\frac{\dot{q}}{e} - \dot{U}) \end{aligned} \quad , \tag{2.24}$$

which is represented by the simplified model in Figs. 2.5(b) where no transformer appears anymore. In the end, it has been shown that the considered coupled system can be drawn through equivalent mechanical or electrical representations. Still, we remark that the simplification of Fig. 2.4(a) into Fig. 2.4(b) is less obvious than that going from Fig. 2.5(a) to Fig. 2.5(b) through the transformer relation. Actually, the electrical representation is often preferred because it may offer an easier analysis for getting the constitutive equations and for simplifying the resulting system.

2.3.2 Optimization of the resonant shunt

When coupling a resonant piezoelectric shunt to a mechanical structure, the damping performance can be optimized by choosing suitable resistance and inductance values. Several methods were proposed to define the optimal values for L and R [2, 43, 77]. It is remarked that they all give relatively close results when dealing with moderate values of the coupling factor $k_c = \sqrt{e^2/(K^E C^\varepsilon)}$ [43, 77, 78]. Here, the method proposed by Thomas et al. [43, 79] is considered. It is focused on a *min-max* optimization on the displacement U of the mass m. Considering that the input excitation is a force F, we want to minimize the maximum of the displacement transfer function U/F. To this end, Eq. (2.21) is first written as

$$\begin{aligned} m\ddot{U} + K^D U &= F + \frac{e}{C^\varepsilon}q \\ L\ddot{q} + R\dot{q} + \frac{1}{C^\varepsilon}q &= \frac{e}{C^\varepsilon}U \end{aligned} \quad \text{where} \quad K^D = K^E + \frac{e^2}{C^\varepsilon}. \tag{2.25}$$

K^D is the stiffness of the structure in Fig. 2.3 when the piezoelectric element is open-circuited, i.e. $q = 0$. Then, Eq. (2.25) is equivalent to

$$\begin{aligned} \frac{1}{\omega_O^2}\ddot{U} + U &= \frac{F}{K^D} + \frac{e}{K^D C^\varepsilon}q \\ \frac{1}{\omega_e^2}\ddot{q} + \frac{2\xi_e}{\omega_e}\dot{q} + q &= eU \end{aligned} \quad , \tag{2.26}$$

where $\omega_e = \dfrac{1}{\sqrt{LC^\varepsilon}}$ is the resonant shunt frequency, $\xi_e = \dfrac{R}{2}\sqrt{\dfrac{C^\varepsilon}{L}}$ is the damping factor and $\omega_O = \sqrt{K^D/m}$ is natural frequency in open-circuit. Recall that $\omega_S = \sqrt{K^E/m}$ and

the coupling factor is thus defined from the open- and short-circuit natural frequencies as

$$k_c = \sqrt{\frac{e^2}{K^E C^\varepsilon}} = \sqrt{\frac{K^D - K^E}{K^E}} = \sqrt{\frac{\omega_O^2 - \omega_S^2}{\omega_S^2}}. \tag{2.27}$$

Under harmonic excitation, one obtains from Eq. (2.26) that

$$\left(1 - \frac{\omega^2}{\omega_O^2}\right) U - \frac{e}{K^D C^\varepsilon} q = \frac{F}{K^D} \quad \text{and} \quad q = \frac{e}{1 - \dfrac{\omega^2}{\omega_e^2} + 2\mathrm{j}\xi_e \dfrac{\omega}{\omega_e}} U \ . \tag{2.28}$$

By remarking from Eq. (2.27) that $e^2/(K^D C^\varepsilon) = (\omega_O^2 - \omega_S^2)/\omega_O^2$, the dimensionless displacement transfer function is expressed as

$$H(\omega) = \frac{U}{F/K^D} = \frac{1 - \dfrac{\omega^2}{\omega_e^2} + 2\mathrm{j}\xi_e \dfrac{\omega}{\omega_e}}{\dfrac{\omega_S^2}{\omega_O^2} - \left(\dfrac{1}{\omega_O^2} + \dfrac{1}{\omega_e^2}\right)\omega^2 + \dfrac{\omega^4}{\omega_O^2 \omega_e^2} + 2\mathrm{j}\xi_e \dfrac{\omega}{\omega_e}\left(1 - \dfrac{\omega^2}{\omega_O^2}\right)}, \tag{2.29}$$

which gives

$$|H(\omega)|^2 = \frac{\left[1 - \dfrac{\omega^2}{\omega_e^2}\right]^2 + 4\dfrac{\omega^2}{\omega_e^2}\xi_e^2}{\left[\dfrac{\omega_S^2}{\omega_O^2} - \left(\dfrac{1}{\omega_O^2} + \dfrac{1}{\omega_e^2}\right)\omega^2 + \dfrac{\omega^4}{\omega_O^2 \omega_e^2}\right]^2 + 4\dfrac{\omega^2}{\omega_e^2}\left[1 - \dfrac{\omega^2}{\omega_O^2}\right]^2 \xi_e^2}. \tag{2.30}$$

The tuning of the resonant shunt consists in determining values for ω_e and ξ_e that minimize the maximum of $|H(\omega)|$. The analytic calculations detailed in Appendix A give

$$\omega_e = \omega_O \quad \text{and} \quad \xi_e = \sqrt{\frac{3}{8}} k_c, \tag{2.31}$$

and those optimal values generate a maximum modulus of the transfer function

$$|H(\omega)|_{\max} \approx \frac{\sqrt{2}}{k_c}. \tag{2.32}$$

In the end, Eq. (2.31) gives the optimal inductance and resistance:

$$L = \frac{1}{C^\varepsilon \omega_O^2} \quad \text{and} \quad R = \sqrt{\frac{3}{2}} \frac{k_c}{C^\varepsilon \omega_O}, \tag{2.33}$$

where k_c is the coupling factor that has been defined in Eq. (2.27) and C^ε is the blocked capacitance, that is the capacitance measured when preventing displacement of the mechanical system ($U = 0$).

The interest of the resonant piezoelectric control is illustrated by observing the modulus of the transfer function $H(\omega)$ around ω_O, the natural frequency in open circuit. First,

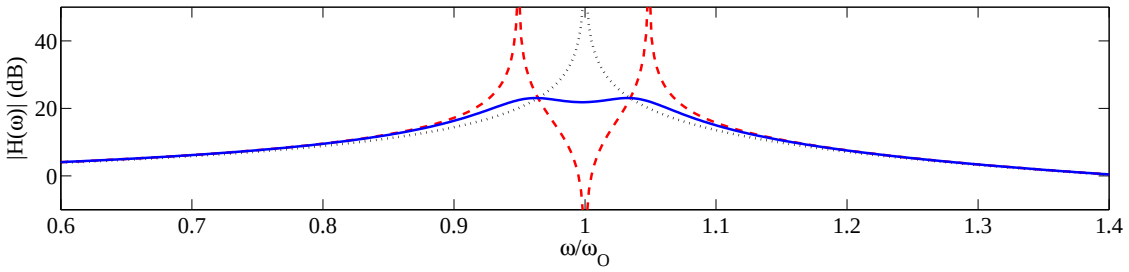

Figure 2.6: Modulus of the transfer function $H(\omega)$ - $(\cdots)$ with an open circuit, (- -) with the optimal inductance and no resistance, (—) with the optimal inductance and the optimal resistance.

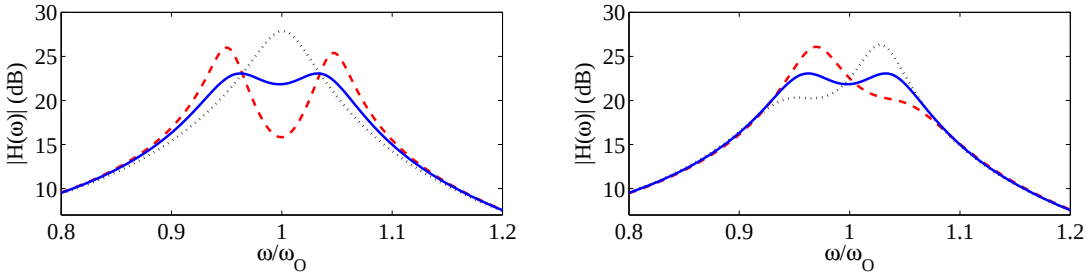

Figure 2.7: Modulus of the transfer function $H(\omega)$: (a) Tuning of the resistance - (—) with the optimal resistance, $(\cdots)$ with twice the optimal resistance, (- -) with half of the optimal resistance. (b) Tuning of the inductance - (—) with the optimal inductance, $(\cdots)$ with 105% of the optimal inductance, (- -) with 95% of the optimal inductance.

Fig. 2.6 shows that the use of a resonant shunt without any resistance creates an antiresonance at ω_e, which is equal to ω_O when the inductance is tuned to its optimal value. This antiresonance is the result of an equivalent stiffness that tends to infinity when Eq. (2.17) is satisfied. Yet, the resonant shunt adds a new degree of freedom, as seen in the equivalent mechanical models in Figs. 2.4(a) and 2.4(b). This explains why two resonances appear on both sides of the antiresonance. The displacement is thus reduced around ω_O but it is significantly increased around the new resonances. Resistance is added into the shunt to get a vibration reduction over a broader frequency range. The optimal resistance in Eq. (2.33) finally leads to a significant vibration reduction when compared to the cases involving an open-circuited PZT or a purely inductive shunt. Then, the optimal tuning of the resonant shunt can be validated. The influence of the resistance R is illustrated in Fig. 2.7(a) when the inductance L is tuned to its optimal value. It is noticed that twice the optimal resistance gives a single maximum, whose value increases with an increase of the resistance. On the contrary, half of the optimal resistance leads to a local minimum surrounded by two local maxima that offer about the same value. The optimal tuning

then corresponds to a case where two maxima appear but their amplitude is minimized. In the following, this optimal damping corresponds to a limit between the so-called under- and overdamped cases. The tuning of the inductance is shown in Fig. 2.7(b), where the resistance is set to its optimal value. We remark that the use of an inductance value that differs from the one given in Eq. (2.33) increases the amplitude of one of the two maxima. Actually, a variation of the inductance moves the electrical resonance away from ω_O, which breaks the approximate symmetry of the transfer function.

2.3.3 Current flowing through the inductor

Once the optimal values of the electrical components are known, it is important to quantify the current flowing through the resonant shunt. Indeed, this allows designing suitable inductors that are not over- or undersized for the considered application. Equation (2.28) shows that the electric charge displacement q is related to the mechanical displacement U through the dimensionless transfer function

$$G(\omega) = \frac{q/e}{U} = \frac{1}{1 - \dfrac{\omega^2}{\omega_e^2} + 2\mathrm{j}\xi_e \dfrac{\omega}{\omega_e}}, \tag{2.34}$$

whose square of the modulus is

$$|G(\omega)|^2 = \frac{1}{\left[1 - \dfrac{\omega^2}{\omega_e^2}\right]^2 + 4\dfrac{\omega^2}{\omega_e^2}\xi_e^2}. \tag{2.35}$$

The maximum of $|G(\omega)|$ is reached when $\omega = \omega_e$. Consequently, $\xi_e = \sqrt{\dfrac{3}{8}} k_c$ gives

$$|G(\omega)|_{\max} \approx \sqrt{\frac{2}{3}} \frac{1}{k_c}. \tag{2.36}$$

In the end, with $i_{\max} = |i(\omega_O)| = \omega_O |q(\omega_O)|$, the maximum current flowing through the shunt is obtained from Eq. (2.36) and the definition of $G(\omega)$ as

$$i_{\max} \approx \sqrt{\frac{2}{3}} \frac{\omega_O}{k_c} |e| U_{\max}. \tag{2.37}$$

The mechanical displacement U has been chosen as a reference to illustrate typical applications where the displacement has to be maintained below a maximum value $U_{\max}$. This value is known because it is defined by the designer of the system. Furthermore, Eq. (2.19) shows that the global coupling coefficient is $e = -C^{\varepsilon} V/U$ in open circuit. If e has not been calculated from the characteristics of the considered system, it can still be obtained experimentally from the ratio between the voltage and the displacement in open circuit.

2.3.4 Experimental investigations

The effectiveness of the resonant shunt damping can be illustrated with an experimental setup involving a cantilever beam controlled by a pair of piezoelectric patches, as shown in Fig. 2.8(a). The beam is excited by a non-contact system involving a coil and a magnet at the free end of the beam. This setup was presented by Thomas et al. [43, 79, 80] for experiments involving resistive and resonant piezoelectric shunts. The aluminum beam is 170 mm long, 25 mm wide and 2 mm thick and the PZT patches are 20 mm long, 25 mm wide and 0.5 mm thick. As seen in Fig. 2.8(b), the collocated patches are bounded near the clamping area [43, 78]. In the present setup, they are polarized in identical directions and connected in parallel for the control of bending modes [2, 71].

The velocity of the beam is measured with a laser vibrometer. The frequency response functions are then obtained by referring to the current in the coil which is considered proportional to the input force over the frequency range of interest [43, 79, 80]. A scanning process allows the extraction of the operating deflection shapes. Three bending modes and one torsional mode are identified below 1 kHz. They are represented in Fig. 2.9 with the frequency response function (FRF) related to the displacement at the free end of the beam. The torsional resonance is hardly observable on the FRF because the measurement is performed close to the neutral axis of the beam. This is not an issue because we focus on the control of the bending modes.

The blocked capacitance is approximated by direct measurement of the piezoelectric capacitance at 100 Hz when no bending motion is allowed: $C^{\varepsilon} = 34.4$ nF. From the results in Fig. 2.9 and from Eqs. (2.27) and (2.33), it then becomes possible to extract the optimal inductance and resistance for the control of the first three bending modes. The results are given in Table 2.2, which presents for each mode the resonance frequencies in short and open circuit, f_S and f_O, the coupling factor k_c and the resulting series inductance L

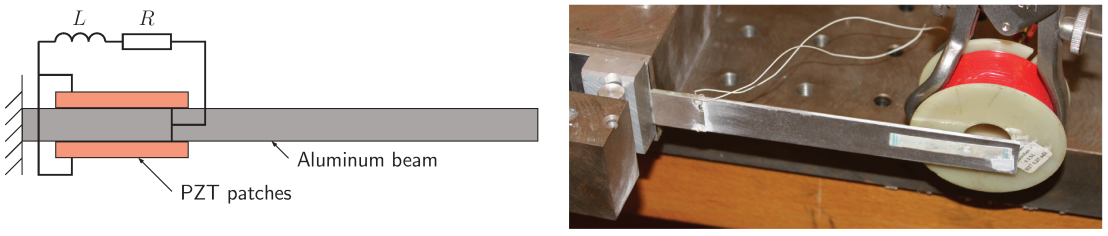

(a) (b)

Figure 2.8: Experimental setup: (a) Cantilever beam with two collocated piezoelectric patches connected to a resonant shunt. (b) Picture of the actual setup showing the coil excitation system.

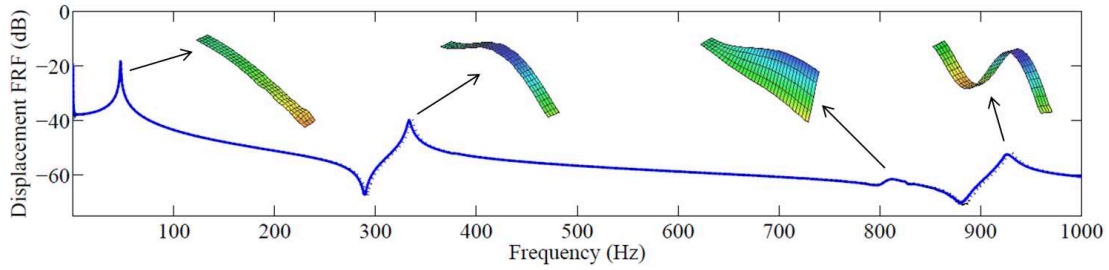

Figure 2.9: Displacement frequency response functions of the beam and corresponding operating deflection shapes obtained experimentally - (—) with short-circuited patches, (· · ·) with open-circuited patches.

Table 2.2: Natural frequencies, piezoelectric coupling factors and optimal shunt specifications for the first three bending modes.

	f_S (Hz)	f_O (Hz)	k_c	L (H)	R (Ω)
Mode 1	47.07	47.46	0.129	330	15 000
Mode 2	333.6	336.1	0.123	6.5	2 100
Mode 3	925.8	930.5	0.101	0.85	610

and series resistance R. We remark that the required inductance exceeds easily 0.5 H and even reaches 330 H for the first bending mode. The inductance for the third mode can be eventually satisfied with the series combination of two standard inductors. However, the control of the first two modes would require numerous components, which would largely exceed the optimal resistance. This highlights a practical limit of the resonant shunt damping strategy when considering low frequency applications. Yet, it is shown in the following section that suitable inductors of reasonable size can still be designed to satisfy the resonant shunt requirements.

2.4 Design of passive inductors

The basics of inductor design are presented by considering the classical equations governing magnetic circuits. The inductance is defined from the properties of the magnetic core, which is selected in order to satisfy the electrical specifications of the resonant shunt. An electrical model of the component is then presented with both series and parallel resistance. Magnetic components are selected in order to damp vibration of the considered cantilever beam with a piezoelectric resonant shunt. Suitable inductors involving two

different types of closed cores are designed and compared with standard inductors.

2.4.1 Basics of electromagnetism

When considering a closed core made of a linear and homogeneous magnetic material of permeability μ, the equations related to the magnetic flux density B, the magnetic field strength H and the magnetic flux φ can be written as follows:

$$B = \mu H, \qquad \varphi = BA_e \qquad \text{and} \qquad Hl_e = Ni. \tag{2.38}$$

The constant A_e defines the effective cross-sectional area of the magnetic core and l_e is the effective magnetic path length. The magnetic flux φ is caused by the current i flowing into a conductor, which is wound around the core with N turns. This is represented in Fig. 2.10(a) in a case involving a toroidal core. With other core geometries, the flux may be split in two magnetic paths, as shown in Fig. 2.10(b) where an EE type core [52, 53] is considered. Note that the present examples do not consider eventual air gaps, which could have been defined from energy considerations. In any case, a changing magnetic flux is generated by a voltage V, which is equal to the time derivative of the total flux going through the N turns of the coil: $V = N\frac{d\varphi}{dt}$. Moreover, the inductance L of an electrical circuit is defined as the ratio of the voltage to the time derivative of the current, i.e. $V = L\frac{di}{dt}$. As a consequence, the inductance can be expressed from Eq. (2.38) by

$$L = A_L N^2 \qquad \text{where} \qquad A_L = \mu_e \mu_0 \frac{A_e}{l_e}. \tag{2.39}$$

The permeability μ is here defined as the product of the vacuum permeability μ_0 times the relative effective permeability μ_e, which is given by the core manufacturers together with the constants A_e and l_e. The permeance, or inductance for one turn, A_L, is thus easily calculated and can even be directly found in most of the core specification documents.

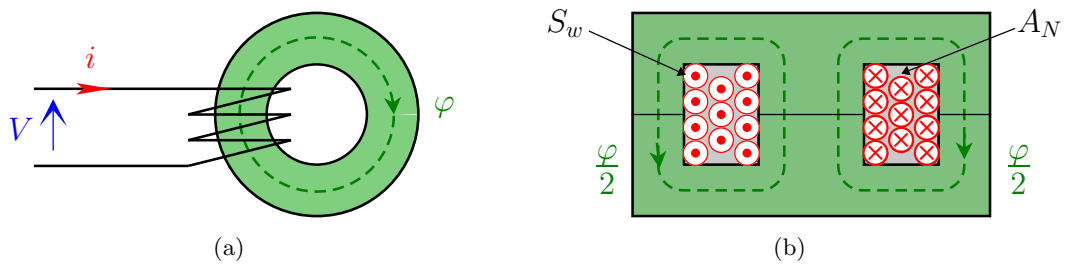

Figure 2.10: Two inductor designs: (a) Toroidal core. (b) EE core.

2.4.2 Magnetic core selection

In piezoelectric damping applications involving resonant shunts, an optimal inductance L and an optimal equivalent series resistance R are generally specified [2, 8, 43, 47, 77, 79, 80]. Equation (2.39) gives the number of turns that is required to satisfy the inductance L with a specific magnetic core. Naturally, the number of turns is restricted by the available room around the coil. This is observed in Fig. 2.10(b), where a 12^{th} turn could not be added because of the fixed window area A_N. This limit is quantified by the filling factor

$$k_u = \frac{NS_w}{A_N}, \tag{2.40}$$

where S_w is the cross-sectional area of the conductor. The factor k_u does not usually exceed 0.5 for a full winding area. This is because a wire with circular cross-section cannot entirely fill the available winding area. Another reason is the presence of insulation layers that limit the proportion of conductor in the total wire cross-section [52, 53]. The manufacturing process is also crucial because it determines the winding arrangements. For instance, a handmade coil with disorganized layers leads to a significant reduction of k_u.

Once the number of turns is defined from Eq. (2.39), the upper limit $k_u = 0.5$ leads to a maximum cross-sectional area of the conductor. The geometry of the core gives the average length per turn l_N. The resistance of a wire of resistivity ρ is then obtained from

$$R_{\text{s}} = \rho \frac{N l_N}{S_w}. \tag{2.41}$$

Note that an inadequate selection of the magnetic core can lead to a case where R_{s} exceeds the optimal resistance R. In practical applications involving closed magnetic cores, we actually need to ensure $R_{\text{s}} \ll R$ because the copper loss only represents a portion of the total loss in the component [52–54, 81]. The introduction of a criterion for the choice of a core that is able to satisfy both specifications on L and R is thus crucial. Equations (2.39), (2.40) and (2.41) are considered and the condition on the resistance

$$R_{\text{s}} \ll R \qquad \text{gives} \qquad c_Q = \left(\frac{k_u A_L A_N}{\rho l_N} \right) \frac{R}{L} \gg 1. \tag{2.42}$$

The criterion c_Q is thus calculated from the core specifications and the electrical properties of the optimal shunt defined in Eq. (2.33). The factor k_u can be set to 0.5 and ρ to 1.7×10^{-8} Ω·m, which is the resistivity of copper [52]. If c_Q is below or close to 1, the considered core cannot satisfy both L and R requirements. Then, another core with a larger ratio $A_L A_N / l_N$ would have to be found.

Two practical limits appear when considering the use of passive inductors. First, the magnetic flux density has to remain below the saturation flux density B_M in order to avoid a strong reduction of the inductance value. The second limit concerns the root mean square

current density $i_{\max}/(\sqrt{2}S_w)$, which cannot exceed $J_{\max}$, the maximum current density that would damage the component. From Eqs. (2.38), (2.39) and (2.40), we get two restrictions on the amplitude of the sinusoidal current flowing through the conductor:

$$i_{\max} < I^B_{\max} = \left(\frac{B_{\max}A_e}{\sqrt{A_L}}\right)\frac{1}{\sqrt{L}} \quad \text{and} \quad i_{\max} < I^J_{\max} = \left(\sqrt{2}k_u J_{\max} A_N \sqrt{A_L}\right)\frac{1}{\sqrt{L}}, \quad (2.43)$$

Consequently, the currents $I^B_{\max}$ and $I^J_{\max}$ inducing respectively the maximum flux and current densities need to be considered as upper limits when introducing the chosen inductor into a specific electrical circuit. A limit on the square of the maximum current can then be written $i^2_{\max} < I^B_{\max} I^J_{\max}$ and combining Eqs. (2.33), (2.37) and (2.43) gives

$$A_e A_N > \frac{\sqrt{2}}{3k_u J_{\max} B_{\max}} \frac{e^2 U^2_{\max}}{k_c^2 C^{\varepsilon}}. \quad (2.44)$$

So, a suitable magnetic core can be chosen from a condition on the product of the core cross-sectional area A_e by the window area A_N. This extends the classical method of the area product [52, 53] to the design of inductors for piezoelectric applications. The condition is here defined from $U_{\max}$, the maximum displacement of the mechanical structure once the resonant shunt is tuned to its optimal impedance. A core is first selected by considering the minimum area product satisfying Eq. (2.44). Then, the conditions in Eqs. (2.43) and (2.42) are verified and one iterates with lager magnetic cores until the three conditions are satisfied independently.

2.4.3 Equivalent circuit models including resistors

A suitable model for the passive inductors is obtained by considering a perfect inductance L_0 combined to a resistance $R_{\rm s}$ in series and a resistance $R_{\rm p}$ in parallel. This electrical model is represented in Fig. 2.11(a). $R_{\rm s}$ is approximated by the resistance in Eq. (2.41) that corresponds to the copper loss, that is the Joule heating in the wire. The parallel resistance $R_{\rm p}$ represents the proximity effect [52] and the loss in the magnetic material, which has two main components: the hysteretic loss and the eddy current loss

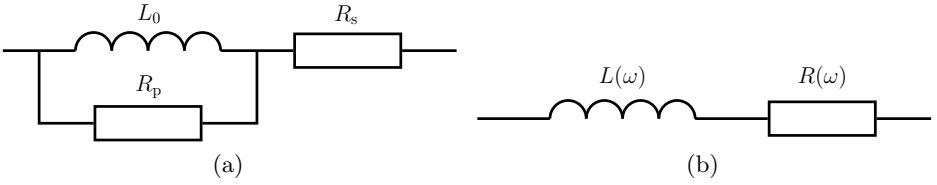

Figure 2.11: Electrical circuit models of an inductor: (a) Model with a series resistance and a parallel resistance. (b) Model involving an equivalent series inductance and an equivalent series resistance.

[52, 53]. R_p is more difficult to evaluate because it depends on the core material, on the frequency and on the flux density. For piezoelectric applications involving high permeability cores of standard size, it has been observed that the energy dissipation induced by R_p is usually larger than the copper loss due to R_s. Nevertheless, in the following experiments the resulting equivalent series resistance is still lower than the optimal shunt resistance.

The equivalent series resistance $R(\omega)$ is represented in Fig. 2.11(b) together with $L(\omega)$, which is the equivalent series inductance. Both values come from the impedance of the electrical model in Fig. 2.11(a), which is recast in $Z(\omega) = R(\omega) + j\omega L(\omega)$ where

$$R(\omega) = R_\mathrm{s} + \frac{R_\mathrm{p}}{1 + \left(\dfrac{R_\mathrm{p}}{L_0\omega}\right)^2} \qquad \text{and} \qquad L(\omega) = \frac{L_0}{1 + \left(\dfrac{L_0\omega}{R_\mathrm{p}}\right)^2}. \tag{2.45}$$

From this formulation, it is remarked that the equivalent series inductance and resistance necessarily depend on frequency. This effect is due to the presence of the parallel resistance R_p. If R_p is constant, $R(\omega)$ is increased and $L(\omega)$ is decreased when ω increases, which explains the non-negligible frequency dependence that is observed when measuring the inductance and resistance of closed core inductors.

2.4.4 Choice of magnetic components for the experimental setup

The inductance requirement for piezoelectric shunt applications is generally too high to be satisfied with standard inductors. This is illustrated by the inductance values appearing in Table 2.2, which all exceed the typical upper limit offered by most of the inductor suppliers, that is 0.5 H. Actually, standard inductors are generally made of copper wire wound around a ferrite cylinder. About half of the magnetic circuit is thus air where the magnetic field has to spread from one end of the cylinder to the other end. The benefit is that air offers a relatively constant permeability, which limits the nonlinearities of the inductor. But the main drawback is the poor permeability of the air that induces low quality factors ($Q = \omega_O L/R$) and limited inductance for standard size components. Other inductor designs that could satisfy the shunt specifications are then required.

Closed magnetic cores can offer significant permeance A_L because the magnetic field does not have to loop through the air. This means that for a specific inductance requirement, the number of turns is considerably reduced when compared to classical ferrite cylinder designs. Then, the total resistance of the wire decreases because of the shorter length of wire and because of the eventual increase of its diameter. As a consequence, closed magnetic cores enable the design of inductors with both low series resistance and high inductance. Two closed cores of similar mass $m^\star$ but different shapes and materials are selected. The first core is a type RM10 ferrite made of T38 material. The core is

Table 2.3: Characteristics of the two magnetic cores with different ferromagnetic materials.

	$m^\star$ (g)	μ_e (-)	A_e (mm^2)	l_e (mm)	A_L (μH)	$B_{\max}$ (T)	A_N (mm^2)	l_N (mm)
Ferrite core	22	5720	98	44	16	0.43	41	52
Nanocrystalline toroid	23	87500	40	79	56	1.20	236	50

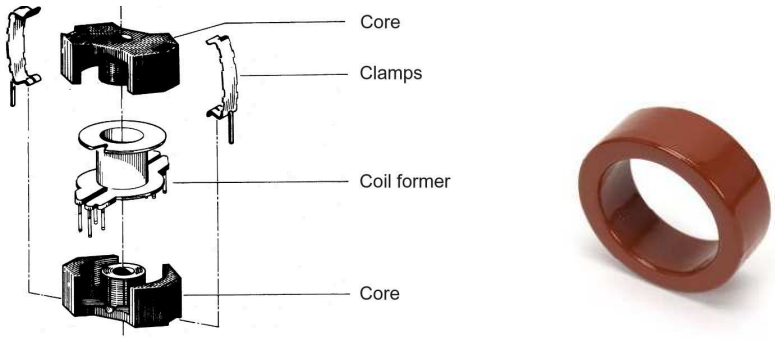

(a) (b)

Figure 2.12: Magnetic cores selected for the design of the inductors: (a) RM ferrite core (TDK). (b) Nanocrystalline toroid (VAC).

described in Table 2.3 and represented in Fig. 2.12(a). It comes with a coil former and clamps in order to facilitate the winding and the assembly of the magnetic component. In terms of geometry, the RM core is rather similar to the classical EE core represented in Fig. 2.10(b). As various shapes and materials are available for this range of components, the ferrite core providing the larger A_L value was selected. Nevertheless, the equivalent permeability of the chosen ferrite material is considerably lower than the permeability of some nanocrystalline materials [52, 53]. The second core that is considered is thus a nanocrystalline toroid of 30 mm outside diameter represented in Fig. 2.12(b). This core made of Vitroperm 500F material offers a larger permeance A_L when compared to the ferrite core, as shown in Table 2.3.

For the considered laboratory experiments, we do not have any specification on the maximum displacement $U_{\max}$, which means that the core dimensions have not been chosen from Eq. (2.44) but from practical reasons related to availability of the components and winding issues. Nevertheless, the selection of the two magnetic cores is validated by the calculation of the criterion c_Q for the three considered bending modes, from Eq. (2.42) and Tables 2.2 and 2.3. k_u is initially set to 0.5 in order to consider a full winding area. The results are presented in Table 2.4 for the ferrite core and in Table 2.5 for the nanocrystalline toroid. Note that $c_Q \gg 1$, which means that both cores can satisfy the L

Table 2.4: Inductor design characteristics with the ferrite core.

	c_Q	N	Φ_w (mm)	k_u	$I^B_{\max}$ (mA)	$I^J_{\max}$ (mA)
Mode 1	17	4520	5/100	0.22	0.58	8.3
Mode 2	118	638	2/10	0.49	4.1	130
Mode 3	268	231	3/10	0.40	11	300

Table 2.5: Inductor design characteristics with the nanocrystalline toroid.

	c_Q	N	Φ_w (mm)	k_u	$I^B_{\max}$ (mA)	$I^J_{\max}$ (mA)
Mode 1	1 366	2416	2/10	0.32	0.35	130
Mode 2	2466	341	5/10	0.28	2.5	830
Mode 3	5616	123	8/10	0.26	7.0	2100

and R specifications if the contribution of the parallel resistance presented in Eq. (2.45) is not too large. The number of turns is then computed from Eq. (2.39) and a standard wire diameter $\Phi_w = 2\sqrt{S_w/\pi}$ is chosen by updating k_u and ensuring its value remains below 0.5. In the end, the maximum currents related to both conditions on the saturation flux density and on the maximum current density are obtained from Eq. (2.43), where $J_{\max}$ is set to 3 A/mm^2 [53]. For the six inductor designs, the maximum current $I^B_{\max}$ is clearly lower than $I^J_{\max}$. In other words, an increase of the current would detune the resonant shunt before overheating the coil. This may be another advantage of the closed core inductors that would ensure the integrity of the electrical components.

The ferrite core reaches its limits when focusing on the first mode of the beam. Table 2.4 gives a solution with 4520 turns of 5/100 copper wire but its practical implementation is tough. Indeed, such a number of turns with a thin and thus delicate wire would require dedicated tools that were not available for the present application. This example shows that ferrite cores are sometimes not enough when considering low frequency applications involving resonant shunts. Cores with larger c_Q ratio are then necessary. Finally, the

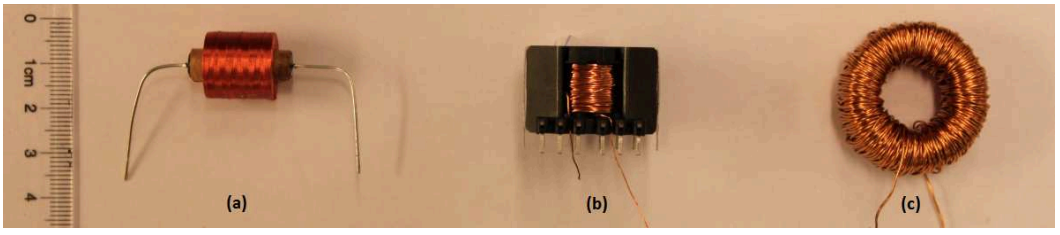

Figure 2.13: Three different inductor designs: (a) Standard inductor involving a ferrite cylinder. (b) Handmade inductor involving a RM ferrite core. (c) Handmade inductor involving a nanocrystalline toroid.

control of the first mode can only be satisfied with the nanocrystalline toroid. This core is wound by hand according to Table 2.5 for the first mode but also for the 2^{nd} and 3^{rd} modes. Ferrite cores are also wound for the 2^{nd} and 3^{rd} modes but not for the first mode because of the aforementioned practical limit. Considering standard inductors, two of them are selected, 0.5 H and 0.32 H, in order to reach 0.82 H by series combination and then satisfy the inductance requirement for the control of the third mode. The three inductor designs are presented in Fig. (2.13), which shows that they all offer similar dimensions.

2.4.5 Damping of vibration with passive inductors

The inductors are successively connected to the pair of piezoelectric patches in order to reduce the vibration amplitude of the beam in Fig. 2.8(b). First, the damping of the third bending mode is targeted. The numbers of turns of the two handmade inductors are adjusted in order to get resonant shunts that are correctly tuned. The ferrite core is wound with 222 turns and the nanocrystalline toroid is wound with 101 turns. The slight difference with the theoretical values presented in Tables 2.4 and 2.5 is explained by the fact that the A_L values appearing in Tables 2.3 are specified at 10 kHz. Yet, the permeance varies nonlinearly with respect to the frequency, as it has been observed for the inductance $L(\omega)$ in Eq. (2.45). Over a frequency range below 10 kHz, the A_L values given by the core manufacturer are thus lower estimates that could be adjusted by measurement at the frequency of interest.

Figure 2.14(a) shows the effect of the shunt made of two standard inductors in series. Only one local maximum is observed, which means that the electrical resistance is above its optimal value. This can be easily verified by measuring the direct current resistance of the inductor which is 1050 Ω, while the optimal resistance presented in Table 2.2 is $R = 610$ Ω. Consequently, even if standard inductors can satisfy the inductance requirement for the damping of the third bending mode, they offer too much resistance to allow an optimal tuning of the resonant shunt. On the contrary, the closed core inductors offer an equivalent series resistance below the optimal shunt resistance. This is presented in Figs. 2.14(b) and 2.14(c), where it is seen that an external series resistance R_{s}^{+} needs to be introduced in order to reach the optimal damping configuration. For the present experiments, it is noticed that R_{s}^{+} is clearly below the optimal resistance $R = 610$ Ω. The series resistance of the wire is yet negligible, as indicated by the large values of the c_Q criterion for the chosen cores. This means that the magnetic loss modeled by the parallel resistance R_{p} cannot be neglected. Fortunately, its influence still yields an equivalent series resistance that is lower than the optimal resistance.

The same conclusions can be drawn when focusing on the damping of the second mode. Here, the ferrite core is wound with 613 turns and the nanocrystalline toroid is wound with

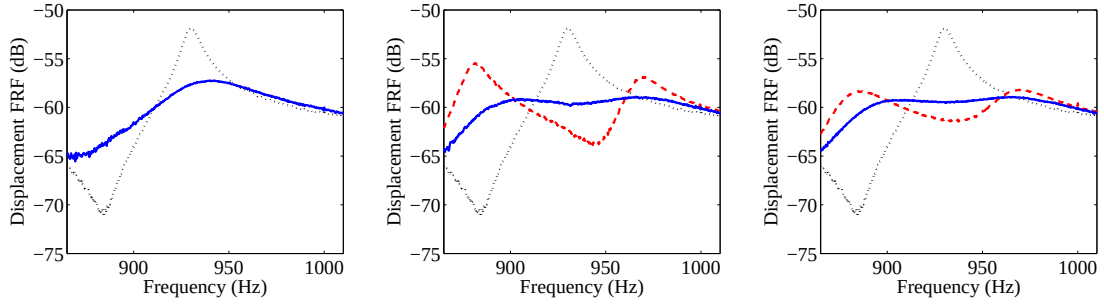

Figure 2.14: Damping of the third bending mode: (a) With standard inductors - (· · ·) open circuit, (—) shunted on inductor without additional resistor. (b) With the ferrite core ($N = 222$) - (· · ·) open circuit, (- -) shunted on inductor without additional resistor, (—) shunted on inductor with additional series resistor $R_{\mathrm{s}}^{+} = 390\ \Omega$. (c) With the nanocrystalline toroid ($N = 101$) - (· · ·) open circuit, (- -) shunted on inductor without additional resistor, (—) shunted on inductor with additional series resistor $R_{\mathrm{s}}^{+} = 260\ \Omega$.

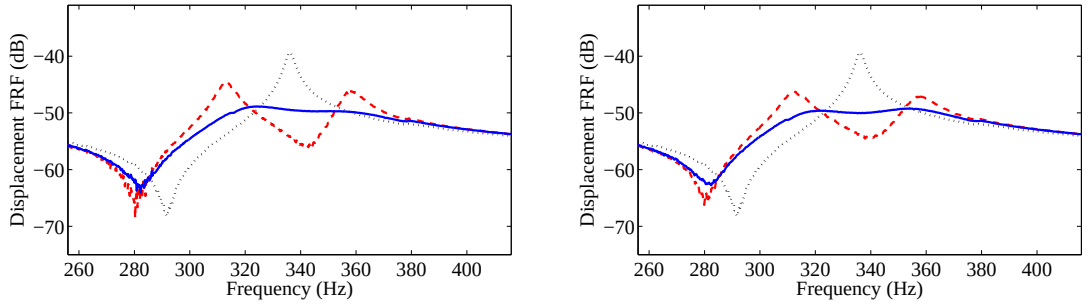

Figure 2.15: Damping of the second bending mode: (a) With the ferrite core ($N = 613$) - (· · ·) open circuit, (- -) shunted on inductor without additional resistor, (—) shunted on inductor with additional series resistor $R_{\mathrm{s}}^{+} = 1.8\ \mathrm{k}\Omega$. (b) With the nanocrystalline toroid ($N = 296$) - (· · ·) open circuit, (- -) shunted on inductor without additional resistor, (—) shunted on inductor with additional series resistor $R_{\mathrm{s}}^{+} = 1.4\ \mathrm{k}\Omega$.

296 turns. Those number of turns are still lower than the ones in Tables 2.4 and 2.5 because of the underestimated A_L values. Figure 2.15 shows that the initially underdamped shunts can be optimized by adding series resistors R_{s}^{+}. As previously, R_{s}^{+} is below the optimal series resistance $R = 2.1\ \mathrm{k}\Omega$ because of the effect of the parallel resistance R_{p}.

The nanocrytalline toroid is the only core that can satisfy the 330 H requirement for the first mode of the beam. The toroid needs 1800 turns to reach this optimal inductance, which differs from the calculated value equal to 2416 turns. Again, the main reason is that the equivalent permeance significantly increases when going to low frequency. Fig-

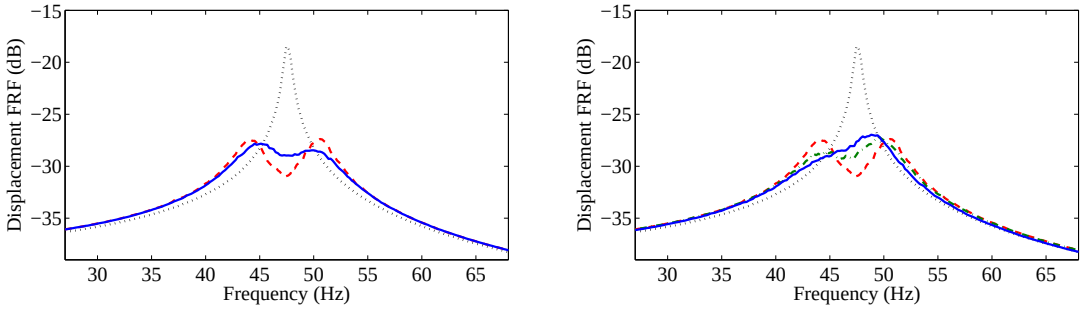

Figure 2.16: Damping of the first bending mode: (a) With the nanocrystalline toroid ($N = 1800$) - ($\cdots$) open circuit, (- -) shunted on inductor without additional resistor, (—) shunted on inductor with additional series resistor $R_s^+ = 6.7$ kΩ. (b) With the nanocrystalline toroid ($N = 1800$) - ($\cdots$) open circuit, (- -) shunted on inductor without additional resistor at $V_e = 1.2$ V, (- · -) shunted on inductor without additional resistor at $V_e = 1.8$ V, (—) shunted on inductor without additional resistor at $V_e = 2.4$ V.

ure 2.16(a) shows that the handmade inductor is able to provide a significant vibration reduction. The magnetic flux density does not reach the saturation limit because the root mean square current produced by the piezoelectric patches is only about 10 μA. This current is measured in the resonant shunt when the excitation amplitude causes an open-circuit displacement equal to 30 μm at the end of the beam and an open-circuit voltage about 1 V. Under this nominal excitation, the external resistance R_s^+ that yields an optimal tuning of the shunt is around 6.7 kΩ. Yet, the resistance of the wire is only 40 Ω and the optimal series resistance has been evaluated to 15 kΩ in Table 2.2. As a consequence, more than half of the energy loss occurs in the magnetic core even after the addition of the external series resistance R_s^+. The energy loss in the magnetic core is modeled by the parallel resistance R_p that appears in Fig. 2.11(a) and Eq. (2.45). The dependence of R_p and L on the amplitude of the excitation is observed experimentally. Indeed, Figure 2.16(b) represents the displacement FRF around the first bending mode for different excitation amplitudes. The root mean square voltage across the inductor is equal to $V_e = 1.2$ V at nominal excitation. This voltage is then set to $V_e = 1.8$ V and to $V_e = 2.4$ V. The modification of the tuning is significant as it is remarked that the equivalent shunt resistance is increased and the electrical resonance moves to lower frequency. Those two effects are due to the nonlinearities of the magnetic material with respect to the excitation amplitude [52–54], which induces an increase of both the equivalent permeability and the energy loss. Those nonlinearities were also observed with the closed core inductors dedicated to the control of the 2nd and 3rd modes but the effect was less obvious. In any case, this example shows a limit of the closed magnetic cores, which are more subjected to nonlinear effects.

2.4.6 Comparison of inductor designs

The previous inductors clearly shows that the closed magnetic cores can lead to inductance values that significantly exceed the values proposed in standard series. Ferrite cores offer decent permeabilities but some applications require nanocrystalline materials for even larger inductance. Both solutions reduce the number of turns in the coil, which means that the copper loss can be significantly decreased. Consequently, when the loss in the magnetic core is limited, closed core inductors present considerably larger quality factors than standard inductors.

When considering the implementation of resonant shunts in industrial products, price or manufacturing process can become important issues. The standard inductors used in the present application cost around $2 per component. The closed core designs are more expensive because a ferrite core inductor is around $5 and the nanocrystalline toroid costs $15. Those prices obviously depend on the number of components that is ordered but they still offer a comparison between the three designs. The standard inductors are usually cheap and offer a wide range of ready-to-use components. On the other hand, closed core inductors need to be specifically designed and manufactured for the considered application because suitable wound cores are not easily available. As seen in Fig. 2.12(a), the ferrite core design offers a cylindrical coil former that can be wound by hand or with a mandrel before its introduction between the two half magnetic circuits. The geometry of the toroid makes winding harder and the automation of the process requires a specific toroidal core winding machine.

Finally, it has been shown that the equivalent series inductance and resistance of the closed core inductors depend on frequency and on current amplitude. Those nonlinearities are insignificant with standard inductors where the magnetic field has to spread through the air, which offers a relatively constant permeability and low magnetic losses. This last limit of the closed core inductors also appears in Table 2.6, which summarizes the comparison between the three inductor designs.

Table 2.6: Comparison of the three inductor designs.

	Ferrite cylinder	Ferrite core	Nanocrystalline toroid
High inductance	-	+	++
Quality factor	-	++	++
Price	++	+	-
Manufacturing	++	+	-
Nonlinearities	++	-	-

2.5 Conclusions

The fundamental equations describing a system subjected to a piezoelectric coupling has been deduced from the 3D linear theory of piezoelectricity. This theory is simplified to the case of a one-dimensional transducer, which can be represented by equivalent electrical or mechanical models. The direct electromechanical analogy is highlighted because it is the one that allows a complete modeling of the piezoelectric actuators with passive components. Then, the coupling is represented by a transformer in the electrical domain and a lever in the mechanical domain. Connecting an inductor and a resistor in parallel with a piezoelectric capacitance creates a resonant shunt that is equivalent to a tuned mass damper. Complete and simplified mechanical models as well as their electrical analogues are given for a better understanding of the equivalence between both of them. From a minimization of the transfer function of the displacement to control, we get optimal inductance and resistance values for the resonant shunt. Those values allow quantifying the electrical current flowing through the inductor, which is required for an adequate design of the magnetic component.

The last section of this chapter focuses on the design of passive inductors for piezoelectric shunt applications. From the basic equations describing a magnetic component, a criterion based on inductance and resistance specifications is proposed in order to choose a suitable magnetic core. Furthermore, a condition on the area product of the core is given to provide guidance in the selection of the component. The electrical model of an inductor with series and parallel resistances is then introduced and related to the classical model involving the equivalent series inductance and series resistance that appear in the resonant shunt. The experimental setup based on a cantilever beam covered by a pair of piezoelectric patches requires inductance up to 330 H for a control based on a passive resonant shunt. It is shown that such a high inductance value is not impractical for piezoelectric applications because of the low amplitude of the current generated by the patches.

Specific designs involving closed magnetic cores are required in order to reach large inductance values with low series resistance. Two magnetic cores are proposed: a RM ferrite and a nanocrystalline toroid. Both solutions can easily provide inductance above 0.5 H, which is considered as the upper limit of standard inductor series. The inductor designs are successively validated by observing significant vibration reduction for the first three bending modes of the cantilever beam. Some limits are still remarked as the nonlinearities induced by the high permeability materials. Nevertheless, closed magnetic cores clearly extend the resonant shunt strategy to lower frequencies that were not reachable with standard inductors. This solution counters the use of synthetic inductors with strictly passive components, which could be of great interest for embedded systems.

Chapter 3

Damping of a rod through a periodic array of piezoelectric patches

Abstract: *Elastic lattice of point masses can be a suitable representation of a continuous rod for the study of longitudinal wave propagation. One can then analyze the effect of a periodic distribution of identical tuned mass dampers or analogous resonant piezoelectric shunts. By extending the classical tuned mass damping strategy, a multimodal tuned mass damper is introduced from the coupling of two lattices offering similar modal properties. The aim of the chapter is to model and implement this multimodal control on a rod coupled to an electrical network. The electromechanical analogy applied to a mechanical lattice gives the required electrical network and the energy conversion is performed through a periodic array of piezoelectric patches. The coupled problem is treated with a transfer matrix formulation, which is based on different models depending on the frequency range of interest. An experimental setup validates the models as wells as the broadband efficiency of the multimodal control.*

Contents

3.1 Introduction

Wave propagation in one-dimensional periodic structures can be analyzed with the transfer matrix formulation. As described by Mead [82], this approach is based on the definition of a unit cell, which periodically repeats with identical mechanical properties. The relation between the mechanical states at both ends of the unit cell is represented by a transfer matrix. This relation is then propagated in order to obtain the global behavior of a finite periodic structure. The transfer matrix method can be applied to the discrete model of a rod, which is represented by a lattice of point masses. Periodic lattices were presented by Brillouin [83], who gave fundamental results related to wave propagation in mechanical and electrical periodic structures. An electromechanical analogy between lattices of different nature was thus already introduced. This analogy was formalized by Bloch [74] and Beranek [84] for more general structures. Those references give useful elements to find the analogues of coupled problems involving electrical components connected to piezoelectric patches [2]. First, a resonant shunt can be compared to a tuned mass damper [1, 41]. By tuning the electrical components, vibration reduction of the main structure is expected [43–45, 79, 80]. This concept was applied by Thorp et al. to the damping of longitudinal waves in a rod periodically covered with piezoelectric patches [4]. The use of the transfer matrix formulation allows studying the propagation constants as well as the global behavior of the coupled structure. It was then extended to the study of transverse waves by taking into account the influence of various linear shunts either passive as the resonant ones [5, 45, 46, 48, 49, 85, 86], hybrid active-passive [87–89] or active as the shunts involving negative capacitance [76, 90, 91]. A limited number of papers considers interconnections of successive piezoelectric patches. A precursory work was presented by Valis et al. [25] on the coupling of an electrical transmission line to a beam. One can then mention the papers of Yu et al. [92] and Li et al. [93], who analyzed the influence of an electrical network on vibration delocalization in a periodic blade assembly. Regarding damping of vibration, dell'Isola et al. introduced several results on the influence of distributed piezoelectric networks on transverse wave propagation [12, 13, 15, 17, 19, 26, 94, 95]. From a continuous formulation, the electric analogue of a beam appears as an optimal network topology [16, 21, 22, 96]. In the end, excepted from dell'Isola et al., only a few more research groups conducted analyzes on wave control through an interconnected array of piezoelectric patches [97–100]. None of the aforementioned studies on electrical networks benefits from the transfer matrix method. Yet, Lu and Tang [101] have shown that this method also applies on piezoelectric networks by adding electrical variables to the mechanical state vectors.

The present chapter deals with the above mentioned concepts in order to present a passive and multimodal control strategy that is implemented for vibration damping of a

rod. First of all, the transfer matrix formulation is presented and applied to a continuous rod which is then discretized into a lattice of point masses. The differences between the continuous model and the lattice model are clarified. Afterwards, two control strategies based on modal coupling are presented for the purpose of converting the vibration energy of a main structure into a distributed damping device. The first resonance-based solution involves a periodic distribution of tuned mass dampers. This mechanical example can be transposed to a piezoelectric application by considering an array of resonant shunts on a rod [4, 102]. An electromechanical unit cell is thus defined as a rod segment ruled by a global piezoelectric coupling. We address the tuning of the electrical components but some limitations arise when considering the practical implementation of the resonant shunt control. The second control strategy considers the coupling of a main structure to a damping lattice having similar modal properties. This leads to an original multimodal tuned mass damper, which is first presented under its mechanical form. The next step is to implement the proposed control by connecting the rod to an electrical network having similar modal properties. The analogous electrical network is obtained from the direct electromechanical analogy [74, 84] and we get a line of inductors with connection to the ground through capacitors. With this discrete network, the transfer matrix formulation simplifies the analysis compared to former analytic formulations where the electrical network has been seen as a continuum [12, 13, 17, 21, 22, 94, 96]. Here, various models are proposed, depending on the required accuracy and the frequency range of interest. The electrical network is always seen as a discrete medium but the mechanical segments are either discrete, homogenized or defined from a finite element model. The models are compared by considering large or short wavelength conditions. Then, experimental validations focus on the effect of the two control strategies on electrical and mechanical frequency response functions around the first four modes of a rod. One of the main result concerns the experimental validation of the multimodal damping strategy. When applying a simple modal coupling condition obtained from the discrete model, the efficiency of the method is proved with significant vibration reduction over a broad frequency range. Another interest of this control strategy is the reduction of the required inductance. This offers a chance to implement a completely passive control, as shown in the proposed experimental setup.

3.2 Longitudinal wave propagation in a discretized rod

The transfer matrix formulation is introduced in order to analyze vibrations of one-dimensional structures. The classical rod model is first considered before looking at its lattice equivalent, which is obtained from a finite difference method applied to the continuous wave equation. The differences between the two models are then clarified in terms of propagation constants and frequency response functions.

3.2.1 Transfer matrix formulation

A one-dimensional periodic structure is a series of identical unit cells [82]. For each unit cell, the relation between the mechanical states at its right and left ends can be described by a transfer matrix $\boldsymbol{T}$ as

$$\begin{bmatrix} \boldsymbol{q_R} \\ \boldsymbol{F_R} \end{bmatrix} = \boldsymbol{T} \begin{bmatrix} \boldsymbol{q_L} \\ \boldsymbol{F_L} \end{bmatrix}, \tag{3.1}$$

where $\boldsymbol{q_L}$ and $\boldsymbol{q_R}$ are the displacements of the left and right ends of the unit cell. $\boldsymbol{F_R}$ is the force applied on the considered cell by its right neighbor and $\boldsymbol{F_L}$ is the force applied by the considered unit cell on its left neighbor. $\boldsymbol{F_L}$ is thus defined as the opposite of the external force acting on the left end. This sign convention leads to the continuity of the state vector. The Floquet-Bloch theory induces that, for a wave propagating in the one-dimensional medium, the motion on the right of a unit cell is equal to $e^{\pm\mu}$ times the motion on the left [82], the sign depending on the direction of the wave. Here, μ is the propagation constant, which is usually defined as $\mu = \delta + \mathrm{j}\theta$, where δ is the attenuation constant, j is the imaginary unit and θ is the phase constant [46]. Alternatively, the propagation constant can be written $\mu = \alpha a + \mathrm{j}ka$, where α is the attenuation rate, k is the wavenumber and a is the length of the unit cell. From Eq. (3.1), if $[\ \boldsymbol{q_L}\ \ \boldsymbol{F_L}\ ]^T$ is an eigenvector of the transfer matrix $\boldsymbol{T}$,

$$\begin{bmatrix} \boldsymbol{q_R} \\ \boldsymbol{F_R} \end{bmatrix} = e^{\pm\mu} \begin{bmatrix} \boldsymbol{q_L} \\ \boldsymbol{F_L} \end{bmatrix}. \tag{3.2}$$

Consequently, $\mu = \ln(\lambda)$, where λ represents an eigenvalue of the transfer matrix $\boldsymbol{T}$. The number of propagation constants μ is thus equal to the dimension of $\boldsymbol{T}$. Yet, as two set of opposite constants are necessarily obtained, only the positive ones are represented in the following applications.

According to the definition of a periodic structure, each unit cell is described by an identical transfer matrix $\boldsymbol{T}$. Consequently, the mechanical state on the right of the n^{th} unit cell is obtained by raising the corresponding transfer matrix to the power of n,

$$\begin{bmatrix} \boldsymbol{q_n} \\ \boldsymbol{F_n} \end{bmatrix} = \boldsymbol{T^n} \begin{bmatrix} \boldsymbol{q_0} \\ \boldsymbol{F_0} \end{bmatrix} = \begin{bmatrix} \boldsymbol{T_n^{qq}} & \boldsymbol{T_n^{qF}} \\ \boldsymbol{T_n^{Fq}} & \boldsymbol{T_n^{FF}} \end{bmatrix} \begin{bmatrix} \boldsymbol{q_0} \\ \boldsymbol{F_0} \end{bmatrix}, \tag{3.3}$$

where the subscript 0 refers to the left end of the first unit cell. Then, when considering a finite number of n unit cells, the boundary conditions need to be introduced. For example, with a prescribed force $\boldsymbol{F_0}$ applied on the left end of a free-free periodic structure, as $\boldsymbol{F_n} = \boldsymbol{0}$, the displacement $\boldsymbol{q_n}$ at the right end is defined from Eq. (3.3) as

$$\boldsymbol{q_n} = (\boldsymbol{T_n^{qF}} - \boldsymbol{T_n^{qq}} \boldsymbol{T_n^{Fq}}^{\boldsymbol{-1}} \boldsymbol{T_n^{FF}}) \boldsymbol{F_0}. \tag{3.4}$$

Eqs. (3.3) and (3.4) represent one of the most classical solution to obtain the relation between the states at both ends of a periodic structure. However, as described by Stephen

[103], such a two-point boundary value problem is ill-conditioned, which can lead to numerical instabilities. The deficiency of Eq. (3.4) has been confirmed when computing some of the frequency response functions (FRFs) illustrating the present manuscript. Indeed, an increase of the upper frequency limits or an increase of the number of unit cells would induce numerical issues. Alternatively, Stephen [103] proposes a numerically reliable formulation based on a "Riccati transfer matrix method". This method is presented below for a case where external forces only apply at one of the two ends of the periodic structure. First, the transfer matrix is partitioned as

$$\begin{bmatrix} \boldsymbol{q}_{i+1} \\ \boldsymbol{F}_{i+1} \end{bmatrix} = \begin{bmatrix} \boldsymbol{T}^{\boldsymbol{qq}} & \boldsymbol{T}^{\boldsymbol{qF}} \\ \boldsymbol{T}^{\boldsymbol{Fq}} & \boldsymbol{T}^{\boldsymbol{FF}} \end{bmatrix} \begin{bmatrix} \boldsymbol{q}_{i} \\ \boldsymbol{F}_{i} \end{bmatrix}, \tag{3.5}$$

where the subscript i goes from 0 to $n-1$ when the periodic structure is made of n unit cells. The procedure proposed by Stephen [103] relies on the Riccati transform, which postulates that the forces and the displacements at both ends of a unit cell are given by

$$\begin{array}{l} \boldsymbol{F}_{i+1} = \boldsymbol{R}_{i+1}\boldsymbol{q}_{i+1} + \boldsymbol{g}_{i+1} \\ \boldsymbol{F}_{i} = \boldsymbol{R}_{i}\boldsymbol{q}_{i} + \boldsymbol{g}_{i} \end{array}, \tag{3.6}$$

where the Riccati matrix $\boldsymbol{R}$ and the column vector of force components $\boldsymbol{g}$ are to be determined. To this end, a recursive scheme is implemented. From Eqs. (3.5) and (3.6), it is found that

$$\begin{array}{l} \boldsymbol{q}_{i+1} = \boldsymbol{T}^{\boldsymbol{qq}}\boldsymbol{q}_{i} + \boldsymbol{T}^{\boldsymbol{qF}}\left[\boldsymbol{R}_{i}\boldsymbol{q}_{i} + \boldsymbol{g}_{i}\right] \\ \boldsymbol{R}_{i+1}\boldsymbol{q}_{i+1} + \boldsymbol{g}_{i+1} = \boldsymbol{T}^{\boldsymbol{Fq}}\boldsymbol{q}_{i} + \boldsymbol{T}^{\boldsymbol{FF}}\left[\boldsymbol{R}_{i}\boldsymbol{q}_{i} + \boldsymbol{g}_{i}\right] \end{array}, \tag{3.7}$$

which leads to

$$\left(\boldsymbol{R}_{i+1}\left[\boldsymbol{T}^{\boldsymbol{qq}} + \boldsymbol{T}^{\boldsymbol{qF}}\boldsymbol{R}_{i}\right] - \left[\boldsymbol{T}^{\boldsymbol{Fq}} + \boldsymbol{T}^{\boldsymbol{FF}}\boldsymbol{R}_{i}\right]\right)\boldsymbol{q}_{i} + \left(\boldsymbol{g}_{i+1} + \left[\boldsymbol{R}_{i+1}\boldsymbol{T}^{\boldsymbol{qF}} - \boldsymbol{T}^{\boldsymbol{FF}}\right]\boldsymbol{g}_{i}\right) = \boldsymbol{0}. \tag{3.8}$$

In order to have Eq. (3.8) true for any arbitrary $\boldsymbol{q}_i$, it is required that

$$\begin{array}{l} \boldsymbol{g}_{i+1} + \left[\boldsymbol{R}_{i+1}\boldsymbol{T}^{\boldsymbol{qF}} - \boldsymbol{T}^{\boldsymbol{FF}}\right]\boldsymbol{g}_{i} = \boldsymbol{0} \\ \boldsymbol{R}_{i+1}\left[\boldsymbol{T}^{\boldsymbol{qq}} + \boldsymbol{T}^{\boldsymbol{qF}}\boldsymbol{R}_{i}\right] - \left[\boldsymbol{T}^{\boldsymbol{Fq}} + \boldsymbol{T}^{\boldsymbol{FF}}\boldsymbol{R}_{i}\right] = \boldsymbol{0} \end{array}, \tag{3.9}$$

which can be reformulated as

$$\begin{array}{l} \boldsymbol{g}_{i} = \left[\boldsymbol{T}^{\boldsymbol{FF}} - \boldsymbol{R}_{i+1}\boldsymbol{T}^{\boldsymbol{qF}}\right]^{-1}\boldsymbol{g}_{i+1} \\ \boldsymbol{R}_{i} = \left[\boldsymbol{T}^{\boldsymbol{FF}} - \boldsymbol{R}_{i+1}\boldsymbol{T}^{\boldsymbol{qF}}\right]^{-1}\left[\boldsymbol{R}_{i+1}\boldsymbol{T}^{\boldsymbol{qq}} - \boldsymbol{T}^{\boldsymbol{Fq}}\right] \end{array}. \tag{3.10}$$

Eq. (3.10) represents the "backward in space" recursive process, which compute all $\boldsymbol{g}_i$ and $\boldsymbol{R}_i$ from the knowledge of their values at the right end of the structure, i.e. $\boldsymbol{g}_n$ and $\boldsymbol{R}_n$. Then, the displacement and force vectors can be computed all along the structure with the "forward in space" process deduced from Eqs. (3.6) and (3.7) as

$$\begin{array}{l} \boldsymbol{q}_{i+1} = \left[\boldsymbol{T}^{\boldsymbol{qq}} + \boldsymbol{T}^{\boldsymbol{qF}}\boldsymbol{R}_{i}\right]\boldsymbol{q}_{i} + \boldsymbol{T}^{\boldsymbol{qF}}\boldsymbol{g}_{i} \\ \boldsymbol{F}_{i+1} = \boldsymbol{R}_{i+1}\boldsymbol{q}_{i+1} + \boldsymbol{g}_{i+1} \end{array}. \tag{3.11}$$

For example, as $\boldsymbol{F_n} = \boldsymbol{0}$ at the non-excited end of a free-free periodic structure and $\boldsymbol{F}_n = \boldsymbol{R}_n \boldsymbol{q}_n + \boldsymbol{g}_n$, one can set $\boldsymbol{R}_n = \boldsymbol{0}$ and $\boldsymbol{g}_n = \boldsymbol{0}$. Furthermore, with a prescribed force $\boldsymbol{F_0}$ applied to the left end, $\boldsymbol{q}_0 = {\boldsymbol{R}_0}^{-1} [\boldsymbol{F}_0 - \boldsymbol{g}_0]$ and the displacement $\boldsymbol{q_n}$ at the right end is then computed from Eqs. (3.10) and (3.11). Note that the use of the Riccati transfer matrix method is not required for problems involving a few state variables along about ten unit cells but it becomes essential when considering more complex cases.

3.2.2 Mechanical analysis of a rod

For a one-dimensional homogeneous medium of Young's modulus Y and density ρ, the longitudinal wave equation can be expressed as

$$\rho \frac{\partial^2 u(x,t)}{\partial t^2} = Y \frac{\partial^2 u(x,t)}{\partial x^2}, \tag{3.12}$$

where $u(x,t)$ refers to the longitudinal displacement. A space-time separation $u(x,t) = U(x)g(t)$ decouples the space and time contributions and gives the dispersion relation:

$$\begin{array}{l} U''(x) + k^2 U(x) = 0 \\ g''(t) + \omega^2 g(t) = 0 \end{array} \quad \text{with} \quad \omega^2 = \frac{Y}{\rho} k^2, \tag{3.13}$$

where $[\cdot]''$ represents the second derivative, ω is the angular frequency and k is the wavenumber. Consequently, the longitudinal displacement amplitude of the rod segment presented in Fig. 3.1 is given by

$$U(x) = U_{\mathrm{L}} \cos(kx) + \frac{U_{\mathrm{R}} - U_{\mathrm{L}} \cos(ka)}{\sin(ka)} \sin(kx), \tag{3.14}$$

where a is the length of the rod segment and the subscripts L and R refer respectively to the positions at $x = 0$ and $x = a$.

The normal force into the rod, $N(x)$, is related to the displacement in Eq. (3.14) through

$$\begin{array}{l} N(x) = YSU'(x) \\ -\rho S \omega^2 U(x) = N'(x) \end{array} , \tag{3.15}$$

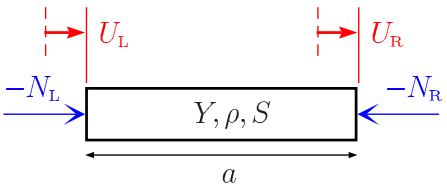

Figure 3.1: Considered rod segment.

where S is the cross-sectional area. Consequently, from the first equation in (3.15), the forces at both ends are obtained from the end displacements of the rod segment as

$$\begin{aligned} N_{\mathrm{L}} &= YSk\frac{U_{\mathrm{R}} - U_{\mathrm{L}}\cos(ka)}{\sin(ka)} \\ N_{\mathrm{R}} &= -YSkU_{\mathrm{L}}\sin(ka) + YSk\frac{U_{\mathrm{R}} - U_{\mathrm{L}}\cos(ka)}{\sin(ka)}\cos(ka) \end{aligned} . \tag{3.16}$$

The two equations can be rearranged into the matrix form

$$\begin{bmatrix} U_{\mathrm{R}} \\ N_{\mathrm{R}} \end{bmatrix} = \begin{bmatrix} \cos(ka) & \frac{1}{YSk}\sin(ka) \\ -YSk\sin(ka) & \cos(ka) \end{bmatrix} \begin{bmatrix} U_{\mathrm{L}} \\ N_{\mathrm{L}} \end{bmatrix}. \tag{3.17}$$

Alternatively, a transfer matrix involving dimensionless state variables can be written as

$$\begin{bmatrix} U^{\star}_{\mathrm{R}} \\ N_{\mathrm{R}^{\star}} \end{bmatrix} = \begin{bmatrix} \cos(ka) & \frac{1}{ka}\sin(ka) \\ -ka\sin(ka) & \cos(ka) \end{bmatrix} \begin{bmatrix} U^{\star}_{\mathrm{L}} \\ N^{\star}_{\mathrm{L}} \end{bmatrix}, \tag{3.18}$$

where $U^{\star} = U/a$ and $N^{\star} = N/(YS)$. This refers to a transfer matrix formulation as in Eq. (3.1), with state vectors involving the dimensionless longitudinal displacements $U^{\star}$ and the normal forces $N^{\star}$.

3.2.3 Lattice model

The purpose of the transfer matrix formulation is not obvious for a homogeneous rod as the global solution can be obtained directly from the analysis of a single unit cell of length l (with $n = 1$). Nevertheless, the transfer matrix formulation becomes useful when looking at periodic models where the global layout is not identical to the local one. For the propagation of longitudinal waves, Brillouin analyzed the periodic lattice model as a discrete representation of a continuous medium [83]. A discrete rod model can be obtained by applying a finite difference method to the continuous equations in Eq. (3.15). When considering the forward, central and backward differences

$$[\cdot]'_{\mathrm{L}} = \tfrac{[\cdot]_{\mathrm{I}} - [\cdot]_{\mathrm{L}}}{a/2}, \qquad [\cdot]'_{\mathrm{I}} = \tfrac{[\cdot]_{\mathrm{R}} - [\cdot]_{\mathrm{L}}}{a}, \qquad \text{and} \qquad [\cdot]'_{\mathrm{R}} = \tfrac{[\cdot]_{\mathrm{R}} - [\cdot]_{\mathrm{I}}}{a/2} \ , \tag{3.19}$$

the following set of discrete equations is obtained:

$$\begin{aligned} -\tfrac{m}{2}\omega^2 U_{\mathrm{L}} &= N_{\mathrm{I}} - N_{\mathrm{L}} \\ -\tfrac{m}{2}\omega^2 U_{\mathrm{R}} &= N_{\mathrm{R}} - N_{\mathrm{I}} \\ N_{\mathrm{I}} &= K(U_{\mathrm{R}} - U_{\mathrm{L}}) \end{aligned} . \tag{3.20}$$

The mass m and the longitudinal stiffness K come directly from the local properties of the rod segment of length a, as

$$m = \rho S a \quad \text{and} \quad K = \frac{YS}{a}. \tag{3.21}$$

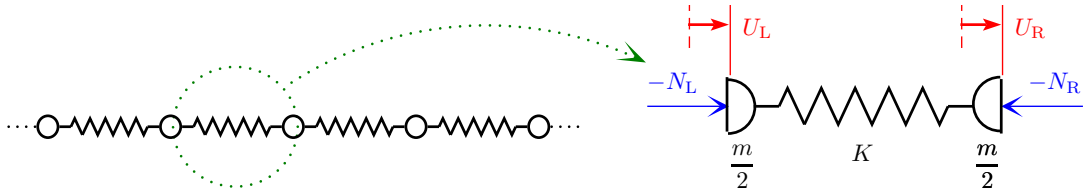

Figure 3.2: Lattice of point masses and corresponding unit cell.

Note that the set of equations (3.20) defines a unit cell made of two half masses $m/2$ at each ends of a spring K as shown in Fig. 3.2. A rod can thus be approximated by a periodic array of lumped masses connected in series by springs of identical stiffness.

As Eq. (3.20) involves the longitudinal displacement and the normal force at both ends of the unit cell, it can be reorganized into the transfer matrix formulation

$$\begin{bmatrix} U_{\mathrm{R}} \\ N_{\mathrm{R}} \end{bmatrix} = \begin{bmatrix} 1-f & \frac{1}{K} \\ -2Kf\left(1-\frac{f}{2}\right) & 1-f \end{bmatrix} \begin{bmatrix} U_{\mathrm{L}} \\ N_{\mathrm{L}} \end{bmatrix}, \tag{3.22}$$

where $f = \omega^2 m/(2K)$, which is equivalent to

$$\begin{bmatrix} U^\star_{\mathrm{R}} \\ N^\star_{\mathrm{R}} \end{bmatrix} = \begin{bmatrix} 1-f & 1 \\ -2f\left(1-\frac{f}{2}\right) & 1-f \end{bmatrix} \begin{bmatrix} U^\star_{\mathrm{L}} \\ N^\star_{\mathrm{L}} \end{bmatrix}, \tag{3.23}$$

where $U^\star = U/a$ and $N^\star = N/(Ka)$. The two eigenvalues of this transfer matrix are $\lambda^+ = 1 - f + \sqrt{f(f-2)}$ and $\lambda^- = 1 - f - \sqrt{f(f-2)}$. Since the eigenvalues are related to the equivalent wavenumber $\bar{k}$ of the discrete problem by $\lambda^\pm = \exp(\pm \mathrm{j}\bar{k}a)$, one gets $f = 1 - \cos(\bar{k}a)$, when $\bar{k}a \leq \pi$, i.e. $f \leq 2$. From the definition of f, this leads to the following non-linear dispersion relation

$$\omega^2 = \frac{Y}{\rho}\left(\bar{k}\ \mathrm{sinc}\left(\frac{\bar{k}a}{2}\right)\right)^2 \quad \text{for} \quad \bar{k}a < \pi, \tag{3.24}$$

where $\mathrm{sinc}(x) = \sin(x)/x$. Already introduced by Brillouin [83], this equation is here obtained from the transfer matrix and it can be compared to the rod dispersion relation presented in Eq. (3.13). Both relations are equivalent when $\bar{k}a$ goes to zero, i.e. when the unit cell is sufficiently small compared to the considered wavelength. As a reference, it can be seen from Eq. (3.24) that with 10 unit cells per wavelength ($\bar{k}a = 2\pi/10$), the frequency obtained with the discrete model differs by less than 2% from the one got with the rod dispersion relation. In any case, by comparing Eqs. (3.17) and (3.22), it is seen that we can convert the lattice into its initial continuous model by applying the following transformations before nondimensionalization:

$$f \to 1 - \cos(ka) \quad \text{and} \quad K \to \frac{YS}{a}\frac{ka}{\sin(ka)}. \tag{3.25}$$

Regarding a free-free rod of length $l = na$ excited at one end, we get the frequency response of the displacement at the other end from the transfer matrix method described in Eq. (3.4). The rod under consideration has a length equal to $l = 1$ m, a cross-sectional area $S = 4$ cm^2 and it is made of aluminum alloy 2017. Its Young's modulus is thus about $Y = 73.9$ GPa and its density is $\rho = 2780$ kg/m^3. The continuous model in Eq. (3.18) is compared to the lattice model in Eq. (3.23), when the rod is discretized in $n = 20$ unit cells. The two phase constants $\theta = ka$ and $\bar{\theta} = \bar{k}a$ in Fig. 3.4 represent the expected linear dispersion relation (3.13) for the continuous rod and the non-linear dispersion relation (3.24) for the lattice, when $\bar{k}a < \pi$. As soon as $\bar{k}a = \pi$, Fig. 3.3 shows that the attenuation constant of the lattice model increases, which creates a so-called "stop band" [104] above $\omega = 2\sqrt{K/m}$, i.e. a frequency around 32.8 kHz. On the other hand, the attenuation constant of the continuous rod is equal to zero all along the frequency band because no damping is introduced in the model. The effect of the stop band on the velocity FRF of the lattice is observed in Fig. 3.5, where no modes occur above 32.8 kHz. We note a clear difference between the two models above the fourth mode, which corresponds to a number of unit cells per wavelength close to 10. In the end, all the previous elements give a way to study the mechanical behavior of a rod as well as its discrete equivalent. The differences between those two models have been evaluated and the conversion from one to the other is clarified in both ways.

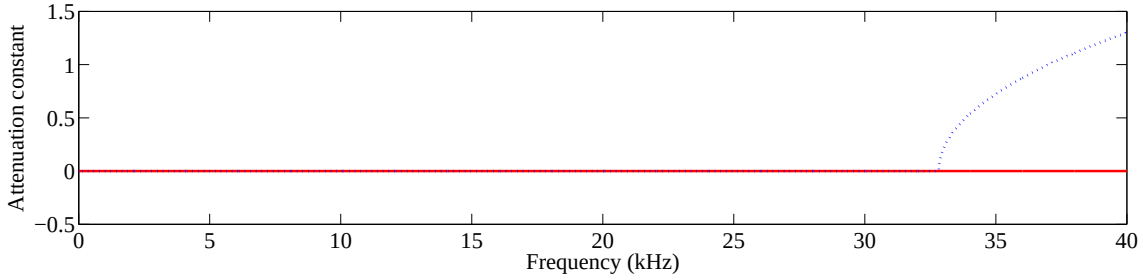

Figure 3.3: Attenuation constants - (—) for the continuous rod, (· · ·) for the lattice model.

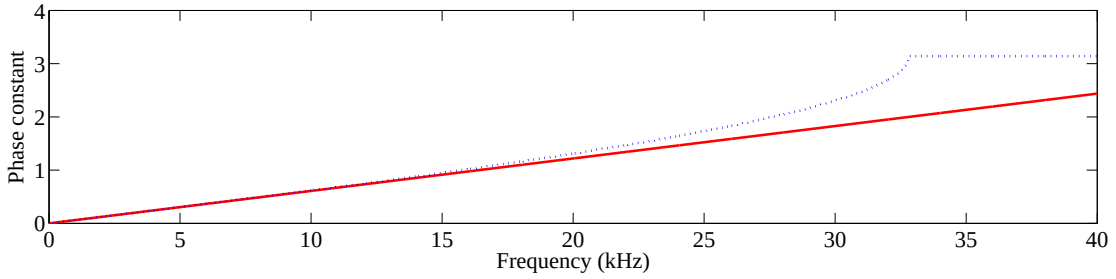

Figure 3.4: Phase constants - (—) for the continuous rod, (· · ·) for the lattice model.

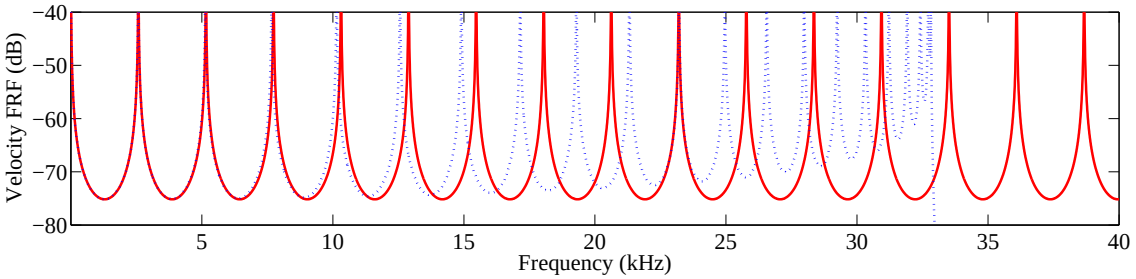

Figure 3.5: Velocity FRFs - (—) for the continuous rod, (· · ·) for the lattice model.

3.3 Array of resonant shunts

A passive damping solution is presented by considering the example of a periodic distribution of tuned mass dampers. The analysis is then extended to the case of a rod covered with an array of piezoelectric resonant shunts. An electromechanical unit cell is defined as a homogeneous medium subjected to a global piezoelectric coupling. From the value of the piezoelectric capacitance, the tuning of the inductors is defined and the practical limits of the control strategy are highlighted.

3.3.1 Distributed tuned mass dampers

A solution to limit vibration of a structure is to add multiple control devices locally. Passive control strategies have the benefit of being self-sufficient and unconditionally stable. When looking at such passive solutions, the tuned mass damping systems are able to convert vibration energy from a main structure to the added masses [1]. As introduced in Chap. 2, this energy transfer applies around a specific frequency, which is chosen by tuning the resonance of the added systems. The strategy can be implemented in a periodic lattice by distributing identical tuned mass systems as proposed in the Vincent's model [83]. An alternative is presented in Fig. 3.6, where a strain in the main structure is converted into a displacement of the added system thanks to a massless lever of e ratio. This stresses the spring of stiffness $\tilde{K}$ which put the tuned mass $\tilde{m}$ into motion.

As with the previous unit cell, the mechanical analysis of this new sub-structure is performed for the purpose of getting the transfer matrix formulation of the problem. For small displacements, we note from Fig. 3.6 that

$$\begin{array}{ll} -\frac{m}{2}\omega^2 U_{\mathrm{L}} = N_{\mathrm{I}} - N_{\mathrm{L}} & \\ -\frac{m}{2}\omega^2 U_{\mathrm{R}} = N_{\mathrm{R}} - N_{\mathrm{I}} & \text{and} \quad -\tilde{m}\omega^2\tilde{U} = -\tilde{K}(\tilde{U} - \tilde{X}_{\mathrm{I}}) \\ N_{\mathrm{I}} = K(U_{\mathrm{R}} - U_{\mathrm{L}}) + F_{\mathrm{I}} & \quad F_{\mathrm{I}} = e\tilde{K}(\tilde{U} - \tilde{X}_{\mathrm{I}}) \\ & \quad \tilde{X}_{\mathrm{I}} = -e(U_{\mathrm{R}} - U_{\mathrm{L}}) \end{array} , \tag{3.26}$$

where F_{I} is the force generated by the lever system, $\tilde{U}$ is the displacement of the mass $\tilde{m}$ and $\tilde{X}_{\mathrm{I}}$ is the displacement of the base of the spring $\tilde{K}$. Then, the internal variables N_{I},

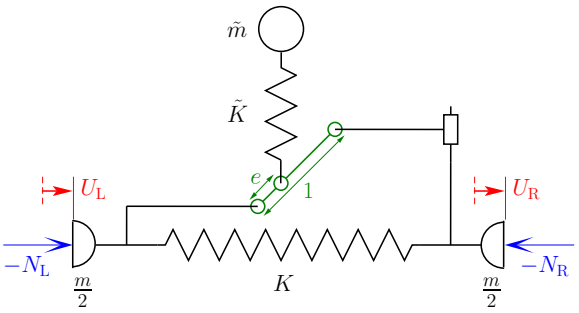

Figure 3.6: A tuned mass damper connected to each unit cell.

F_{I}, $\tilde{U}$ and U_{I} are removed from the system of equations (3.26) and we get the formulation

$$\begin{bmatrix} U_{\mathrm{R}}^{\star} \\ N_{\mathrm{R}}^{\star} \end{bmatrix} = \begin{bmatrix} 1 - f\tilde{f} & \tilde{f} \\ -2f\left(1 - \frac{f\tilde{f}}{2}\right) & 1 - f\tilde{f} \end{bmatrix} \begin{bmatrix} U_{\mathrm{L}}^{\star} \\ N_{\mathrm{L}}^{\star} \end{bmatrix}, \quad \text{where} \quad \tilde{f} = \frac{1 - \omega^2 \frac{\tilde{m}}{\tilde{K}}}{1 - \omega^2 \frac{\tilde{m}}{\tilde{K}}\left(1 + e^2 \frac{\tilde{K}}{K}\right)}. \quad (3.27)$$

When $e = 0$, it can be seen that $\tilde{f} = 1$ and the transfer matrix becomes equal to the one presented in Eq. (3.23). Without coupling, the added system has no effect and the structure behaves as a simple lattice. Then, for $e \neq 0$ and $\omega = \sqrt{\tilde{K}/\tilde{m}}$, which correspond to the natural frequency of the added spring-mass systems, $\tilde{f}$ becomes equal to zero. Therefore, $U_{\mathrm{R}} = U_{\mathrm{L}}$ for every unit cells. The displacement is the same in the entire primary lattice and no strain is observable whatever the boundary conditions.

The independent tuned mass damping strategy can be applied to the one meter free-free rod considered in Sec. 3.2. This finite structure is still discretized into a lattice of $n = 20$ unit cells and each one is fitted with an identical tuned mass damper, as presented in Fig. 3.6. The added mass $\tilde{m}$ is then set to one tenth of the mass m and $\tilde{K}$ is tuned so that the natural frequency of the spring-mass systems corresponds to the first natural frequency of the main structure.

The right end velocity is computed from Eqs. (3.4) and (3.27) by applying a harmonic unit force to the left end of the lattice. The results are shown in Fig. 3.7, where three cases are presented. The first one corresponds to a situation with a lever ratio e equal to 0. The lattice is vibrating without any effect of the added system and the first four natural frequencies are displayed. As no damping is added in the model, the velocity goes naturally to infinity at those particular frequencies. The second case is computed with $e = 1$ and again without damping. Around the first natural frequency the initial resonance is no more observable as the energy is transferred to the added masses. Yet, new resonances appear on both sides of the previous one, as it is classically observed when using undamped tuned mass systems [1]. The amplitude of those new resonances can be reduced by introducing damping. The solution provided in most of the tuned mass strategies consists in adding a damper in parallel to the springs of stiffness $\tilde{K}$. However, it is also possible to consider

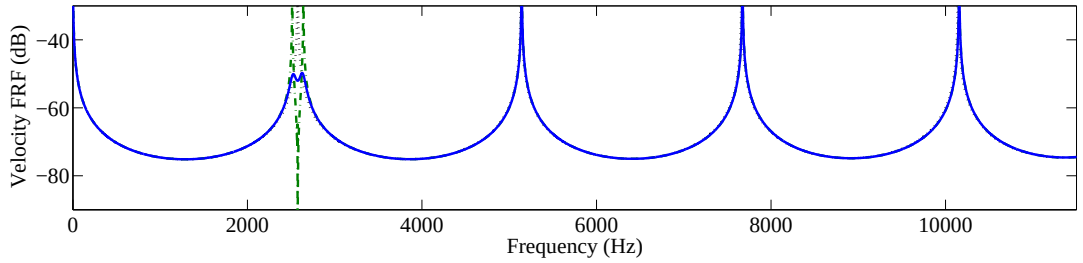

Figure 3.7: Velocity FRFs with independent tuned masses - $(\cdots)$ with $e = 0$, $(\text{- } \cdot \text{ -})$ with $e = 1$ and $\tilde{c} = 0$, $(—)$ with $e = 1$ and $\tilde{c} = 5$.

a damper linking directly the tuned masses to the ground [41], as presented in Chap. 2. This last solution is implemented by replacing the tuned masses $\tilde{m}$ by $\tilde{m} - j\tilde{c}/\omega$, where $\tilde{c}$ is the viscous coefficient of the added dampers. With $\tilde{c} = 5$ N/(m/s), the velocity amplitude around the first resonance is significantly reduced. This illustrates the efficiency of the independent tuned mass dampers for a control focusing on one particular resonance.

3.3.2 Shunted piezoelectric unit cell

The previous distributed control can be implemented on a rod with an array of resonant shunts. Indeed, it has been shown in Chap. 2 that an inductor shunted on a piezoelectric patch represents the analogue of a tuned mass system. So, a homogeneous rod is covered with a periodic distribution of shunted piezoelectric patches, as seen in Fig. 3.8. An electromechanical periodic structure is obtained and the unit cell that repeats along the main direction is isolated. The rod segment has a length a, a width b and a thickness h_s. It is symmetrically covered with a pair of piezoelectric patches of length l_p, width b and thickness h_p, which are connected in parallel and polarized in opposite directions for the control of longitudinal vibrations [4, 102]. V_I is the voltage on the external electrodes and q_I is the current flowing to the pair of piezoelectric patches. No resistor is represented in the piezoelectric shunt because electrical damping can be introduced through equivalent

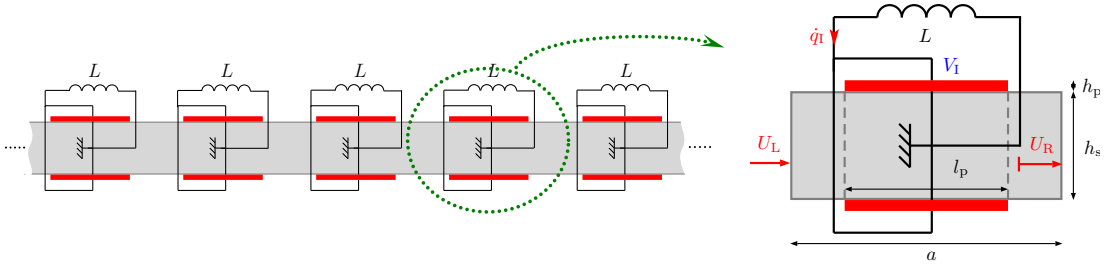

Figure 3.8: Array of shunted piezoelectric patches and corresponding electromechanical unit cell.

	Rod (Aluminum 2017)	Patches (PIC 151)
Length (mm)	$20 \times a = 20 \times 50$	$l_\mathrm{p} = 30$
Width (mm)	$b = 20$	$b = 20$
Thickness (mm)	$h_\mathrm{s} = 20$	$h_\mathrm{p} = 0.5$
Density (kg/m^3)	$\rho_\mathrm{s} = 2780$	$\rho_\mathrm{p} = 7800$
Young's modulus (GPa)	$Y_\mathrm{s} = 73.9$	$1/s_{11}^E = 66.7$
Charge constant (pC/N)	-	$d_{31} = -210$
Permittivity (nF/m)	-	$\epsilon_{33}^\sigma = 21.2$

Table 3.1: Dimensions and material properties for the rod and for the piezoelectric patches.

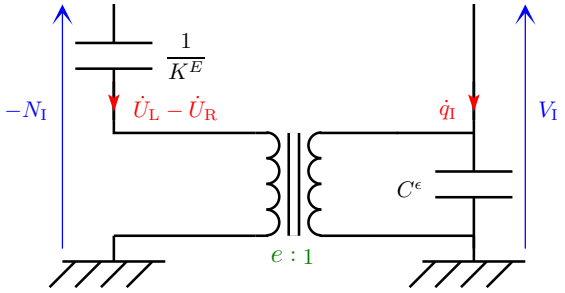

Figure 3.9: Global model of the piezoelectric unit cell.

complex values of the electrical components. The geometric and material properties in Table 3.1 are taken into account in the following numerical applications.

The unit cell in Fig. 3.8 is a composite laminate made of an elastic rod segment and two piezoelectric patches. Yet, this unit cell can be firstly seen as an homogenized medium governed by a global piezoelectric coupling similar to the discrete model described in Chap. 2 for a single piezoelectric patch. If K^E is the longitudinal stiffness of the unit cell when the patches are short-circuited and C^ε is the total piezoelectric capacitance when the unit cell is fixed, then the coupling can be approximated by

$$\begin{array}{l} N_\mathrm{I} = K^E \Delta U - e V_\mathrm{I} \\ q_\mathrm{I} = e \Delta U + C^\varepsilon V_\mathrm{I} \end{array} , \tag{3.28}$$

where N_I represents the normal force and $\Delta U = U_\mathrm{R} - U_\mathrm{L}$ is the difference between the right and left displacements. This discrete model can also be represented by the electrical circuit in Fig. 3.9 where the global coupling coefficient e appears in the transformer ratio [72]. Note that this model is valid only if the considered wavelength is large compared to the length a of the unit cell. From this large wavelength condition, the rod segment can be approximated by its lattice model described in Eq. (3.20), which gives

$$\begin{array}{l} -\frac{m}{2}\omega^2 U_\mathrm{L} = N_\mathrm{I} - N_\mathrm{L} \\ -\frac{m}{2}\omega^2 U_\mathrm{R} = N_\mathrm{R} - N_\mathrm{I} \end{array} , \quad \text{where} \quad m = \rho_\mathrm{s} h_\mathrm{s} b a + 2\rho_\mathrm{p} h_\mathrm{p} b l_\mathrm{p}. \tag{3.29}$$

Regarding the electrical circuit, we get $V_\mathrm{I} = -\mathrm{j}\omega L \dot{q}_\mathrm{I}$ when the shunt is made of a single

inductor L. Combining Eqs. (3.28) and (3.29) then leads to the transfer matrix formulation

$$\begin{bmatrix} U_{\mathrm{R}}^{\star} \\ N_{\mathrm{R}}^{\star} \end{bmatrix} = \begin{bmatrix} 1 - f\tilde{f} & \tilde{f} \\ -2f\left(1 - \frac{f\tilde{f}}{2}\right) & 1 - f\tilde{f} \end{bmatrix} \begin{bmatrix} U_{\mathrm{L}}^{\star} \\ N_{\mathrm{L}}^{\star} \end{bmatrix}, \quad \text{where} \quad \tilde{f} = \frac{1 - \omega^2 LC^{\varepsilon}}{1 - \omega^2 LC^{\varepsilon}\left(1 + \frac{e^2}{K^E C^{\varepsilon}}\right)} \tag{3.30}$$

and $f = \omega^2 m/(2K^E)$. Finally, Eq. (3.30) is equivalent to the purely mechanical problem in Eq. (3.27) after updating the global constants to suit with the present electromechanical case. Those global constants still need to be defined in order to allow the calculation of the transfer matrix.

3.3.3 Determination of the global constants

The stiffness K^E corresponds to the longitudinal stiffness of the short-circuited unit cell. In this situation, the equivalent Young's modulus of the piezoelectric material is $Y_{\mathrm{p}}^E = 1/s_{11}^E$, which is given in Table 3.1. If the Young's modulus of the rod is Y_{s}, the stiffness K^E is then obtained from the geometry of the unit cell. When considering that the cross-sections remain undeformed,

$$\frac{1}{K^E} = \frac{l_{\mathrm{p}}}{Y_{\mathrm{s}}S_{\mathrm{s}} + 2Y_{\mathrm{p}}^E S_{\mathrm{p}}} + \frac{a - l_{\mathrm{p}}}{Y_{\mathrm{s}}S_{\mathrm{s}}}, \tag{3.31}$$

where $S_{\mathrm{s}} = bh_{\mathrm{s}}$ and $S_{\mathrm{p}} = bh_{\mathrm{p}}$ are the rod and patch cross-sectional areas. In order to complete the model, the capacitance C^{ε} and the global coupling coefficient e still need to be defined. C^{ε} is the capacitance of the pair of patches when ΔU is equal to zero. It is not simply equal to two times $C_{\mathrm{p}}^{\varepsilon}$, the blocked capacitance of a single isolated patch at constant stain, for two reasons. First, even with $U_{\mathrm{L}} = U_{\mathrm{R}} = 0$, the patches are not completely blocked along the direction '1' when $a \neq l_{\mathrm{p}}$. Second, the definition of $C_{\mathrm{p}}^{\varepsilon}$ in Chap. 2 is only valid if the considered piezoelectric patch is free in its transverse directions. Here, the two patches cannot freely extend in the direction '2' because they are glued onto the rod. Even if no external force is applied, a patch is always constrained by the elastic material on which it is glued. Consequently, its capacitance is significantly lower than the capacitance of a free single patch. The analytic calculation of C^{ε} is not trivial and requires to take into account 3D effects. The same problem appears when focusing on the global coupling coefficient e, which cannot be obtained directly from a simple one dimensional model. This was analyzed by Maurini et al. [18, 71], who presented corrected 1D coefficients obtained from a 3D formulation. For instance, when considering thin piezoelectric patches compared to the main elastic structure, i.e. $h_p/h_s \ll 1$, it has been shown that, in the longitudinal case, the blocked capacitance can be approximated by

$$C^{\varepsilon} = 2\epsilon_{33}^{\varepsilon\star}\frac{bl_{\mathrm{p}}}{h_{\mathrm{p}}}\left(1 + 2k_{31}^2\frac{1 + \nu_{\mathrm{p}}^E}{1 - \nu_{\mathrm{p}}^E - 2k_{31}^2}\frac{Y_{\mathrm{p}}^E}{Y_{\mathrm{s}}}\frac{h_{\mathrm{p}}}{h_{\mathrm{s}}}\right) \quad \text{where} \quad \epsilon_{33}^{\varepsilon\star} = \epsilon_{33}^{\sigma}\left(1 - \frac{2k_{31}^2}{1 - \nu_{\mathrm{p}}^E}\right), \tag{3.32}$$

$k_{31}^2 = d_{31}^2/(s_{11}^E \epsilon_{33}^\sigma)$, and ν_p^E is the Poisson's ratio of the patches at constant electric field. However, the proposed analytic calculations do not take into account the effect of the bounding layer between the patches and the main structure [18]. This non-perfect bonding might influence the results when the thickness of the bonding layer is not negligible compared the thickness of the patches. It then becomes important to be able to determine the global constants from direct measurements on the considered piezoelectric structure.

A method for getting global constants is found from the discrete model in Eq. (3.28). If C^σ is the global capacitance obtained when $N_\mathrm{I} = 0$, we get $\Delta U = eV_\mathrm{I}/K^E$ and thus $C^\sigma = C^\varepsilon + e^2/K^E$. Furthermore, when $q_\mathrm{I} = 0$, then $V_\mathrm{I} = -e\Delta U/C^\varepsilon$, so that the equivalent stiffness in open circuit is $K^D = K^E + e^2/C^\varepsilon$. Alternatively, C^σ and K^D can be obtained directly from Fig. 3.9, which refers to the same model. Consequently, Eq. (3.33) gives the expressions for the remaining global constants:

$$\begin{aligned} C^\varepsilon &= C^\sigma \frac{K^E}{K^D} \\ e &= \sqrt{C^\sigma K^E \left(1 - \frac{K^E}{K^D}\right)} \end{aligned} . \tag{3.33}$$

K^D is calculated in the same way as K^E by replacing Y_p^E by Y_p^D in Eq. (3.31). The equivalent Young's modulus in open-circuit has been defined in Chap. 2 as $Y_\mathrm{p}^D = 1/(s_{11}^E - d_{31}^2/\epsilon_{33}^\sigma)$. Recall that this expression is valid only if the considered wavelength is large compared to the length of the unit cell. Moreover, it requires a stress equal to zero along both transverse directions, which actually happens if the patch and the main structure have close Poisson's ratios. The measurement of C^ε is difficult in practice because it would require to block the ends of a unit cell. Yet, the capacitance in free conditions C^σ is more easily reachable because it can be obtained by direct measurement in free conditions.

3.3.4 Practical limits

The target angular frequency ω_O of a resonant shunt control is defined by the tuning of the inductance through

$$\omega_O = \frac{1}{\sqrt{LC^\varepsilon}}. \tag{3.34}$$

Actually, this condition simplify the transfer matrix in Eq. (3.30) into a rigid body motion case because $\tilde{f}$ is then equal to zero. For the case presented in Fig. 3.8, as C^ε is evaluated to 35.3 nF, the inductance L has to be around 110 mH for the control of the first longitudinal mode. This value is achievable with passive inductors but we note that lower frequency applications could be more critical. For example, with the same piezoelectric patches, a control at 25 Hz would require inductors above 1000 H. This questions the practical feasibility of the damping system, especially if the shunt has to be reproduced over a

large number of n unit cells. Increasing the number of piezoelectric patches does not solve the problem because the piezoelectric capacitance C^{ε} is approximately proportional to the surface area of the patches. So, for a constant thickness and volume of piezoelectric material, C^{ε} is proportional to $1/n$ and, from Eq. (3.34), L is proportional to n/ω_O^2. As a consequence, the strategy involving a succession of resonant shunts have significant limits on its frequency range of interest when considering a large number of small-size unit cells, as might appear through meta-material applications.

A second limitation concerns the lack of multimodal control with classical resonant shunts involving a single inductor. A variation of the n inductance values could be introduced in order to generate a broader control [105]. Here, we could consider four sets of $n/4$ inductors tuned to the first four modes of the rod. The problem is that each shunt brings damping on a single frequency band. Then, an increase of the number of modes to control decreases the number of shunts dedicated to each mode, which limits the damping efficiency. A solution to benefit from each piezoelectric patch on several frequency bands is to implement multi-resonant shunts. Various electrical topologies can be found in the literature as the "current blocking" [10] or "current flowing" [8, 11] branches. Yet, a simultaneous control of p mechanical modes would require at least p inductors and $(p-1)$ capacitors per shunts, which means $n \times p$ inductors and $n \times (p-1)$ capacitors for the whole periodic structure involving n unit cells. A large number of unit cells would thus lead to an impractical number of electrical components. As a consequence, the passive implementation of such a control system is once again compromised.

3.4 Coupling of a rod to its electrical analogue

A multimodal extension of the classical tuned mass damping strategy is proposed by coupling a lattice of point masses to its modal equivalent. The passive control is then represented in the electrical domain and the electrical analogue of a rod is defined. This analogous electrical network interconnects the array of piezoelectric patches in order to implement the multimodal damping of a rod. We present a simple tuning condition based on the global properties of a single unit cell.

3.4.1 Multimodal tuned mass damper

The previous control strategy consists in connecting identical unimodal devices to a multimodal structure. By extension, it is possible to consider a coupling between two multimodal structures. This concept can be illustrated by analyzing two lattices involving the same number of unit cells. The main lattice is the structure that needs to be controlled and the other one is considered as a multimodal control device. If all the natural frequencies

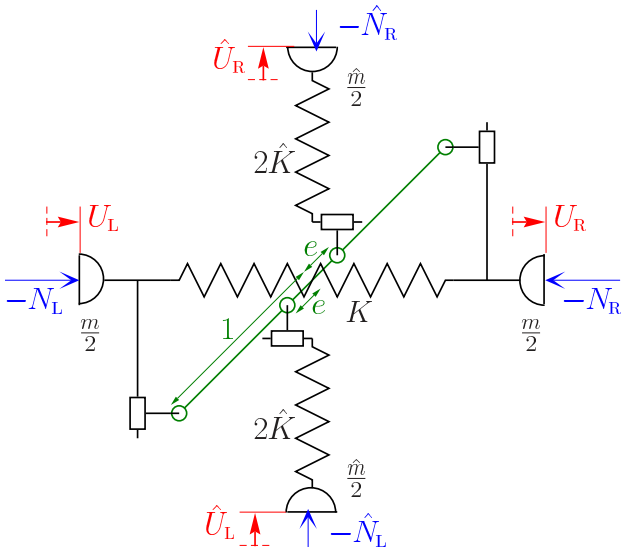

Figure 3.10: Unit cell for the coupling of two lattices.

of the control device are simultaneously tuned to those of the main structure, this added system should behave as a multimodal tuned mass damper.

The first step is to find a way to mechanically connect the two lattices in order to allow energy transfers between facing pairs of unit cells. A solution is presented in Fig. 3.10 as a generalization of the tuned mass damper architecture in Fig. 3.6. The fundamental difference is that the added masses are no more free but are inherent components of the secondary lattice. When the lever ratio e is equal to 0, the two lattices of n unit cells are completely independent. On the contrary, if e is different from zero, they interact through the n lever mobilities. The study of the global problem requires to focus on the unit cell presented in Fig. 3.10. For small displacements of the massless lever, we get

$$\begin{array}{l} -\frac{m}{2}\omega^2 U_{\mathrm{L}} = N_{\mathrm{I}} - N_{\mathrm{L}} \\ -\frac{m}{2}\omega^2 U_{\mathrm{R}} = N_{\mathrm{R}} - N_{\mathrm{I}} \\ N_{\mathrm{I}} = K(U_{\mathrm{R}} - U_{\mathrm{L}}) + F_{\mathrm{I}} \\ F_{\mathrm{I}} = e\hat{N}_{\mathrm{I}} \end{array} \quad \text{and} \quad \begin{array}{l} -\frac{\hat{m}}{2}\omega^2 \hat{U}_{\mathrm{L}} = \hat{N}_{\mathrm{I}} - \hat{N}_{\mathrm{L}} \\ -\frac{\hat{m}}{2}\omega^2 \hat{U}_{\mathrm{R}} = \hat{N}_{\mathrm{R}} - \hat{N}_{\mathrm{I}} \\ \hat{N}_{\mathrm{I}} = \hat{K}(\hat{U}_{\mathrm{R}} - \hat{U}_{\mathrm{L}} - \hat{X}_{\mathrm{I}}) \\ \hat{X}_{\mathrm{I}} = -e(U_{\mathrm{R}} - U_{\mathrm{L}}) \end{array}, \tag{3.35}$$

where F_{I} is the force generated by the lever system, $\hat{N}_{\mathrm{I}}$ is the normal force in the springs $2\hat{K}$ and $\hat{X}_{\mathrm{I}}$ is the displacement difference between the two points connecting the springs $2\hat{K}$ to the lever. This system of equations is equivalent to

$$\begin{bmatrix} U_{\mathrm{R}} \\ \hat{U}_{\mathrm{R}} \\ N_{\mathrm{R}} \\ \hat{N}_{\mathrm{R}} \end{bmatrix} = \begin{bmatrix} 1-f & e\frac{\hat{K}}{K}\hat{f} & \frac{1}{K} & -\frac{e}{K} \\ ef & 1-(1+\Lambda)\hat{f} & -\frac{e}{K} & \frac{1+\Lambda}{\hat{K}} \\ -2Kf\left(1-\frac{f}{2}\right) & -e\hat{K}f\hat{f} & 1-f & ef \\ -e\hat{K}f\hat{f} & -2\hat{K}\hat{f}\left(1-\frac{1+\Lambda}{2}\hat{f}\right) & e\frac{\hat{K}}{K}\hat{f} & 1-(1+\Lambda)\hat{f} \end{bmatrix} \begin{bmatrix} U_{\mathrm{L}} \\ \hat{U}_{\mathrm{L}} \\ N_{\mathrm{L}} \\ \hat{N}_{\mathrm{L}} \end{bmatrix}, \tag{3.36}$$

where $f = \omega^2 m/(2K)$, $\hat{f} = \omega^2 \hat{m}/(2\hat{K})$ and $\Lambda = e^2\hat{K}/K$. This transfer matrix formulation can then be written with dimensionless state variables $U^\star = U/a$, $N^\star = N/(Ka)$, $\hat{U}^\star = \hat{U}/(ea)$ and $\hat{N}^\star = \hat{N}/(e\hat{K}a)$ as

$$\begin{bmatrix} U_{\mathrm{R}}^\star \\ \hat{U}_{\mathrm{R}}^\star \\ N_{\mathrm{R}}^\star \\ \hat{N}_{\mathrm{R}}^\star \end{bmatrix} = \begin{bmatrix} 1-f & \Lambda\hat{f} & 1 & -\Lambda \\ f & 1-(1+\Lambda)\hat{f} & -1 & 1+\Lambda \\ -2f\left(1-\frac{f}{2}\right) & -\Lambda f\hat{f} & 1-f & \Lambda f \\ -f\hat{f} & -2\hat{f}\left(1-\frac{1+\Lambda}{2}\hat{f}\right) & \hat{f} & 1-(1+\Lambda)\hat{f} \end{bmatrix} \begin{bmatrix} U_{\mathrm{L}}^\star \\ \hat{U}_{\mathrm{L}}^\star \\ N_{\mathrm{L}}^\star \\ \hat{N}_{\mathrm{L}}^\star \end{bmatrix}, \tag{3.37}$$

By forcing $\hat{N}_{\mathrm{L}}^\star$ and $\hat{N}_{\mathrm{R}}^\star$ to zero, it is seen that the unit cell in Fig. 3.6 is a special case of the one illustrated in Fig. 3.10. Indeed, the 4×4 transfer matrix in Eq. (3.37) can be condensed into a 2×2 matrix which is equal to the matrix in Eq. (3.27), with

$$\tilde{m} = \frac{\hat{m}}{4}, \qquad \tilde{K} = \hat{K} \qquad \text{and thus} \quad \tilde{f} = \frac{1-\dfrac{\hat{f}}{2}}{1-(1+\Lambda)\dfrac{\hat{f}}{2}}. \tag{3.38}$$

After having connected the two lattices, a second step consists in tuning the added lattice to suit the modal properties of the main lattice. It can be seen from Eq. (3.23) that two lattice having a same f value, i.e. a same mass-stiffness ratio, would have identical dimensionless transfer matrices. Then, identical boundary conditions lead to a similar eigenmode problems for both lattices. In this situation, all the natural frequencies and mode shapes are identical in both structures. In order to show the effect of the modal coupling, the example free-free lattice with $n = 20$ unit cells is still considered. The mass $\hat{m}$ is arbitrarily set to $m/100$ and the modal coupling condition on the mass-stiffness ratio gives:

$$\hat{K} = \hat{m}\frac{K}{m}. \tag{3.39}$$

Considering the boundary conditions, the end forces of the secondary lattice, $\hat{N}_0$ and $\hat{N}_n$, are set to zero in order to satisfy the equivalence with the main free-free structure.

The 4×4 transfer matrix in Eq. (3.37) is used to compute the frequency response function of the right end velocity in the main lattice. The results of the multimodal coupling are shown in Fig. 3.11. When e is equal to zero, the frequency response function is the same as the one obtained without control. Indeed, no energy is transferred to the added masses which have thus no effect on the main lattice. However, the shape of the response is clearly different when e differs from 0. A tuned mass effect is then observable around all the initial natural frequencies. As mentioned previously, the amplitudes can be reduced by adding damping in the control system. Again, replacing $\hat{m}$ by $\hat{m} - j\hat{c}/\omega$ is equivalent to the addition of dampers between the ground and the masses of the secondary

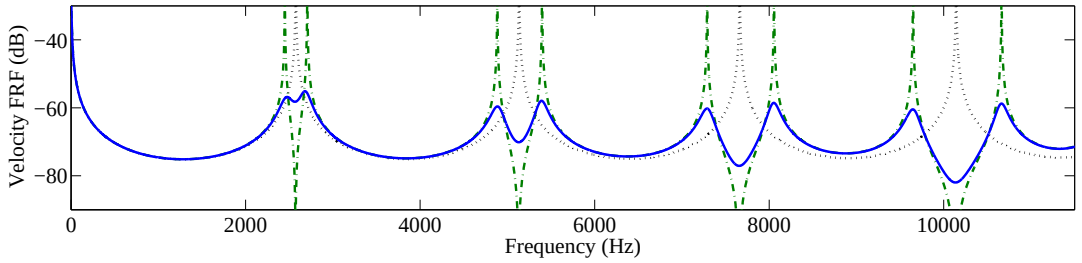

Figure 3.11: Velocity FRFs with a multimodal coupling - $(\cdots)$ with $e = 0$, $(\text{- } \cdot \text{ -})$ with $e = 1$ and $\hat{c} = 0$, $(—)$ with $e = 1$ and $\hat{c} = 1$.

lattice. With $\hat{c} = 1$ N/(m/s), it is seen that the velocity is strongly reduced whatever the considered frequency. This highlights the interest of the multimodal tuned mass damping strategy compared to a unimodal control. It is still remarked that the modal coupling condition presented in Eq. (3.39) does not take into account the influence of the damping parameter. Even if damping slightly shifts the resonances of the secondary lattice, we remark in the following practical applications that this shift is insignificant compared to the error induced by the discrete approximation of a continuous structure.

3.4.2 Electrical analogue of a rod

The previous lattice models can be transposed in the electrical domain by applying the direct electromechanical analogy [74, 84]. This analogy assumes the equivalence between force and voltage and between velocity and current. Consequently, a mass is equivalent to an inductance and stiffness is equivalent to the inverse of a capacitance. Thereby, a lattice of point masses corresponds to an electrical network made of a line of inductors with connections to the ground through capacitors [83]. This is illustrated in Fig. 3.12 together with the corresponding electrical unit cell. The equations governing the electrical unit cell,

$$\begin{aligned} -N_{\mathrm{L}} + N_{\mathrm{I}} &= \mathrm{j}\omega\tfrac{m}{2}\dot{U}_{\mathrm{L}} \\ -N_{\mathrm{I}} + N_{\mathrm{R}} &= \mathrm{j}\omega\tfrac{m}{2}\dot{U}_{\mathrm{R}} \\ -N_{\mathrm{I}} &= \tfrac{K}{\mathrm{j}\omega}(\dot{U}_{\mathrm{L}} - \dot{U}_{\mathrm{I}}) \end{aligned} \quad , \tag{3.40}$$

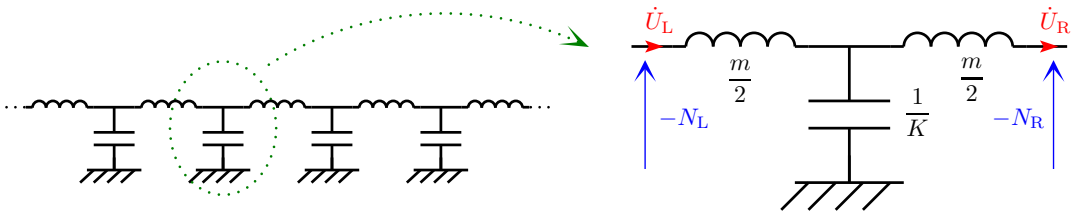

Figure 3.12: Electrical analogue of a lattice of point masses and corresponding unit cell.

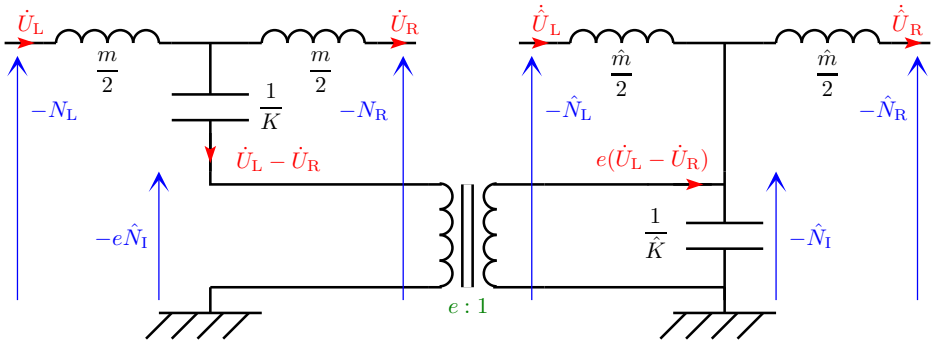

Figure 3.13: Unit cell for the coupling of two electrical networks.

are the same as in Eq. (3.20) for the mechanical lattice unit cell, which validates the analogous network. The analogues of the left and right currents are the derivatives of the left and right displacements. Yet, the two voltages are equivalent to the opposite of the normal forces in order to respect their definition that ensures an extension of the unit cell for a positive normal force.

As for the mechanical lattices, it is possible to consider the coupling of two electrical networks. The system of equation Eq. (3.35) is thus reformulated into

$$\begin{aligned} -N_\mathrm{L}+N_\mathrm{I} &= \mathrm{j}\omega\tfrac{m}{2}\dot{U}_\mathrm{L} \\ -N_\mathrm{I}+N_\mathrm{R} &= \mathrm{j}\omega\tfrac{m}{2}\dot{U}_\mathrm{R} \\ -N_\mathrm{I} &= \tfrac{K}{\mathrm{j}\omega}(\dot{U}_\mathrm{L}-\dot{U}_\mathrm{R})-e\hat{N}_\mathrm{I} \end{aligned} \quad \text{and} \quad \begin{aligned} -\hat{N}_\mathrm{L}+\hat{N}_\mathrm{I} &= \mathrm{j}\omega\tfrac{\hat{m}}{2}\dot{\hat{U}}_\mathrm{L} \\ -\hat{N}_\mathrm{I}+\hat{N}_\mathrm{R} &= \mathrm{j}\omega\tfrac{\hat{m}}{2}\dot{\hat{U}}_\mathrm{R} \\ -\hat{N}_\mathrm{I} &= \tfrac{\hat{K}}{\mathrm{j}\omega}\left(\dot{\hat{U}}_\mathrm{L}-\dot{\hat{U}}_\mathrm{R}+e(\dot{U}_\mathrm{L}-\dot{U}_\mathrm{R})\right) \end{aligned} . \tag{3.41}$$

In this way, the analogue of the coupled mechanical unit cell in Fig. 3.10 is presented in Fig. 3.13. The electrical equations are exactly the same as when coupling two mechanical lattices. A transformer of e ratio transfers the energy from a network to the other. This is the analogue of the lever represented in the mechanical model. The electric transfer matrix corresponding to the coupling of two networks can thus be directly obtained from Eq. (3.37). By setting $\hat{N}_\mathrm{L}=\hat{N}_\mathrm{R}=0$ in the electrical circuit in Fig. 3.13, it appears the electrical analogue of a tuned mass system, as presented in Fig. 3.6 with a tuned mass $\tilde{m}=\hat{m}/4$. Finally, all the presented discrete mechanical models can thus be transposed into their electrical analogues. The corresponding transfer matrices are the same and can be used to study wave propagation in an electrical network.

3.4.3 Interconnected array of piezoelectric patches

The multimodal damping strategy illustrated in Fig. 3.11 for a purely mechanical case can be extended to an electromechanical problem involving a rod coupled to its analogous electrical network. Indeed, by comparing the coupled unit cell in Fig. 3.13 to the model

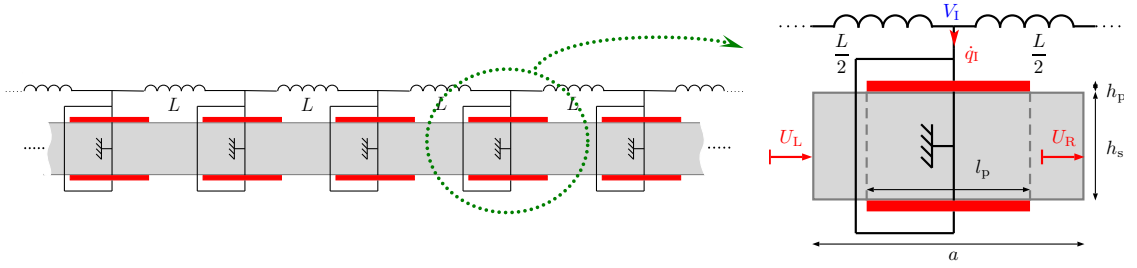

Figure 3.14: Interconnected array of piezoelectric patches and corresponding electromechanical unit cell.

related to the piezoelectric coupling in Fig. 3.9, we conceive that a multimodal control can be achieved by interconnecting successive piezoelectric patches with suitable inductors. The periodic electrical network interconnecting the array of patches is represented in Fig. 3.14 together with the corresponding electromechanical unit cell. The analogue of a discretized rod is thus implemented as in Fig. 3.12 because each piezoelectric patch acts as a capacitor.

A multimodal control is ensured by applying the modal coupling condition (3.39) adapted to the electromechanical problem:

$$\frac{1}{LC^{\varepsilon}} = \frac{K^E}{m}. \tag{3.42}$$

So, the tuning of the network does not depend directly on a target frequency but it depends on the local properties of the structure to control. By taking into account the numerical values in Table 3.1, the inductance L is around 3 mH. This value is significantly lower than the 110 mH inductance required for the control of the first longitudinal mode with distributed resonant shunts. Furthermore, the modal coupling condition and the definition of the global constants show that the required inductance decreases with an increase of the number of unit cells. Indeed, for a piezoelectric material covering the whole length of the rod but divided into n electrodes, the individual capacitance C^{ε} and the mass of a rod segment are proportional to $1/n$, while the stiffness K^E is proportional to n. From Eq. (3.42), this means that L is proportional to $1/n$. This conclusion was already highlighted by Maurini et al. [15, 17, 18] from the analysis of an electrical continuum. The relation is here illustrated from the discrete formulation and it still means that an increase of the number of unit cells leads to lower values of the n individual inductors. As a consequence, it becomes possible to look at lower frequency applications without being limited by the inductance values proposed in standard series of passive inductors. This strongly increases the potential of the multimodal damping strategy, which was already attractive for its broadband capabilities.

3.5 Transfer matrix models for longitudinal propagation

For the study of a one-dimensional electromechanical structure, a periodic layout enables the use of a transfer matrix method that applies on state vectors including both mechanical and electrical variables. Even if the electrical medium is discrete, the mechanical structure can be approximated either by its discrete equivalent, by its homogenized forms or by its finite element model. Offering an increasing complexity, those formulations are compared in order to define their respective limits. Depending on the frequency range of interest and the required accuracy, it is then possible to choose a suitable model for the analysis of damping systems involving a piezoelectric network.

3.5.1 Discrete model based on global properties

In order to study a finite structure consisting of n unit cells as the one presented in Fig. 3.14, a first step is to define its electromechanical transfer matrix. Contrary to previous studies on distributions of piezoelectric patches which focus on an homogenization of the electrical network [12, 13, 17, 21, 22, 22, 94, 96], it is here chosen to discretize the mechanical medium. This simplifies the problem and offers equivalence to the discrete electrical network. From a mechanical point of view, the discrete model can be illustrated by Fig. 3.15, where the total mass of the unit cell is discretized in two half masses $m/2 = (\rho_s S_s a + 2\rho_p S_p l_p)/2$, where ρ_s and ρ_p are respectively the rod and patch densities. Even if the mechanical representation could be appropriate, it is chosen to focus on the electrical representation, which offers an easier analysis. By taking into account the global piezoelectric coupling in Fig. 3.9 and the electrical network that is connected to the patches in Fig. 3.14, the discrete electromechanical unit cell can be represented by the electric scheme in Fig. 3.16, where appear the global constants obtained in Sec. 3.3. The same electrical architecture as in Fig 3.13 is obtained, which means that our discretized electromechanical unit cell is equivalent to the purely mechanical system in Fig. 3.10. So, from the equivalent transfer matrix in Eq. (3.37), the coupled system is modeled by the

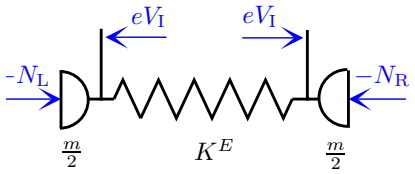

Figure 3.15: Discrete model for the rod segment.

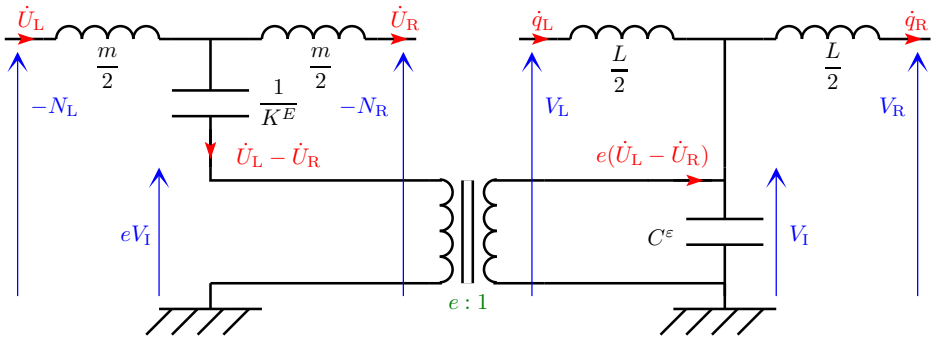

Figure 3.16: Discrete model of the electromechanical unit cell.

formulation

$$\begin{bmatrix} U_\mathrm{R}^\star \\ q_\mathrm{R}^\star \\ N_\mathrm{R}^\star \\ V_\mathrm{R}^\star \end{bmatrix} = \begin{bmatrix} 1-f & \Lambda\hat{f} & 1 & \Lambda \\ f & 1-(1+\Lambda)\hat{f} & -1 & -(1+\Lambda) \\ -2f\left(1-\frac{f}{2}\right) & -\Lambda f\hat{f} & 1-f & -\Lambda f \\ f\hat{f} & 2\hat{f}\left(1-\frac{1+\Lambda}{2}\hat{f}\right) & -\hat{f} & 1-(1+\Lambda)\hat{f} \end{bmatrix} \begin{bmatrix} U_\mathrm{L}^\star \\ q_\mathrm{L}^\star \\ N_\mathrm{L}^\star \\ V_\mathrm{L}^\star \end{bmatrix}, \quad (3.43)$$

where $f = \omega^2 m/(2K^E)$, $\hat{f} = \omega^2 LC^\varepsilon/2$ and $\Lambda = e^2/(K^E C^\varepsilon)$, which corresponds to the square of a coupling factor similar to the one presented in Chap. 2. According to Eq. (3.37) and the direct electromechanical analogy, the dimensionless variables are $U^\star = U/a$, $N^\star = N/(K^E a)$, $q^\star = q/(ea)$ and $V^\star = C^\varepsilon V/(ea)$. Note the sign modification of some terms of the matrix due to the fact that a voltage in the electrical domain is analogous to the opposite of the normal force in the mechanical domain. Furthermore, the present 4×4 matrix, as well as the following transfer matrices, can be condensed into a 2×2 matrix in order to consider an independent resonant shunt rather than the connection to a network. This requires to set $V_\mathrm{L}^\star$ and $V_\mathrm{R}^\star$ to zero. With the discrete model, the 2×2 matrix form in Eq. (3.30) is recovered with an electrical resonance at $2/\sqrt{LC^\varepsilon}$ because the equivalent resonant shunt inductance is here equal to $L/4$.

3.5.2 Fully homogenized model for the rod segment

The transformation of the unit cell presented in Fig. 3.14 into its discrete model in Fig. 3.16 requires to approximate the continuous rod by a discrete lattice. As mentioned in Sec. 3.2, this is valid only when the considered wavelength is large compared to the length of the unit cells. For shorter wavelength, the continuity of the mechanical medium can be ensured with the homogenized rod model presented in Fig. 3.17. The Young's modulus Y^E, the density ρ and the cross-sectional area S come from a homogenization along the whole unit cell. A homogenized model is thus obtained, where the definition of e and C^ε

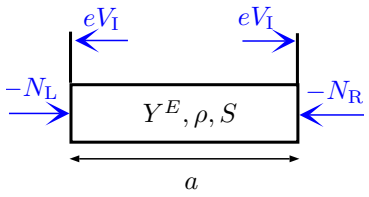

Figure 3.17: Fully homogenized model for the rod segment.

remains the same as in the discrete model:

$$\begin{array}{l} N_\mathrm{I} = Y^E S\varepsilon - eV_\mathrm{I} \\ q_\mathrm{I} = e\Delta U + C^\varepsilon V_\mathrm{I} \end{array}, \quad \text{where} \quad Y^E = \frac{K^E a}{S} \quad \text{and} \quad S = S_\mathrm{s} + 2S_\mathrm{p}\frac{l_\mathrm{p}}{a}. \tag{3.44}$$

It is seen from Fig. 3.17 that a force $N_\mathrm{R} + eV_\mathrm{I}$ is applied to the right of the rod segment and a force $-(N_\mathrm{L} + eV_\mathrm{I})$ is applied to its left. Consequently, the classical rod transfer matrix in Eq. (3.18) can be used to described the relation between those two forces and the corresponding end displacements, as

$$\begin{bmatrix} U_\mathrm{R}^\star \\ N_\mathrm{R}^\star + \Lambda V_\mathrm{I}^\star \end{bmatrix} = \boldsymbol{T_m} \begin{bmatrix} U_\mathrm{L}^\star \\ N_\mathrm{L}^\star + \Lambda V_\mathrm{I}^\star \end{bmatrix}, \quad \text{where} \quad \boldsymbol{T_m} = \begin{bmatrix} \cos(ka) & \frac{1}{ka}\sin(ka) \\ -ka\sin(ka) & \cos(ka) \end{bmatrix}. \tag{3.45}$$

The wavenumber k is obtained from the rod dispersion relation $k = \omega\sqrt{\rho/Y^E}$, where $\rho = m/(Sa)$ is the homogenized density of the unit cell. The dimensionless voltage variable $V_\mathrm{I}^\star$ appears in Eq. (3.45) but as the electrical network is still discrete, it is determined from Fig. 3.16 that

$$V_\mathrm{I}^\star = \begin{bmatrix} \hat{f} & 1 \end{bmatrix} \begin{bmatrix} q_\mathrm{L}^\star \\ V_\mathrm{L}^\star \end{bmatrix}, \quad \text{where} \quad \hat{f} = \omega^2 \frac{LC^\varepsilon}{2} \tag{3.46}$$

Furthermore, the relation between the electrical state vectors is also obtained from Fig. 3.16. A contribution due to the electromechanical coupling is added to a purely electrical contribution:

$$\begin{bmatrix} q_\mathrm{R}^\star \\ V_\mathrm{R}^\star \end{bmatrix} = \boldsymbol{T_e} \begin{bmatrix} q_\mathrm{L}^\star \\ V_\mathrm{L}^\star \end{bmatrix} + (U_\mathrm{L}^\star - U_\mathrm{R}^\star) \begin{bmatrix} 1 \\ \hat{f} \end{bmatrix} \quad \text{where} \quad \boldsymbol{T_e} = \begin{bmatrix} 1-\hat{f} & -1 \\ 2\hat{f}(1-\frac{\hat{f}}{2}) & 1-\hat{f} \end{bmatrix} \tag{3.47}$$

Note that the electrical transfer matrix $\boldsymbol{T_e}$ is similar to the lattice transfer matrix in Eq. (3.23) because the considered electrical network is the analogue of a lattice of point masses. Combining Eqs. (3.45), (3.46) and (3.47) leads to the matrix system

$$\begin{bmatrix} \boldsymbol{I_2} & \boldsymbol{0} \\ \begin{bmatrix} 1 & 0 \\ \hat{f} & 0 \end{bmatrix} & \boldsymbol{I_2} \end{bmatrix} \begin{bmatrix} U_\mathrm{R}^\star \\ N_\mathrm{R}^\star \\ q_\mathrm{R}^\star \\ V_\mathrm{R}^\star \end{bmatrix} = \begin{bmatrix} \boldsymbol{T_m} & \Lambda(\boldsymbol{T_m} - \boldsymbol{I_2}) \begin{bmatrix} 0 & 0 \\ \hat{f} & 1 \end{bmatrix} \\ \begin{bmatrix} 1 & 0 \\ \hat{f} & 0 \end{bmatrix} & \boldsymbol{T_e} \end{bmatrix} \begin{bmatrix} U_\mathrm{L}^\star \\ N_\mathrm{L}^\star \\ q_\mathrm{L}^\star \\ V_\mathrm{L}^\star \end{bmatrix}, \tag{3.48}$$

so the transfer matrix for the homogenized model is formulated as

$$\begin{bmatrix} U_{\mathrm{R}}^{\star} \\ N_{\mathrm{R}}^{\star} \\ q_{\mathrm{R}}^{\star} \\ V_{\mathrm{R}}^{\star} \end{bmatrix} = \begin{bmatrix} \boldsymbol{T_m} & \Lambda(\boldsymbol{T_m} - \boldsymbol{I_2}) \begin{bmatrix} 0 & 0 \\ \hat{f} & 1 \end{bmatrix} \\ -\begin{bmatrix} 1 & 0 \\ \hat{f} & 0 \end{bmatrix} (\boldsymbol{T_m} - \boldsymbol{I_2}) & \boldsymbol{T_e} - \Lambda \begin{bmatrix} 1 & 0 \\ \hat{f} & 0 \end{bmatrix} (\boldsymbol{T_m} - \boldsymbol{I_2}) \begin{bmatrix} 0 & 0 \\ \hat{f} & 1 \end{bmatrix} \end{bmatrix} \begin{bmatrix} U_{\mathrm{L}}^{\star} \\ N_{\mathrm{L}}^{\star} \\ q_{\mathrm{L}}^{\star} \\ V_{\mathrm{L}}^{\star} \end{bmatrix}. \quad (3.49)$$

The unit cell is here described by a semi-continuous transfer matrix that respects both the continuity of the mechanical structure and the discrete nature of the electrical network. By replacing $\boldsymbol{T_m}$ and $\boldsymbol{T_e}$ by their respective matrices and by permuting the state vectors to get back to a formulation equivalent to Eq. (3.43), one finds

$$\begin{bmatrix} U_{\mathrm{R}}^{\star} \\ q_{\mathrm{R}}^{\star} \\ N_{\mathrm{R}}^{\star} \\ V_{\mathrm{R}}^{\star} \end{bmatrix} = \begin{bmatrix} \mathrm{c} & \Lambda \mathrm{sinc} \hat{f} & \mathrm{sinc} & \Lambda \mathrm{sinc} \\ 1-\mathrm{c} & 1-(1+\Lambda \mathrm{sinc})\hat{f} & -\mathrm{sinc} & -(1+\Lambda \mathrm{sinc}) \\ -\frac{1+\mathrm{c}^2}{\mathrm{sinc}} & -\Lambda(1-\mathrm{c})\hat{f} & \mathrm{c} & -\Lambda(1-\mathrm{c}) \\ (1-\mathrm{c})\hat{f} & 2\hat{f}\left(1-\frac{1+\Lambda \mathrm{sinc}}{2}\hat{f}\right) & -\mathrm{sinc}\hat{f} & 1-(1+\Lambda \mathrm{sinc})\hat{f} \end{bmatrix} \begin{bmatrix} U_{\mathrm{L}}^{\star} \\ q_{\mathrm{L}}^{\star} \\ N_{\mathrm{L}}^{\star} \\ V_{\mathrm{L}}^{\star} \end{bmatrix}, \quad (3.50)$$

where $\mathrm{c} = \cos(\sqrt{m/K^E}\omega)$ and $\mathrm{sinc} = \sin(\sqrt{m/K^E}\omega)/(\sqrt{m/K^E}\omega)$. Actually, we would find the exact same discrete transfer matrix as in Eq. (3.43) if $\boldsymbol{T_m}$ was replaced by its discrete lattice approximation in Eq. (3.23). On the other hand, we remark that the continuity of the mechanical medium can be recovered from a discrete approximation by applying the transformation in Eq. (3.25) after redimensioning the matrix in Eq. (3.43).

The transfer matrix in Eq. (3.50) can also be condensed in a 2×2 transfer matrix when considering the special case of an independent resonant shunt as presented in Fig. 3.8. Indeed, with an inductance L connected to the pair of piezoelectric patches, $V_{\mathrm{L}}^{\star} = V_{\mathrm{R}}^{\star} = 0$ leads to

$$\begin{bmatrix} U_{\mathrm{R}}^{\star} \\ N_{\mathrm{R}}^{\star} \end{bmatrix} = \begin{bmatrix} 1-(1-\mathrm{c})\tilde{f} & \mathrm{sinc}\tilde{f} \\ -2\frac{(1-\mathrm{c})}{\mathrm{sinc}}\left(1-\frac{1-\mathrm{c}}{2}\tilde{f}\right) & 1-(1-\mathrm{c})\tilde{f} \end{bmatrix} \begin{bmatrix} U_{\mathrm{L}}^{\star} \\ N_{\mathrm{L}}^{\star} \end{bmatrix}, \quad (3.51)$$

where $\tilde{f} = \dfrac{1-\omega^2 LC^{\varepsilon}}{1-\omega^2 LC^{\varepsilon}(1+\Lambda \mathrm{sinc})}$, which can be compared to its discrete approximation in Eq. (3.30). Here, the proposed transfer matrix formulations ensure the mechanical continuity but note that, because of the homogenization of the unit cell, the spatial discontinuity induced by the thickness of the piezoelectric patches is not considered.

3.5.3 Piecewise homogenized model for the rod segment

A piecewise homogenized one-dimensional model of the unit cell allows taking into account the mechanical discontinuity created by the addition of patches on the main structure. This can be illustrated by the model presented in Fig. 3.18, where three different rod segments are connected together. The central portion 'sp' represents the part of the

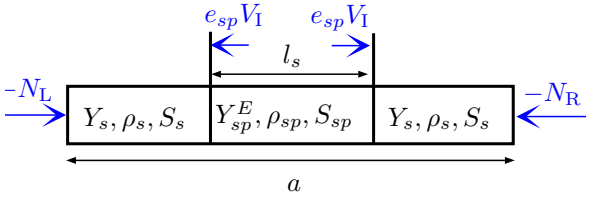

Figure 3.18: Piecewise homogenized model for the rod segment.

structure which is covered by the patches. By considering a normal force N_{sp} in this rod segment, the problem can be expressed under the same form as in Eq. (3.44) through

$$\begin{array}{l} N_{\mathrm{sp}} = Y^E_{\mathrm{sp}} S_{sp} \varepsilon_{sp} - e_{\mathrm{sp}} V_{\mathrm{I}} \\ q_{\mathrm{I}} = e_{\mathrm{sp}} \Delta U_{\mathrm{sp}} + C^{\varepsilon}_{\mathrm{sp}} V_{\mathrm{I}} \end{array} , \quad \text{where} \quad Y^E_{\mathrm{sp}} = \frac{Y_{\mathrm{s}} S_{\mathrm{s}} + 2 Y^E_{\mathrm{p}} S_{\mathrm{p}}}{S_{\mathrm{sp}}} \tag{3.52}$$

and $S_{\mathrm{sp}} = S_{\mathrm{s}} + 2S_{\mathrm{p}}$. The constants referring to the 'sp' portion differ from the global constants obtained for the discrete model as the two patches do not cover the whole unit cell ($a \neq l_{\mathrm{p}}$). Nevertheless, e_{sp} and C^{ε}_{sp} are determined with the same method as in Eq. (3.33). The system of equations (3.52) can be transformed into a transfer matrix formulation $\boldsymbol{T}_{\mathrm{sp}}$ similar to Eq. (3.49) by remarking that the problem focusing on the 'sp' rod segment is equivalent to the one presented for the fully homogenized model. Here, ρ is simply replaced by $\rho_{\mathrm{sp}} = (\rho_{\mathrm{s}} S_{\mathrm{s}} + 2\rho_{\mathrm{p}} S_{\mathrm{p}})/S_{\mathrm{sp}}$, which is the homogenized density of the 'sp' rod segment. As the two 's' rod segments are purely elastic, their mechanical transfer matrices $\boldsymbol{T}_{\mathrm{s}}$ can be determined in the same way as $\boldsymbol{T}_{\mathrm{m}}$ in Eq. (3.45), but with the use of the constants Y_{s}, ρ_{s} and S_{s}. Finally, if the 4×4 matrix $\boldsymbol{T}_{\mathrm{sp}}$ corresponds to the 'sp' rod segment, the problem can be expressed as

$$\begin{bmatrix} U^{\star}_{\mathrm{R}} \\ N^{\star}_{\mathrm{R}} \\ Q^{\star}_{\mathrm{R}} \\ V^{\star}_{\mathrm{R}} \end{bmatrix} = \begin{bmatrix} \boldsymbol{T}_{\mathrm{s}} & \boldsymbol{0} \\ \boldsymbol{0} & \boldsymbol{I_2} \end{bmatrix} \boldsymbol{T}_{\mathrm{sp}} \begin{bmatrix} \boldsymbol{T}_{\mathrm{s}} & \boldsymbol{0} \\ \boldsymbol{0} & \boldsymbol{I_2} \end{bmatrix} \begin{bmatrix} U^{\star}_{\mathrm{L}} \\ N^{\star}_{\mathrm{L}} \\ Q^{\star}_{\mathrm{L}} \\ V^{\star}_{\mathrm{L}} \end{bmatrix}, \quad \text{where} \quad \boldsymbol{I_2} = \begin{bmatrix} 1 & 0 \\ 0 & 1 \end{bmatrix}. \tag{3.53}$$

In this transfer matrix formulation, the order of the variables in the state vectors differs from Eqs. (3.43) and (3.50) and has to be modified for any numerical comparison.

3.5.4 Finite element model

The three previous models are based on analytic formulations but the electromechanical transfer matrix can also be obtained from a finite element analysis. The considered numerical model is the one presented by Thomas et al. [70, 79] for the analysis of shunted piezoelectric patches. In the present case involving two patches connected in parallel and thus only one piezoelectric degree of freedom per unit cell, the finite element formulation

can be simplified into

$$\begin{bmatrix} \boldsymbol{M_m} & \mathbf{0} \\ \mathbf{0} & 0 \end{bmatrix} \begin{bmatrix} \ddot{\boldsymbol{q}}_{\boldsymbol{m}} \\ \ddot{V}_{\mathrm{I}} \end{bmatrix} + \begin{bmatrix} \boldsymbol{K_m} & \boldsymbol{K_c} \\ -\boldsymbol{K_c}^{\boldsymbol{T}} & C^{\varepsilon}_{\mathrm{sp}} \end{bmatrix} \begin{bmatrix} \boldsymbol{q_m} \\ V_{\mathrm{I}} \end{bmatrix} = \begin{bmatrix} \boldsymbol{F_m} \\ q_{\mathrm{I}} \end{bmatrix}, \tag{3.54}$$

where $\boldsymbol{M_m}$, $\boldsymbol{K_m}$ and $\boldsymbol{K_c}$ are respectively the mass, stiffness and coupling matrices that are defined in Appendix B. As the patches are not shunted by an impedance but connected to a network, the electrical variables cannot be condensed in the mechanical problem, which requires a novel formulation. Actually, it is possible to define the electric charge q_{I} relatively to a charge vector $\boldsymbol{q_e} = \begin{bmatrix} q_{\mathrm{L}} & q_{\mathrm{R}} \end{bmatrix}^T$ and it is found from Fig. 3.16 that

$$q_{\mathrm{I}} = \boldsymbol{S_q q_e} \quad \text{where} \quad \boldsymbol{S_q} = \begin{bmatrix} 1 & -1 \end{bmatrix}. \tag{3.55}$$

Furthermore, by analogy with the force vector $\boldsymbol{F_m}$ and the displacement vector $\boldsymbol{q_m}$, we define a voltage vector $\boldsymbol{F_e} = \begin{bmatrix} V_{\mathrm{L}} & -V_{\mathrm{R}} \end{bmatrix}^T$ as the dual of the charge vector $\boldsymbol{q_e}$. The signs are chosen according to the analogy with external forces applied to the unit cell. The voltage vector is the result of two contributions: $\boldsymbol{F_e} = \boldsymbol{F_e^e} + \boldsymbol{F_e^m}$. The first contribution, $\boldsymbol{F_e^e}$ is purely electrical and corresponds to the voltage vector when $\boldsymbol{q_m} = \mathbf{0}$, i.e. when no mechanical displacement is allowed. From the electrical network in Fig. 3.16,

$$\boldsymbol{F_e^e} = \left[\boldsymbol{K_e} - \omega^2 \boldsymbol{M_e}\right] \boldsymbol{q_e}, \tag{3.56}$$

where $\boldsymbol{K_e} = \begin{bmatrix} \frac{1}{C^{\varepsilon}_{\mathrm{sp}}} & -\frac{1}{C^{\varepsilon}_{\mathrm{sp}}} \\ -\frac{1}{C^{\varepsilon}_{\mathrm{sp}}} & \frac{1}{C^{\varepsilon}_{\mathrm{sp}}} \end{bmatrix}$ and $\boldsymbol{M_e} = \begin{bmatrix} \frac{L}{2} & 0 \\ 0 & \frac{L}{2} \end{bmatrix}$ are the electrical analogues of stiffness and mass matrices. Note the use of the piezoelectric capacitance $C^{\varepsilon}_{\mathrm{sp}}$, which account for the fact that we do not consider any global homogenization of the unit cell. Then, the second contribution to the voltage vector is obtained when $\boldsymbol{q_e} = \mathbf{0}$. This condition induces that $q_{\mathrm{I}} = 0$ and $V_{\mathrm{I}} = V_{\mathrm{L}} = V_{\mathrm{R}}$. Also, Eq. (3.54) gives $V_{\mathrm{I}} = \boldsymbol{K_c}^{\boldsymbol{T}} \boldsymbol{q_m} / C^{\varepsilon}_{sp}$ when $q_{\mathrm{I}} = 0$. Consequently,

$$\boldsymbol{F_e^m} = \frac{1}{C^{\varepsilon}_{sp}} \boldsymbol{S_V} \boldsymbol{K_c}^{\boldsymbol{T}} \boldsymbol{q_m} \quad \text{where} \quad \boldsymbol{S_V} = \begin{bmatrix} 1 & -1 \end{bmatrix}^T = \boldsymbol{S_q}^T. \tag{3.57}$$

In the end, Eqs. (3.54),(3.55), (3.56) and (3.57) give a dynamic stiffness matrix combining mechanical and electrical degrees of freedom:

$$\left[\begin{bmatrix} \boldsymbol{K_m} + \frac{1}{C^{\varepsilon}_{sp}} \boldsymbol{K_c} \boldsymbol{K_c}^{\boldsymbol{T}} & \frac{1}{C^{\varepsilon}_{sp}} \boldsymbol{K_c} \boldsymbol{S_q} \\ \frac{1}{C^{\varepsilon}_{sp}} (\boldsymbol{K_c} \boldsymbol{S_q})^{\boldsymbol{T}} & \boldsymbol{K_e} \end{bmatrix} - \omega^2 \begin{bmatrix} \boldsymbol{M_m} & \mathbf{0} \\ \mathbf{0} & \boldsymbol{M_e} \end{bmatrix} \right] \begin{bmatrix} \boldsymbol{q_m} \\ \boldsymbol{q_e} \end{bmatrix} = \begin{bmatrix} \boldsymbol{F_m} \\ \boldsymbol{F_e} \end{bmatrix}. \tag{3.58}$$

With a restriction to the longitudinal case, $\boldsymbol{q_m} = [U_{\mathrm{L}} \;\; \boldsymbol{q}_{\mathrm{I}} \;\; U_{\mathrm{R}}]$ and $\boldsymbol{F_m} = [-N_{\mathrm{L}} \;\; \mathbf{0} \;\; N_{\mathrm{R}}]$, where $\boldsymbol{q}_{\mathrm{I}}$ is the mechanical displacement vector of the internal nodes of the unit cell. The

dynamic stiffness matrix presented in Eq. (3.58) is then rearranged to bring together the mechanical and electrical left and right components, as

$$\begin{bmatrix} \tilde{\boldsymbol{D}}_{\boldsymbol{LL}} & \tilde{\boldsymbol{D}}_{\boldsymbol{LI}} & \tilde{\boldsymbol{D}}_{\boldsymbol{LR}} \\ \tilde{\boldsymbol{D}}_{\boldsymbol{IL}} & \tilde{\boldsymbol{D}}_{\boldsymbol{II}} & \tilde{\boldsymbol{D}}_{\boldsymbol{IR}} \\ \tilde{\boldsymbol{D}}_{\boldsymbol{RL}} & \tilde{\boldsymbol{D}}_{\boldsymbol{RI}} & \tilde{\boldsymbol{D}}_{\boldsymbol{RR}} \end{bmatrix} \begin{bmatrix} \boldsymbol{q}_{\mathrm{L}} \\ \boldsymbol{q}_{\mathrm{I}} \\ \boldsymbol{q}_{\mathrm{R}} \end{bmatrix} = \begin{bmatrix} \boldsymbol{F}_{\mathrm{L}} \\ \boldsymbol{0} \\ \boldsymbol{F}_{\mathrm{R}} \end{bmatrix} \text{ where } \boldsymbol{F}_{\mathrm{L}} = \begin{bmatrix} -N_{\mathrm{L}} \\ V_{\mathrm{L}} \end{bmatrix}, \ \boldsymbol{F}_{\mathrm{R}} = \begin{bmatrix} N_{\mathrm{R}} \\ -V_{\mathrm{R}} \end{bmatrix}, \quad (3.59)$$

$\boldsymbol{q}_{\mathrm{L}} = \begin{bmatrix} U_{\mathrm{L}} & q_{\mathrm{L}} \end{bmatrix}^T$ and $\boldsymbol{q}_{\mathrm{R}} = \begin{bmatrix} U_{\mathrm{R}} & q_{\mathrm{R}} \end{bmatrix}^T$. With this partitioning, the procedures of the Wave Finite Element Method [106–108] can be implemented. It starts with an elimination of the internal degrees of freedoms

$$\begin{bmatrix} \boldsymbol{D}_{\boldsymbol{LL}} & \boldsymbol{D}_{\boldsymbol{LR}} \\ \boldsymbol{D}_{\boldsymbol{RL}} & \boldsymbol{D}_{\boldsymbol{RR}} \end{bmatrix} \begin{bmatrix} \boldsymbol{q}_{\mathrm{L}} \\ \boldsymbol{q}_{\mathrm{R}} \end{bmatrix} = \begin{bmatrix} \boldsymbol{F}_{\mathrm{L}} \\ \boldsymbol{F}_{\mathrm{R}} \end{bmatrix}, \quad \text{where} \quad \begin{array}{l} \boldsymbol{D}_{\boldsymbol{LL}} = \tilde{\boldsymbol{D}}_{\boldsymbol{LL}} - \tilde{\boldsymbol{D}}_{\boldsymbol{LI}} \tilde{\boldsymbol{D}}_{\boldsymbol{II}}^{-1} \tilde{\boldsymbol{D}}_{\boldsymbol{IL}} \\ \boldsymbol{D}_{\boldsymbol{LR}} = \tilde{\boldsymbol{D}}_{\boldsymbol{LR}} - \tilde{\boldsymbol{D}}_{\boldsymbol{LI}} \tilde{\boldsymbol{D}}_{\boldsymbol{II}}^{-1} \tilde{\boldsymbol{D}}_{\boldsymbol{IR}} \\ \boldsymbol{D}_{\boldsymbol{RL}} = \tilde{\boldsymbol{D}}_{\boldsymbol{RL}} - \tilde{\boldsymbol{D}}_{\boldsymbol{RI}} \tilde{\boldsymbol{D}}_{\boldsymbol{II}}^{-1} \tilde{\boldsymbol{D}}_{\boldsymbol{IL}} \\ \boldsymbol{D}_{\boldsymbol{RR}} = \tilde{\boldsymbol{D}}_{\boldsymbol{RR}} - \tilde{\boldsymbol{D}}_{\boldsymbol{RI}} \tilde{\boldsymbol{D}}_{\boldsymbol{II}}^{-1} \tilde{\boldsymbol{D}}_{\boldsymbol{IR}} \end{array}, \quad (3.60)$$

followed by a transformation of the condensed dynamic stiffness matrix into a transfer matrix:

$$\begin{bmatrix} U_{\mathrm{R}} \\ q_{\mathrm{R}} \\ N_{\mathrm{R}} \\ -V_{\mathrm{R}} \end{bmatrix} = \begin{bmatrix} -\boldsymbol{D}_{\boldsymbol{LR}}^{-1} \boldsymbol{D}_{\boldsymbol{LL}} & \boldsymbol{D}_{\boldsymbol{LR}}^{-1} \\ -\boldsymbol{D}_{\boldsymbol{RL}} + \boldsymbol{D}_{\boldsymbol{RR}} \boldsymbol{D}_{\boldsymbol{LR}}^{-1} \boldsymbol{D}_{\boldsymbol{LL}} & -\boldsymbol{D}_{\boldsymbol{RR}} \boldsymbol{D}_{\boldsymbol{LR}}^{-1} \end{bmatrix} \begin{bmatrix} U_{\mathrm{L}} \\ q_{\mathrm{L}} \\ N_{\mathrm{L}} \\ -V_{\mathrm{L}} \end{bmatrix}. \quad (3.61)$$

Here, the use of dimensionless state variables is not explicit because the transfer matrix is built from classical mass, stiffness and coupling matrices. Yet, a nondimensionalization can be easily introduced afterwards, when implementing the numerical computing.

3.5.5 Model comparison for large wavelength

The previous models are compared by considering the example of a free-free rod covered with $n = 20$ pairs of piezoelectric patches. Table 3.1 gives the geometry and the material properties of the unit cell. The twenty successive unit cells are electrically connected with a line of inductors having identical values $L = m/(K^E C^\varepsilon) = 3$ mH in order to satisfy the modal coupling condition (3.42). When short-circuiting both ends of the network, this modal coupling condition tunes the electrical modes to the ones of the analogous mechanical lattice. A tuned mass effect can thus be obtained on several modes together and the vibration amplitudes are reduced by introducing damping in the network. In the present example, a resistance $R_{\mathrm{s}}^L = 3\ \Omega$ is added in series with the inductors by replacing L by $L - jR_{\mathrm{s}}^L/\omega$.

First, we consider a frequency range spanning from 1 Hz to 20 kHz, which covers the first seven modes of the uncontrolled rod. In the following figures, the results referring to the homogenized and the finite element model are not represented because their difference

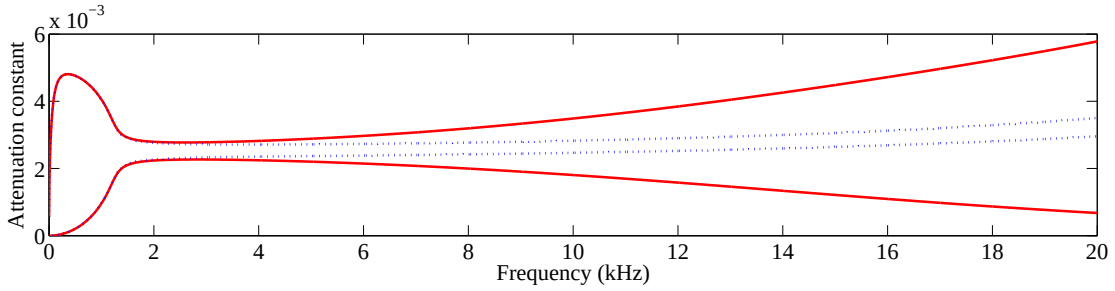

Figure 3.19: Attenuation constants - (···) for the discrete model, (—) for the piecewise homogenized model.

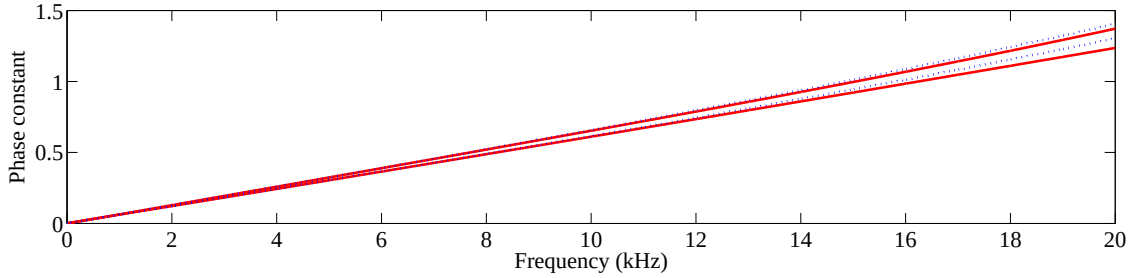

Figure 3.20: Phase constants - (···) for the discrete model, (—) for the piecewise homogenized model.

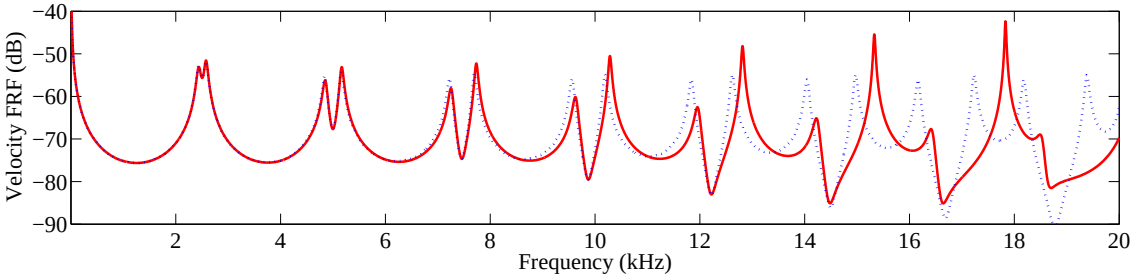

Figure 3.21: Velocity FRFs - (···) for the discrete model, (—) for the piecewise homogenized model.

with the piecewise homogenized model is not noticeable over the considered frequency range. The attenuation and phase constants obtained with the discrete and the piecewise homogenized model are represented in Figs. 3.19 and 3.20. Each model offers two positive propagation constants because they are built with 4×4 transfer matrices. Note that the coupling of a rod to an analogous dissipative network modifies the wave propagation because it creates a frequency band where none of the two attenuation constants is close to zero, which induces damping of a wave propagating in the electromechanical waveguide. This is confirmed by the velocity FRFs in Fig. 3.21 showing damping through a multimodal tuned mass effect, similar to the results in Sec. 3.4 for a purely mechanical coupling. It is

remarked that the discrete model is no more reliable above 10 kHz, which corresponds to about 10 unit cells per wavelength. As predicted in Fig. 3.5, the position of the mechanical resonances are shifted to lower frequencies because the mechanical medium is modeled by a lattice. Then, when the network is tuned to reproduce the modal properties of the lattice, the discrete model does not take into account the increasing mistuning between the continuous and the discrete structures. This modeling approximation is clearly noticed in Figs. 3.19 and 3.21, which confirm that, even if the discrete model is useful for the understanding of the multimodal coupling, it is restricted to large wavelength compared to the length of the unit cell.

3.5.6 Model comparison for short wavelength

The transfer matrix models are then compared at higher frequencies, from 40 kHz to 60 kHz, when the wavelength is close to the length of the unit cells. The finite element model still tends to the piecewise homogenized model but the homogenized model presents a different response. Note that no propagation occurs in the electrical network at such high frequencies. In accordance with the results in Fig 3.3 for the mechanical lattice, one can define $\omega = 2/\sqrt{LC^{\varepsilon}}$ as the lower bound for the stop band of the discrete electrical network, which gives a frequency around 32 kHz. As a consequence, the electrical network has almost no influence on mechanical wave propagation above 32 kHz and this is the reason why we only compute, in Figs. 3.22 and 3.23, the propagation constants corresponding to the mechanical part of the problem.

The piecewise homogenized model offers a stop band phenomenon around 50 kHz due to the mechanical discontinuity induced by the addition of patches on the unit cell. This effect clearly appears in Figs. 3.22 and 3.23 and it is confirmed by the velocity FRF in Fig. 3.24, where no modes occur around 50 kHz. On the contrary, such a stop band phenomenon does not appear with the homogenized model as the mechanical discontinuity induced by the patches is not taken into account. The homogenized model is thus inappropriate in

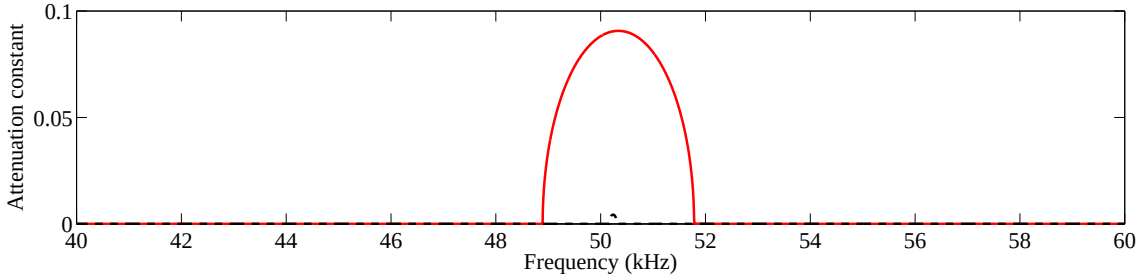

Figure 3.22: Attenuation constants - (−−) for the homogenized model, (—) for the piecewise homogenized model.

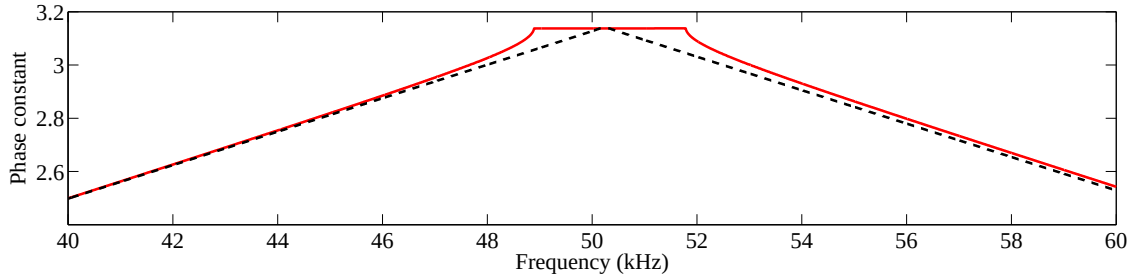

Figure 3.23: Phase constants - (−−) for the homogenized model, (—) for the piecewise homogenized model.

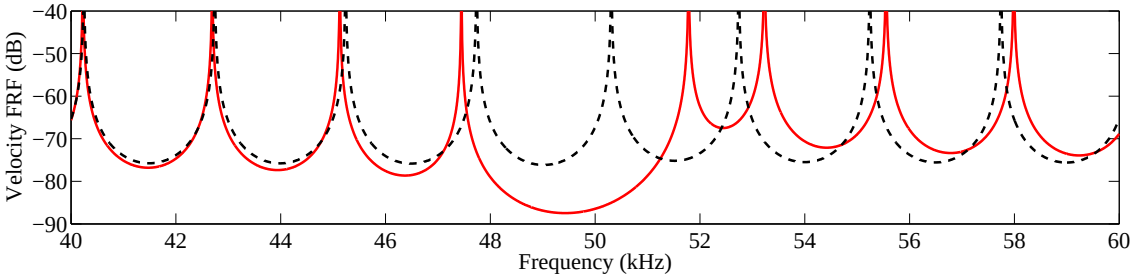

Figure 3.24: Velocity FRFs - (−−) for the homogenized model, (—) for the piecewise homogenized model.

the present case. Yet, since the control strategy involving the electrical network has here no effect, the interest of an analysis at such high frequencies is not obvious.

3.6 Experiments on rod damping

The two control strategies based on independent resonant shunts and on a multi-resonant network are applied to the damping of a rod covered with a periodic array of piezoelectric patches. In both cases, the use of standard electrical components leads to purely passive solutions. The experimental results are compared to the numerical results obtained with the transfer matrix model involving a homogenized mechanical medium.

3.6.1 Experimental setup

The main structure is a one meter rod in aluminum alloy 2017, which is periodically covered with $n = 20$ pairs of piezoelectric patches. Referring to Fig. 3.8, the geometry of the setup is given in Table 3.1. Concerning the piezoelectric material, we select the PIC 151 ceramic whose properties are also described in Table 3.1. The resulting structure is suspended by elastic straps in order to tend to a free-free configuration. As presented

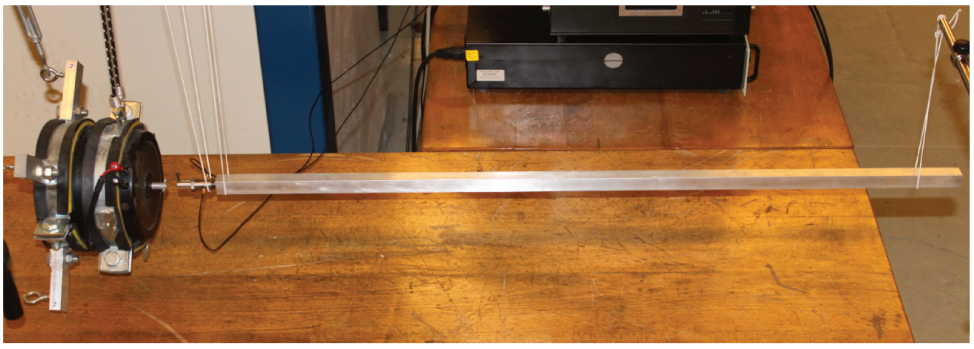

Figure 3.25: Suspended rod before bonding of the piezoelectric patches.

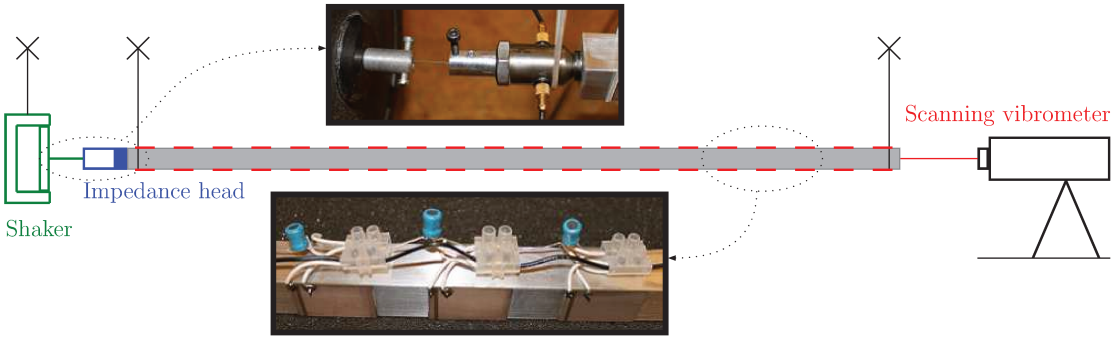

Figure 3.26: Setup involving a rod coupled to its analogous electrical network.

in Fig. 3.25 and 3.26, a suspended shaker is connected to one end of the rod through an impedance head that measures the acceleration and the transmitted force. At the other end, a laser vibrometer measures the velocity. A white noise excitation is generated and two signals are analyzed: the velocity acquired by the vibrometer and the force measured by the impedance head. A last step consists in obtaining the transfer function between the velocity and the force signals. To this end, a fast Fourier transform is performed over an 11.5 kHz frequency range with a 2 Hz resolution.

The first analysis is conducted without connecting any electrical components to the piezoelectric patches. The experimental frequency response functions are compared to the results obtained with homogenized mechanical model computed from Eq. (3.4) and (3.18). It is seen that the model can be improved by considering three new elements related to the setup. First, it is remarked that the impedance head is not directly connected to the rod because a small connecting element is used for practical purpose. This means that the measured force N_{mes} is not exactly equal to N_0, which is the force applied by the rod to the connecting element according to the definition of the normal force. The displacement of the connecting element is equal to U_0 and the difference between the two normal forces is thus $N_0 - N_{\text{mes}} = \omega^2 m_{\text{add}} U_0$, the acceleration times the mass of the connecting element

that is equal to 4 grams. Consequently,

$$\frac{N_{\text{mes}}}{N_0} = 1 + \omega^2 m_{\text{add}} \frac{U_0}{N_0}. \tag{3.62}$$

This force ratio is used to correct the frequency response function obtained from Eq. (3.4). Secondly, it is observed that the stiffness added by the patches is slightly lower than the theoretical value obtained with the longitudinal model. This is most likely due to 3D effects and to the unconsidered glue layer that bond the patches to the rod. The stiffness loss is corrected in the model by adding a coefficient γ that modify the value of the Young's modulus in short and open circuit (γY_{p}^E and γY_{p}^D). The coefficient γ is fixed to 0.86 to fit with the experimental results. At last, the third addition in the model concerns the mechanical damping. It is observed experimentally that the maximum velocity at resonance decreases with an increase of the mode number. This can be modeled by an equivalent complex Young's modulus as $Y(1 + \text{j}\eta(\omega))$, where $\eta(\omega) = \alpha\omega$. The coefficient α is evaluated to 3×10^{-8} s in order to get close to the first four maxima of the velocity with open-circuited piezoelectric patches.

Concerning the electrical components, as it was chosen to focus on a completely passive control solution, they are selected in standard series with a 10% tolerance. As mentioned in Chap. 2, the internal resistance of the standard inductors is not negligible and often too high for the piezoelectric damping applications. Consequently, we had to select an inductor series offering low resistance components. At the same time, no specific resistors need to be added, which simplifies the network. The suppliers of standard electrical components proposing a set of discrete values, it is not always possible to find inductors that suits with the inductance L that is required for a modal coupling. However, it is possible to adjust the tuning by adding capacitors in parallel to the piezoelectric patches. This increases the capacitance C^ε and gives a new degree of freedom in the choice of L. Nanofarad or tenth of nanofarad are available in standard series of metallized polyester film capacitors. This suits with the value of C^ε which was evaluated to 35.3 nF for a pair of piezoelectric patches.

3.6.2 Damping with independent resonant shunts

The implementation of the first control strategy involves independent resonant systems. The periodicity of the structure is maintained by distributing identical resonant shunts all along the rod. The first resonance of the free-free rod is chosen as the target of the control strategy (2500 Hz). Consequently, the electrical resonance needs to be tuned to this specific frequency. Direct measurements on a set of 20 inductors selected in a 100 mH series give an inductance L = 96 mH and a series resistance $R_{\text{s}}^L = 80\ \Omega$. For this inductance, a tuning at 2500 Hz requires to increase C^ε by 6.2 nF. This is performed by placing individual

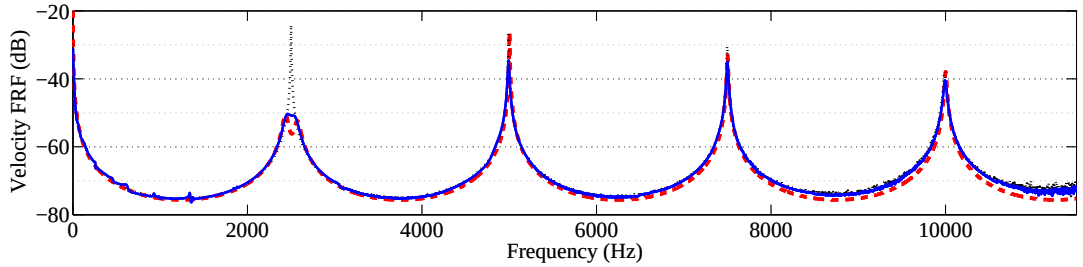

Figure 3.27: Velocity FRFs with distributed shunts - ($\cdots$) for the experiment with open-circuited patches, (—) for the experiment with resonant shunts, (−−) for the transfer matrix model with resonant shunts.

capacitors in parallel to the pairs of piezoelectric patches. The FRF corresponding to the end velocity obtained with an existing unit force is presented in Fig. 3.27. The four first modes of the free-free rod are observed over the 11.5 kHz frequency range. The passive damping system gives a reduction of about 25 dB on the velocity amplitude of the 1$^{\text{st}}$ resonance. However, the other resonances only present a limited attenuation. This agrees with the frequency response obtained in Fig. 3.7 for a similar strategy with a purely mechanical lattice model.

Regarding the correlation between the electromechanical model and the actual setup, the theoretical response involving the 2×2 matrix in Eq. (3.51) is compared to the experimental results. As conducted in Sec. 3.5, the damping is taken into account by replacing the tuned inductance by $L - \mathrm{j}R_{\mathrm{s}}^{L}/\omega$. This corresponds to the inductance model that is obtained when adding a resistor R_{s}^{L} in series with an inductor. The expectations concerning the velocity reduction on the first mode are satisfied as there is a difference of less than 1 dB between the two maxima. Nevertheless, the theoretical curve presents a local minimum, which is a characteristic of a slightly underdamped tuned mass system [1, 2, 43, 79]. This double peak shape does not clearly appear in the present experiment. It is observed higher damping compared to the prediction of the model. Actually, the 10% tolerance of the standard passive components creates small tuning differences all along the twenty shunts. As introduced in [4], the electrical resonances are distributed around an average frequency value, which flattens the experimental FRF. In any case, a significant vibration reduction is obtained on one particular mode with a completely passive system. Yet, it remains the question of the frequency range of interest. For a constant capacitance, the resonance frequency of the shunt is proportional to $1/\sqrt{L}$. Consequently, if the target frequency is divided by two, the inductance needs to be four times larger. This becomes a real problem when looking at low frequencies, as it would requires large inductance components that are not in the scope of standard passive series.

3.6.3 Multi-resonant network

The next experiment is related to the validation of the multimodal damping strategy. For the geometry and material properties described in Table 3.1, the application of the modal coupling condition in Eq. (3.42) gives an inductance L equal to 2.8 mH. As it was possible to find a set of components presenting this average inductance, no capacitors need to be added. All the capacitance is supported by the pairs of piezoelectric patches. So, the electrical network was realized by connecting successive unit cells with the selected inductors. Both ends of the line are then closed with a $L/2$ inductance. This allows respecting the unit cell architecture and the zero voltage boundary conditions which are the equivalent of the free-free mechanical boundary conditions for the rod.

It is possible to verify the tuning of the electrical network before looking at its effect on vibration reduction. A white noise voltage is applied at one end of the network and a voltage is measured in the middle of the network. This gives the electrical FRF presented in Fig. 3.28. The mechanical analogue of this experiment would be to measure the force in the middle of the rod when applying a force at one end. As a free-free configuration is analyzed, the middle of the rod is a node for the even force modes. The same remark applies to the voltage as the electrical network was designed to tend to the analogue of the free-free rod. This is confirmed by the electrical frequency response function where only the odd resonances appear. A second remark concerns the "sharp" antiresonances that are observed on the electrical response. They correspond to an energy transfer from the network to the rod around the mechanical resonances. Consequently, the tuning of the network is electrically validated by controlling that the antiresonances are centered on the electrical resonances.

The experimental voltage FRF is then compared to the result obtained with the proposed transfer matrix model through the computing of the 4×4 matrix in Eq. (3.50). As suggested for inductors in Chap. 2, it is found that an accurate result is obtained when

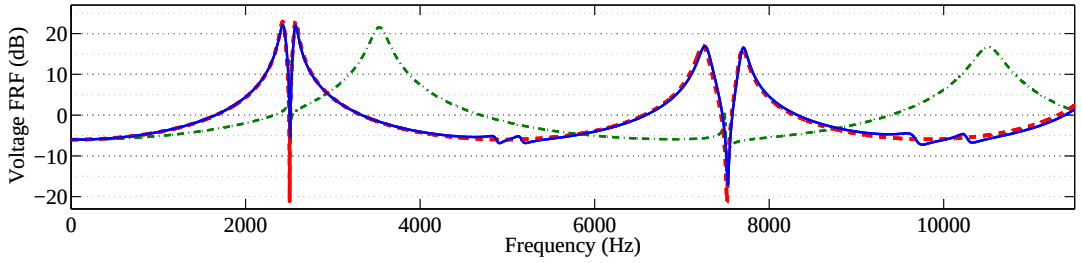

Figure 3.28: Voltage FRFs with the multimodal damping - (—) for the experiment with a tuned network, (– –) for the transfer matrix model with a tuned network, (- · -) for the transfer matrix model with a detuned network.

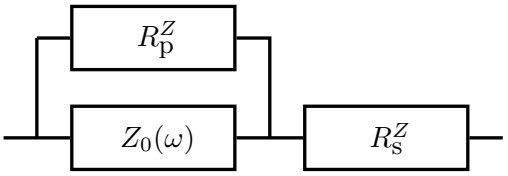

Figure 3.29: Model for the electrical components.

using both series and parallel resistance, R_{s}^{Z} and R_{p}^{Z}, when modeling the electrical components. This model, presented in Fig. 3.29, applies on inductors with $Z_0(\omega) = \mathrm{j}\omega L_0$ and on capacitors with $Z_0(\omega) = 1/(\mathrm{j}\omega C_0^{\varepsilon})$. Here, L_0 and C_0^{ε} refer to the perfect inductance and capacitance, which were simply denoted L and C^{ε} in the previous sections when no internal damping was considered. From the proposed damping model, the total impedance is then defined by $Z(\omega) = \mathrm{j}\omega L(\omega)$ or $Z(\omega) = 1/(\mathrm{j}\omega C^{\varepsilon}(\omega))$. Consequently, the equivalent electrical elements to introduce in the transfer matrices are

$$\begin{aligned} L(\omega) &= \frac{R_{\mathrm{p}}^{L} L_0}{R_{\mathrm{p}}^{L} + \mathrm{j}\omega L_0} + \frac{R_{\mathrm{s}}^{L}}{\mathrm{j}\omega} \\ C^{\varepsilon}(\omega) &= \frac{1 + \mathrm{j}\omega R_{\mathrm{p}}^{C} C_0^{\varepsilon}}{\mathrm{j}\omega(R_{\mathrm{s}}^{C} + R_{\mathrm{p}}^{C}) - R_{\mathrm{s}}^{C} R_{\mathrm{p}}^{C} C_0^{\varepsilon} \omega^2} \end{aligned} . \tag{3.63}$$

The following average values were measured directly on the electrical components over the considered frequency range: $R_{\mathrm{s}}^{L} = 1.3\ \Omega$, $R_{\mathrm{p}}^{L} = 12\ k\Omega$, $R_{\mathrm{s}}^{C} = 2.8\ \Omega$ and $R_{\mathrm{p}}^{C} = 180\ k\Omega$. Those values are then used to compute the electrical FRF. It can be remarked in Fig. 3.28 that the theoretical antiresonances are deeper than the experimental ones. In fact, for practical reasons, the rod was placed on a foam carpet during electrical measurements, which adds mechanical damping and reduces the depth of the antiresonances. Apart from antiresonances, the numerical and experimental curves are sufficiently close to validate the transfer matrix model that can then be used for a network evaluation purpose. Indeed, it is also represented in Fig. 3.28 a numerical FRF for a network that does not ensure the coupling condition in Eq. (3.42) because only half of the required inductance is introduced. In this last case, it is clear that the electrical resonances are not centered on the mechanical ones.

3.6.4 Multimodal damping by analogous coupling

Once the electrical network is correctly tuned, the effect of the multimodal coupling on the mechanical vibrations is observed. Figure 3.30 represents the experimental frequency response functions with a tuned network and with open-circuited patches. The performances are significant because the reduction is close to 25 dB for the first three resonances. This clearly highlights the efficiency of a multimodal damping involving an

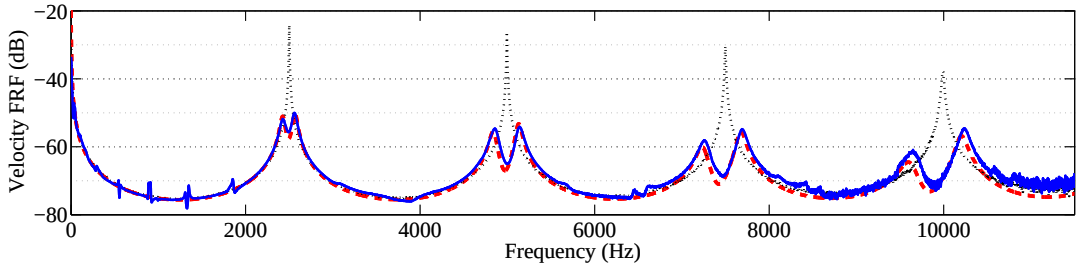

Figure 3.30: Velocity FRFs for the multimodal damping strategy - $(\cdots)$ for the experiment with open-circuited patches, $(—)$ for the experiment with an analogous network, $(--)$ for the transfer matrix model with an analogous network.

analogous electrical network. It can still be remarked that a slight increase of the damping would flattens the response and add a vibration reduction of a few decibels. The 2.8 mH inductors selected in a standard series thus offers a series resistance which could be larger for the present application. In any case, the experimental results are compared to the matrix computation in Eq. (3.50) that can take into account the sub-optimal resistance. Both responses are very similar, which gives a strong support to the semi-continuous transfer matrix formulation for vibration control analysis. Note that the only adjusted model parameters are γ and α, i.e. the stiffness loss and the viscous damping coefficients, which are determined from the purely mechanical responses. All the other constants come from direct electrical measurements or from material specifications. In the end, the vibration reduction is so large that the addition of γ and α in the model does not induce noticeable differences when the multimodal coupling operates.

Concerning the tuning of the electrical network, it can be seen from Fig. 3.30 that the induced antiresonances are placed at lower frequencies than the initial mechanical resonances. This effect is not pronounced for the first modes but is more observable for higher modes, which present an antisymmetry of their local maxima. This increasing mistuning is due to the fact that the electrical network is the analogue of the discrete structure. As seen in Sec. 3.2, for a wavelength equal to 10 unit cells, there is a frequency difference close to 2% between the continuous rod and its discrete analogue. With 20 cells on a free-free structure, this frequency difference is obtained around the fourth modes. Here, the mistuning remains limited but it becomes non-negligible for higher modes. If a larger number of modes needs to be controlled, it is still possible to increase the number of unit cells. This simply enhances the frequency range over which the discretized behavior remains close the continuous one.

3.7 Conclusions

In this chapter, it is observed that a continuous rod can be seen as a periodic structure and analyzed through a transfer matrix formulation. This formulation is relevant when modeling a rod with a lattice of point masses that are connected with springs. The differences between the continuous and the discrete models are presented. The lattice is compared to the considered wavelength as the unit cells need to be sufficiently small to approximate a continuous structure. Secondly, solutions leading to the conversion of vibration energy from a main lattice to a control system are investigated. A first strategy consists in using independent tuned mass dampers that are distributed all along the structure. A constant tuning gives the possibility to target one specific frequency, which corresponds to the resonance of the added systems. In a context of rod vibration control with piezoelectric patches, the electromechanical analogy implies that the tuned mass damping strategy is analogous to the use of distributed resonant shunts. After defining the unit cell of the electromechanical problem, its global properties are obtained from a discrete model of the piezoelectric coupling. The tuning of the inductors is then defined according to the target control frequency. However, a large number of piezoelectric unit cells or low frequency multimodal applications lead to practical limitations because of the required inductance and the number of electrical components.

An alternate control strategy is then proposed. It is based on the coupling of a main structure to its modal equivalent. The unit cell that couples two mechanical lattices is presented and we propose a simple modal coupling condition. With similar dispersion relations and boundary conditions, it is possible to reach a multimodal tuned mass damping that applies to all the natural frequencies of the main structure. This solution is transposed to the electrical domain by using a direct electromechanical analogy. The electrical analogue of a mechanical lattice points out the fact that a multimodal damping can be achieved by connecting an electrical network to a continuous rod. This leads to the definition of a 4×4 transfer matrix that allows propagation in both mechanical and electrical waveguides.

Four electromechanical models are presented and compared. While the electrical medium is discrete, the mechanical structure can be approximated either by its discrete equivalent, by a piecewise or full homogenized model, or by a finite element model. The main advantage of the discrete model is its simplicity. This model is useful to understand the multimodal coupling, but it is limited to a maximal frequency related to a minimum of 10 unit cells per wavelength. The full homogenized model allows taking into account the mechanical continuity and is sufficiently accurate over the frequency range where the multimodal control is effective. The piecewise homogenized model is required to analyze the

stop-band induced by the mechanical discontinuities. However, this phenomenon, which occurs for wavelength close to the length of the unit cell, is outside the scope of the multimodal control since the electrical resonances are placed at lower frequencies. Finally, the finite element model tends to the piecewise homogenized model when increasing the number of elements.

Experiments on a rod equipped with 20 pairs of piezoelectric patches validate the simulations for both mechanical and electrical responses. Furthermore, the two control strategies are implemented with standard passive components. The multimodal damping strategy is clearly validated as the vibration reduction is significant on all the observed modes. Another strong interest of this strategy is that the inductance can be reduced by increasing the number of unit cells. This differs from the more classical independent shunts strategy that becomes impractical when looking at low frequencies. Finally, it is seen that the use of a network linking successive piezoelectric elements can offer substantial benefits, for both control performances and practical implementation.

Chapter 4

Multimodal damping of a beam coupled to its electrical analogue

Abstract: *A multimodal damping strategy is implemented by coupling a beam to its analogous electrical network. This network comes from the direct electromechanical analogy applied to a transverse lattice of point masses that represents the discrete model of a beam. The mechanical and electrical structures are connected together through an array of piezoelectric patches. Four models are proposed to describe wave propagation in the electromechanical medium. The models are based on the transfer matrix formulation and consider a finite number of patches. It is shown that a simple coupling condition gives a network that approximates the modal properties of the beam. A multimodal tuned mass effect is then obtained and a broadband damping is introduced by choosing a suitable positioning for resistors in the network. The strategy and the models are experimentally validated by coupling a free-free beam to a completely passive network made of inductors and transformers. A multimodal vibration reduction is observed, which proves the efficiency of the control solution and its potential in terms of practical implementation.*

Contents

4.1 Introduction

Piezoelectric shunts can offer significant vibration reductions when an electrical resonance is tuned to the mechanical natural frequency to control [2, 43]. The concept of resonant shunt was extended to the synthesis of metamaterials when came the idea of distributing an array of piezoelectric patches all over a mechanical structure. Considering one-dimensional media, longitudinal wave propagation was first considered [4, 102] and the strategy was then applied to bending waves control [45, 46, 48, 49, 85, 86, 105]. The classical passive resonant shunts can also be replaced by more broadband but not passive solutions as amplified resonant shunts [88, 89], switch techniques [109–112] and negative capacitance shunts [76, 90, 91, 113]. A periodicity of the one-dimensional structures enables the use of the transfer matrix formulation [46, 82]. Structural discontinuities induces band gaps [114–116] that can potentially be combined to the ones introduced by the piezoelectric shunts [4, 46, 48, 88, 89, 91, 102]. Yet, as presented in the previous references and in Chap. 3, the strategy benefiting from the mechanical band gaps introduced by the addition of piezoelectric patches is limited to wavelength sufficiently small compared to the length of the patches. Consequently, it does not apply to the control of the first modes of the considered periodic structures.

Furthermore, we have seen that an identical tuning of resonant shunts leads to a control only around a single frequency and, still, high values of inductance are often required, which forces the use of non-passive synthetic inductors [46, 48, 49]. It is yet possible to reduce the required inductance by implementing an electrical network interconnecting successive piezoelectric patches. This strategy was firstly described by Valis et al. [25] who analyzed the coupling between traveling waves in an electrical transmission line and bending waves in a beam. The network consists of a line of inductors connected to the ground through the piezoelectric capacitance, as was also considered by dell'Isola and Vidoli [12, 94, 117] and by Bergamini et al. [100] later on. With this simple network, a modal damping can be achieved by introducing resistors and by tuning an electrical resonance to a target frequency [26]. However, even if a line of inductors can generate a broadband damping for a rod, it cannot reproduce the modal properties of a beam [13, 19].

Multimodal damping of a beam requires the implementation of higher-order networks [13, 17, 97–99, 117]. A limit is that the proposed networks needs active control or includes negative capacitors or negative inductors, which cannot be passive electrical components [27–29]. A solution for a passive multimodal control is to find a network that matches a specified number of modes to control from a numerical optimization constrained by the use of only inductors and capacitors [95]. Yet, when considering a large number of mechanical modes, this solution leads to a network with an impractical number of electrical compo-

nents. A suitable passive electrical architecture involving transformers and inductors was proposed by Porfiri et al. [16, 19, 21, 22, 96]. As it was shown that a multimodal control can be achieved with a network approximating the beam modal properties, the electrical topology is obtained from an electromechanical analogy [30, 37, 74]. This analogy, used by Brillouin [83] on longitudinal periodic lattices, was considered in Chap. 3 to implement the broadband control of longitudinal wave. When the damping strategy is extended to the control of bending waves, the periodic layout of the resulting electromechanical structure still allows using the transfer matrix method [82, 106]. This method has often been implemented in problems involving independent piezoelectric shunts [46, 48, 49] but rarely with an interconnection of successive patches [101]. This last case requires the definition of state vectors that combine both mechanical and electrical degrees of freedom, because a real electromechanical waveguide is taken into account. The electrical part is then described with the discrete equations governing the lumped electrical components but the continuous mechanical medium can be approximated by various models.

In this chapter, the Euler Bernoulli beam model is presented, as well as its equivalent transverse lattice obtained from a finite difference method. The direct electromechanical analogy is applied to this lattice in order to find the analogous electrical network of a beam. Both mechanical and electrical structures are then coupled through an array of piezoelectric patches. The analysis of the coupling is given by a linear model focusing on the global properties of a single unit cell subjected to bending motion. For the tuning of the network, a multimodal coupling condition is deduced from the global constants defining the electromechanical unit cell. Novel transfer matrix models are then proposed in order to consider the coupling of a continuous beam to its discrete analogue. Those models can be applied to real cases where the number of patches is not unlimited. We first describe the electromechanical transfer matrices for a discrete or a fully homogenized beam. Two other models are also presented: a piecewise homogenized model and a finite element model, which both take into account the mechanical discontinuity induced by the addition of piezoelectric patches. The models are then compared in order to define their respective limits and to select the most appropriate depending on the frequency range of interest. The next section details the practical implementation of the analogous electrical network. Recommendations are given regarding the number of piezoelectric patches, the positioning of damping elements and the design of the transformers. Finally, the models and the damping strategy are experimentally validated with a passive analogous network consisting of inductors and transformers. A method is also proposed to verify the tuning of the network from purely electrical measurements. All of this shows the potential of the strategy for multimodal vibration reduction and proves its practical feasibility.

4.2 Bending wave propagation in a discretized beam

The transfer matrix formulation is able to model wave propagation in a one-dimensional periodic structure. This applies to beams through a transfer matrix obtained from the Euler-Bernoulli theory. It is then remarked that a beam can be discretized into a periodic lattice that approximates the continuous beam dispersion relation. The corresponding mechanical unit cell is presented together with its electrical analogue.

4.2.1 Mechanical analysis of a beam

Wave propagation in a beam can be described by the Euler-Bernoulli theory, which considers small deflections, no shear strain and no rotational inertia. With no distributed load, if Y is the Young's modulus of the beam, ρ its density, S its cross-sectional area and I its second moment of area, the bending wave differential equation is written as

$$\rho S \frac{\partial^2 w(x,t)}{\partial t^2} = -YI \frac{\partial^4 w(x,t)}{\partial x^4}, \tag{4.1}$$

where $w(x,t)$ represents the transverse displacement at longitudinal location x and time t. A space-time separation $w(x,t) = W(x)g(t)$ applied to the wave equation (4.1) gives two uncoupled differential equations and the corresponding dispersion relation:

$$\begin{aligned} &W^{(4)}(x) - k^4 W(x) = 0 \\ &g''(t) + \omega^2 g(t) = 0 \end{aligned} \qquad \text{with} \quad \omega^2 = \frac{YI}{\rho S} k^4, \tag{4.2}$$

where $[\cdot]^{(4)}$ represents the fourth order derivative, $[\cdot]''$ is the second order derivative, ω is the angular frequency and k is the wavenumber. Under harmonic excitation, the solution of the differential equation related to the displacement is written as

$$W(x) = A\cos(kx) + B\sin(kx) + C\cosh(kx) + D\sinh(kx). \tag{4.3}$$

The constants A, B, C and D depend on the boundary conditions, which are represented in Fig. 4.1 for a beam segment of length a. Note that the angle θ_L shows a negative value because it is represented in a clockwise direction. According to the Euler-Bernoulli

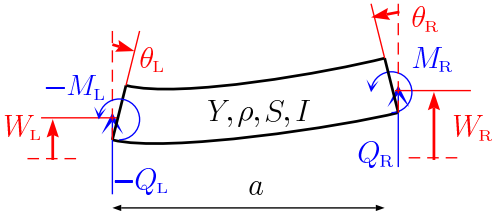

Figure 4.1: Considered beam segment.

beam theory, the transverse displacement $W(x)$, the rotation of the cross-section $\theta(x)$, the bending moment $M(x)$ and the shear force $Q(x)$ are governed by

$$\begin{array}{l} \theta(x) = W'(x) \\ M(x) = YI\theta'(x) \\ Q(x) = -M'(x) \\ -\rho S\omega^2 W(x) = Q'(x) \end{array} , \tag{4.4}$$

If the subscript L refers to the position $x = 0$, Eqs. (4.3) and (4.4) gives

$$\begin{array}{l} W_{\mathrm{L}} = A + C \\ \theta_{\mathrm{L}} = k(B + D) \\ M_{\mathrm{L}} = YIk^2(-A + C) \\ Q_{\mathrm{L}} = YIk^3(B - D) \end{array} , \quad \text{so} \quad \begin{array}{l} A = \frac{1}{2}(W_{\mathrm{L}} - \frac{1}{YIk^2} M_{\mathrm{L}}) \\ B = \frac{1}{2}(\frac{1}{k}\theta_{\mathrm{L}} + \frac{1}{YIk^3} Q_{\mathrm{L}}) \\ C = \frac{1}{2}(W_{\mathrm{L}} + \frac{1}{YIk^2} M_{\mathrm{L}}) \\ D = \frac{1}{2}(\frac{1}{k}\theta_{\mathrm{L}} - \frac{1}{YIk^3} Q_{\mathrm{L}}) \end{array} . \tag{4.5}$$

Furthermore, for $x = a$, we define the state variables on the right of the unit cell as

$$\begin{array}{l} W_{\mathrm{R}} = A\mathrm{c} + B\mathrm{s} + C\mathrm{ch} + D\mathrm{sh} \\ \theta_{\mathrm{R}} = k\left(-A\mathrm{s} + B\mathrm{c} + C\mathrm{sh} + D\mathrm{ch}\right) \\ M_{\mathrm{R}} = YIk^2\left(-A\mathrm{c} - B\mathrm{s} + C\mathrm{ch} + D\mathrm{sh}\right) \\ Q_{\mathrm{R}} = -YIk^3\left(A\mathrm{s} - B\mathrm{c} + C\mathrm{sh} + D\mathrm{ch}\right) \end{array} , \tag{4.6}$$

where $\mathrm{c} = \cos(ka)$, $\mathrm{ch} = \cosh(ka)$, $\mathrm{s} = \sin(ka)$ and $\mathrm{sh} = \sinh(ka)$. Eqs. (4.5) and (4.6) can then be rearranged into the matrix form

$$\begin{bmatrix} W_{\mathrm{R}}^\star \\ \theta_{\mathrm{R}}^\star \\ M_{\mathrm{R}}^\star \\ Q_{\mathrm{R}}^\star \end{bmatrix} = \begin{bmatrix} \frac{\mathrm{c}+\mathrm{ch}}{2} & \frac{1}{ka}\frac{\mathrm{s}+\mathrm{sh}}{2} & -\frac{1}{(ka)^2}\frac{\mathrm{c}-\mathrm{ch}}{2} & \frac{1}{(ka)^3}\frac{\mathrm{s}-\mathrm{sh}}{2} \\ -ka\frac{\mathrm{s}-\mathrm{sh}}{2} & \frac{\mathrm{c}+\mathrm{ch}}{2} & \frac{1}{ka}\frac{\mathrm{s}+\mathrm{sh}}{2} & \frac{1}{(ka)^2}\frac{\mathrm{c}-\mathrm{ch}}{2} \\ -(ka)^2\frac{\mathrm{c}-\mathrm{ch}}{2} & -ka\frac{\mathrm{s}-\mathrm{sh}}{2} & \frac{\mathrm{c}+\mathrm{ch}}{2} & -\frac{1}{ka}\frac{\mathrm{s}+\mathrm{sh}}{2} \\ -(ka)^3\frac{\mathrm{s}+\mathrm{sh}}{2} & (ka)^2\frac{\mathrm{c}-\mathrm{ch}}{2} & ka\frac{\mathrm{s}-\mathrm{sh}}{2} & \frac{\mathrm{c}+\mathrm{ch}}{2} \end{bmatrix} \begin{bmatrix} W_{\mathrm{L}}^\star \\ \theta_{\mathrm{L}}^\star \\ M_{\mathrm{L}}^\star \\ Q_{\mathrm{L}}^\star \end{bmatrix} , \tag{4.7}$$

where $W^\star = W/a$, $\theta^\star = \theta$, $M^\star = aM/(YI)$ and $Q^\star = a^2Q/(YI)$. The system of equations (4.7) is related to the transfer matrix formulation introduced in Chap. 3. In the present chapter, the displacement state vector is $\boldsymbol{q} = [W^\star\ \theta^\star]^T$ and the force state vector is $\boldsymbol{F} = [M^\star\ Q^\star]^T$. Dimensionless state variables are still employed in order to simplify the matrix expression and to improve its conditioning.

4.2.2 Lattice model

The analysis of a homogeneous beam does not require to split the structure into several unit cells as the analytic formulation can be directly obtained with a beam segment equal to the whole beam length. However, when considering a non-homogeneous medium as a discrete model, the local layout of the unit cells differs from the one of the complete structure. The transfer matrix formulation becomes then helpful as it allows computing the global mechanical behavior from the definition of a single unit cell.

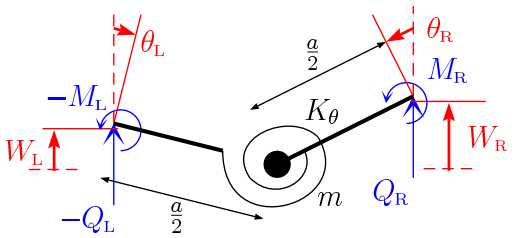

Figure 4.2: Discrete model of a beam segment.

The discrete model of a beam can be obtained through a finite difference procedure combining forward, central and backward differences:

$$[\cdot]'_{\mathrm{L}} = \frac{[\cdot]_{\mathrm{I}} - [\cdot]_{\mathrm{L}}}{a/2}, \qquad [\cdot]'_{\mathrm{I}} = \frac{[\cdot]_{\mathrm{R}} - [\cdot]_{\mathrm{L}}}{a}, \qquad \text{and} \qquad [\cdot]'_{\mathrm{R}} = \frac{[\cdot]_{\mathrm{R}} - [\cdot]_{\mathrm{I}}}{a/2} \ . \tag{4.8}$$

where the subscript I defines the center of the considered unit cell. By applying those finite differences to the system of equations (4.4), one gets discrete relations between the left, center and right state variables of a discretized beam unit cell as

$$\begin{array}{l} \frac{a}{2}\theta_{\mathrm{L}} = W_{\mathrm{I}} - W_{\mathrm{L}} \\ \frac{a}{2}\theta_{\mathrm{R}} = W_{\mathrm{R}} - W_{\mathrm{I}} \\ M_{\mathrm{I}} = K_\theta(\theta_{\mathrm{R}} - \theta_{\mathrm{L}}) \\ \frac{a}{2}Q_{\mathrm{L}} = M_{\mathrm{L}} - M_{\mathrm{I}} \\ \frac{a}{2}Q_{\mathrm{R}} = M_{\mathrm{I}} - M_{\mathrm{R}} \\ -m\omega^2 W_{\mathrm{I}} = Q_{\mathrm{R}} - Q_{\mathrm{L}} \end{array} , \tag{4.9}$$

where the mass m and the bending stiffness K_θ are defined from the material and geometric properties of the beam segment:

$$m = \rho S a \quad \text{and} \quad K_\theta = \frac{YI}{a}. \tag{4.10}$$

It can be remarked that Eq. (4.9) defines a mechanical structure consisting of two massless rigid bars of length $a/2$ linked together by a pivot joint. A lumped mass m and a torsion spring K_θ are placed at the pivot location, as represented in Fig. 4.2 which satisfies Eq. (4.9) for small displacements. W_{I} corresponds to the displacement of the mass m and M_{I} is the torque applied to the torsion spring K_θ. As a consequence, a beam can be approximated by a succession of identical unit cells referring to Fig. 4.2. This gives a lattice describing transverse wave propagation, which can be seen as an extension of the previous spring-mass lattice approximating wave propagation in a rod [83].

Equations (4.9) is reorganized into the transfer matrix formulation

$$\begin{bmatrix} W^\star_{\mathrm{R}} \\ \theta^\star_{\mathrm{R}} \\ M^\star_{\mathrm{R}} \\ Q^\star_{\mathrm{R}} \end{bmatrix} = \begin{bmatrix} 1 & 1 & \frac{1}{2} & -\frac{1}{4} \\ 0 & 1 & 1 & -\frac{1}{2} \\ \frac{f}{2} & \frac{f}{4} & 1 & -1 \\ -f & -\frac{f}{2} & 0 & 1 \end{bmatrix} \begin{bmatrix} W^\star_{\mathrm{L}} \\ \theta^\star_{\mathrm{L}} \\ M^\star_{\mathrm{L}} \\ Q^\star_{\mathrm{L}} \end{bmatrix}, \tag{4.11}$$

where $f = \omega^2 m a^2 / K_\theta$. As seen in Chap. 3, the eigenvalues of a transfer matrix are related to the propagation constants of the corresponding one-dimensional problem [46, 82]. For the 4×4 matrix in Eq. (4.11), we get the four eigenvalues

$$\begin{aligned} \lambda_1^{\pm} &= 1 - \frac{\sqrt{f}}{2}\left(1 \pm \sqrt{1 - \frac{4}{\sqrt{f}}}\right) \\ \lambda_2^{\pm} &= 1 + \frac{\sqrt{f}}{2}\left(1 \pm \sqrt{1 + \frac{4}{\sqrt{f}}}\right) \end{aligned} . \tag{4.12}$$

Both eigenvalues λ_2^+ and λ_2^- are real numbers, which means that they refer to evanescent waves for any positive value of f [82]. On the other hand, λ_1^+ and λ_1^- are complex numbers when $f < 16$. Those eigenvalues thus correspond to propagating waves and they are related to the wavenumber of the discrete problem $\bar{k}$ through $\lambda_1^{\pm} = \exp(\pm \mathrm{j}\bar{k}a)$. Consequently, it is found that $f = (2\sin(\bar{k}a/2))^4$ when $\bar{k}a < \pi$, i.e. $f < 16$. This gives the lattice dispersion relation

$$\omega^2 = \frac{YI}{\rho S}\left(\bar{k}\ \mathrm{sinc}\left(\frac{\bar{k}a}{2}\right)\right)^4 . \tag{4.13}$$

By comparing this equation to the beam dispersion relation in Eq. (4.2), it is seen that they are equivalent when $\bar{k}a$ goes to zero. This condition occurs when the length of the unit cell is sufficiently small compared to the considered wavelength. As a reference, it is seen from Eq. (4.13) that 10 unit cells per wavelength ($\bar{k}a = 2\pi/10$) gives a frequency for the discrete model which is 3.2% lower than the frequency obtained with the continuous beam dispersion relation. As a conclusion, it is shown that a beam can be approximated by the lattice of point masses introduced in Fig. 4.2 as long as the number of unit cells per wavelength is sufficiently large to satisfy the desired frequency accuracy.

The transverse lattice is compared to the continuous model by considering a $l = 1$ m beam of Young's modulus $Y = 73.9$ GPa, density $\rho = 2780$ kg/m^3 and square cross-sectional area $S = 4$ cm^2. For any eigenvalue λ of the transfer matrices in Eqs. (4.7) and (4.11), we compute the real and imaginary parts of $\ln(\lambda)$, which gives the attenuation and phase constants [46, 82]. As they appear in pairs of opposite values, only the positive constants are represented in Figs. 4.3 and 4.4. Two positive propagation constants are found for each model because they refer to 4×4 transfer matrices. For the lattice model, we remark a stop band above $\omega = 4/a\sqrt{K_\theta/m}$ (i.e. $f = 16$), which corresponds to a frequency equal to 7.58 kHz. Around this frequency and above it, the validity of the Euler-Bernoulli beam is questionable but this classical continuous model is still adequate for a comparison with a discrete model. Above 7.58 kHz, none of the attenuation constants is equal to zero and, at the same time, the phase constants are equal to 0 or π. This indicates that no wave can propagate in the discrete medium at such high frequencies. For $\omega < 4/a\sqrt{K_\theta/m}$, which is equivalent to $\bar{k}a < \pi$, the results related to the phase constants in Fig. 4.4 are consistent with the continuous and lattice dispersion relations in Eqs. (4.2) and (4.13).

Regarding a finite structure of $n = 20$ unit cells of length $a = 50$ mm, the frequency response functions (FRFs) can be computed from the Ricatti transfer matrix method presented in Chap. 3. A free-free beam and its equivalent lattice model are excited at one end with a transverse unit force and the velocity at the other end is represented in Fig. 4.5. The stop band phenomenon is obvious since no resonance appears above 7.58 kHz. Furthermore, we note that the approximation of the continuous beam by a lattice model starts showing its limits above the fourth resonance (around 1 kHz) as the differences in terms of natural frequencies becomes non-negligible. This confirms the previous recommendation based on a minimum of 10 unit cells per wavelength in order to get a suitable representation of a continuous medium with a discrete model.

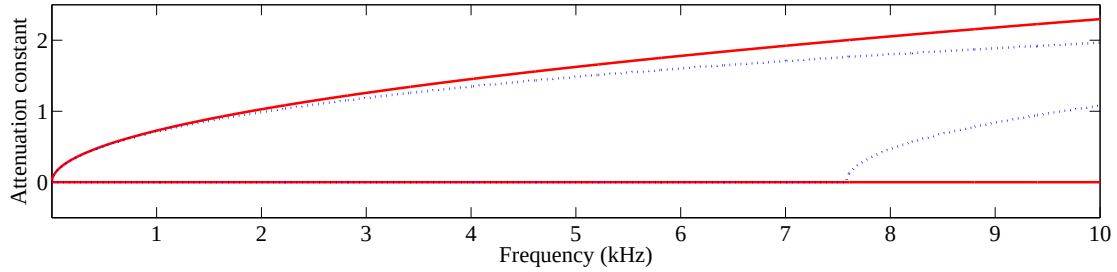

Figure 4.3: Attenuation constants - (—) for the continuous rod, (· · ·) for the lattice model.

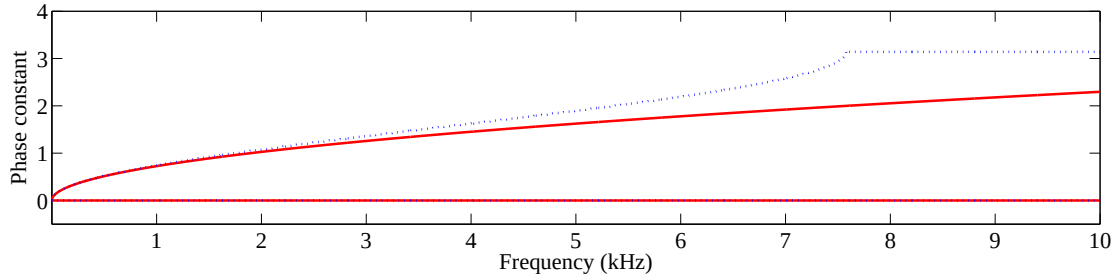

Figure 4.4: Phase constants - (—) for the continuous rod, (· · ·) for the lattice model.

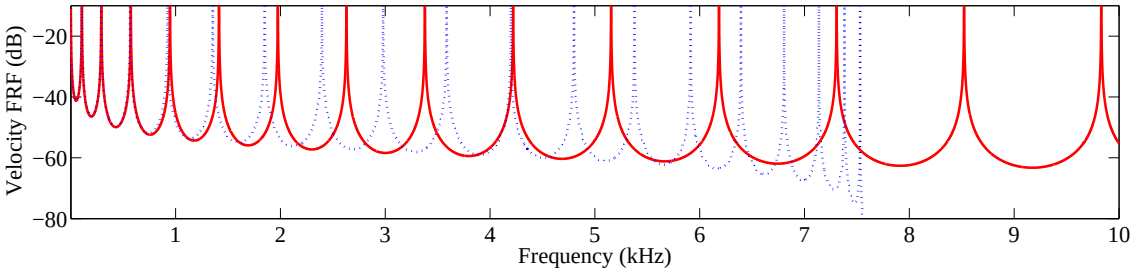

Figure 4.5: Velocity FRFs - (—) for the continuous rod, (· · ·) for the lattice model.

4.2.3 Electrical analogue of a beam

The system of equations (4.9) was first represented through the mechanical unit cell in Fig. 4.2 but it is also possible to define an analogous electrical representation. Using the direct electromechanical analogy [74, 84], a voltage is analogous to a force or a moment and a current is analogous to a linear velocity or an angular velocity. As a consequence, a mass is represented by an inductance and a stiffness by the inverse of a capacitance. When focusing on the unit cell presented in Fig. 4.2, it is also required to find the electrical analogues for the two levers of length $a/2$. We note from Eq. (4.9) that the length $a/2$ corresponds to the proportionality constant between the transverse velocity differences and the angular velocities of the two rigid bars. Moreover, $a/2$ is also the proportionality constant between the bending moment differences and the shear forces in the same bars. This is finally modeled by an electrical transformer, where the ratio $a/2$ of the voltages on both windings is the inverse of the respective ratio of the currents. All of this is illustrated in Fig. 4.6 where conventional electrical notations are replaced by their analogues that refer to the mechanical unit cell in Fig. 4.2. Note that the electrical unit cell strictly satisfies Eq. (4.9), which can be reformulated as

$$\begin{array}{l} \frac{a}{2}\dot{\theta}_{\mathrm{L}} = \dot{W}_{\mathrm{I}} - \dot{W}_{\mathrm{L}} \\ \frac{a}{2}\dot{\theta}_{\mathrm{R}} = \dot{W}_{\mathrm{R}} - \dot{W}_{\mathrm{I}} \\ -M_{\mathrm{I}} = \frac{K_\theta}{\mathrm{j}\omega}(\dot{\theta}_{\mathrm{L}} - \dot{\theta}_{\mathrm{R}}) \\ -M_{\mathrm{L}} + M_{\mathrm{I}} = -\frac{a}{2}Q_{\mathrm{L}} \\ -M_{\mathrm{I}} + M_{\mathrm{R}} = -\frac{a}{2}Q_{\mathrm{R}} \\ -Q_{\mathrm{L}} + Q_{\mathrm{R}} = \mathrm{j}\omega m \dot{W}_{\mathrm{I}} \end{array} , \tag{4.14}$$

where $\dot{W}_{\mathrm{I}} = \mathrm{j}\omega W_{\mathrm{I}}$ represents the current flowing through the inductor m and M_{I} is the voltage across the capacitance $1/K_\theta$. Actually, the electrical network could have been directly obtained from Eq. (4.9) without first appeal to the electromechanical analogy. Yet, applying the electromechanical analogy to the mechanical unit cell in Fig. 4.2 makes easier the determination and the understanding of the network topology.

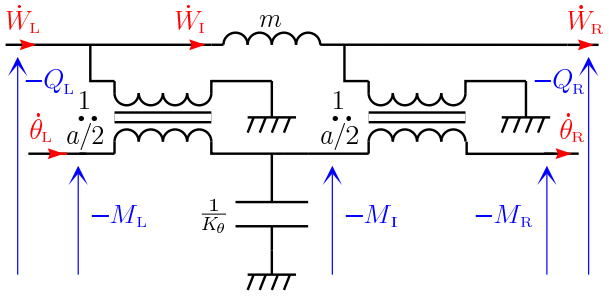

Figure 4.6: Electrical analogue of the discrete beam segment.

A periodic electrical network is formed by connecting identical electrical unit cells in series. It is remarked that two transformers in series can be replaced by a single one with a doubled transformation ratio a. This is the equivalent of a rigid connection of two levers of length $a/2$, which gives a single lever of length a. Consequently, we get a network topology similar to the one already introduced by MacNeal in 1949 [30, 37]. Porfiri et al. also got the same topology from a finite difference method on the Timoshenko equations followed by simplifications through Euler-Bernoulli assumptions [16, 22], which leads to a passive network that necessarily involves electrical transformers [21]. Finally, it becomes possible to implement an electrical network that approximates the modal behavior of a beam. The electrical connections at both ends of the network depend on the analogous mechanical boundary conditions. For example, when referring to the direct electromechanical analogy, the analogue of a clamped beam would require open electrical connections. Indeed, a zero-current is analogous to a zero-velocity. On the other hand, a free-free beam requires grounded electrical connections at both ends, as a zero-voltage is analogous to a zero-force or a zero-moment. Then, as the network is made of discrete electrical components, its model refers to the transfer matrix in Eq. (4.11) and the lattice dispersion relation (4.13). Electrical frequency response functions can thus be computed with the same transfer matrix method as the one implemented for the beam and for its lattice model.

4.3 Coupling of a beam to its electrical analogue

As shown in Chap. 3, wave propagation in a mechanical structure can be controlled by a coupling to an electrical network exhibiting a similar dispersion relation. So, a beam is coupled to its analogous electrical network through a periodic array of piezoelectric patches. A unit cell is defined by considering both mechanical and electrical propagation media. Afterwards, the linear piezoelectricity theory gives a global piezoelectric model, which brings an electrical tuning condition depending on the properties of a single unit cell.

4.3.1 Electromechanical unit cell

A periodic array of piezoelectric patches is distributed on a homogeneous beam. An electrical network interconnects the patches, which creates an electrical waveguide. As presented by Vidoli and dell'Isola [94] and Maurini et al. [17, 18], a wide-band energy exchange is achieved by connecting a mechanical structure to its electrical analogue. So, the chosen network is the periodic electrical analogue of a beam in order to implement a broadband control of bending modes [19, 21, 22]. As seen in Fig. 4.7, an electromechanical periodic structure is obtained and a unit cell of length a can be defined. The thickness of the main structure is h_s and its width is b. The piezoelectric patches have a thickness

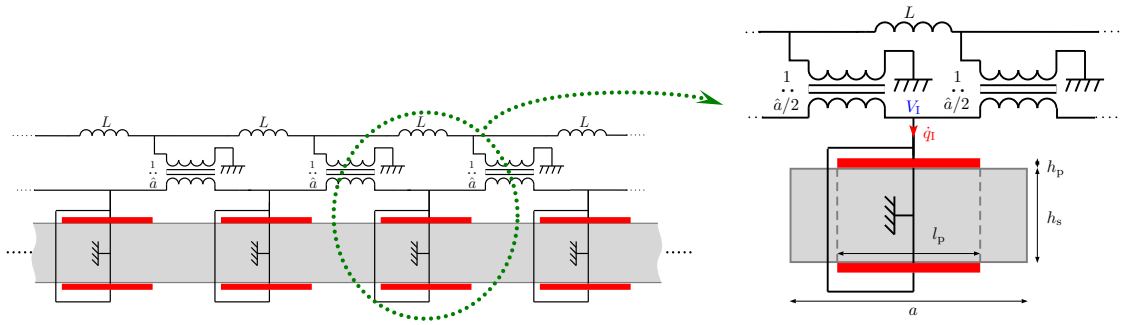

Figure 4.7: Beam coupled to its analogous electrical network through a periodic array of piezoelectric patches and corresponding electromechanical unit cell.

	Beam (Aluminum 2017)	Patches (PIC 151)
Length (mm)	$20 \times a = 20 \times 50$	$l_\mathrm{p} = 30$
Width (mm)	$b = 20$	$b = 20$
Thickness (mm)	$h_\mathrm{s} = 20$	$h_\mathrm{p} = 0.5$
Density (kg/m^3)	$\rho_\mathrm{s} = 2780$	$\rho_\mathrm{p} = 7800$
Young's modulus (GPa)	$Y_\mathrm{s} = 73.9$	$1/s_{11}^E = 66.7$
Charge constant (pC/N)	-	$d_{31} = -210$
Permittivity (nF/m)	-	$\epsilon_{33}^\sigma = 21.2$

Table 4.1: Dimensions and material properties for the beam and for the piezoelectric patches.

h_p, a width b and a length l_p, with $l_\mathrm{p} \leq a$. Listed in Table 4.1, the same numerical values as in Chap. 3 are employed in the following sections. In terms of electrical variables, $\dot{q}_\mathrm{I}$ is the current flowing from the network to the pair of patches and V_I is the voltage on the electrodes connected to the network. As the two piezoelectric patches are connected in parallel, they need to be transversely polarized in identical directions in order to generate a non-zero voltage when bending excitation occurs [2, 17, 22, 71]. Because the piezoelectric patches are equivalent to capacitors in the electrical domain, no external capacitors are required to implement the analogous network and the electrical part of the unit cell only consists of two transformers of ratio $\hat{a}/2$ and one inductor L.

The mechanical part of the unit cell in Fig. 4.7 is made of an elastic beam segment symmetrically covered with two piezoelectric patches. This structure can be seen as a homogenized medium governed by a global piezoelectric coupling, similar to the homogenized model in Chap. 3 but reformulated for bending motion. We first consider a simplified case where the patches cover the whole beam segment ($a = l_\mathrm{p}$). We also make use of the fact that, for large wavelength compared to the unit cell, a longitudinal strain ε_1 in a piezoelectric patch can be approximated by $\Delta U_\mathrm{p}/l_\mathrm{p}$, where ΔU_p is the difference of the displacements at both ends of the patch. So, ΔU_p is approximated by $-(h_\mathrm{s} + h_\mathrm{p})\Delta\theta/2$,

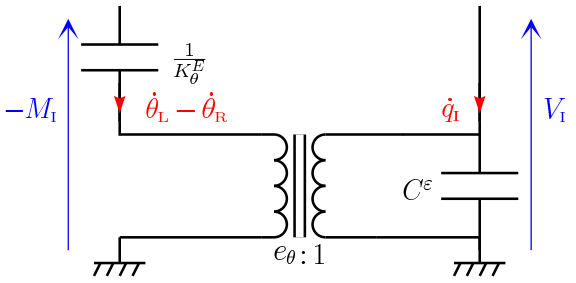

Figure 4.8: Model of the piezoelectric coupling for a unit cell subjected to bending.

when $\Delta\theta = \theta_\mathrm{R} - \theta_\mathrm{L}$ represents the difference of the rotations at both ends of the unit cell. From the definition of the blocked capacitance C_p^ε of a single piezoelectric patch and its coupling coefficient e_p introduced in Chap. 2, we get the bending model

$$\begin{aligned} M_\mathrm{I} &= K_\theta^E \Delta\theta - e_\theta V_\mathrm{I} \\ q_\mathrm{I} &= e_\theta \Delta\theta + C^\varepsilon V_\mathrm{I} \end{aligned} \quad , \tag{4.15}$$

where $C^\varepsilon = 2C_\mathrm{p}^\varepsilon$ and $e_\theta = -(h_\mathrm{s} + h_\mathrm{p})e_\mathrm{p}$. Here, M_I is the bending moment and K_θ^E is the bending stiffness when the pair of patches is short-circuited. When $a = l_\mathrm{p}$, K_θ^E is equal to $(Y_\mathrm{s} I_\mathrm{s} + 2Y_\mathrm{p}^E I_\mathrm{p})/a$, where $I_\mathrm{s} = b h_\mathrm{s}^3/12$, $I_\mathrm{p} = b((h_\mathrm{s} + 2h_\mathrm{p})^3 - h_\mathrm{s}^3)/24$ and $Y_\mathrm{p}^E = 1/s_{11}^E$.

The global formulation (4.15) can be illustrated through the electric circuit in Fig. 4.8. This model is still based on the direct electromechanical analogy, as it is the only analogy that allows the passive electrical representation of an energy conversion system based on the action of electrostatic forces [74]. The transformer represents the piezoelectric coupling, which connects the mechanical branch, on the left of the circuit, to the electrical branch on the right [72, 73]. This model comes directly from the one-dimensional linear piezoelectricity theory and is usually employed to describe a single piezoelectric patch [84]. It is here extended to the bending of the whole unit cell by focusing on its global properties.

4.3.2 Determination of the global constants

Two limits appear in the previous formulation. First of all, it seems important to keep the possibility to consider a unit cell where the patches do not cover the entire beam segment ($a \neq l_\mathrm{p}$), which occurs in most practical configurations. Secondly, the definition of the blocked capacitance C_p^ε and piezoelectric coupling e_p in Chap. 2 assumes a free stress state along the direction '2' of the patches. This does not represent any classical implementation because, when the patches are glued on a structure, it obviously acts along both directions '1' and '2'. This clearly affects the equivalent permittivity which has been used to calculate C_p^ε. So, the analytic calculation of the blocked capacitance is not trivial and it requires to perform a three-dimensional analysis. This was presented by Maurini

et al. [18, 71], who proposed a correction of the equivalent material properties. In order to get the global properties defined in the global bending model (4.15), we focus on a more practical solution that follows the same method as was described in Chap. 3 for the longitudinal unit cell.

For a general case considering $a \neq l_\mathrm{p}$, the global bending stiffness is obtained from the geometry and the material properties of the unit cell in Fig. 4.7 by

$$\frac{1}{K_\theta^E} = \frac{l_\mathrm{p}}{Y_\mathrm{s} I_\mathrm{s} + 2 Y_\mathrm{p}^E I_\mathrm{p}} + \frac{a - l_\mathrm{p}}{Y_\mathrm{s} I_\mathrm{s}}. \tag{4.16}$$

Then, if K_θ^D refers to the bending stiffness in open circuit ($\dot{q}_\mathrm{I} = 0$), it can be seen from Fig. 4.8 that $K_\theta^D = K_\theta^E + e_\theta^2 / C^\varepsilon$. In a similar manner, the free capacitance C^σ is obtained when no bending moment is applied to the unit cell ($M_\mathrm{I} = 0$), which gives $C^\sigma = C^\varepsilon + e_\theta^2 / K_\theta^E$. The global coupling coefficient e_θ and the blocked capacitance C^ε are thus expressed from

$$\begin{aligned} C^\varepsilon &= C^\sigma \frac{K_\theta^E}{K_\theta^D} \\ e_\theta &= \sqrt{C^\sigma K_\theta^E \left(1 - \frac{K_\theta^E}{K_\theta^D}\right)} \end{aligned} . \tag{4.17}$$

The short-circuit bending stiffness K_θ^E is already known but it still remains to define the open-circuit bending stiffness K_θ^D and the free capacitance C^σ. K_θ^D is obtained directly from Eq. (4.16) by replacing the piezoelectric Young's modulus in short-circuit Y_p^E by $Y_\mathrm{p}^D = 1/(s_{11}^E - d_{31}^2/\epsilon_{33}^\sigma)$, that represents the equivalent Young's modulus in open-circuit. Concerning the capacitance C^σ, it would still require a 3D calculation but it can also be directly measured on the patches. This electrical measurement is actually not an easy task with C^ε as it would be required to prevent rotations at both ends of the unit cell. That is the reason why we focus on C^σ, which offers an easier measurement based on free mechanical boundary conditions.

4.3.3 Modal coupling condition

Regarding the analogous electrical network that interconnects successive piezoelectric unit cells, its main interest is that it can approximate the modal behavior of the whole mechanical structure. A modal coupling optimizing the energy transfer between the two media is obtained when they have a same dispersion relation and analogous boundary conditions [17]. The considered network being discrete, its electrical components are tuned to equal the dispersion relation related to the lattice model of the beam. When looking at Eq. (4.11), we note that two discrete unit cell having an identical f value, i.e. a same ratio $K_\theta/(a^2 m)$, would present identical dimensionless transfer matrices. Consequently, with analogous boundary conditions, a transverse lattice and its analogous electrical network

exhibit the same natural frequencies and the same mode shapes if

$$\frac{1}{\hat{a}^2}\frac{1}{LC^{\varepsilon}} = \frac{1}{a^2}\frac{K_{\theta}^{E}}{m}. \tag{4.18}$$

For the unit cell described in Table 4.1, the blocked capacitance C^{ε} is evaluated to 35.3 nF and we thus get an inductance L around 200 mH. With an analogous network satisfying this coupling condition, the resonances do not only match along the frequency domain but also on the spatial domain thanks to similar mode shapes. Here is thus added an electrical space dimension, which does not appear with an array of independent resonant shunts [4, 46, 48, 102].

The global capacitance of a unit cell C^{ε} is approximately proportional to A_{p}, the surface area of a piezoelectric patch. For a fixed thickness of the patches and a fixed length and width of the beam, A_{p} is then proportional to $1/n$, where n is the number of unit cells. So, the modal coupling condition (4.18) shows that a prescribed amount of piezoelectric material leads to $L \propto 1/n^3$. This was also noticed by Maurini et al. [17, 18] from the analysis of fourth-order homogenized networks. An increase in the number of unit cells gives lower values of the required inductance. It then becomes possible to consider lower frequency applications without being limited by restrictions on the available inductance values.

4.4 Transfer matrix models for bending wave propagation

Four transfer matrix models are proposed for the electromechanical unit cell. All of them take into account a discrete electrical network but they differ in the definition of the mechanical medium. The first model considers a discretized beam, whereas the second is fully homogenized. Then, the discontinuity induced by the piezoelectric patches is introduced in a piecewise homogenized model. This third transfer matrix formulation is consistent with the last model, which is based on a finite element method. Offering an increasing complexity, those four models are compared in order to define their respective limits.

4.4.1 Discrete model based on global properties

Our goal is to model a beam that is coupled to a network of electrical components through a periodic array of piezoelectric patches. So, we deal with two waveguides of different natures: the beam is continuous and the electrical network is discrete. In order to simplify the analysis, it is convenient to set up an analytic model combining two structures of identical nature. This is the reason why most of the papers focusing on the

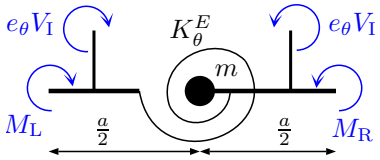

Figure 4.9: Discrete model for the beam segment.

piezoelectric coupling of a beam to an electrical network perform a homogenization of the electrical medium [17, 21, 22, 25, 94–96, 99]. This homogenization is justified for a large number of piezoelectric elements. Nevertheless, when considering practical implementations, the number of components is not unlimited and the network needs to be modeled as a discrete structure. Consequently, another solution bringing together two structures of similar nature is to discretize the mechanical medium. The beam is thus approximated by its lattice model presented Fig. 4.2. When considering the effect of the piezoelectric coupling in Eq. (4.15), the discrete model of the unit cell is illustrated in Fig. 4.9. The torsional spring refers to the bending stiffness K_θ^E and the lumped mass is the total mass of the continuous unit cell $m = \rho_\mathrm{s} S_\mathrm{s} a + 2\rho_\mathrm{p} S_\mathrm{p} l_\mathrm{p}$, where ρ_s and ρ_p are respectively the density of the main structure and the density of the piezoelectric patches, while $S_\mathrm{s} = b h_\mathrm{s}$ and $S_\mathrm{p} = b h_\mathrm{p}$ are the beam and patch cross-sectional areas. The shear force is not represented in Fig. 4.9 because it does not depend directly on the piezoelectric coupling, contrary to the total bending moment, which is increased by $e_\theta V_\mathrm{I}$ according to Eq. (4.15).

When the discrete mechanical unit cell is coupled to its analogous electrical network, the resulting discrete electromechanical unit cell results from a combination of the electrical representations in Figs. 4.6, 4.7 and 4.8. Therefore, the electromechanical problem can be seen as the coupling of two electrical networks having the same topology, which is represented in Fig. 4.10. The currents $\dot{q}_w$ and $\dot{q}_\theta$ are the analogues of the velocities $\dot{W}$

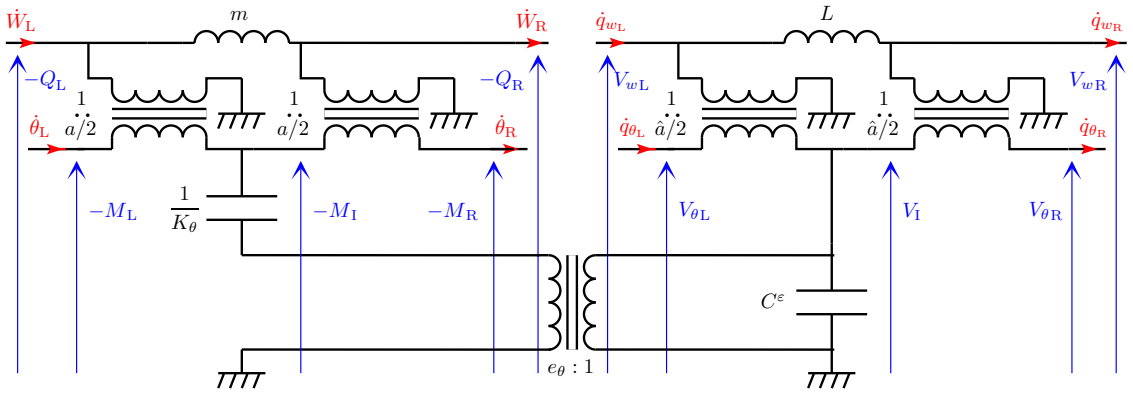

Figure 4.10: Discrete model for the electromechanical unit cell.

and $\dot{\theta}$ and the voltages V_θ and V_w are the analogues of the bending moments $-M$ and the shear forces $-Q$. The network capacitance is equal to the blocked capacitance of the pair of patches C^ε if no additional capacitors are introduced in the network. The equations governing the electrical circuit in Fig. 4.10 are

$$\begin{array}{ll}
\frac{a}{2}\dot{\theta}_\mathrm{L} = \dot{W}_\mathrm{I} - \dot{W}_\mathrm{L} & \frac{a}{2}\dot{q}_{\theta_\mathrm{L}} = \dot{q}_{w_\mathrm{I}} - \dot{q}_{w_\mathrm{L}} \\
\frac{a}{2}\dot{\theta_\mathrm{R}} = \dot{W}_\mathrm{R} - \dot{W}_\mathrm{I} & \frac{a}{2}\dot{q}_{\theta_\mathrm{R}} = \dot{q}_{w_\mathrm{R}} - \dot{q}_{w_\mathrm{I}} \\
-M_\mathrm{I} = \dfrac{K_\theta}{\mathrm{j}\omega}(\dot{\theta}_\mathrm{L} - \dot{\theta}_\mathrm{R}) + e_\theta V_\mathrm{I} \quad \text{and} & V_\mathrm{I} = \dfrac{1}{\mathrm{j}\omega C^\varepsilon}\left(\dot{q}_{\theta_\mathrm{L}} - \dot{q}_{\theta_\mathrm{R}} + e_\theta(\dot{\theta}_\mathrm{L} - \dot{\theta}_\mathrm{R})\right) \\
-M_\mathrm{L} + M_\mathrm{I} = -\frac{a}{2}Q_\mathrm{L} & V_{\theta\mathrm{L}} - V_\mathrm{I} = \frac{\hat{a}}{2}V_{w\mathrm{L}} \\
-M_\mathrm{I} + M_\mathrm{R} = -\frac{a}{2}Q_\mathrm{R} & V_\mathrm{I} - V_{\theta\mathrm{R}} = \frac{\hat{a}}{2}V_{w\mathrm{R}} \\
-Q_\mathrm{L} + Q_\mathrm{R} = \mathrm{j}\omega m\dot{W}_\mathrm{I} & V_{w\mathrm{L}} - V_{w\mathrm{R}} = \mathrm{j}\omega L\dot{q}_{w_\mathrm{I}}
\end{array} , \tag{4.19}$$

where $\dot{W}_\mathrm{I}$ and $\dot{q_{w\mathrm{I}}}$ are the currents flowing through the inductors m and L. From this system of equations, the relation between the electromechanical state vectors at the right and left ends of the unit cell is given by the transfer matrix formulation

$$\begin{bmatrix} W^\star_\mathrm{R} \\ \theta^\star_\mathrm{R} \\ q_{w\mathrm{R}}^\star \\ q_{\theta\mathrm{R}}^\star \\ M^\star_\mathrm{R} \\ Q^\star_\mathrm{R} \\ V_{\theta\mathrm{R}}^\star \\ V_{w\mathrm{R}}^\star \end{bmatrix} = \begin{bmatrix} 1 & 1 & 0 & 0 & \frac{1}{2} & -\frac{1}{4} & \frac{\Lambda}{2} & -\frac{\Lambda}{4} \\ 0 & 1 & 0 & 0 & 1 & -\frac{1}{2} & \Lambda & -\frac{\Lambda}{2} \\ 0 & 0 & 1 & 1 & -\frac{1}{2} & \frac{1}{4} & -\frac{1+\Lambda}{2} & \frac{1+\Lambda}{4} \\ 0 & 0 & 0 & 1 & -1 & \frac{1}{2} & -(1+\Lambda) & \frac{1+\Lambda}{2} \\ \frac{f}{2} & \frac{f}{4} & 0 & 0 & 1 & -1 & 0 & 0 \\ -f & -\frac{f}{2} & 0 & 0 & 0 & 1 & 0 & 0 \\ 0 & 0 & -\frac{\hat{f}}{2} & -\frac{\hat{f}}{4} & 0 & 0 & 1 & -1 \\ 0 & 0 & \hat{f} & \frac{\hat{f}}{2} & 0 & 0 & 0 & 1 \end{bmatrix} \begin{bmatrix} W^\star_\mathrm{L} \\ \theta^\star_\mathrm{L} \\ q_{w\mathrm{L}}^\star \\ q_{\theta\mathrm{L}}^\star \\ M^\star_\mathrm{L} \\ Q^\star_\mathrm{L} \\ V_{\theta\mathrm{L}}^\star \\ V_{w\mathrm{L}}^\star \end{bmatrix} , \tag{4.20}$$

where $f = \omega^2 m a^2/K_\theta^E$, $\hat{f} = \omega^2 L C^\varepsilon \hat{a}^2$ and $\Lambda = e_\theta^2/(K_\theta^E C^\varepsilon)$, which corresponds to the square of a global coupling factor similar to what has been introduced for the longitudinal case in Chap. 3. As in Eq. (4.7), the symbol '$\star$' denotes dimensionless state variables, which are highlighted for the sake of conciseness of the transfer matrix and to improve its conditioning: $W^\star = W/a$, $\theta^\star = \theta$, $M^\star = M/K_\theta^E$, $Q^\star = aQ/K_\theta^E$, $q_w^\star = q_w/(e_\theta \hat{a})$, $q_\theta^\star = q_\theta/e_\theta$, $V_\theta^\star = C^\varepsilon V_\theta/e_\theta$ and $V_w^\star = \hat{a}C^\varepsilon V_w/e_\theta$. It then becomes possible to compute the behavior of a succession of several electromechanical unit cells from the Ricatti transfer matrix method presented in Chap. 3, with $\boldsymbol{q} = [W^\star\ \theta^\star\ q_w^\star\ q_\theta^\star]^T$ and $\boldsymbol{F} = [M^\star\ Q^\star\ V_\theta^\star\ V_w^\star]^T$ defining the "displacement" and "force" vectors.

4.4.2 Fully homogenized model for the beam segment

The discrete model has been obtained by approximating a continuous beam segment with a lattice model. As mentioned in Sec. 4.2, this approximation is valid only when the considered wavelength is large compared to the length of the unit cells. A minimum of 10 unit cells per wavelength allows a frequency error of less than 4% as given by Eq. (4.13).

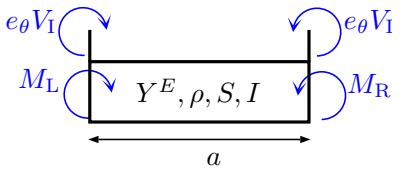

Figure 4.11: Fully homogenized model for the beam segment.

Yet, when the number of piezoelectric patches is limited, the discrete model becomes too inaccurate to describe the behavior of the continuous mechanical structure. As highlighted by Bisegna et al. [99], it is thus essential to develop a semi-continuous model that maintains the continuity of the beam together with a discrete electrical network.

In order to keep the model as simple as possible, it is here chosen to consider a homogeneous beam segment, as the one presented in Fig. 4.11, where the discontinuity induced by the thickness of the patches is not taken into account. So, we can keep using the global constants appearing in Eq. (4.15) for the discrete model, but the continuity of the mechanical medium is recovered by replacing $\Delta\theta$ by $a\theta'(x)$ in the bending moment equation. The piezoelectric coupling on the continuous beam segment is then

$$\begin{array}{l} M(x) = Y^E I \theta'(x) - e_\theta V_\mathrm{I} \\ q_\mathrm{I} = e_\theta \Delta\theta + C^\varepsilon V_\mathrm{I} \end{array}, \tag{4.21}$$

where $Y^E I = K_\theta^E a$. Figure 4.11 shows that a bending moment $M_\mathrm{R} + e_\theta V_\mathrm{I}$ is applied on the right side of the beam segment and a bending moment $-(M_\mathrm{L} + e_\theta V_\mathrm{I})$ is applied on its left side. We can thus consider a modified bending variable $M(x) + e_\theta V_\mathrm{I}$ which is equal to $Y^E I \theta'(x)$, so it does not depend on the electrical state anymore. A purely mechanical transfer matrix $\boldsymbol{T_m}$ is then used to described the relation between the dimensionless forces and displacements at both ends as

$$\begin{bmatrix} W_\mathrm{R}^\star \\ \theta_\mathrm{R}^\star \\ M_\mathrm{R}^\star + \Lambda V_\mathrm{I}^\star \\ Q_\mathrm{R}^\star \end{bmatrix} = \boldsymbol{T_m} \begin{bmatrix} W_\mathrm{L}^\star \\ \theta_\mathrm{L}^\star \\ M_\mathrm{L}^\star + \Lambda V_\mathrm{I}^\star \\ Q_\mathrm{L}^\star \end{bmatrix}, \quad \text{where} \quad V_\mathrm{I}^\star = \frac{C^\varepsilon}{e_\theta} V_\mathrm{I}. \tag{4.22}$$

As we focus on a homogeneous Euler-Bernouilli beam segment, $\boldsymbol{T_m}$ is the transfer matrix in Eq. (4.7) with $k = \sqrt[4]{\rho S \omega^2 / Y^E I}$ and $\rho S = m/a$.

Concerning the electrical medium which is unchanged, note from Fig. 4.10 that

$$V_\mathrm{I}^\star = \begin{bmatrix} 0 & 0 & 1 & -\frac{1}{2} \end{bmatrix} \begin{bmatrix} q_{w\mathrm{L}}^\star \\ q_{\theta\mathrm{L}}^\star \\ V_{\theta\mathrm{L}}^\star \\ V_{w\mathrm{L}}^\star \end{bmatrix}. \tag{4.23}$$

Furthermore, Fig. 4.10 shows that the electrical propagation results from the superposition of a purely electrical contribution, involving an electrical transfer matrix $\boldsymbol{T_e}$, and a second

contribution due to the coupling e_θ:

$$\begin{bmatrix} q_{w_{\mathrm{R}}}^\star \\ q_{\theta_{\mathrm{R}}}^\star \\ V_{\theta_{\mathrm{R}}}^\star \\ V_{w_{\mathrm{R}}}^\star \end{bmatrix} = \boldsymbol{T_e} \begin{bmatrix} q_{w_{\mathrm{L}}}^\star \\ q_{\theta_{\mathrm{L}}}^\star \\ V_{\theta_{\mathrm{L}}}^\star \\ V_{w_{\mathrm{L}}}^\star \end{bmatrix} + (\theta_{\mathrm{L}}^\star - \theta_{\mathrm{R}}^\star) \begin{bmatrix} \frac{1}{2} \\ 1 \\ 0 \\ 0 \end{bmatrix}, \quad \text{where} \quad \boldsymbol{T_e} = \begin{bmatrix} 1 & 1 & -\frac{1}{2} & \frac{1}{4} \\ 0 & 1 & -1 & \frac{1}{2} \\ -\frac{\hat{f}}{2} & -\frac{\hat{f}}{4} & 1 & -1 \\ \hat{f} & \frac{\hat{f}}{2} & 0 & 1 \end{bmatrix}. \tag{4.24}$$

We remark that $\boldsymbol{T_e}$ is similar to the transfer matrix of the lattice model in Eq. (4.11) because the considered electrical network is the analogue of a discretized beam. Combining Eqs. (4.22), (4.23) and (4.24) leads to the matrix form

$$\begin{bmatrix} \boldsymbol{I_4} & \boldsymbol{0_4} \\ \begin{bmatrix} \begin{bmatrix} 0 & \frac{1}{2} \\ 0 & 1 \end{bmatrix} \boldsymbol{0_2} \\ \boldsymbol{0_2} \quad \boldsymbol{0_2} \end{bmatrix} & \boldsymbol{I_4} \end{bmatrix} \begin{bmatrix} W_{\mathrm{R}}^\star \\ \theta_R^\star \\ M_{\mathrm{R}}^\star \\ Q_{\mathrm{R}}^\star \\ q_{w_{\mathrm{R}}}^\star \\ q_{\theta_{\mathrm{R}}}^\star \\ V_{\theta_{\mathrm{R}}}^\star \\ V_{w_{\mathrm{R}}}^\star \end{bmatrix} = \begin{bmatrix} \boldsymbol{T_m} & \Lambda\left(\boldsymbol{T_m} - \boldsymbol{I_4}\right) \begin{bmatrix} \boldsymbol{0_2} & \boldsymbol{0_2} \\ \boldsymbol{0_2} & \begin{bmatrix} 1 & -\frac{1}{2} \\ 0 & 0 \end{bmatrix} \end{bmatrix} \\ \begin{bmatrix} \begin{bmatrix} 0 & \frac{1}{2} \\ 0 & 1 \end{bmatrix} \boldsymbol{0_2} \\ \boldsymbol{0_2} \quad \boldsymbol{0_2} \end{bmatrix} & \boldsymbol{T_e} \end{bmatrix} \begin{bmatrix} W_{\mathrm{L}}^\star \\ \theta_{\mathrm{L}}^\star \\ M_{\mathrm{L}}^\star \\ Q_{\mathrm{L}}^\star \\ q_{w_{\mathrm{L}}}^\star \\ q_{\theta_{\mathrm{L}}}^\star \\ V_{\theta_{\mathrm{L}}}^\star \\ V_{w_{\mathrm{L}}}^\star \end{bmatrix}, \tag{4.25}$$

which can be reorganized into

$$\begin{bmatrix} W_{\mathrm{R}}^\star \\ \theta_R^\star \\ M_{\mathrm{R}}^\star \\ Q_{\mathrm{R}}^\star \\ q_{w_{\mathrm{R}}}^\star \\ q_{\theta_{\mathrm{R}}}^\star \\ V_{\theta_{\mathrm{R}}}^\star \\ V_{w_{\mathrm{R}}}^\star \end{bmatrix} = \begin{bmatrix} \boldsymbol{T_m} & \Lambda\left(\boldsymbol{T_m} - \boldsymbol{I_4}\right) \begin{bmatrix} \boldsymbol{0_2} & \boldsymbol{0_2} \\ \boldsymbol{0_2} & \begin{bmatrix} 1 & -\frac{1}{2} \\ 0 & 0 \end{bmatrix} \end{bmatrix} \\ -\begin{bmatrix} \begin{bmatrix} 0 & \frac{1}{2} \\ 0 & 1 \end{bmatrix} \boldsymbol{0_2} \\ \boldsymbol{0_2} \quad \boldsymbol{0_2} \end{bmatrix} \left(\boldsymbol{T_m} - \boldsymbol{I_4}\right) & \boldsymbol{T_e'} \end{bmatrix} \begin{bmatrix} W_{\mathrm{L}}^\star \\ \theta_{\mathrm{L}}^\star \\ M_{\mathrm{L}}^\star \\ Q_{\mathrm{L}}^\star \\ q_{w_{\mathrm{L}}}^\star \\ q_{\theta_{\mathrm{L}}}^\star \\ V_{\theta_{\mathrm{L}}}^\star \\ V_{w_{\mathrm{L}}}^\star \end{bmatrix}, \tag{4.26}$$

where $\boldsymbol{I_4}$ is a 4×4 identity matrix, $\boldsymbol{0_4}$ is a 4×4 zero matrix, $\boldsymbol{0_2}$ is a 2×2 zero matrix and

$$\boldsymbol{T_e'} = \boldsymbol{T_e} - \Lambda \begin{bmatrix} \begin{bmatrix} 0 & \frac{1}{2} \\ 0 & 1 \end{bmatrix} \boldsymbol{0_2} \\ \boldsymbol{0_2} \quad \boldsymbol{0_2} \end{bmatrix} \left(\boldsymbol{T_m} - \boldsymbol{I_4}\right) \begin{bmatrix} \boldsymbol{0_2} & \boldsymbol{0_2} \\ \boldsymbol{0_2} & \begin{bmatrix} 1 & -\frac{1}{2} \\ 0 & 0 \end{bmatrix} \end{bmatrix}. \tag{4.27}$$

In the end, Eq. (4.26) is the transfer matrix formulation giving the relation between the displacements, electric charges, forces and voltages at both ends of a unit cell involving a homogenized mechanical medium. Note that permutations are required to get the same form as in Eqs. (4.20), involving "displacement" and "force" state vectors $\boldsymbol{q} = [W^\star\ \theta^\star\ q_w^\star\ q_\theta^\star]^T$ and $\boldsymbol{F} = [M^\star\ Q^\star\ V_\theta^\star\ V_w^\star]^T$.

4.4.3 Piecewise homogenized model for the beam segment

The previous homogenized model does not take into account the mechanical discontinuity induced by the addition of piezoelectric patches on the beam. This can be corrected by

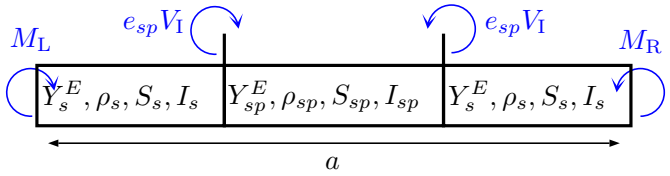

Figure 4.12: Piecewise homogenized model for the beam segment.

discriminating the purely elastic segments 's' from the segments 'sp' involving a piezoelectric contribution. The piecewise homogenized model is thus made of three beam segments, as presented in Fig. 4.12. In the 'sp' segment covered by the pair of piezoelectric patches, the problem can be expressed under a homogenized form similar to Eq. (4.21):

$$\begin{array}{l} M_{\mathrm{sp}}(x) = Y_{\mathrm{sp}}^E I_{\mathrm{sp}} \theta_{\mathrm{p}}'(x) - e_{\mathrm{sp}} V_{\mathrm{I}} \\ q_{\mathrm{I}} = e_{\mathrm{sp}} \Delta\theta_{\mathrm{p}} + C_{\mathrm{sp}}^{\varepsilon} V_{\mathrm{I}} \end{array} , \quad \text{where} \quad Y_{\mathrm{sp}}^E I_{\mathrm{sp}} = Y_{\mathrm{s}} I_{\mathrm{s}} + 2 Y_{\mathrm{p}}^E I_{\mathrm{p}}. \tag{4.28}$$

The 'sp' constants appearing in the previous system of equations are not equal to the ones in Eq. (4.21) because they refer to the central segment of the unit cell, without considering the purely elastic segments. Nevertheless, e_{sp} and $C_{\mathrm{sp}}^{\varepsilon}$ can be calculated with the same method as in Eq. (4.17) by considering a global stiffness that refers to the sole 'sp' segment.

As the one-dimensional problem focusing on the 'sp' beam segment is equivalent to the previous homogenized model, a 8×8 transfer matrix $\boldsymbol{T}_{\mathrm{sp}}$ is built on the same form as Eq. (4.26) but with homogenized constants referring to the 'sp' segment. The two 's' beam segments are purely elastic, so their 4×4 mechanical transfer matrices $\boldsymbol{T}_{\mathrm{s}}$ are similar to $\boldsymbol{T_m}$ but with the use of the constants Y_{s}, ρ_{s}, S_{s} and I_{s}. As a result, the piecewise homogenized model of the electromechanical unit cell is given by

$$\begin{bmatrix} W_{\mathrm{R}}^{\star} \\ \theta_{\mathrm{R}}^{\star} \\ M_{\mathrm{R}}^{\star} \\ Q_{\mathrm{R}}^{\star} \\ q_{w\mathrm{R}}^{\star} \\ q_{\theta\mathrm{R}}^{\star} \\ V_{\theta\mathrm{R}}^{\star} \\ V_{w\mathrm{R}}^{\star} \end{bmatrix} = \begin{bmatrix} \boldsymbol{T}_{\mathrm{s}} & \boldsymbol{0} \\ \boldsymbol{0} & \boldsymbol{I_4} \end{bmatrix} \boldsymbol{T}_{\mathrm{sp}} \begin{bmatrix} \boldsymbol{T}_{\mathrm{s}} & \boldsymbol{0} \\ \boldsymbol{0} & \boldsymbol{I_4} \end{bmatrix} \begin{bmatrix} W_{\mathrm{L}}^{\star} \\ \theta_{\mathrm{L}}^{\star} \\ M_{\mathrm{L}}^{\star} \\ Q_{\mathrm{L}}^{\star} \\ q_{w\mathrm{L}}^{\star} \\ q_{\theta\mathrm{L}}^{\star} \\ V_{\theta\mathrm{L}}^{\star} \\ V_{w\mathrm{L}}^{\star} \end{bmatrix}. \tag{4.29}$$

As for the homogenized model, the present formulation is based on a distinction between groups of mechanical and electrical variables, which defines the arrangement of the state vectors. Again, simple permutations allow presenting the problem under a form highlighting "force" and "displacement" vectors, as proposed in Eq. (4.20).

4.4.4 Finite element model

A convenient finite element model was proposed by Thomas et al. [70, 79], who focused on thin piezoelectric patches shunted with independent electrical circuits. The model is based on a condensation of the electrical degrees of freedom in order to recast the system into a standard elastic vibration problem. However, as mentioned in Chap. 3, this method is not applicable when considering connections of different patches with an electrical network. There are electrical nodes that interconnect successive unit cells, which means that the corresponding electrical degrees of freedom cannot be condensed. Before condensation, the finite element formulation is expressed as follows

$$\begin{bmatrix} \boldsymbol{M_m} & \mathbf{0} \\ \mathbf{0} & 0 \end{bmatrix} \begin{bmatrix} \ddot{\boldsymbol{q}}_{\boldsymbol{m}} \\ \ddot{V}_{\mathrm{I}} \end{bmatrix} + \begin{bmatrix} \boldsymbol{K_m} & \boldsymbol{K_c} \\ -\boldsymbol{K_c}^{\boldsymbol{T}} & C_{\mathrm{sp}}^{\varepsilon} \end{bmatrix} \begin{bmatrix} \boldsymbol{q_m} \\ V_{\mathrm{I}} \end{bmatrix} = \begin{bmatrix} \boldsymbol{F_m} \\ q_{\mathrm{I}} \end{bmatrix}, \tag{4.30}$$

where $\boldsymbol{M_m}$, $\boldsymbol{K_m}$ and $\boldsymbol{K_c}$ are respectively the mass, stiffness and coupling matrices defined in Appendix B. The capacitance $C_{\mathrm{sp}}^{\varepsilon}$ is used in the one dimensional model because it has to represent the piezoelectric capacitance when no bending motion is allowed. The electric charge q_{I} flowing toward the pair of piezoelectric patches is obtained from the topology of the analogous network in Fig. 4.10 as

$$q_{\mathrm{I}} = \boldsymbol{S_q q_e} \quad \text{where} \quad \boldsymbol{S_q} = \begin{bmatrix} 0 & 1 & 0 & -1 \end{bmatrix} \quad \text{and} \quad \boldsymbol{q_e} = \begin{bmatrix} q_{w\mathrm{L}} & q_{\theta\mathrm{L}} & q_{w\mathrm{R}} & q_{\theta\mathrm{R}} \end{bmatrix}^T. \tag{4.31}$$

By analogy with the force vector $\boldsymbol{F_m}$ and the displacement vector $\boldsymbol{q_m}$, the voltage vector $\boldsymbol{F_e} = \begin{bmatrix} V_{w\mathrm{L}} & V_{\theta\mathrm{L}} & -V_{w\mathrm{R}} & -V_{\theta\mathrm{R}} \end{bmatrix}^T$ is defined as the dual of the electric charge vector $\boldsymbol{q_e}$. The principle of superposition allows considering that the voltage vector $\boldsymbol{F_e}$ is a sum of two contributions. The first contribution is obtained when no mechanical displacement is allowed ($\boldsymbol{q_m} = \mathbf{0}$) and the second contribution excludes external charge displacements ($\boldsymbol{q_e} = \mathbf{0}$), then $\boldsymbol{F_e} = \boldsymbol{F_e^e} + \boldsymbol{F_e^m}$. The purely electrical contribution $\boldsymbol{F_e^e}$ only depends on the choice of the electrical network. Similarly to established practices in mechanical problems, we define the electrical matrices $\boldsymbol{K_e}$ and $\boldsymbol{M_e}$ as equivalents of stiffness and mass matrices:

$$\boldsymbol{F_e^e} = \left[\boldsymbol{K_e} - \omega^2 \boldsymbol{M_e}\right] \boldsymbol{q_e}. \tag{4.32}$$

When considering the electrical analogue of a beam, $\boldsymbol{M_e}$ can be found from the network in Fig. 4.10 with $e_\theta = 0$ and no "electrical stiffness", which means a piezoelectric capacitance that goes to infinity, so that $V_{\mathrm{I}} = 0$. We thus get

$$\boldsymbol{M_e} = \frac{L}{2} \begin{bmatrix} 1 & \hat{a}/2 & 0 & 0 \\ \hat{a}/2 & \hat{a}^2/4 & 0 & 0 \\ 0 & 0 & 1 & -\hat{a}/2 \\ 0 & 0 & -\hat{a}/2 & \hat{a}^2/4 \end{bmatrix}. \tag{4.33}$$

Yet, the matrix $\boldsymbol{K_e}$ cannot be obtained directly from Fig. 4.10 with $e_\theta = 0$ and no "electrical mass", i.e. $L = 0$. Actually, $\boldsymbol{K_e}$ is not defined, unless we introduce additional degrees

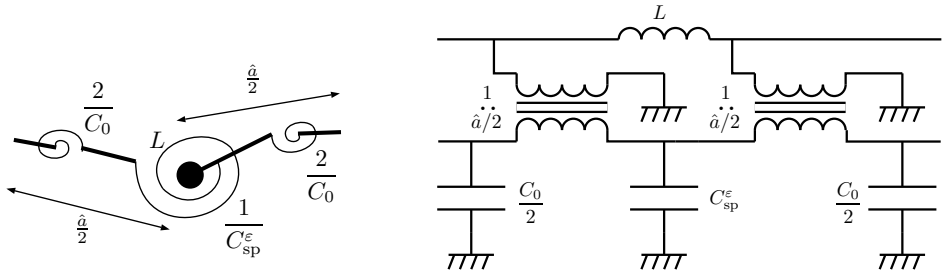

Figure 4.13: Additional compliance to allow the definition of a stiffness matrix: (a) Modified unit cell in the mechanical domain. (b) Modified unit cell in the electrical domain.

of freedom. This can be understood by looking at the lattice model in Fig. 4.2, where the displacements and angles at both ends of the unit cell cannot be chosen independently because the kinematics enforces $W_{\mathrm{R}} - W_{\mathrm{L}} = \frac{a}{2}(\theta_{\mathrm{L}} + \theta_{\mathrm{R}})$. This constraint is relaxed by adding compliance through springs $2/C_0$, as seen in Fig. 4.13(a). Then, if the additional springs $2/C_0$ are close to the ends of the unit cell, the electrical analogue is represented in Fig. 4.13(b) with capacitors $C_0/2$ at both ends of the 'θ' electrical line, which adds two electrical degrees of freedom. The "stiffness" matrix $\boldsymbol{K_e}$ of this modified electrical unit cell is thus obtained by setting $L = 0$ in Fig. 4.13(b) or by considering the static stiffness matrix of the mechanical unit cell in Fig. 4.13(a). In any case, one finds that

$$\boldsymbol{K_e} = \frac{4}{\hat{a}^2 C_0} \begin{bmatrix} 1 & \frac{\hat{a}}{2} & -1 & \frac{\hat{a}}{2} \\ \frac{\hat{a}}{2} & \frac{\hat{a}^2}{4}\frac{C_{\mathrm{sp}}^{\varepsilon}+2C_0}{C_{\mathrm{sp}}^{\varepsilon}+C_0} & -\frac{\hat{a}}{2} & \frac{\hat{a}^2}{4}\frac{C_{\mathrm{sp}}^{\varepsilon}}{C_{\mathrm{sp}}^{\varepsilon}+C_0} \\ -1 & -\frac{\hat{a}}{2} & 1 & -\frac{\hat{a}}{2} \\ \frac{\hat{a}}{2} & \frac{\hat{a}^2}{4}\frac{C_{\mathrm{sp}}^{\varepsilon}}{C_{\mathrm{sp}}^{\varepsilon}+C_0} & -\frac{\hat{a}}{2} & \frac{\hat{a}^2}{4}\frac{C_{\mathrm{sp}}^{\varepsilon}+2C_0}{C_{\mathrm{sp}}^{\varepsilon}+C_0} \end{bmatrix}. \tag{4.34}$$

Note that the capacitance C_0 is a numerical parameter that has to be small compared to $C_{\mathrm{sp}}^{\varepsilon}$. A good practice is to set C_0 between $C_{\mathrm{sp}}^{\varepsilon} \times 10^{-3}$ and $C_{\mathrm{sp}}^{\varepsilon} \times 10^{-9}$ to conceal its influence on electrical propagation and to avoid numerical issues.

The contribution $\boldsymbol{F_e^m}$ is equal to $\boldsymbol{F_e}$ when $\boldsymbol{q_e} = \boldsymbol{0}$. Fig. 4.10 shows that $\boldsymbol{q_e} = \boldsymbol{0}$ induces that $q_{\mathrm{I}} = 0$. Then, $q_{\mathrm{I}} = 0$ means that $V_{w\mathrm{L}} = V_{w\mathrm{R}} = 0$ and $V_{\theta\mathrm{L}} = V_{\theta\mathrm{R}} = V_{\mathrm{I}}$. Furthermore, Eq. (4.30) gives $V_{\mathrm{I}} = \boldsymbol{K_c}^{\boldsymbol{T}}\boldsymbol{q_m}/C_{\mathrm{sp}}^{\varepsilon}$ when $q_{\mathrm{I}} = 0$. As a consequence,

$$\boldsymbol{F_e^m} = \frac{1}{C_{\mathrm{sp}}^{\varepsilon}}\boldsymbol{S_V}\boldsymbol{K_c}^{\boldsymbol{T}}\boldsymbol{q_m} \quad \text{where} \quad \boldsymbol{S_V} = \begin{bmatrix} 0 & 1 & 0 & -1 \end{bmatrix}^T = \boldsymbol{S_q}^T. \tag{4.35}$$

Finally, Eqs. (4.30), (4.31), (4.32) and (4.35) lead to the following dynamic stiffness matrix involving a combination of mechanical and electrical degrees of freedom similar to what

has been found in Chap. 3 with a simpler electrical network:

$$\left[\begin{bmatrix} \boldsymbol{K_m} + \frac{1}{C^{\varepsilon}_{\mathrm{sp}}}\boldsymbol{K_c}\boldsymbol{K_c}^{\boldsymbol{T}} & \frac{1}{C^{\varepsilon}_{\mathrm{sp}}}\boldsymbol{K_c}\boldsymbol{S_q} \\ \frac{1}{C^{\varepsilon}_{\mathrm{sp}}}(\boldsymbol{K_c}\boldsymbol{S_q})^{\boldsymbol{T}} & \boldsymbol{K_e} \end{bmatrix} - \omega^2 \begin{bmatrix} \boldsymbol{M_m} & \boldsymbol{0} \\ \boldsymbol{0} & \boldsymbol{M_e} \end{bmatrix}\right] \begin{bmatrix} \boldsymbol{q_m} \\ \boldsymbol{q_e} \end{bmatrix} = \begin{bmatrix} \boldsymbol{F_m} \\ \boldsymbol{F_e} \end{bmatrix}. \quad (4.36)$$

With a restriction to the transverse case, $\boldsymbol{q_m} = \begin{bmatrix} W_{\mathrm{L}} & \theta_{\mathrm{L}} & \boldsymbol{q}_{\mathrm{I}} & W_{\mathrm{R}} & \theta_{\mathrm{R}} \end{bmatrix}^T$ and $\boldsymbol{F_m} = \begin{bmatrix} -Q_{\mathrm{L}} & -M_{\mathrm{L}} & \boldsymbol{0} & Q_{\mathrm{R}} & M_{\mathrm{R}} \end{bmatrix}^T$, where $\boldsymbol{q}_{\mathrm{I}}$ is the mechanical displacement vector of the internal nodes of the unit cell. The dynamic stiffness matrix in Eq. (4.36) can be reorganized in order to distinguish the left, right and internal degrees of freedom as

$$\begin{bmatrix} \tilde{\boldsymbol{D}}_{\boldsymbol{LL}} & \tilde{\boldsymbol{D}}_{\boldsymbol{LI}} & \tilde{\boldsymbol{D}}_{\boldsymbol{LR}} \\ \tilde{\boldsymbol{D}}_{\boldsymbol{IL}} & \tilde{\boldsymbol{D}}_{\boldsymbol{II}} & \tilde{\boldsymbol{D}}_{\boldsymbol{IR}} \\ \tilde{\boldsymbol{D}}_{\boldsymbol{RL}} & \tilde{\boldsymbol{D}}_{\boldsymbol{RI}} & \tilde{\boldsymbol{D}}_{\boldsymbol{RR}} \end{bmatrix} \begin{bmatrix} \boldsymbol{q}_{\mathrm{L}} \\ \boldsymbol{q}_{\mathrm{I}} \\ \boldsymbol{q}_{\mathrm{R}} \end{bmatrix} = \begin{bmatrix} \boldsymbol{F}_{\mathrm{L}} \\ \boldsymbol{0} \\ \boldsymbol{F}_{\mathrm{R}} \end{bmatrix}, \text{ where } \boldsymbol{F}_{\mathrm{L}} = \begin{bmatrix} -Q_{\mathrm{L}} \\ -M_{\mathrm{L}} \\ V_{w\mathrm{L}} \\ V_{\theta\mathrm{L}} \end{bmatrix}, \ \boldsymbol{F}_{\mathrm{R}} = \begin{bmatrix} Q_{\mathrm{R}} \\ M_{\mathrm{R}} \\ -V_{w\mathrm{R}} \\ -V_{\theta\mathrm{R}} \end{bmatrix}, \quad (4.37)$$

$\boldsymbol{q}_{\mathrm{L}} = \begin{bmatrix} W_{\mathrm{L}} & \theta_{\mathrm{L}} & q_{w\mathrm{L}} & q_{\theta\mathrm{L}} \end{bmatrix}^T$ and $\boldsymbol{q}_{\mathrm{R}} = \begin{bmatrix} W_{\mathrm{R}} & \theta_{\mathrm{R}} & q_{w\mathrm{R}} & q_{\theta\mathrm{R}} \end{bmatrix}^T$. With this partitioning, the Wave Finite Element Method [106–108] can be applied. First, the internal degrees of freedoms are condensed through

$$\begin{bmatrix} \boldsymbol{D_{LL}} & \boldsymbol{D_{LR}} \\ \boldsymbol{D_{RL}} & \boldsymbol{D_{RR}} \end{bmatrix} \begin{bmatrix} \boldsymbol{q}_{\mathrm{L}} \\ \boldsymbol{q}_{\mathrm{R}} \end{bmatrix} = \begin{bmatrix} \boldsymbol{F}_{\mathrm{L}} \\ \boldsymbol{F}_{\mathrm{R}} \end{bmatrix}, \quad \text{where} \quad \begin{array}{l} \boldsymbol{D_{LL}} = \tilde{\boldsymbol{D}}_{\boldsymbol{LL}} - \tilde{\boldsymbol{D}}_{\boldsymbol{LI}}\tilde{\boldsymbol{D}}_{\boldsymbol{II}}^{-\boldsymbol{1}}\tilde{\boldsymbol{D}}_{\boldsymbol{IL}} \\ \boldsymbol{D_{LR}} = \tilde{\boldsymbol{D}}_{\boldsymbol{LR}} - \tilde{\boldsymbol{D}}_{\boldsymbol{LI}}\tilde{\boldsymbol{D}}_{\boldsymbol{II}}^{-\boldsymbol{1}}\tilde{\boldsymbol{D}}_{\boldsymbol{IR}} \\ \boldsymbol{D_{RL}} = \tilde{\boldsymbol{D}}_{\boldsymbol{RL}} - \tilde{\boldsymbol{D}}_{\boldsymbol{RI}}\tilde{\boldsymbol{D}}_{\boldsymbol{II}}^{-\boldsymbol{1}}\tilde{\boldsymbol{D}}_{\boldsymbol{IL}} \\ \boldsymbol{D_{RR}} = \tilde{\boldsymbol{D}}_{\boldsymbol{RR}} - \tilde{\boldsymbol{D}}_{\boldsymbol{RI}}\tilde{\boldsymbol{D}}_{\boldsymbol{II}}^{-\boldsymbol{1}}\tilde{\boldsymbol{D}}_{\boldsymbol{IR}} \end{array}. \quad (4.38)$$

Then, the resulting condensed dynamic stiffness matrix is transformed into a transfer matrix [46, 106]:

$$\begin{bmatrix} W_{\mathrm{R}} \\ \theta_{\mathrm{R}} \\ q_{w\mathrm{R}} \\ q_{\theta\mathrm{R}} \\ Q_{\mathrm{R}} \\ M_{\mathrm{R}} \\ -V_{w\mathrm{R}} \\ -V_{\theta\mathrm{R}} \end{bmatrix} = \begin{bmatrix} -\boldsymbol{D_{LR}^{-1}}\boldsymbol{D_{LL}} & \boldsymbol{D_{LR}^{-1}} \\ -\boldsymbol{D_{RL}} + \boldsymbol{D_{RR}}\boldsymbol{D_{LR}^{-1}}\boldsymbol{D_{LL}} & -\boldsymbol{D_{RR}}\boldsymbol{D_{LR}^{-1}} \end{bmatrix} \begin{bmatrix} W_{\mathrm{L}} \\ \theta_{\mathrm{L}} \\ q_{w\mathrm{L}} \\ q_{\theta\mathrm{L}} \\ Q_{\mathrm{L}} \\ M_{\mathrm{L}} \\ -V_{w\mathrm{L}} \\ -V_{\theta\mathrm{L}} \end{bmatrix}. \quad (4.39)$$

The signs and the positions of the variables in the state vectors are the result of the analogy between the mechanical and electrical part of the coupled problem. The state vectors are easily reorganized through permutations, which have been combined with the computing of a dimensionless transfer matrix.

4.4.5 Model comparison for large wavelength

The models are first compared over a frequency range where the wavelength is at least four times longer than the length of a unit cell. Frequency response functions are computed

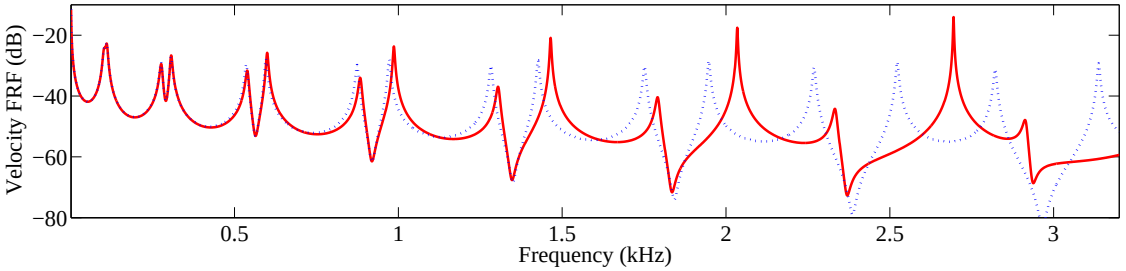

Figure 4.14: Velocity FRFs - (···) for the discrete model, (—) for the piecewise homogenized model.

for a one meter free-free beam, which is periodically covered with 20 pairs of piezoelectric patches. The finite electromechanical structure thus consists of $n = 20$ identical unit cells as defined in Table 4.1. Regarding the electrical network, the transformer ratio $\hat{a}$ is set arbitrarily to 1 and the inductance value is tuned to $L = a^2 m/(\hat{a}^2 K_\theta^E C^\varepsilon) = 200$ mH in order to satisfy the multimodal coupling condition defined in Eq. (4.18). This condition induces that the electrical network approximates the dispersion relation of the beam, which is required to implement the analogous coupling. Then, a resistance $R_s^L = 20\ \Omega$ is added in series with the inductors by replacing L by $L - \mathrm{j}R_s^L/\omega$. The only external excitation is a transverse force at one end of the beam. All the other forces, moments and voltages at the ends of the structure are equal to zero. Indeed, the two electrical lines of the network are short-circuited at both ends in order to satisfy analogous boundary conditions. Once the mechanical and electrical characteristics are defined, the four transfer matrix models in Eqs.(4.20), (4.26), (4.29) and (4.39) are compared. The Ricatti transfer matrix method presented in Chap. 3 is applied in order to compute the FRFs representing the ratio of the velocity at one end over the excitation force at the other end.

The finite element model tends to the piecewise homogenized model when increasing the number of elements. Furthermore, the results obtained with the fully homogenized model are very close to those of the piecewise homogenized model over the frequency range of interest. This is the reason why only the FRFs obtained with the discrete and the piecewise homogenized model are represented in Fig. 4.14, from 1 Hz to 3.2 kHz. This frequency range covers the first seven bending modes of the beam when no coupling occurs. The resistance $R_s^L = 20\ \Omega$ has been chosen to minimize the maximum velocity around the first bending mode. As obtained with a rod in Chap. 3, an antiresonance surrounded by two new resonances appears around the initial natural frequencies. The equivalent of a tuned mass damping is thus implemented on several modes together, which validates the modal coupling condition (4.18).

Note that the discrete model is no more reliable when the frequency is increased,

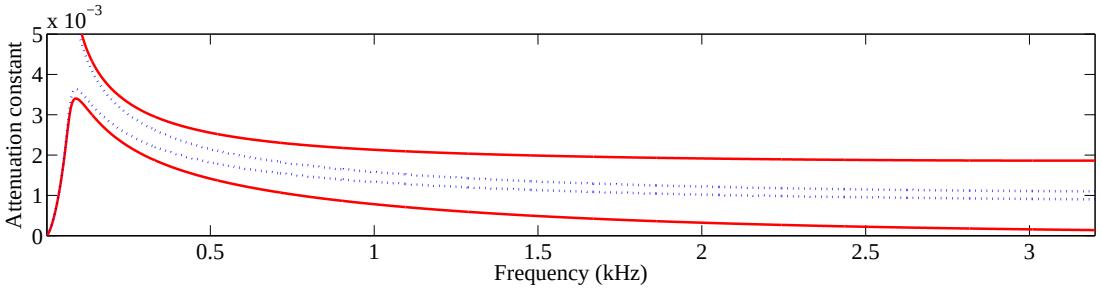

Figure 4.15: Attenuation constants - (···) for the discrete model, (—) for the piecewise homogenized model.

i.e. when the wavelength is shortened. For the present example, a limit of validity can be set to 1 kHz, which corresponds to about 10 unit cells per wavelength. With the discrete model, the positions of the mechanical resonances are shifted because the mechanical medium is modeled by a lattice. Thus, it does not take into account the increasing mistuning between the continuous and the discrete media. Depending on the application, the discrete model can still be sufficient as long as the number of unit cells per wavelength is high enough. For example, the error observed around the fourth mode would have been insignificant for a structure made of $n = 40$ unit cells. The difference between the discrete model and the piecewise homogenized model is even more evident when looking at their two lowest attenuation constants shown in Fig. 4.15. With the discrete model, none of the attenuation constants tends to zero, which means that no wave can freely propagate. On the contrary, one of the attenuation constants of the piecewise homogenized model tends to zero and this is the result of the detuning between the discrete electrical network and the continuous beam. This inherent detuning between two structures of different natures brings that the efficiency of the control strategy is reduced when going to high frequencies, which is in agreement with the results in Fig 4.14.

4.4.6 Model comparison for short wavelength

When looking at wavelength approaching the length of the unit cell, the finite element model still tends to the piecewise homogenized model, but the fully homogenized model exhibits a different response. Indeed, the effect of the mechanical discontinuity induced by the addition of piezoelectric patches creates a stop band for bending propagation in the beam [4, 46, 48, 88, 102]. This occurs when the wavelength becomes smaller than two times the length of a unit cell ($ka = \pi$), which here occurs between 18 and 19 kHz. The computation of the lowest propagation constants in Figs. 4.16 and 4.17 highlights the stop band and the difference between the piecewise and fully homogenized models. Surprisingly, we also note a stop band with the fully homogenized model. This is explained by the

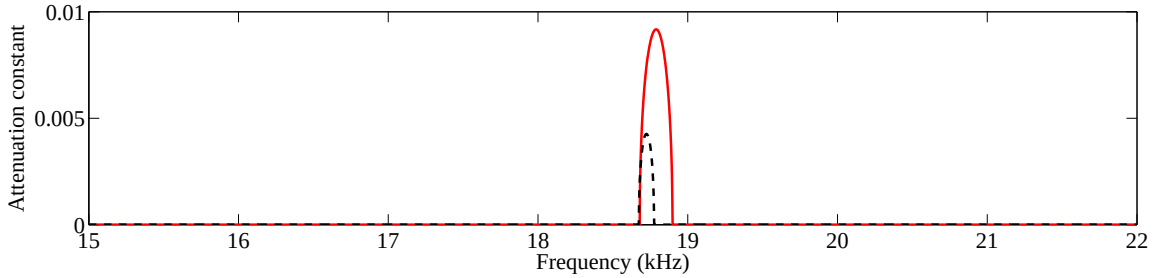

Figure 4.16: Attenuation constants - (−−) for the fully homogenized model, (—) for the piecewise homogenized model.

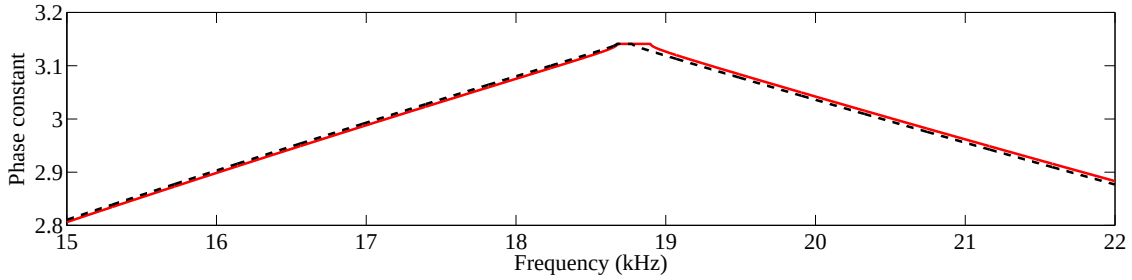

Figure 4.17: Phase constants - (−−) for the fully homogenized model, (—) for the piecewise homogenized model.

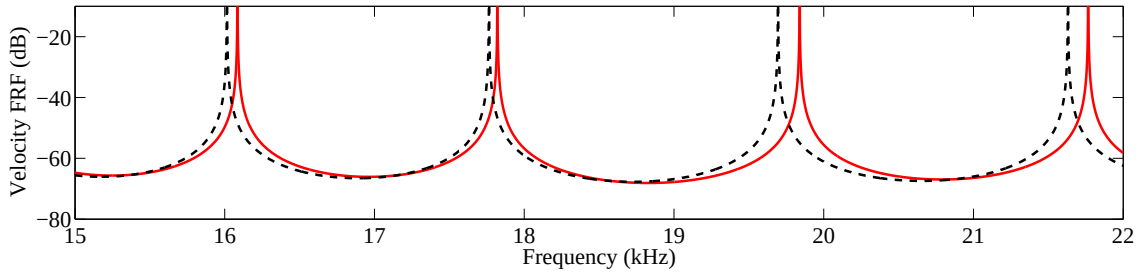

Figure 4.18: Velocity FRFs - (−−) for the homogenized model, (—) for the piecewise homogenized model.

fact that, even without considering structural discontinuity, the patches induce additional moments on both sides of the unit cell, as represented in Fig. 4.11. This generates a periodic discontinuity that leads to a moderate stop band effect. This stop band is not negligible compared to the one obtained with the piecewise homogenized model because the effect of the mechanical discontinuity is actually quite small in the present example. In the previous chapter, the stop band for longitudinal waves was significant with the same geometry, but a similar effect for bending wave would require a considerably thicker discontinuity. In conclusion, strong structural modifications would be needed in order to benefit from such stop bands for bending wave attenuation.

The frequency response functions in Fig. 4.18 confirm the effect of the stop band. There is already a slight difference in the positioning of the resonances below 18 kHz, but it is even more pronounced after the stop band, which is larger with the piecewise homogenized model. Nevertheless, the effect is quite negligible, especially when considering that the validity of the Euler-Bernoulli model is questionable at such high frequencies. It is also remarked that the considered frequency range is clearly beyond the last electrical resonance. No electrical propagation occurs above 7.5 kHz, similarly to what has been observed through the analysis of the lattice model in Fig. 4.5. So, the discrete electrical network does not influence the results above 7.5 kHz and the FRFs are essentially due to propagation in the mechanical waveguide.

4.5 Design of the analogous electrical network

The implementation of a multimodal damping through an analogous electrical network requires the choice of the number of elements involved in the array of piezoelectric patches. Moreover, we have to define suitable inclusions of resistors in the electrical network, so that it generates an actual broadband damping. From those results, magnetic transformers are designed according to their equivalent circuit model adapted to the present application.

4.5.1 Array of piezoelectric patches

When considering a distributed piezoelectric control, a first step is to determine the number of patches that will cover the mechanical structure to control. It has been shown in Sec. 4.2 that a suitable approximation of a continuous beam by a lattice model requires a minimum number of unit cells per wavelength. As a discrete electrical analogue reproduces the modes of the lattice model, it cannot perfectly match the modes of the continuous beam but it can provide a suitable approximation if the number of unit cells is high enough. With an insufficient number of patches, the electrical resonances would not match the corresponding mechanical modes and the multimodal control performances could be considerably reduced. This is observed in Fig. 4.19, where the influence of the number of unit cells is highlighted. The velocity FRFs are computed with the model based on a fully homogenized beam segment, as defined in Sec. 4.4. The accuracy of this model has been proven for sufficiently large wavelength compared to the unit cell and that is why it is used in the following calculations. The antiresonances are related to the resonances of the electrical network and they validate the efficiency of the multimodal coupling. Yet, we clearly note from the case involving 20 unit cells that the antiresonances are shifted to lower frequencies for the highest modes. This shows the limits of the discrete electrical network, which offers a suitable approximation of the beam modal properties for a

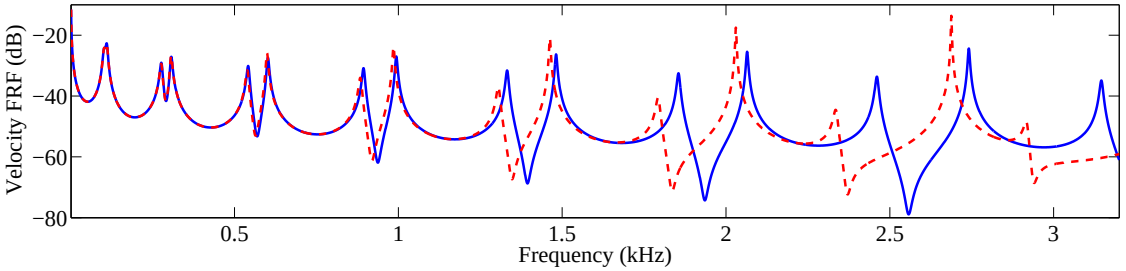

Figure 4.19: Velocity FRFs computed with a fully homogenized beam segment - (−−) with 20 unit cells, (—) with 40 unit cells.

limited number of modes only. With 40 unit cells, the discrete electrical network is still appropriate over the considered frequency range because the antiresonances stay approximately centered relatively to the resonances, even around 2.5 kHz. So, it is essential to determine the highest mode to control before defining the number of unit cells, i.e. the number of piezoelectric patches. For example, if we focus on the first four modes of the free-free beam (up to 1 kHz), 20 pairs of patches are enough. This corresponds to about 10 unit cells per wavelength for the fourth bending mode. This classical limit related to the discrete approximation can thus be used to define the minimum number of patches for an appropriate multimodal control.

Once the number of patches is chosen, the definition of their dimensions is related to the dimensions of the host structure. Actually, the capacitance of a piezoelectric patch C^{ϵ} is roughly proportional to its surface area A_{p} and inversely proportional to its thickness h_{p}. So, a recommendation to reduce the inductance requirements is to spread the piezoelectric material on the maximum surface area. The length a and the width b of the unit cell represents the maximum dimensions for the sides of the patches. Note that a minimum gap of a few millimeters between two patches is usually required in order to avoid practical issues related to the gluing process. Another solution that would facilitate the implementation of an array involving a high number of elements might be to create a set of transducers from a single piezoelectric patch by cutting the electrode layer periodically. The piezoelectric thickness h_{p} can be determined from an eventual limitation on the mass added to the main structure. The choice of the piezoelectric patches also depends on the dimensions offered by the manufacturers. Piezoelectric plates of sides up to 70 mm are usually available and can be cut into smaller pieces. The thickness selection is constrained by the standard dimensions offered by the manufacturers and 0.1 mm can be seen as a lower limit due to availability and difficult handling (risk of breakage). Regarding the choice of the material, the coupling factor k_{31} has to be maximized to improve damping performances. It is also recommended to choose a high permittivity material in order to increase the piezoelectric capacitance and then decrease the inductance requirements.

4.5.2 Optimal resistor positioning for a broadband damping

A reduction of vibration over a broad frequency range requires the tuning of the inductors but also the introduction of suitable damping components. A classical solution presented in most papers focusing on piezoelectric shunts is to add resistors in series with the inductors [2, 4, 43, 48, 49, 101, 102]. Another less common solution consist in connecting resistors in parallel with the inductors [15, 17, 26, 95, 99]. It then becomes possible to tune the resistors in order to reach a vibration reduction optimum, which is here defined as a minimum amplitude on the velocity FRF. However, even if for both damping strategies an optimum can be reached at one particular frequency, there is no reason to expect an optimal damping over a broad frequency range. A damping model was proposed by Porfiri et al. [21] to get a multimodal damping with the analogous network of a beam. The solution is to add resistors R_{s}^{T} in series with the windings of the transformers. This is presented on the network segment in Fig. 4.20, which also shows R_{s}^{L} and R_{p}^{L}, the series and parallel resistors on the inductors.

In Fig. 4.21, the three damping solutions are compared by computing the transfer matrix of the fully homogenized model in Eq. (4.26) with the effect of resistors added in Eqs. (4.23) and (4.24). The free-free coupled beam previously described in Table 4.1 is still the relevant case. The damping is considered optimal around one mode when the corresponding highest local maximum of the velocity FRF is reduced to its minimum value. We define as underdamped a mode where it can be seen a local minimum and overdamped thus corresponds to a case where there is no local minimum. Independently of the chosen damping model, the resistors are tuned to reach an optimum around the first initial mode of the beam. When the only damping contribution is in series with the inductors ($R_{\mathrm{s}}^{T} = 0\ \Omega$ and $R_{\mathrm{p}}^{L} \to +\infty$), $R_{\mathrm{s}}^{L} = 20\ \Omega$ leads to the maximal vibration reduction around the first mode but it also gives a clear underdamped behavior for higher

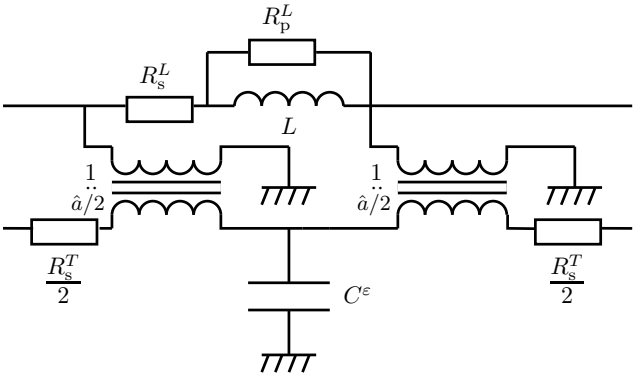

Figure 4.20: Electrical network segment including resistors.

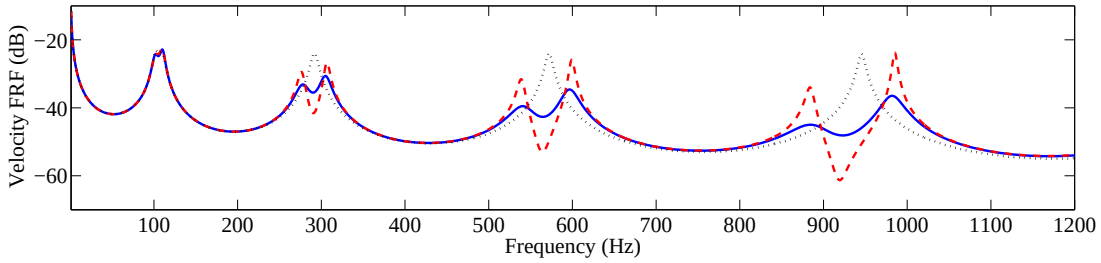

Figure 4.21: Velocity FRFs with an electrical network satisfying the modal coupling condition - (−−) with a series resistance $R_{\mathrm{s}}^{L} = 20\ \Omega$ on the inductors, $(\cdots)$ with a parallel resistance $R_{\mathrm{p}}^{L} = 1000\ \Omega$ on the inductors, (—) with a series resistance $R_{\mathrm{s}}^{T} = 150\ \Omega$ on the transformers.

modes. On the other hand, with $R_{\mathrm{p}}^{L} = 1000\ \Omega$, $R_{\mathrm{s}}^{L} = 0$ and $R_{\mathrm{s}}^{T} = 0$, the first mode is still optimized but the other ones are overdamped. At last, when $R_{\mathrm{s}}^{T} = 150\ \Omega$, $R_{\mathrm{s}}^{L} = 0$ and $R_{\mathrm{p}}^{L} \to +\infty$, it appears a slightly underdamped behavior around the first four modes. It is thus observed that the damping involving resistors in the transformer windings leads to highest vibration reduction around each mode.

Nevertheless, the damping is optimal only for the first mode, while it could be expected from [21] an optimal damping for all the modes together. The first reason is that this last reference focuses on an electrical continuum. The present work considers a discrete network, which cannot match exactly the modes of the continuous mechanical structure. This effect can be observed through the positions of the local maxima for which the asymmetry increases with the frequency. The second reason explaining why the present damping with R_{s}^{T} is not optimal is related to the boundary conditions. It was mentioned in [21] that the proposed optimal damping is only valid with boundary conditions ensuring global solutions represented by trigonometric eigenfunctions. This is true for a simply supported beam but not for the considered case of a free-free beam. Finally, although not optimal in a general case involving a finite number of patches and no trigonometric boundary conditions, the damping involving the resistance R_{s}^{T} remains a satisfactory sub-optimal solution compared to the other damping models. Depending on the choice of the electrical components, several equivalent resistors can be combined together but a recommendation would be to keep R_{s}^{T} as the main dissipative element.

4.5.3 Equivalent circuit model of a transformer

The passive electrical analogue of a beam involves ideal transformers. Yet, real magnetic transformers are usually far from ideal because of the parasitic effects related to their practical design. The equivalent circuit of a non-ideal transformer is represented in

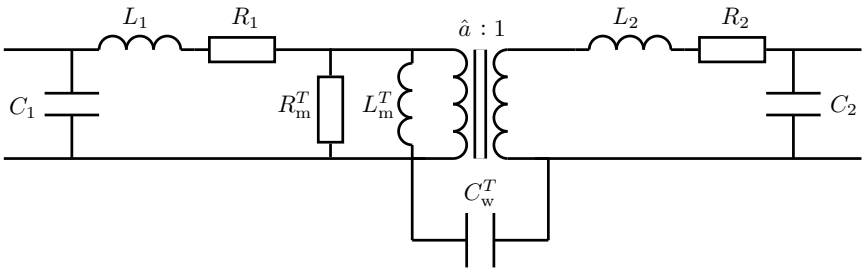

Figure 4.22: Equivalent circuit of a non-ideal transformer.

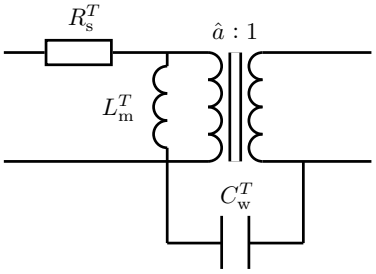

Figure 4.23: Simplified equivalent circuit of a non-ideal transformer.

Fig. 4.22 for a general case with no restrictions on the frequency range of interest [52, 53]. R_1 and R_2 are the direct-current resistance of the primary and secondary windings, while L_1 and L_2 corresponds to their leakage inductance. Furthermore, C_1 and C_2 are the primary and secondary winding capacitance. At last, C_{w}^T is the winding-to-winding capacitance, L_{m}^T is the magnetizing inductance and R_{m}^T is the core-loss resistance [52].

Considering real applications involving the electrical analogue of a beam, it has been remarked that, compared to the inductance L introduced in the network, the leakage inductance elements L_1 and L_2 are generally negligible and do not need to be modeled. Also, modeling the winding capacitance C_1 or C_2 is not required because the transformers have to be operated far below their self-resonance frequency [52]. A last simplification of the equivalent circuit concerns the damping elements. We have seen in the previous subsection that damping should be introduced through resistors in series with the transformers windings. Actually, no external resistors are required if the transformers are designed in order to offer a suitable direct-current resistance through R_1 and R_2. Then, for the present applications, it has been observed that the damping generated by the winding resistance (i.e. copper losses) significantly exceeds the damping in the magnetic core (i.e. iron losses). This means that R_{m}^T does not need to be modeled in the equivalent circuit of a transformer when dealing with the proposed examples on multimodal damping with an analogous electrical network. In the end, the equivalent circuit in Fig. 4.22 can be simplified into the circuit in Fig. 4.23. The resistance R_{s}^T takes into account the copper losses in

both windings because we note that $R_{\mathrm{s}}^T = R_1 + \hat{a}^2 R_2$ when the current flowing through the magnetizing inductance L_{m}^T is negligible compared to the current in the ideal transformer.

4.5.4 Design of transformers for the analogous network

The design of transformers requires to pay a close attention to the parasitic element R_{s}^T, C_{w}^T and L_{m}^T, which might ruin the analogous damping strategy if they are not chosen correctly. The segment of the analogous electrical network in Fig. 4.20 is updated by considering a non-ideal transformer and this leads to the circuit in Fig. 4.24. No damping element is represented around the inductor and we take advantage of the fact that, when connecting successive electrical unit cells, two transformers of ratio $\hat{a}/2$ can be replaced by a single transformer of ratio $\hat{a}$. Here, we thus focus on a non-symmetrical unit cell which is more representative of the practical implementation of the electrical network. In principle, the winding resistance R_{s}^T does not need to be minimized because it can be part of the damping optimization as shown previously when considering the resistor positioning for broadband damping. So, an optimal value for R_{s}^T can be defined from numerical optimizations, which means that external resistors are not required.

Regarding the winding-to-winding capacitance C_{w}^T, we note in Fig. 4.24 that it has one end connected to the ground and the other end connected to the piezoelectric capacitance C^{ε}. This is equivalent to two capacitors in parallel, which gives a total capacitance equal to $C^{\varepsilon} + C_{\mathrm{w}}^T$. As a consequence, the addition of a winding-to-winding capacitance in the transformers is equivalent to an increase of the piezoelectric capacitance. It has been shown that an increase of the capacitance decreases the piezoelectric coupling and thereby decreases the damping performance [7, 43, 79]. So, C_{w}^T has to be minimized by ensuring a sufficient electrical isolation between the primary and secondary windings when manufacturing the transformers.

The last parasitic element is the magnetizing inductance L_{m}^T that needs to be maximized in order to force the current to flow through the ideal transformer. The magnetizing

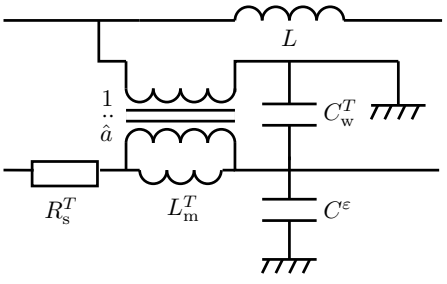

Figure 4.24: Non-ideal transformer in the analogous electrical network.

inductance L_{m}^{T} is in the 'θ' electrical line but it could also be represented on the other side of the transformer with a value $L_{\mathrm{m}}^{T}/\hat{a}^2$. Then, this inductance has to be considerably larger than L, so that it does not influence the electrical propagation. It has been remarked that setting $L_{\mathrm{m}}^{T}/\hat{a}^2 \geq 50L$ is generally enough for multimodal damping applications. From the modal coupling condition $L = a^2 m/(\hat{a}^2 K_{\theta}^{E} C^{\varepsilon})$, we get

$$L_{\mathrm{m}}^{T} \geq 50 \frac{a^2 m}{K_{\theta}^{E} C^{\varepsilon}}. \tag{4.40}$$

Actually, the piezoelectric capacitance C^{ε} has to be replaced by $C^{\varepsilon} + C_{\mathrm{w}}^{T}$ if the winding-to-winding capacitance is not negligible. This additional capacitance is usually determined from direct measurements after manufacturing [52], so it is not taken into account in the initial steps of the transformer design. Anyway, it would only decrease the minimum requirement on the magnetizing inductance. Note from Eq. (4.40) that the choice of the magnetizing inductance does not depend on the transformer ratio $\hat{a}$. This shows that, even if the required inductance L can be reduced with an increase of the transformer ratio, the transformers still have to satisfy a fixed requirement on the magnetizing inductance. Fig. 4.23 shows that L_{m}^{T} is the inductance of the primary when the secondary is open-circuited. As seen in Chap. 2, this inductance is calculated from the permeance A_{L}^{T} of the selected magnetic core through $L_{\mathrm{m}}^{T} = A_{L}^{T} {N_1}^2$, where N_1 is the number of turns of the primary winding.

In conclusion, the design of the transformers starts with the calculation of the minimum magnetizing inductance L_{m}^{T}, which comes from the properties of the mechanical structure to control and the piezoelectric capacitance, as shown in Eq. (4.40). Then, the number of turns of the primary N_1 and the number of turns of the secondary $N_2 = N_1/\hat{a}$ are obtained from

$$N_1 = \sqrt{\frac{L_{\mathrm{m}}^{T}}{A_{L}^{T}}}. \tag{4.41}$$

In the end, $R_{\mathrm{s}}^{T} = R_1 + \hat{a}^2 R_2$, leads to

$$R_{\mathrm{s}}^{T} = \rho N_1 \left(\frac{l_{N_1}}{S_{w_1}} + \hat{a} \frac{l_{N_2}}{S_{w_2}} \right), \tag{4.42}$$

where l_{N_1} and l_{N_2} are the average length per turn on the primary and secondary windings, S_{w_1} and S_{w_2} are the cross-sectional area of the respective wires and ρ is the wire's resistivity. The cross-sectional areas S_{w_1} and S_{w_2} are thus selected in order to satisfy the R_{s}^{T} optimum determined from numerical simulations. Here, we do not present any considerations related to the selection of the magnetic core. Yet, as detailed in Chap. 2, the magnetic core has obviously to offer an adequate window utilization factor and no magnetic saturation. This last condition leads to a limitation on the voltage applied to

the transformer, hence a limitation on the maximum mechanical excitation. For an industrial application, the problem would be considered differently: knowing the excitation, the dimensions of the magnetic components are minimized to set the saturation limit just above the actual conditions.

4.6 Experiments on beam damping

The multimodal damping strategy based on analogous coupling is validated with a setup involving a one meter free-free beam. Piezoelectric patches are periodically distributed and connected to the analogous network of passive components. The properties of the electrical network are verified by measuring voltage frequency response functions. Once the network is tuned, a mechanical analysis shows the efficiency of the strategy for bending vibration reduction.

4.6.1 Experimental setup

The structure described in Table 4.1 constitutes the setup used to validate the multimodal damping strategy. The same 20 pairs of piezoelectric patches as in Chap. 3 cover the one meter bar made of aluminum alloy 2017. The resulting structure is suspended by elastic straps in order to approximate free-free boundary conditions. Then, as presented in Figs. 4.25, 4.26(a) and 4.26(b), a suspended shaker is connected transversely to one end of the beam through an impedance head that measures the acceleration and the transmitted force. A white noise excitation is generated from the shaker and the transverse velocity of the beam is measured with a scanning laser vibrometer. To compute the velocity FRF, the force measured by the impedance head and the velocity at the free end of the beam are taken into account. The FRF is then obtained with a fast Fourier transform over a 1.2 kHz frequency range with a 0.2 Hz resolution.

The analysis is firstly performed without adding any electrical components on the piezoelectric patches. We focus on the first four modes that can be extracted thanks to a spatial scanning procedure that gives the results presented in Fig. 4.27. Afterward, the experimental FRF in open circuit is compared to the results obtained with the purely

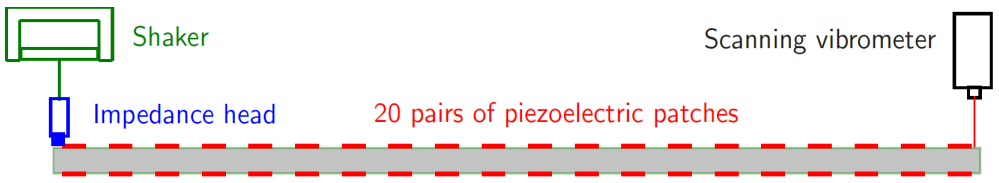

Figure 4.25: Experimental setup for the analysis of bending waves.

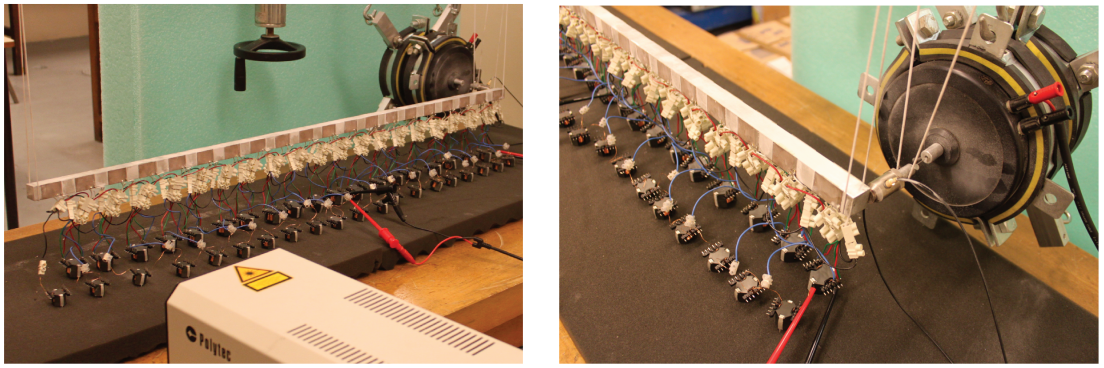

(a) (b)

Figure 4.26: Experimental setup involving a beam coupled to its analogous electrical network: (a) Placement of the shaker and the vibrometer. (b) Transverse excitation with the suspended shaker.

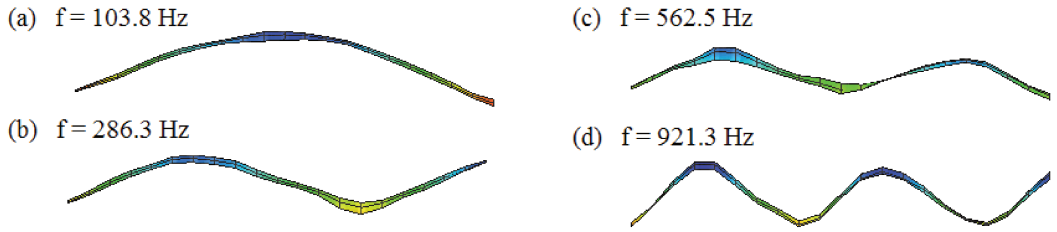

Figure 4.27: Operating deflection shapes measured with the scanning vibrometer: (a) 1st mode. (b) 2nd mode. (c) 3rd mode. (d) 4th mode.

mechanical homogenized model computed from Eq. (4.7). Concerning corrections of the model, the decrease of the piezoelectric Young's modulus determined from longitudinal experiments in Chap. 3 is maintained with the same multiplying coefficient $\gamma = 0.86$. Here, the effect of the connecting element between the impedance head and the beam is not taken into account because it does not induce substantial modifications of the measured force at frequencies below 5 kHz. Yet, as the electrical connectors are part of the mechanical structure, there is a slight increase of the total moving mass. This effect is taken into account by multiplying the equivalent density by a coefficient $\beta = 1.03$, which is determined from the experimental FRFs. Finally, a mechanical damping model is required to approach the velocity maxima appearing when no control occurs. This global damping needs to model the internal dissipation in the structure as well as the damping due to the imperfect boundary conditions and the presence of the electrical connectors. It is remarked that a viscous damping applied to the transverse displacement of the beam represents a suitable damping model for the first four modes. This is introduced in Eq. (4.7)

by multiplying the density by a coefficient evaluated to $\alpha = 1 - 27\mathrm{j}/\omega$ in order to fit the first four experimental maxima.

4.6.2 Coupling to a non-analogous network

When considering damping of transverse waves, it is clear that an electrical network involving a simple line of inductors is not optimal. Indeed, this network has been defined in Chap. 3 from a discretization of a structure satisfying a dispersion relation referring to longitudinal wave propagation. Nevertheless, the non-analogous network can be used for the damping of one specific mode [15, 17, 26]. This requires to adjust the positions of the n^{th} mechanical mode to be controlled, on the positions of the n^{th} electrical mode of the network. Compared to the distributed shunts strategy, the advantage is that the value of the inductance can be reduced by increasing the number of unit cells.

With 100 mH individual inductors and 4.7 nF additional capacitors on a single line of piezoelectric patches, the 9^{th} natural frequency of the network is close to the 9^{th} natural frequency for bending motion. As expected, the experimental results presented in Fig. 4.28 show a strong reduction of the amplitude of the 9^{th} mode. It is also interesting to notice that the non-optimal network has a non-negligible effect on modes for which it was not tuned. For example, the 3^{rd} electrical mode is very close to the 5^{th} mechanical mode and it induces a significant reduction. Likewise, the 10^{th} mechanical mode is just between two electrical modes, which create a large damping. So, this experiment shows that, even if it is not optimal on a broad frequency range, a simple non-analogous network can induce multimodal effects when looking at vibration reduction.

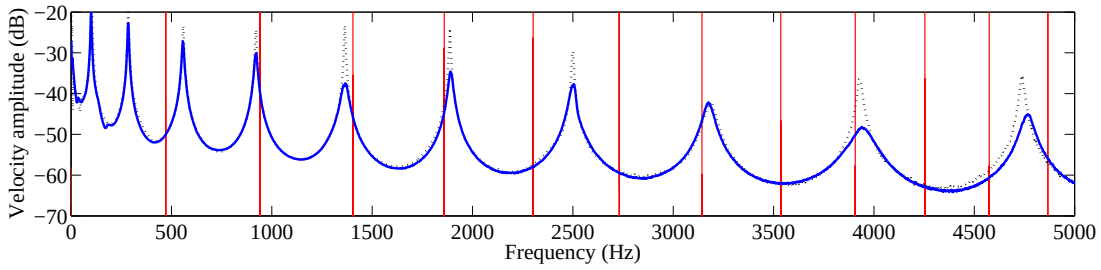

Figure 4.28: Velocity FRFs with the non-analogous network - (· · ·) with short-circuited patches, (—) with the non-analogous network and (—) for the positions of the electrical modes.

4.6.3 Passive analogous network

After preliminary experiments with a non-analogous network, the analogue of a beam is implemented in order to validate the analogous control strategy. It is chosen to create a completely passive solution without any synthetic components. No capacitors are required because the capacitance C^{ε} involved in Fig. 4.10 is offered by the piezoelectric patches. Concerning the magnetic components, i.e. the inductors and the transformers, they are specifically designed for the present application in order to satisfy the electrical requirements presented in Sec. 4.5. Note that we have decided to use the same bar as the one used for the longitudinal experiment presented in Chap. 3. However, the patches are polarized in opposite directions, which means that bending motion does not generate any charge displacement if to opposite patches are connected in parallel. Thus, a double winding was required on the primary of the transformers to inverse one of the voltage signs. It was then chosen to design transformers with a ratio $\hat{a} = 1$ and a resistance R_{s}^{T} around 150 Ω in order to approach the optimal damping determined in Sec. 4.5 without adding external resistors. The inductance L satisfying the modal coupling condition (4.18) is equal to 200 mH, so the required magnetizing inductance L_{m}^{T} is 10 H. Regarding the magnetic core, we select the same type RM10 ferrite as the one used in Chap. 2. Equation (4.41) thus gives $N_1 = 791$ turn for the primary of the transformer. To make easier the winding process, it was decided to wind simultaneously the two primary and the secondary with three identical wires. Consequently, the average lengths per turn are equal, $l_{N_1} = l_{N_2} = l_N$, and the total cross-sectional area of the primary is equal to two times the cross-sectional area of the secondary: $S_{w_1} = 2S_{w_2}$. One gets from Eq. (4.42) that $R_{\mathrm{s}}^{T} = 3\rho N_1 l_N/(2S_{w_2})$, where S_{w_2} is the cross-sectional area of the wire. The length l_N is equal to 52 mm with the selected magnetic core, which gives a theoretical wire diameter equal to 9.4×10^{-5} m with $\rho = 1.7 \times 10^{-8}$ Ωm and $R_{\mathrm{s}}^{T} = 150$ Ω. Copper wire with a 0.1 mm diameter was available and this slight increase in the diameter compared to the theoretical value allows for an increase of the number of turns up to $N_1 = 900$ to reach the resistance $R_{\mathrm{s}}^{T} = 150$ Ω.

After winding with $N_1 = 900$, direct measurements on the transformers at 1 kHz gives a resistance $R_{\mathrm{s}}^{T} = 153$ Ω, a magnetizing inductance $L_T = 12.1$ H and a capacitance between windings $C_{\mathrm{w}}^{T} = 25.2$ nF. Such a high winding-to-winding capacitance was not expected but could have been avoided by winding the primary and the secondary separately. As C_{w}^{T} is not negligible compared to C^{ε}, the modal coupling condition (4.18) needs to be computed with a global capacitance $C^{\varepsilon} + C_{\mathrm{w}}^{T}$. A theoretical inductance value $L = 118$ mH is obtained with C^{ε} equal to 35.3 nF. A RM8 ferrite made of N30 material and offering a permeance $A_L^L = 5700$ nH for one turn is selected and wound with 140 turns of 0.3 mm diameter copper wire. The manufactured inductors are finally around $L = 121$ mH and offer a negligible equivalent series resistance. On the other hand, the loss in the magnetic

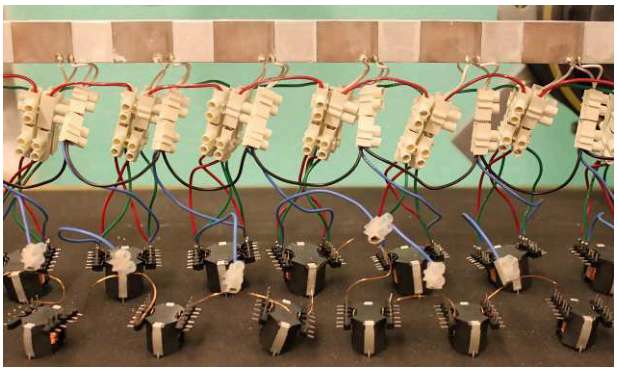

Figure 4.29: Electrical network involving inductors and transformers.

core, or iron loss, can be represented by a parallel resistance, which is evaluated to 72 kΩ. The same type of parallel damping is also introduced into the piezoelectric capacitance, where the equivalent parallel resistance is evaluated to 332 kΩ at 1 kHz. Those additional damping elements are considered for refining the models but we note that the inductors and the piezoelectric capacitance generates a negligible damping compared to what occurs in the transformers. All the components are put together according to Fig. 4.7, which gives the network presented in Fig. 4.29, where the line of components on the bottom of the picture represents the inductors. Just above are the transformers, which are connected to the piezoelectric array through standard terminal blocks.

4.6.4 Electrical frequency response functions

The tuning of the electrical network can be verified before observing its effect on mechanical vibration reduction. A white noise voltage V_w is applied at one end of the 'w' line and the voltage is measured in the middle, between the 10^{th} and the 11^{th} inductors. The experimental electrical FRF in Fig. 4.30 is shown together with the numerical computation based on the semi-continuous transfer matrix model in Eq. (4.26). An analogous experiment in the mechanical domain would be to measure the shear force in the middle of the beam when applying a transverse force excitation at one end. With free-free boundary conditions, the middle of the beam is a node for the odd shear force modes. The same remark applies to the voltage in the inductor line as the electrical network was designed to tend to the analogue of the free-free beam. As a consequence, the measured voltage only tracks the even modes. The lowest resonance, around 290 Hz, is thus the second electrical resonance of the network and the one around 920 Hz is the fourth electrical resonance of the network. We also remark "sharp" antiresonances that are the result of the mechanical resonances. Actually, part of the energy injected in the network flows to the coupled beam around the mechanical resonances, which creates cuts in the frequency spectrum. So, the

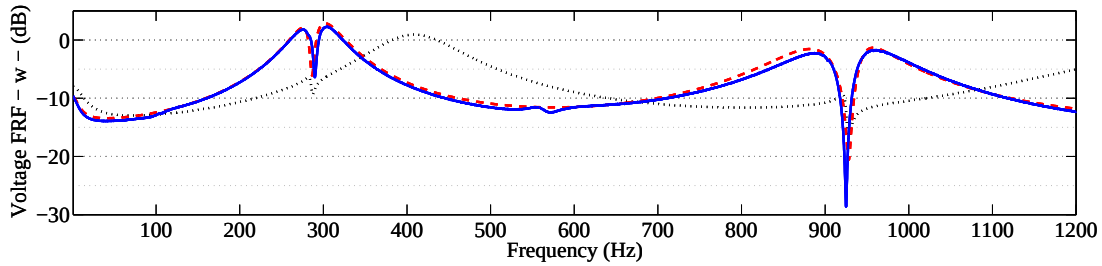

Figure 4.30: Voltage FRFs for a measure between the 10^{th} and the 11^{th} inductors - (—) for the experiment with a tuned network, (−−) for the transfer matrix model with a tuned network, (· · ·) for the transfer matrix model with a detuned network.

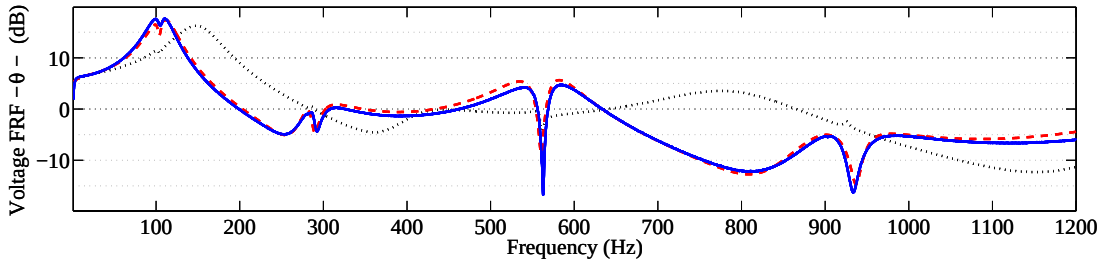

Figure 4.31: Voltage FRFs for a measure on the 10^{th} pair of patches - (—) for the experiment with a tuned network, (−−) for the transfer matrix model with a tuned network, (· · ·) for the transfer matrix model with a detuned network.

tuning of the network is validated by verifying that the "sharp" antiresonances are centered on the "smooth" resonances. This is the case with the tuned electrical values but not for a detuned network with half of the required inductance, as it is also observed in Fig. 4.30.

With measurement of the voltage V_θ in the middle of the network, it is possible to extract the odd modes. This is explained by the fact that the middle of a free-free beam is a node for the even modes related to the bending moment, which is the analogue of V_θ. But the problem is that we do not have access to the measurement of the voltage V_θ in the middle of the network. This is because the two successive $\hat{a}/2$ transformers are replaced by a single $\hat{a}$ transformers to reduce the number of components. Nevertheless, it is still possible to observe the odd modes by measuring the voltage on one of the closest node, the 10^{th} pair of piezoelectric patches. The results are represented in Fig. 4.31 that also shows the case of a detuned network with half of the required inductance. As the measurement is not performed in the exact middle of the network, the even modes also appear. It is still possible to verify that the odd electrical resonances match the mechanical ones. As a consequence, the previous electrical FRFs allow being sure that the network is correctly tuned, even before doing any mechanical testing. The electrical FRFs also enable

validating the presented transfer matrix formulation that takes into account the modeling of the electrical components. It is observed in Figs. 4.30 and 4.31 that the numerical and experimental responses are sufficiently close to validate the transfer matrix model. This model can thus be used for the optimization of the electrical network, before its actual implementation.

4.6.5 Multimodal damping by analogous coupling

Once the electrical network is correctly tuned, it becomes possible to observe the effect of the multimodal coupling on the mechanical vibrations. In Fig. 4.32, the velocity FRF with a tuned network is compared to the velocity FRF with open-circuited patches. Reductions around 7 dB are observed for the first mode, 10 dB for the second and third modes and 16 dB for the fourth mode, which shows the efficiency of the damping strategy involving an analogous electrical network. However, we do not get a velocity FRF similar to what has been presented in Fig. 4.21. The system seems to be overdamped as no local minimum appears, even with the prescribed resistance R_{s}^{T}. This is due to the fact that the added winding-to-winding capacitance C_{w}^{T} was clearly non-negligible compared to the piezoelectric capacitance C^{ε}, which was not expected before manufacturing the transformers. The final global capacitance of the unit cell was almost doubled and this led to a decrease of the required inductance L. As the transformer resistance has been defined without considering any capacitance addition, it is finally too high for the present inductance. It is noticed that the capacitance C_{w}^{T} could have been considerably reduced by separating the winding of the transformers and using an internal insulation layer. If this choice had been considered for the manufacturing of the transformers, the results would have been definitely closer to the FRF represented in Fig. 4.21.

In the end, the comparison between the experiments and the transfer matrix model in Eq. (4.26) also validates the theoretical formulation when looking at the mechanical

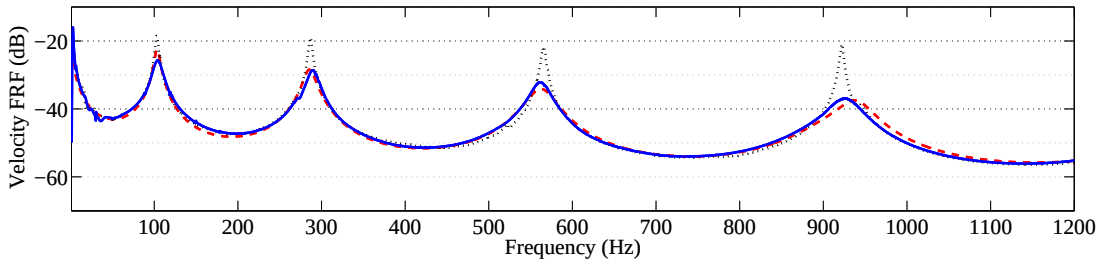

Figure 4.32: Velocity FRFs - ($\cdots$) for the experiment with open-circuited patches, (—) for the experiment with a tuned network, (−−) for the fully homogenized beam model with a tuned network.

FRF. It can still be remarked that there are slight differences concerning the maximal amplitudes, especially for the first mode that is 3 dB below its theoretical value. This means that an unconsidered damping was added when performing the experiments with the full network. In fact, the mechanical damping coefficient α was determined with open-circuited patches, when all the electrical connectors presented in Fig. 4.29 were not yet mounted. The electrical network itself thus increases the purely mechanical damping. This is a point that could be improved in future experiments in order to better characterize the vibration reduction which is only induced by the electromechanical coupling.

4.7 Conclusions

A multimodal damping strategy has been developed in this chapter by coupling a beam to its analogous electrical network through an array of piezoelectric patches. A lattice model approximating the mechanical properties of the beam is obtained by applying a finite difference method to the Euler-Bernoulli equations. The dispersion relation, the propagation constants and the frequency response functions of the lattice model are compared to the results obtained with a continuous beam. The analogous electrical network is found by applying the direct electromechanical analogy on the discrete model of a beam. Then, a description of the piezoelectric coupling is presented through a linear model including the global properties of the unit cells. The method to determine the global piezoelectric coupling coefficient and the blocked capacitance is given accordingly. This leads to the definition of a modal coupling condition that tunes the modes of the electrical network to the ones of the mechanical structure to control.

For modeling of wave propagation, contrary to previous studies that focus on a homogenized electrical medium, the network is kept discrete to get closer to real applications involving a finite number of piezoelectric patches. Four novel transfer matrix models are proposed and compared. They differ in the definition of the mechanical medium which can be discrete, fully homogenized, piecewise homogenized or based on a finite element model. The finite element model tends to the piecewise homogenized model which is the most accurate because it takes into account the mechanical discontinuity induced by the piezoelectric patches. Yet, for problems involving analogous control with a discrete electrical network, the fully homogenized model is generally sufficient because the eventual stop band effect occurs at frequencies where the proposed control is no more efficient. Also, the discrete model is convenient because of its easy implementation but it should be limited to wavelength above ten times the length of the unit cell.

The design of the analogous electrical network is described through recommendations related to the transformers and the piezoelectric array. Similarly to what we got for

the validity of the discrete model, about ten piezoelectric patches per wavelength are required to ensure a sufficient approximation of a continuous beam with a discrete electrical network and thus generate a suitable multimodal coupling. Then, it is shown that series resistance in the transformer windings offers damping over a broader frequency range than single series or parallel resistance on the inductors. This is fortunate because the design of transformers with a sufficient magnetizing inductance leads to a non-negligible winding resistance. The transformers can thus be designed by taking into account an optimal damping condition based on numerical simulations, so that no external resistors are required.

To the best of our knowledge, we implemented the first experimental validation of a multimodal damping strategy involving a beam coupled to its discrete electrical analogue. Without any external power, the control offers a significant vibration reduction over a broad frequency range. We also show that it is possible to verify the tuning of the network from electrical measurements. Whether it is electrical or mechanical frequency response functions, they can be computed with the proposed transfer matrix models, which show a good correlation with the experimental results. Those transfer matrix models thus represent an appropriate tool for the design of piezoelectric damping systems involving a one-dimensional analogous network.

Chapter 5

Analogous piezoelectric control applied to the damping of a plate

Abstract: *Multimodal damping of a plate can be achieved by a coupling to an electrical network exhibiting similar modal properties. A suitable topology for such a network is obtained by a finite difference formulation of the mechanical equations, followed by a direct electromechanical analogy. This procedure is applied to the Kirchhoff-Love theory in order to find the electrical analogue of a clamped plate. The resulting passive electrical network is implemented with inductors, transformers and the inherent capacitance of the piezoelectric patches. The electrical modes are tuned to approach several mechanical modes simultaneously. This yields a broadband reduction of the plate vibrations through an array of interconnected piezoelectric patches. The robustness of the control strategy is evaluated by introducing perturbations in the mechanical or electrical designs. In the end, the use of an analogous electrical network appears as an efficient and robust solution for the multimodal control of a plate.*

Contents

5.1 Introduction

Control solutions involving an array of piezoelectric resonant shunts have been proposed in order to damp vibrations of plates [6, 50, 51, 118–121]. The use of several piezoelectric patches of reduced dimensions limits the problem of charge cancellation and can eventually introduce an additional stop band effect over the considered frequency range. However, this strategy does not apply in the low frequency range, where the simultaneous control of several plate modes requires the synthesis of multi-resonant shunts. Such shunts with multiple inductors were proposed by Wu [10] and then implemented on a one-dimensional piezoelectric array [46]. The multimodal approach of Wu and other similar concepts require n inductors per patch to affect n modes, which may lead to a system with an impractically large number of components. A broadband control can still be implemented with negative capacitance, which simplifies the electrical layout and offers good performances [122–127]. The main drawback is that a negative capacitance needs to be synthesized with an active circuit and the control can thus suffer from stability issues. A solution for the multimodal control of a plate with a passive electrical network was presented by Vidoli and dell'Isola [128]. The network consists of distributed inductors that interconnect the piezoelectric patches in order to generate 2D electrical modes that match the mechanical modes, both in the spatial and frequency domains. This idea was then extended by Giorgio et al. [129, 130] to systems involving only a few piezoelectric patches. The main limit remains the practical implementation of a suitable passive network. As we need to reproduce the modal properties of mechanical structures with an electrical system, suitable topologies can be found by applying an electromechanical analogy [20, 74, 131]. Around 1950's, MacNeal et al. already proposed and validated electrical analogues for numerous mechanical structures as rods, beams [30, 37], plates [30, 38] and shells [39]. Those passive networks finally reappeared for the analogous control of one-dimensional structures [19, 21]. With this approach, the number of components per piezoelectric patch is independent of the number of modes that are targeted. For the control of thin plates, Alessandroni et al. [23, 24] proposed an analogous network ensuring a broadband piezoelectric damping. Unfortunately, the large number of electrical components makes difficult its practical implementation. A simpler electrical network can be obtained by reconsidering the Kirchhoff-Love theory. The new topology is presented in the present chapter and applied to the damping of a clamped plate.

With a real experimental setup, it becomes possible to evaluate the robustness of the control strategy. The effect of parameter variations needs to be investigated because it has been shown that solutions involving resonant shunts can be very sensitive to electrical mistunings [2, 9]. In practical applications, even if the robustness can be slightly improved with an overestimated damping [132], it seems difficult to maintain a fine tuning of

a single resonant shunt without autonomous adaptation of the electrical parameters [133]. Nevertheless, in the case of a distributed solution involving an array of resonant shunts, uncertainties between components does not lead to a significant degradation of the performance [4]. This is also true with electrical analogous networks as observed in Chap. 3 where experiments involving inductors with a $\pm 10\%$ tolerance were in good agreement with deterministic simulations. Then, the question related to the effect of an uniform detuning of the electrical parameters still arises, because it could seriously affect the damping performances [134, 135]. Another issue concerns the influence of defects appearing locally or along the boundary of the mechanical or the electrical domains.

In this chapter, we focus on a new analogous network that reproduces the behavior of a plate. The proposed electrical network is obtained by extending the procedure applied to rods and beams in the previous chapters. It consists of a finite difference formulation of the equations describing the mechanical medium, followed by a direct electromechanical analogy. A 2D electrical network involving capacitors, inductors and transformers is thus defined. It is modeled numerically by assembling element matrices into a global system representing the analogue of a dynamic stiffness matrix. The passive electrical network is then implemented in a case focusing on the analogue of a clamped plate. Electrical modes are observed experimentally, which validates the analogous electrical topology. Afterward, we consider the damping of a clamped plate coupled to the electrical network through an array of piezoelectric patches. By extension of the one-dimensional bending model developed in Chap. 4, a discrete electromechanical unit cell is built for describing the 2D piezoelectric coupling to a multiport network. The models are validated through experiments that also show the efficiency of the proposed control strategy. Depending on the application, the electrical network is then tuned by adding resistors or by modifying the values of the inductors. An optimal tuning gives a reference for evaluating the robustness of the control with respect to parameter variations. The performance loss induced by an uniform variation of the network inductance is quantified. Local or boundary modifications are also introduced experimentally. In any case, significant vibration reduction is maintained, which validates the interest of the damping strategy.

5.2 Electrical analogue of a square plate unit cell

A finite difference method is applied to the Kirchhoff-Love plate equation of motion in order to get a discrete mechanical model. This model is then converted in the electrical domain by applying a direct electromechanical analogy. Depending on the considered plate boundary conditions, electrical ports are short- or open-circuited on the edges of the network. The whole electrical network is then modeled by implementing an assembly of

element matrices. This leads to a numerical validation of the proposed electrical analogue.

5.2.1 Finite difference model of a plate

According to the Kirchhoff-Love theory, the governing differential equation for a thin plate of Young's modulus Y, density ρ, Poisson's ratio ν and thickness h is given by

$$-D\left(\frac{\partial^4 w}{\partial x^4}+2\frac{\partial^4 w}{\partial x^2\partial y^2}+\frac{\partial^4 w}{\partial y^4}\right)=\rho h\frac{\partial^2 w}{\partial t^2},\quad \text{where}\quad D=\frac{Yh^3}{12(1-\nu^2)}. \tag{5.1}$$

$w=W(x,y)g(t)$ is the transverse displacement, x and y are the two space variables, t is the time variable and D is the bending stiffness. Focusing on harmonic motion, $g(t)$ is a trigonometric function satisfying $\partial^2 g/\partial t^2=-\omega^2 g$. Consequently, the system of equations

$$\begin{aligned} &\frac{\partial Q_x}{\partial x}+\frac{\partial Q_y}{\partial y}=-\rho ha\omega^2 W && && M=aD\left(\frac{\partial\theta_x}{\partial x}+\frac{\partial\theta_y}{\partial y}\right)\\ &Q_x=-\frac{\partial M}{\partial x} && \text{and} && \theta_x=\frac{\partial W}{\partial x}\\ &Q_y=-\frac{\partial M}{\partial y} && && \theta_y=\frac{\partial W}{\partial y} \end{aligned} \tag{5.2}$$

is equivalent to Eq. (5.1). The constant a corresponds to the side of a square plate unit cell, so that Eq. (5.2) is a two-dimensional extension of the state variable system for an Euler-Bernouilli beam, as presented in Chap. 4. The variables Q_x and Q_y still represent shear forces and the angles along the principal directions, θ_x and θ_y, satisfy the Kirchhoff-Love assumption which states that the segments normal to the undeformed midplane remain straight after deformation. Yet, the moment variable M appearing in Eq. (5.2) does not refer to any classical variable of the plate theory [136]. It is here introduced for the definition of an adequate finite difference model.

The continuous plate element is discretized by applying the finite difference scheme

$$\begin{aligned} &\left(\frac{\partial[\cdot]}{\partial x}\right)_{\mathrm{L}}=\frac{[\cdot]_{\mathrm{I}}-[\cdot]_{\mathrm{L}}}{a/2} && && \left(\frac{\partial[\cdot]}{\partial y}\right)_{\mathrm{B}}=\frac{[\cdot]_{\mathrm{I}}-[\cdot]_{\mathrm{B}}}{a/2}\\ &\left(\frac{\partial[\cdot]}{\partial x}\right)_{\mathrm{I}}=\frac{[\cdot]_{\mathrm{R}}-[\cdot]_{\mathrm{L}}}{a} && \text{and} && \left(\frac{\partial[\cdot]}{\partial y}\right)_{\mathrm{I}}=\frac{[\cdot]_{\mathrm{T}}-[\cdot]_{\mathrm{B}}}{a}\ ,\\ &\left(\frac{\partial[\cdot]}{\partial x}\right)_{\mathrm{R}}=\frac{[\cdot]_{\mathrm{R}}-[\cdot]_{\mathrm{I}}}{a/2} && && \left(\frac{\partial[\cdot]}{\partial y}\right)_{\mathrm{T}}=\frac{[\cdot]_{\mathrm{T}}-[\cdot]_{\mathrm{I}}}{a/2} \end{aligned} \tag{5.3}$$

where 'I' is the position at the center of the square unit cell and 'L', 'R', 'B' and 'T' refer to the left, right, bottom and top sides, according to the grid in Fig. 5.1. This finite

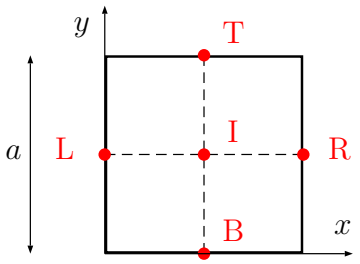

Figure 5.1: Finite difference grid for a square plate unit cell.

difference approximation is applied to Eq. (5.2), which gives

$$\begin{aligned} &Q_\mathrm{R} - Q_\mathrm{L} + Q_\mathrm{T} - Q_\mathrm{B} = -m\omega^2 W_\mathrm{I} \\ &Q_\mathrm{L} = -\frac{M_\mathrm{I} - M_\mathrm{L}}{a/2} \\ &Q_\mathrm{R} = -\frac{M_\mathrm{R} - M_\mathrm{I}}{a/2} \\ &Q_\mathrm{B} = -\frac{M_\mathrm{I} - M_\mathrm{B}}{a/2} \\ &Q_\mathrm{T} = -\frac{M_\mathrm{T} - M_\mathrm{I}}{a/2} \end{aligned} \quad \text{and} \quad \begin{aligned} &M_\mathrm{I} = D\left(\theta_\mathrm{R} - \theta_\mathrm{L} + \theta_\mathrm{T} - \theta_\mathrm{B}\right) \\ &\theta_\mathrm{L} = \frac{W_\mathrm{I} - W_\mathrm{L}}{a/2} \\ &\theta_\mathrm{R} = \frac{W_\mathrm{R} - W_\mathrm{I}}{a/2} \\ &\theta_\mathrm{B} = \frac{W_\mathrm{I} - W_\mathrm{B}}{a/2} \\ &\theta_\mathrm{T} = \frac{W_\mathrm{T} - W_\mathrm{I}}{a/2} \end{aligned} \tag{5.4}$$

where $m = \rho h a^2$ is the mass of the square plate unit cell.

5.2.2 Analogous electrical unit cell

The finite difference model in Eq. (5.4) can be converted into its analogous network made of discrete electrical components. Contrary to previous studies on plate electrical analogues [24, 30], we focus on the direct electromechanical analogy, which is compatible with the electrical representation of a piezoelectric transducer [74]. This direct analogy is based on the velocity-current and force-voltage equivalences. So, Eq. (5.4) can be rewritten as

$$\begin{aligned} &-Q_\mathrm{L} - (Q_\mathrm{B} - Q_\mathrm{T}) + Q_\mathrm{R} = \mathrm{j}\omega m \dot{W}_\mathrm{I} \\ &-M_\mathrm{L} + M_\mathrm{I} = -\tfrac{a}{2} Q_\mathrm{L} \\ &-M_\mathrm{I} + M_\mathrm{R} = -\tfrac{a}{2} Q_\mathrm{R} \\ &-M_\mathrm{B} + M_\mathrm{I} = -\tfrac{a}{2} Q_\mathrm{B} \\ &-M_\mathrm{I} + M_\mathrm{T} = -\tfrac{a}{2} Q_\mathrm{T} \end{aligned} \quad \text{and} \quad \begin{aligned} &-M_\mathrm{I} = \frac{D}{\mathrm{j}\omega}\left(\dot{\theta}_\mathrm{L} - \dot{\theta}_\mathrm{R} + \dot{\theta}_\mathrm{B} - \dot{\theta}_\mathrm{T}\right) \\ &\tfrac{a}{2}\dot{\theta}_\mathrm{L} = \dot{W}_\mathrm{I} - \dot{W}_\mathrm{L} \\ &\tfrac{a}{2}\dot{\theta}_\mathrm{R} = \dot{W}_\mathrm{R} - \dot{W}_\mathrm{I} \\ &\tfrac{a}{2}\dot{\theta}_\mathrm{B} = \dot{W}_\mathrm{I} - \dot{W}_\mathrm{B} \\ &\tfrac{a}{2}\dot{\theta}_\mathrm{T} = \dot{W}_\mathrm{T} - \dot{W}_\mathrm{I} \end{aligned} \tag{5.5}$$

which highlights the derivatives of the transverse and angular displacements that are going to be used as electrical current variables. It then becomes possible to represent the system of equations (5.5) with the electrical circuit given in Fig. 5.2. The electrical transformers of ratio $a/2$ allow the implementation of the forward and backward finite differences

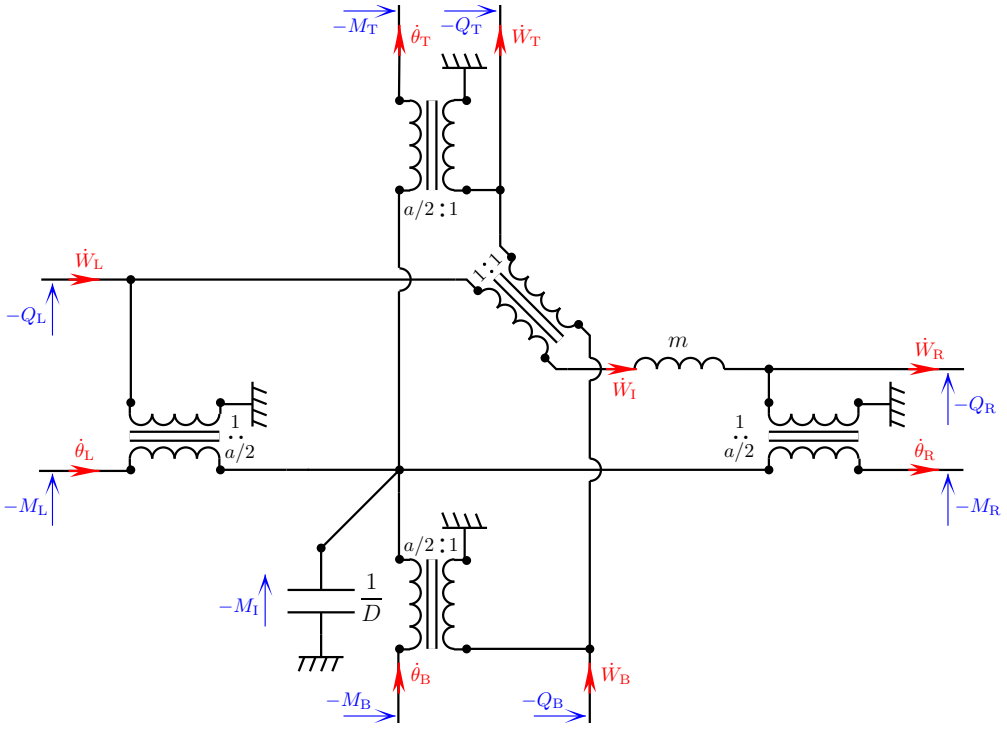

Figure 5.2: Electrical unit cell as a direct analogue of the plate finite difference model.

that satisfy the definition of θ and Q as spatial derivatives of w and $-M$, respectively. Furthermore, the inductance represents the mass m of the unit cell and the capacitance is equal to the inverse of the bending stiffness D, in agreement with the direct electromechanical analogy. The proposed two-dimensional unit cell in Fig. 5.2 can finally be seen as a two-dimensional extension of the beam electrical analogue which has been presented in Chap.4. The electrical circuit in Fig. 5.2 has to be replicated along the x and y directions in order to create the electrical analogue of a plate.

A single electrical unit cell is implemented with one inductor, one capacitor and five transformers. Note that the connection of adjacent unit cells reduces the number of components. Indeed, a series of two transformers of ratio $a/2$ can be replaced by a single transformer with a ratio equal to a. Then, the average number of transformers per unit cell tends to three when increasing the number of unit cells. Actually, it has been found afterward that the proposed topology is a special case of the "Dynamic analog for a constant thickness plate" introduced by MacNeal in 1949 [30]. This analogous network has been obtained from a rectangular plate element and the result is a unit cell made of one capacitor, four inductors and two transformers. It can be shown that the case of the square unit cell simplifies MacNeal's electrical network into the one of the present section, which involves fewer electrical components, i.e. one inductor, one capacitor and three transformers. We

also obtain a simpler network when compared to the topology proposed by Alessandroni et al. [23, 24] with one capacitor, three inductors and six transformers per unit cell. As a consequence, the new topology simplifies the practical implementation of the analogous network for experimental validation and application to piezoelectric damping.

5.2.3 Electrical boundary conditions

When implementing an analogous electrical network with a set of several unit cells as the one proposed in Fig. 5.2, the electrical states on the edges of the complete network also have to satisfy an analogy with mechanical boundary conditions. For instance, for clamped boundary conditions along an edge at $x = 0$,

$$W(0, y) = 0 \quad \text{and} \quad \theta(0, y) = 0. \tag{5.6}$$

If this condition applies to the left of the unit cell in Fig. 5.2, we get

$$\dot{W}_{\mathrm{L}} = 0 \quad \text{and} \quad \dot{\theta}_{\mathrm{L}} = 0, \tag{5.7}$$

which means that both electrical port have to remain open-circuited. As explained below, other boundary conditions involving simply-supported edges or free edges are less obvious because they require application of the Kirchhoff-Love plate theory. The classical state variable formulation of the differential equation in Eq. (5.1) can be expressed as follows:

$$\begin{aligned} &\frac{\partial Q_x}{\partial x} + \frac{\partial Q_y}{\partial y} = -\rho h a \omega^2 W && && M_x = -aD\left(\frac{\partial^2 W}{\partial x^2} + \nu \frac{\partial^2 W}{\partial y^2}\right) \\ &Q_x = \frac{\partial M_x}{\partial x} - \frac{\partial M_{xy}}{\partial y} && \text{and} && M_y = -aD\left(\frac{\partial^2 W}{\partial y^2} + \nu \frac{\partial^2 W}{\partial x^2}\right) . \\ &Q_y = \frac{\partial M_y}{\partial y} - \frac{\partial M_{xy}}{\partial x} && && M_{xy} = aD(1-\nu)\frac{\partial^2 W}{\partial x \partial y} \end{aligned} \tag{5.8}$$

This corresponds to the variables used by Timoshenko [136] in which we have introduced the length coefficient a in order to get variables Q and M homogeneous to forces and moments. Q_x and Q_y are shear forces and their definition is actually the same as in Eq. (5.2). M_x, M_y and M_{xy} are respectively the bending moments along x, the bending moment along y and the twisting moment. Simply-supported boundary condition along an edge at $x = 0$ corresponds to zero bending moment along x and zero displacement as

$$W(0, y) = 0 \quad \text{and} \quad M_x(0, y) = 0. \tag{5.9}$$

So, $\left.\frac{\partial^2 W}{\partial y^2}\right|_{0,y} = 0$ and because $M_x = -aD\left(\frac{\partial^2 W}{\partial x^2} + \nu \frac{\partial^2 W}{\partial y^2}\right)$, we also get $\left.\frac{\partial^2 W}{\partial x^2}\right|_{0,y} = 0$. The variable M involved in Eq. (5.2) and in Fig. 5.2 is not equal to the bending moment M_x nor M_y but it is a linear combination of both of them through

$$M = aD\left(\frac{\partial^2 W}{\partial y^2} + \frac{\partial^2 W}{\partial x^2}\right) = -\frac{1}{1+\nu}\left(M_x + M_y\right). \tag{5.10}$$

With simply-supported boundary conditions, as the second derivatives of W along both x and y directions are equal to zero, $M(0,y)=0$. Consequently, if this applies to the left of the unit cell in Fig. 5.2,

$$\dot{W}_{\mathrm{L}}=0 \quad \text{and} \quad M_{\mathrm{L}}=0, \tag{5.11}$$

which corresponds to an open-circuited 'w' electrical line and a short-circuited 'θ' line.

Free boundary condition along the same edge at $x=0$ correspond to a zero bending moment M_x and a zero effective shear force V_x:

$$M_x(0,y)=0 \quad \text{and} \quad V_x(0,y)=0, \tag{5.12}$$

where the effective shear force has been defined by Timoshenko [136] as

$$V_x=Q_x-\frac{\partial M_{xy}}{\partial y}=-aD\left(\frac{\partial W^3}{\partial x^3}+(2-\nu)\frac{\partial^3 W}{\partial x\partial y^2}\right). \tag{5.13}$$

The boundary condition $V_x(0,y)=0$ thus gives

$$Q_x(0,y)=aD(1-\nu)\frac{\partial^3 W}{\partial x\partial y^2}\Big|_{0,y}=aD(1-\nu)\frac{\partial^2\theta_x}{\partial y^2}\Big|_{0,y}. \tag{5.14}$$

Furthermore, the boundary condition $M_x(0,y)=0$ leads to $\dfrac{\partial^2 W}{\partial x^2}\Big|_{0,y}=-\nu\dfrac{\partial^2 W}{\partial y^2}\Big|_{0,y}$, so

$$M(0,y)=aD(1-\nu)\frac{\partial^2 W}{\partial y^2}\Big|_{0,y}. \tag{5.15}$$

Finally, with the discrete finite difference scheme, Eqs. (5.14) and (5.15) are equivalent to

$$Q_{\mathrm{L}}=\frac{D(1-\nu)}{a}(\theta_{\mathrm{L}}^{+}-2\theta_{\mathrm{L}}+\theta_{\mathrm{L}}^{-}) \quad \text{and} \quad M_{\mathrm{L}}=\frac{D(1-\nu)}{a}(W_{\mathrm{L}}^{+}-2W_{\mathrm{L}}+W_{\mathrm{L}}^{-}), \tag{5.16}$$

where the superscripts '+' and '-' refer to the neighboring unit cells along the x axis. We note that Q_{L}, which is the analogue of a voltage in the 'w' electrical line, is a linear combination of charge displacements occurring in three distinct 'θ' electrical lines. A similar situation occurs with M_{L}, voltage in the 'θ' electrical line, which is a linear combination of charge displacements occurring in three distinct 'w' lines. Consequently, even if the boundary conditions in Eq. (5.16) can be implemented with an active control system, it seems that it cannot be achieved with simple electrical connections when considering the circuit in Fig. 5.2. This highlights a limit of the proposed network topology, which allows an easy implementation of clamped or simply-supported boundary conditions, but no passive solution for free boundary conditions.

5.2.4 Element "mass" and "stiffness" matrices

The electrical circuit in Fig. 5.2 defines a single unit cell of the proposed analogous network, which represents the finite difference model of a square plate unit cell. In order to model a complete electrical network or a complete plate made of several unit cell, it is decided to focus on an assembly of element matrices, as classically performed through finite element procedures. By considering a force and a displacement vector,

$$\begin{array}{c} \boldsymbol{F}_{\boldsymbol{m}}^{\mathrm{e}} = \left[\begin{array}{cccccccc} -Q_{\mathrm{B}} & -M_{\mathrm{B}} & -Q_{\mathrm{L}} & -M_{\mathrm{L}} & Q_{\mathrm{R}} & M_{\mathrm{R}} & Q_{\mathrm{T}} & M_{\mathrm{T}} \end{array} \right]^T \\ \text{and} \quad \boldsymbol{q}_{\boldsymbol{m}}^{\mathrm{e}} = \left[\begin{array}{cccccccc} W_{\mathrm{B}} & \theta_{\mathrm{B}} & W_{\mathrm{L}} & \theta_{\mathrm{L}} & W_{\mathrm{R}} & \theta_{\mathrm{R}} & W_{\mathrm{T}} & \theta_{\mathrm{T}} \end{array} \right]^T \end{array}, \tag{5.17}$$

one might want to define an element dynamic stiffness matrix $\boldsymbol{D}_{\boldsymbol{m}}^{\mathrm{e}}$ as

$$\boldsymbol{F}_{\boldsymbol{m}}^{\mathrm{e}} = \boldsymbol{D}_{\boldsymbol{m}}^{\mathrm{e}} \boldsymbol{q}_{\boldsymbol{m}}^{\mathrm{e}}. \tag{5.18}$$

The signs in the force vector are chosen in order to involve external forces applied to the unit cell. As, Q_{B}, M_{B}, Q_{L} and M_{L} represent mechanical actions applied by the considered unit cell to its bottom or left neighbors, their opposite values are introduced into the force vector. The calculation of the dynamic stiffness matrix $\boldsymbol{D}_{\boldsymbol{m}}^{\mathrm{e}}$ relies on the set of equations (5.2), which has to be reorganized to make appear the force components as linear combinations of the displacements. Yet, we remark that the displacements are not independent variables. Indeed, Eq. (5.4) shows that if all four angles have prescribed values, the choice of a single displacement enforces the value of the other ones. This means that the dynamic stiffness matrix cannot be defined. Additional degrees of freedom are required to relax the kinematic constraints linking angles and displacements. To this end, additional components are inserted in the electrical circuit representing the plate unit cell, as was performed in Chap. 4 for one-dimensional bending. The modified circuit is represented in Fig. 5.3, where capacitors $C_0/2$ are added at the ends of the 'θ' electrical lines in order to allow the definition of the dynamic stiffness matrix $\boldsymbol{D}_{\boldsymbol{m}}^{\mathrm{e}}$. Additional inductors $L_\theta/2$ are also introduced in the 'θ' electrical lines. Those inductors are actually the analogues of moments of inertia. Moreover, they can be used to model parasitic elements in non-ideal transformers when considering the analysis of the analogous electrical network.

Electrical variables have been used in Fig. 5.3 for showing that the analysis of an electrical network can reproduce methods usually implemented for the analysis of mechanical structures. Indeed, one can define an electrical "dynamic stiffness matrix" $\boldsymbol{D}_{\boldsymbol{e}}^{\mathrm{e}}$, which satisfies

$$\boldsymbol{F}_{\boldsymbol{e}}^{\mathrm{e}} = \boldsymbol{D}_{\boldsymbol{e}}^{\mathrm{e}} \boldsymbol{q}_{\boldsymbol{e}}^{\mathrm{e}}, \tag{5.19}$$

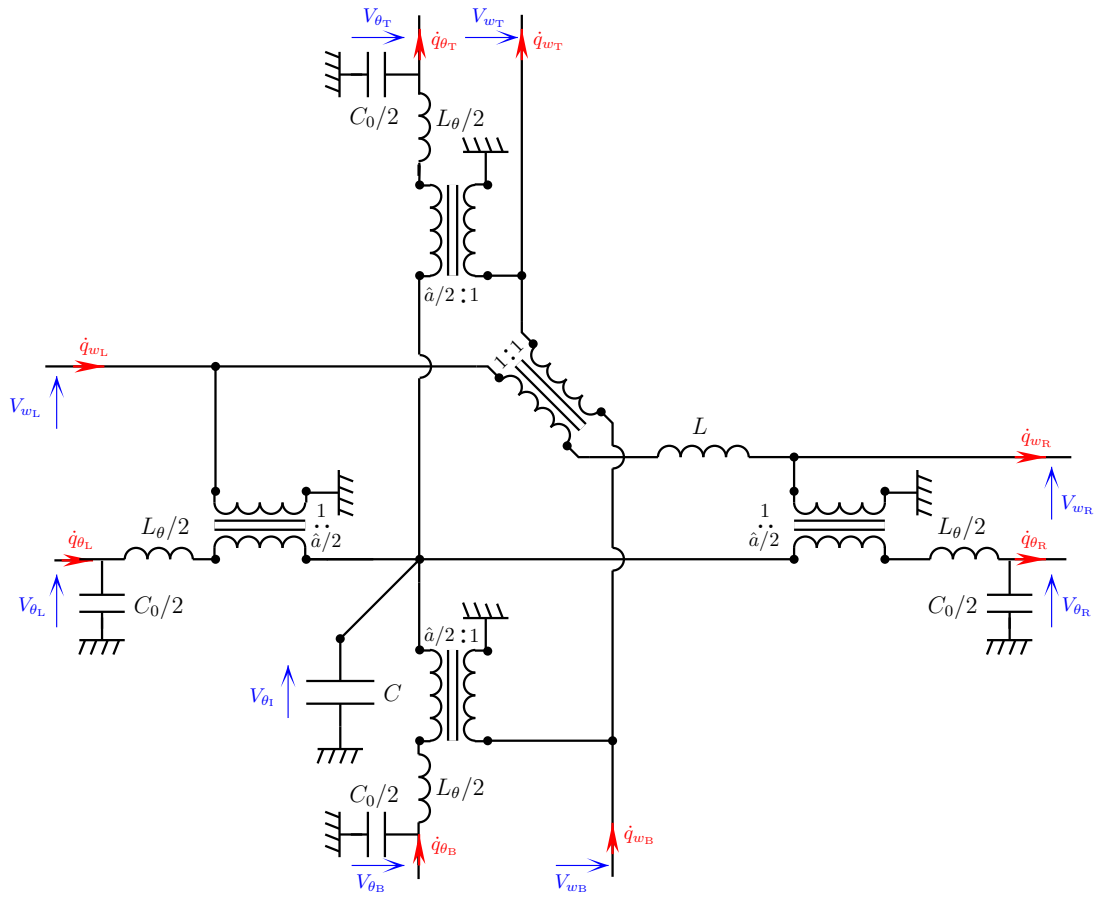

Figure 5.3: Modified unit cell for calculation of the element dynamic stiffness matrix.

where

$$\boldsymbol{F}_{\boldsymbol{e}}^{\mathrm{e}} = \begin{bmatrix} V_{w\mathrm{B}} & V_{\theta\mathrm{B}} & V_{w\mathrm{L}} & V_{\theta\mathrm{L}} & -V_{w\mathrm{R}} & -V_{\theta\mathrm{R}} & -V_{w\mathrm{T}} & -V_{\theta\mathrm{T}} \end{bmatrix}^T$$
$$\text{and} \quad \boldsymbol{q}_{\boldsymbol{e}}^{\mathrm{e}} = \begin{bmatrix} q_{w\mathrm{B}} & q_{\theta\mathrm{B}} & q_{w\mathrm{L}} & q_{\theta\mathrm{L}} & q_{w\mathrm{R}} & q_{\theta\mathrm{R}} & q_{w\mathrm{T}} & q_{\theta\mathrm{T}} \end{bmatrix}^T \tag{5.20}$$

are the voltage vector and the electrical charge displacement vector, the analogues of the force and displacement vectors, $\boldsymbol{F}_{\boldsymbol{m}}^{\mathrm{e}}$ and $\boldsymbol{q}_{\boldsymbol{m}}^{\mathrm{e}}$. Note that the signs in $\boldsymbol{F}_{\boldsymbol{e}}^{\mathrm{e}}$ are the opposites of the signs in $\boldsymbol{F}_{\boldsymbol{m}}^{\mathrm{e}}$ because the voltages are analogous to the opposite of the force contributions, as shown in Fig. 5.2. The "dynamic stiffness matrix" $\boldsymbol{D}_{\boldsymbol{e}}^{\mathrm{e}}$ is obtained by writing down all the discrete electrical equations referring to Fig. 5.3, eliminating the internal variables and solving for the side voltage variables. Element "stiffness" and "mass" matrices are then defined through

$$\boldsymbol{D}_{\boldsymbol{e}}^{\mathrm{e}} = \boldsymbol{K}_{\boldsymbol{e}}^{\mathrm{e}} - \omega^2 \boldsymbol{M}_{\boldsymbol{e}}^{\mathrm{e}}, \tag{5.21}$$

which means that $\boldsymbol{K}_{\boldsymbol{e}}^{\mathrm{e}}$ corresponds to a "static stiffness matrix":

$$\boldsymbol{K}_{\boldsymbol{e}}^{\mathrm{e}} = \boldsymbol{D}_{\boldsymbol{e}}^{\mathrm{e}} \quad \text{when} \quad \omega = 0. \tag{5.22}$$

So, by setting $\omega = 0$ in the symbolic expression for $\boldsymbol{D}_{\boldsymbol{e}}^{\mathrm{e}}$ we get

$$\boldsymbol{K}_{\boldsymbol{e}}^{\mathrm{e}} = \frac{1}{\hat{a}^2 C_0} \begin{bmatrix} 6 & 3\hat{a} & -2 & -\hat{a} & -2 & \hat{a} & -2 & \hat{a} \\ 3\hat{a} & \frac{\hat{a}^2}{2}\frac{3C+8C_0}{C+2C_0} & -\hat{a} & -\frac{\hat{a}^2}{2}\frac{C}{C+2C_0} & -\hat{a} & \frac{\hat{a}^2}{2}\frac{C}{C+2C_0} & -\hat{a} & \frac{\hat{a}^2}{2}\frac{C}{C+2C_0} \\ -2 & -\hat{a} & 6 & 3\hat{a} & -2 & \hat{a} & -2 & \hat{a} \\ -\hat{a} & -\frac{\hat{a}^2}{2}\frac{C}{C+2C_0} & 3\hat{a} & \frac{\hat{a}^2}{2}\frac{3C+8C_0}{C+2C_0} & -\hat{a} & \frac{\hat{a}^2}{2}\frac{C}{C+2C_0} & -\hat{a} & \frac{\hat{a}^2}{2}\frac{C}{C+2C_0} \\ -2 & -\hat{a} & -2 & -\hat{a} & 6 & -3\hat{a} & -2 & \hat{a} \\ \hat{a} & \frac{\hat{a}^2}{2}\frac{C}{C+2C_0} & \hat{a} & \frac{\hat{a}^2}{2}\frac{C}{C+2C_0} & -3\hat{a} & \frac{\hat{a}^2}{2}\frac{3C+8C_0}{C+2C_0} & \hat{a} & -\frac{\hat{a}^2}{2}\frac{C}{C+2C_0} \\ -2 & -\hat{a} & -2 & -\hat{a} & -2 & \hat{a} & 6 & -3\hat{a} \\ \hat{a} & \frac{\hat{a}^2}{2}\frac{C}{C+2C_0} & \hat{a} & \frac{\hat{a}^2}{2}\frac{C}{C+2C_0} & \hat{a} & -\frac{\hat{a}^2}{2}\frac{C}{C+2C_0} & -3\hat{a} & \frac{\hat{a}^2}{2}\frac{3C+8C_0}{C+2C_0} \end{bmatrix}. \tag{5.23}$$

As in Chap. 4, the capacitance C_0 has only been introduced to allow the calculation of $\boldsymbol{K}_{\boldsymbol{e}}^{\mathrm{e}}$. It is a numerical parameter that has to be small compared to C but high enough to avoid numerical issues. A value of C_0 around $C \times 10^{-6}$ was found to be adequate for the following computations. Then, it still remains to define the element "mass matrix" $\boldsymbol{M}_{\boldsymbol{e}}^{\mathrm{e}}$. Equation (5.21) gives

$$\boldsymbol{M}_{\boldsymbol{e}}^{\mathrm{e}} = \frac{\boldsymbol{K}_{\boldsymbol{e}}^{\mathrm{e}} - \boldsymbol{D}_{\boldsymbol{e}}^{\mathrm{e}}}{\omega^2}. \tag{5.24}$$

Contrary to $\boldsymbol{K}_{\boldsymbol{e}}^{\mathrm{e}}$, the matrix $\boldsymbol{M}_{\boldsymbol{e}}^{\mathrm{e}}$ can be defined in the case of $C_0 = 0$ and it is found that

$$\boldsymbol{M}_{\boldsymbol{e}}^{\mathrm{e}} = \boldsymbol{M}_{\boldsymbol{e}}^{\boldsymbol{L}} + \boldsymbol{M}_{\boldsymbol{e}}^{\boldsymbol{L_\theta}}, \tag{5.25}$$

where

$$\boldsymbol{M}_{\boldsymbol{e}}^{\boldsymbol{L}} = \frac{L}{16} \begin{bmatrix} 1 & \frac{\hat{a}}{2} & 1 & \frac{\hat{a}}{2} & 1 & -\frac{\hat{a}}{2} & 1 & -\frac{\hat{a}}{2} \\ \frac{\hat{a}}{2} & \frac{\hat{a}^2}{4} & \frac{\hat{a}}{2} & \frac{\hat{a}^2}{4} & \frac{\hat{a}}{2} & -\frac{\hat{a}^2}{4} & \frac{\hat{a}}{2} & -\frac{\hat{a}^2}{4} \\ 1 & \frac{\hat{a}}{2} & 1 & \frac{\hat{a}}{2} & 1 & -\frac{\hat{a}}{2} & 1 & -\frac{\hat{a}}{2} \\ \frac{\hat{a}}{2} & \frac{\hat{a}^2}{4} & \frac{\hat{a}}{2} & \frac{\hat{a}^2}{4} & \frac{\hat{a}}{2} & -\frac{\hat{a}^2}{4} & \frac{\hat{a}}{2} & -\frac{\hat{a}^2}{4} \\ 1 & \frac{\hat{a}}{2} & 1 & \frac{\hat{a}}{2} & 1 & -\frac{\hat{a}}{2} & 1 & -\frac{\hat{a}}{2} \\ -\frac{\hat{a}}{2} & -\frac{\hat{a}^2}{4} & -\frac{\hat{a}}{2} & -\frac{\hat{a}^2}{4} & -\frac{\hat{a}}{2} & \frac{\hat{a}^2}{4} & -\frac{\hat{a}}{2} & \frac{\hat{a}^2}{4} \\ 1 & \frac{\hat{a}}{2} & 1 & \frac{\hat{a}}{2} & 1 & -\frac{\hat{a}}{2} & 1 & -\frac{\hat{a}}{2} \\ -\frac{\hat{a}}{2} & -\frac{\hat{a}^2}{4} & -\frac{\hat{a}}{2} & -\frac{\hat{a}^2}{4} & -\frac{\hat{a}}{2} & \frac{\hat{a}^2}{4} & -\frac{\hat{a}}{2} & \frac{\hat{a}^2}{4} \end{bmatrix} \tag{5.26}$$

and

$$\boldsymbol{M}_{\boldsymbol{e}}^{\boldsymbol{L_\theta}} = \frac{L_\theta}{2a^2} \begin{bmatrix} 3 & 0 & -1 & 0 & -1 & 0 & -1 & 0 \\ 0 & \frac{\hat{a}^2}{4} & 0 & \frac{\hat{a}^2}{4} & 0 & -\frac{\hat{a}^2}{4} & 0 & -\frac{\hat{a}^2}{4} \\ -1 & 0 & 3 & 0 & -1 & 0 & -1 & 0 \\ 0 & \frac{\hat{a}^2}{4} & 0 & \frac{\hat{a}^2}{4} & 0 & -\frac{\hat{a}^2}{4} & 0 & -\frac{\hat{a}^2}{4} \\ -1 & 0 & -1 & 0 & 3 & 0 & -1 & 0 \\ 0 & -\frac{\hat{a}^2}{4} & 0 & -\frac{\hat{a}^2}{4} & 0 & \frac{\hat{a}^2}{4} & 0 & \frac{\hat{a}^2}{4} \\ -1 & 0 & -1 & 0 & -1 & 0 & 3 & 0 \\ 0 & -\frac{\hat{a}^2}{4} & 0 & -\frac{\hat{a}^2}{4} & 0 & \frac{\hat{a}^2}{4} & 0 & \frac{\hat{a}^2}{4} \end{bmatrix}. \tag{5.27}$$

The electrical "dynamic stiffness matrix" in Eq. (5.21) is computed with the values of the electrical parameters: L, L_θ, C and $\hat{a}$. The exact same mass and stiffness matrices can be used when considering a mechanical plate element referring to Eq. (5.18). This simply

requires to replace the inductance L by the mass m of the unit cell, the capacitance C by the inverse of the bending stiffness D and the transformer ratio $\hat{a}$ by the length a of the unit cell.

5.2.5 Numerical validation of the finite difference model

A structure as a plate or its analogous electrical network can be modeled by replicating the unit cell in Fig. 5.3 along the x and y directions. Following an assembly process, as in the finite element method, a global stiffness matrix $\boldsymbol{K}$ and a global mass matrix $\boldsymbol{M}$ are built from the element matrices in Eqs. (5.23) and (5.25). From these global matrices, it thus becomes possible to perform a modal analysis by solving the following generalized eigenvalue problem:

$$\left[\boldsymbol{K} - \omega^2 \boldsymbol{M}\right] \boldsymbol{q} = \boldsymbol{0}. \tag{5.28}$$

Here, we do not make any difference between mechanical or electrical problems because the method applies similarly in both domains. In the following, we compute the modes of a mechanical plate without rotational inertia ($L_\theta = 0$) but we note that we would get the exact same results with an electrical network satisfying

$$\frac{1}{\hat{a}^2}\frac{1}{LC} = \frac{1}{a^2}\frac{D}{m}. \tag{5.29}$$

This corresponds to an extension of the modal coupling condition defined for bending in Chap. 4 because a beam model corresponds a special case of the present 2D model.

A modal analysis is performed in order to validate the proposed finite difference model. We consider a plate of side $l_x = 400$ mm, width $l_y = 320$ mm and thickness $h = 1.9$ mm. The Young's modulus of the plate is $Y = 69$ GPa, its Poisson's ratio is $\nu = 0.33$ and its density is $\rho = 2700$ kg/m^3. Simply-supported boundary conditions are taken into account in order to study the convergence of the finite difference model. Indeed, with those boundary conditions the natural frequencies of any modes 'm-n' are known analytically [136] and expressed as

$$f_{mn} = \frac{\pi}{2}\sqrt{\frac{D}{\rho h}}\left[\left(\frac{m}{l_x}\right)^2 + \left(\frac{n}{l_y}\right)^2\right]. \tag{5.30}$$

The natural frequencies of the first five modes of the plate are represented by horizontal continuous lines in Fig. 5.4(a). Then, the markers corresponds to the natural frequencies computed with either 5×4, 10×8, 15×12, 20×16 or 25×20 unit cells. It is observed that the natural frequencies of the discrete model approach those of a continuous plate when increasing the number of elements. Furthermore, the computed mode shapes also give a suitable approximation of the theoretical trigonometric modes, as seen in Fig. 5.4(b) with 25×20 unit cells. As could have been expected, the highest modes require a larger number

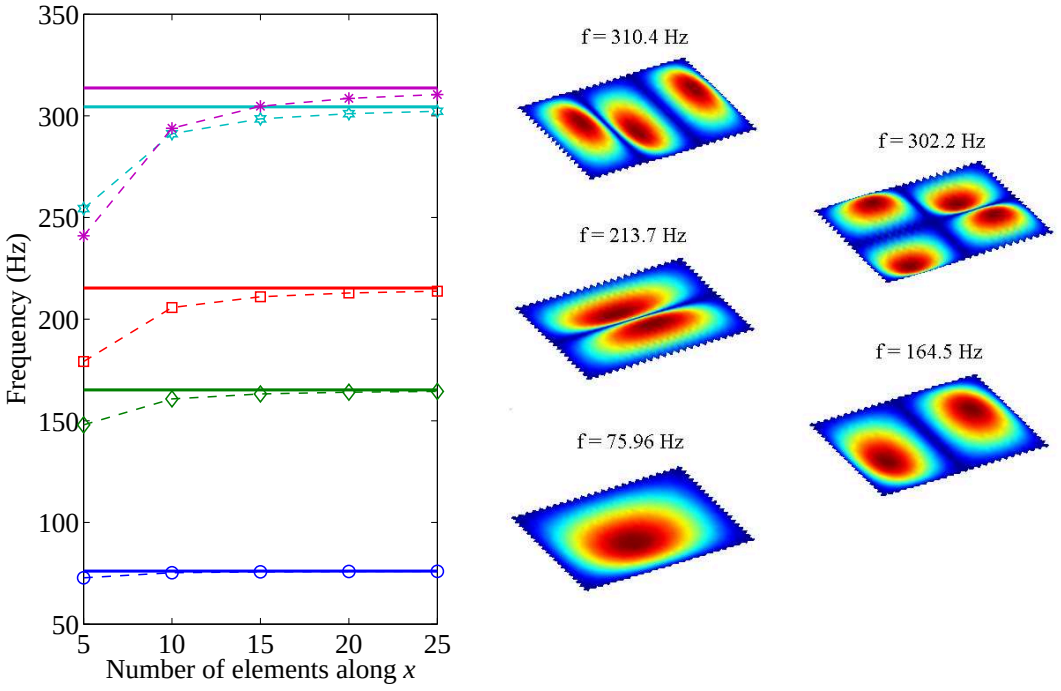

(a) (b)

Figure 5.4: Modal analysis with the finite difference model: (a) Convergence of the model. (b) Mode shapes computed with 25×20 unit cells.

of unit cell for a similar precision on the eigenvalues. The same recommendation as in Chaps. 3 and 4 can be formulated: at least 10 unit cells per wavelength are required to get a suitable approximation of a continuous plate. This corresponds to 15×12 unit cells for the present example focusing on the first five modes of a simply-supported plate. Actually, Fig. 5.4(a) shows that 15×12 unit cells offer a frequency error of less than 3%.

The finite difference model also allows the computation of frequency response functions from

$$\left[\boldsymbol{K} - \omega^2 \boldsymbol{M}\right] \boldsymbol{q} = \boldsymbol{F}, \tag{5.31}$$

where the force vector $\boldsymbol{F}$ contains terms representing harmonic excitation of the structure. If a transverse force F_{sim} is applied to the left of the unit cell (i, j), i.e. the i^{th} unit cell along the x axis and the j^{th} unit cell along the y axis, then

$$F_{\text{sim}} = Q_{\text{R}}^{(i-1,j)} - Q_{\text{L}}^{(i,j)}, \tag{5.32}$$

is the term that would appear in the force vector $\boldsymbol{F}$. By analogy, the excitation of an

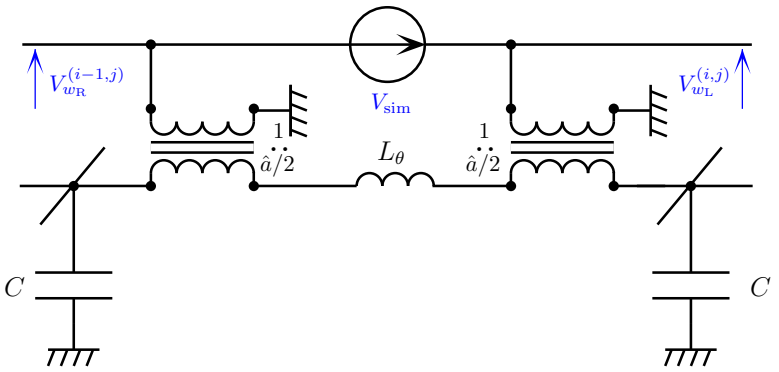

Figure 5.5: Voltage excitation applied between the unit cells $(i-1, j)$ and (i, j).

electrical network corresponds to a voltage

$$V_{\mathrm{sim}} = -V_{w_{\mathrm{R}}}^{(i-1,j)} + V_{w_{\mathrm{L}}}^{(i,j)}. \tag{5.33}$$

Figure 5.3 indicates that this excitation is a voltage applied between two transformers in the 'w' electrical line. This is represented in Fig. 5.5 without taking into account the capacitors $C_0/2$. For a frequency analysis of an electrical network, a scalar V_{sim} is thus inserted in the vector $\boldsymbol{F}$ to simulate the voltage excitation appearing in Fig. 5.5. Frequency response functions are not show here but, as the modal analysis, they validate the proposed finite difference model of a plate and thereby the analogous electrical network. The next step is then to implement the analogous network with a set of real electrical components.

5.3 Experimental validation of the plate electrical analogue

The electrical analogue of a clamped plate is assembled by using passive magnetic components, which had to be specifically designed for the present application. By analogy with modal vibration analysis of a mechanical structure, the network is excited with a voltage and electrical distributions of the current are measured. The topology of the network is validated by observing "electrical mode shapes" that are analogous to what is classically observed with a clamped plate.

5.3.1 Implementation of the analogous electrical network

In order to validate the electrical topology, the analogue of a clamped plate is built by connecting together 5×4 identical unit cells. This coarse mesh was chosen for practical reasons related to the number of electrical components. Even for the second mode, the resulting network cannot offer a minimum of 10 unit cells per wavelength, as was suggested

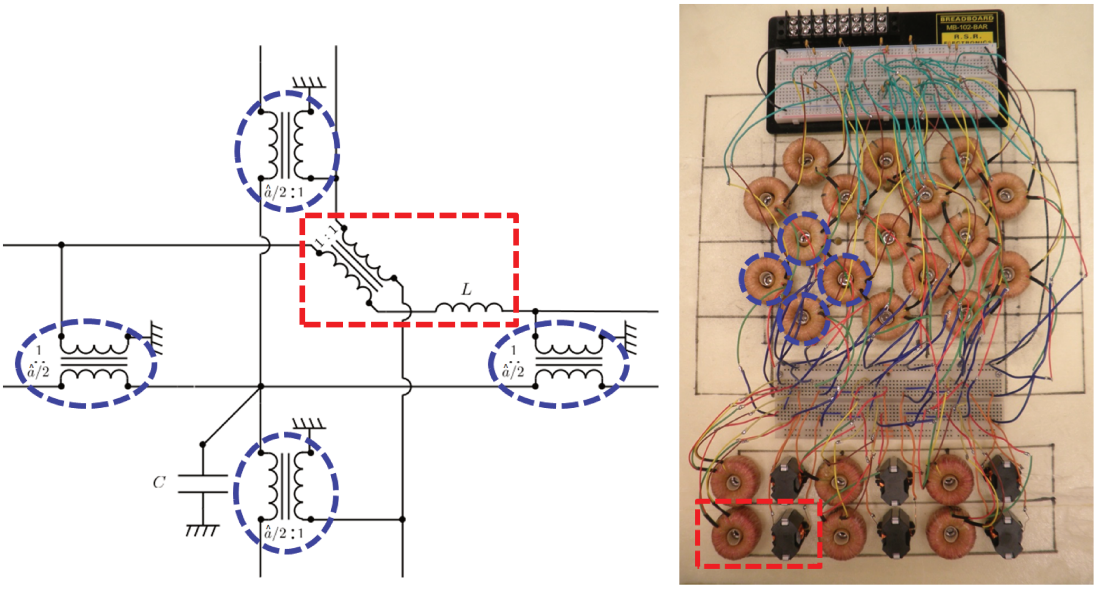

(a) (b)

Figure 5.6: Implementation of the analogous network: (a) Electrical unit cell. (b) Network made of 5×4 unit cells.

in Chaps. 3 and 4. There is thus no reason to expect an accurate correlation between the electrical resonance frequencies and those of a continuous plate but we can still hope for distributions of the electrical current that properly reproduce plate-like mode shapes. As we focus on the analogue of a clamped plate, the zero-displacement and zero-angle boundary conditions along the four edges of the plate are implemented by keeping the electrical ports open at the boundaries of the network. Thus, no current flows through the inductors and transformers along the four edges of the network, which means that those components are not required and can be removed from the network. For the same reason related to the choice of the boundary conditions, the capacitors at the four corners of the network are not necessary. A last simplification concerns the pairs of $\hat{a}/2$ ratio transformers, which can be replaced by single transformers of ratio $\hat{a}$. In the end, the network is assembled with 16 capacitors $C = 470$ nF, 17 transformers of ratio 4:1, 6 transformers of ratio 1:1 and 6 inductors $L = 0.9$ H. The positioning of the electrical components is highlighted in Figs. 5.6(a) and 5.6(b), where we note the frames with dashed lines that indicate the correspondence between the topology of the unit cell and the actual electrical network.

No parasitic elements are represented in the electrical unit cell in Fig. 5.6(a). Yet, the design of suitable transformers requires to take into account their magnetizing inductance L_{m}^{T} and their winding resistance R_{s}^{T}. Those additional elements are seen in Fig. 5.7(a) for the $\hat{a}$:1 transformer resulting from the connection in series of two $\hat{a}/2$:1 transformers. This

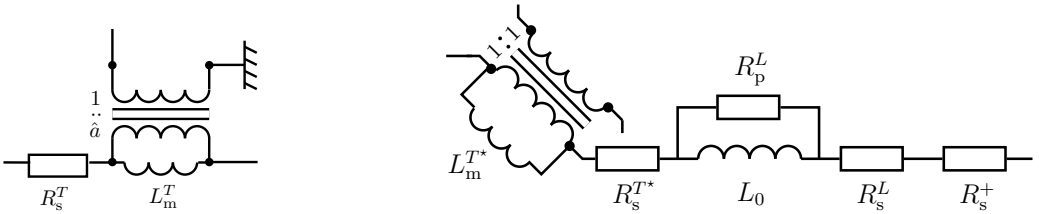

Figure 5.7: Equivalent circuits with parasitic elements: (a) Transformer of ratio $\hat{a}$:1. (b) Inductor connected to the 1:1 transformer.

corresponds to the electrical model proposed in Chap 4, without winding to winding capacitance, whose influence is negligible in the following design of magnetic components. The same electrical model is considered for the 1:1 transformer. As represented in Fig. 5.7(b), the corresponding magnetizing inductance and winding resistance are respectively $L_{\rm m}^{T^\star}$ and $R_{\rm s}^{T^\star}$. Note that the winding where we have placed the $R_{\rm s}^{T^\star}$ resistance is the one connected to the inductor. Moreover, the damping in the inductor can be modeled by a series resistance $R_{\rm s}^L$ and a parallel resistance $R_{\rm p}^L$. Another element to consider is the resistance $R_{\rm s}^+$ that can be added in series with the inductors L for a tuning purpose. In the end, the total series resistance in the electrical line of the inductor is equal to $R_{\rm s}^L + R_{\rm s}^{T^\star} + R_{\rm s}^+$.

The inductors are made by winding copper wire around the same type RM10 ferrite as the ones used in Chap. 2. Because their permeance is $A_L = 16$ μH, we need $\sqrt{L/A_L} = 237$ turns to generate an inductance $L = 0.9$ H. The series resistance is $R_{\rm s}^L = 2.6$ Ω with a copper wire diameter equal to 0.32 mm and the parallel resistance of the inductors is then evaluated experimentally to $R_{\rm p}^L = 200$ kΩ. Concerning the design of the transformers, following what has been proposed in Chap. 4, a sufficient magnetizing inductance is required to approximate an ideal transformer with a magnetic component. Still, the magnetizing inductance of the secondary winding (in the 'w' electrical line) has to be at least 50 times larger than the inductance L. This means that

$$L_{\rm m}^T \geq 50\hat{a}^2 L, \tag{5.34}$$

where $L_{\rm m}^T = A_L^T N_1^2$ is the magnetizing inductance of the primary winding (in the 'θ' electrical line), A_L^T is the permeance of the magnetic core and N_1 is the number of turns of the primary winding. With a transformer ratio $\hat{a} = 4$, Eq. (5.34) gives $L_{\rm m}^T \geq 720$ H. This high inductance value can be satisfied with a nanocrystalline toroidal core Nanophy 30×20×10 offering a permeance A_L^T around 100 μH. After winding $N_1 = 3000$ turns for the primary and $N_2 = 750$ turns for the secondary, a magnetizing inductance $L_{\rm m}^T/\hat{a}^2 = 57$ H is measured at 100 Hz and 1 V on the secondary winding. This means that $L_{\rm m}^T = 912$

H, which satisfies Eq. (5.34). Wires of diameters 0.15 mm and 0.22 mm are used for the primary and secondary windings, leading to a total winding resistance $R_{\mathrm{s}}^{T} = 353\ \Omega$. At last, the 1:1 transformers also need to offer a magnetizing inductance $L_{\mathrm{m}}^{T^\star}$ above 50 times the inductance L. This condition is satisfied with two windings of 750 turns on the same nanocrystalline toroid as for the 4:1 transformers. A winding resistance $R_{\mathrm{s}}^{T^\star} = 21\ \Omega$ is then obtained with a wire of 0.25 mm diameter.

5.3.2 Setup for the analysis of the electrical analogue

As the proposed electrical network represents the analogue of a clamped plate, it was decided to validate the electrical behavior with classical instrumentation normally dedicated to mechanical modal analysis. The setup is represented in Fig. 5.8 where a clamped plate and its electrical analogue appear together in order to show the analogy in terms of data acquisition. If the considered structure is the mechanical plate, we acquire the input force and the velocity, which is scanned on several points with a vibrometer. If the electrical network is analyzed, the signals of interest are not force and velocity but their direct analogues: an input voltage and the current flowing through the inductors. The direct measurement of the current would require the introduction of instruments

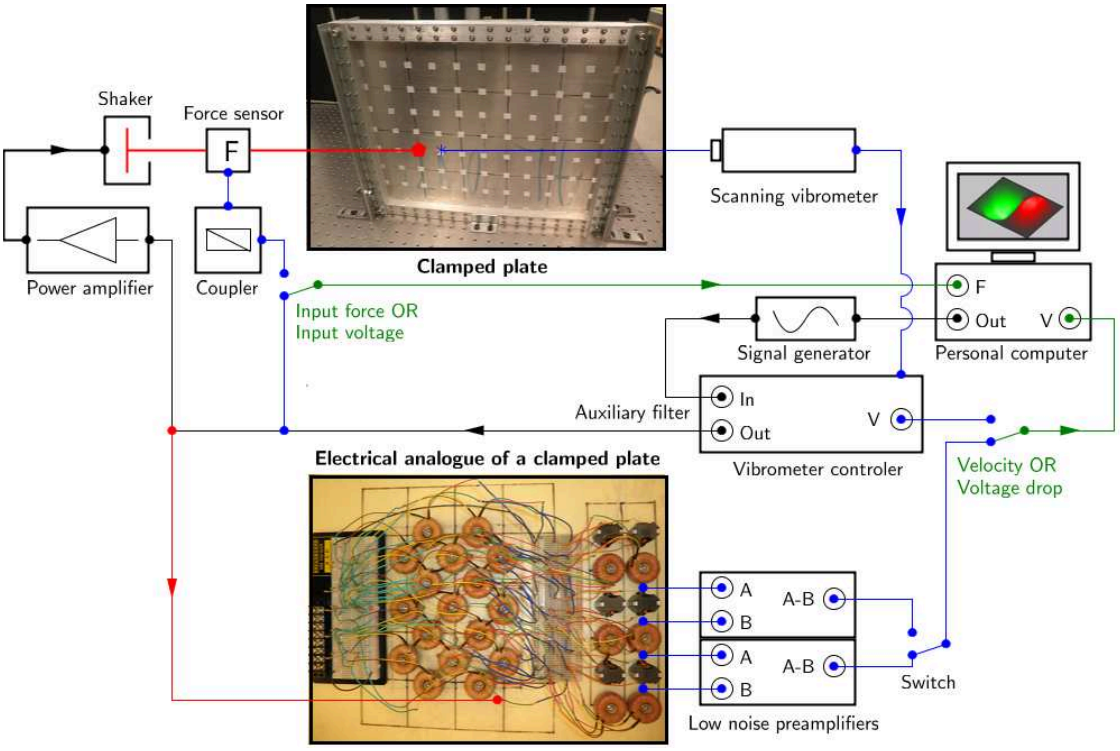

Figure 5.8: Experimental setup for the modal analysis of a clamped plate or for its analogous electrical network.

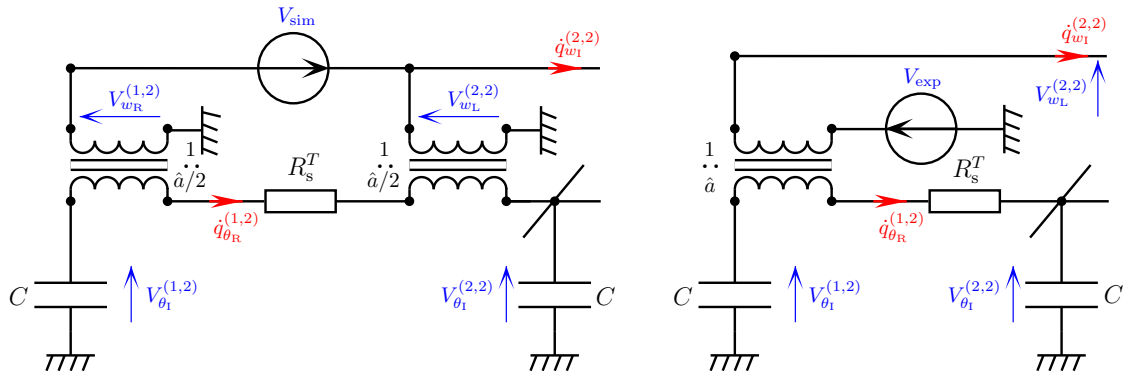

Figure 5.9: Voltage excitation as the analogue of an external transverse force between the unit cells (1,2) and (2,2): (a) Theoretical excitation between two transformers. (b) Simplified electrical circuit.

in the network, but this could modify its electrical properties. A less intrusive solution consists in measuring the voltage drop across the inductors, which is finally the analogue of the acceleration. This differential voltage is measured by using a low noise preamplifier offering a differential function. The resulting signal and the voltage input are sent to the workstation, where the electrical FRF is computed. Spatial distributions of the electrical variables can be obtained by scanning several points of the electrical network. This requires the use of two preamplifiers and a switch, which allows changing the measurement location without any delay. While the voltage drop is measured on one inductor, we have time to prepare the electrical connections for the next measurement. This is crucial because the scanning process is controlled by the vibrometer software that generates an instantaneous switching between measurement points.

The positioning of the voltage input exciting the electrical network is not obvious when we want to ensure an analogy with an external force that would be applied to a plate. Actually, the solution is given in Fig. 5.5 for an excitation between the unit cells $(i-1,j)$ and (i,j). For $i=j=2$, electrical simplifications at the boundaries gives the electrical circuit in Fig. 5.9(a), where appears the winding resistance R_{s}^{T} that replaces the inductance L_θ used for the model in Sec. 5.2. The problem is that in our network all the pairs of $\hat{a}/2$:1 transformers have been replaced by $\hat{a}$:1 transformers. It is thus not possible to directly generate a voltage V_{sim} simulating a transverse force between the unit cells (1,2) and (2,2). Yet, we remark that Fig. 5.9(a) gives

$$V_{\theta_{\text{I}}}^{(1,2)} - V_{\theta_{\text{I}}}^{(2,2)} = \frac{\hat{a}}{2} V_{w_{\text{R}}}^{(1,2)} + \mathrm{j}\omega R_{\text{s}}^{T} \dot{q}_{\theta_{\text{R}}}^{(1,2)} + \frac{\hat{a}}{2} V_{w_{\text{L}}}^{(2,2)} \quad . \tag{5.35}$$

Furthermore, there is a relation between the voltage excitation V_{sim} and the voltage across

the transformers as

$$V_{\text{sim}} = V_{w_{\text{L}}}^{(2,2)} - V_{w_{\text{R}}}^{(1,2)}. \tag{5.36}$$

Equations (5.35) and (5.36) thus lead to

$$V_{w_{\text{L}}}^{(2,2)} = \frac{1}{\hat{a}} \left(V_{\theta_{\text{I}}}^{(1,2)} - \text{j}\omega R_{\text{s}}^{T} \dot{q}_{\theta_{\text{R}}}^{(1,2)} - V_{\theta_{\text{I}}}^{(2,2)} \right) + \frac{1}{2} V_{\text{sim}}, \tag{5.37}$$

which is combined with

$$\dot{q}_{w_{\text{I}}}^{(2,2)} = \hat{a} \dot{q}_{\theta_{\text{R}}}^{(1,2)} \tag{5.38}$$

in order to give the simplified electrical scheme in Fig. 5.9(b) where

$$V_{\text{exp}} = \frac{1}{2} V_{\text{sim}}. \tag{5.39}$$

All of this shows that placing a voltage excitation V_{exp} between the ground and the secondary winding of the $\hat{a}$:1 transformer allows generating the analogue of a force between the (1,2) and (2,2) unit cells of the experimental network.

5.3.3 Electrical distributions and frequency response functions

The spatial distributions of the electrical current are represented in Fig. 5.10 together with an electrical FRF representing the ratio of the voltage drop across the inductor in the (2,2) unit cell to the excitation voltage $V_{\text{exp}} = 2$ V. It is shown in Fig. 5.10 that the addition of resistors $R_{\text{s}}^{+} = 180\ \Omega$ in series with the inductors of the network gives an electrical FRF, where the 6 electrical resonances induced by the 6 inductors are hardly observable. On the other hand, the resonances are clearly identified when $R_{\text{s}}^{+} = 0\ \Omega$. They can still be qualified as "smooth" when compared to the "sharp" resonances of a lightly damped mechanical system. The relatively low quality factor of the electrical resonances is mainly due to the internal resistance of the transformers.

The experimental results are compared to simulations computed with the model developed in Sec. 5.2. The inductance values L and L_θ appearing in Eqs. (5.26) and (5.27) are replaced by their complex values including damping elements. Impedance calculations based on Figs. 5.7(a) and 5.7(b) gives the equivalent inductance values

$$\begin{gathered} L(\omega) = \frac{R_{\text{p}}^{L} L_0}{R_{\text{p}}^{L} + \text{j}\omega L_0} + \frac{R_{\text{s}}^{L} + R_{\text{s}}^{T\star} + R_{\text{s}}^{+}}{\text{j}\omega} \\ \text{and} \quad L_\theta(\omega) = \frac{R_{\text{s}}^{T}}{\text{j}\omega} \end{gathered} . \tag{5.40}$$

As stated previously, a voltage drop is measured across the inductor of the unit cell (2,2).

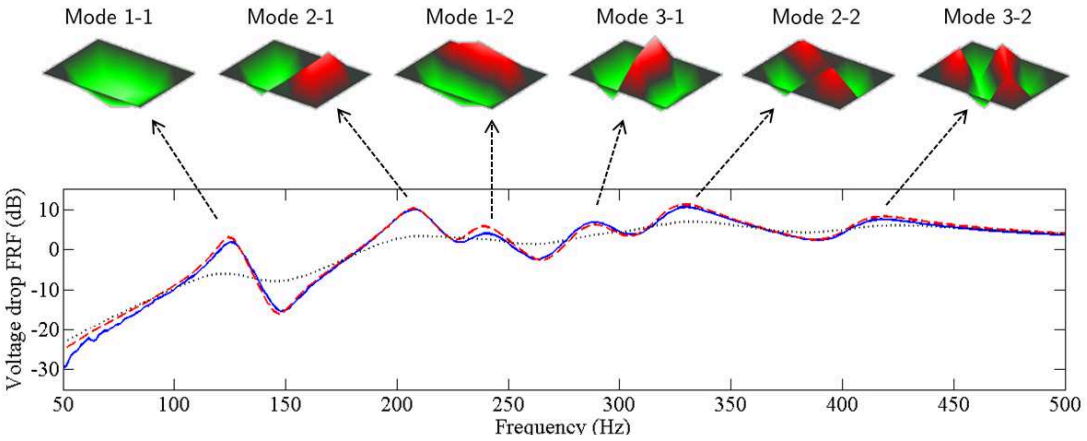

Figure 5.10: Experimental current distributions with respect to the voltage FRF with $L = 0.9$ H and $C = 470$ nF - (—) experimental FRF with $R_{\mathrm{s}}^{+} = 0\ \Omega$, (– –) simulated FRF with $R_{\mathrm{s}}^{+} = 0\ \Omega$, $(\cdots)$ simulated FRF with $R_{\mathrm{s}}^{+} = 180\ \Omega$.

In our model, this corresponds to a voltage

$$V_{\mathrm{drop}} = -\omega^2 L(\omega) q_{w_{\mathrm{I}}}^{(2,2)}. \tag{5.41}$$

where $q_{w_{\mathrm{I}}}^{(2,2)}$ is the displacement of electric charges through the considered inductor. This charge displacement is defined as

$$q_{w_{\mathrm{I}}}^{(2,2)} = q_{w_{\mathrm{L}}}^{(2,2)} + \frac{\hat{a}}{2} q_{\theta_{\mathrm{L}}}^{(2,2)}, \tag{5.42}$$

where $q_{w_{\mathrm{L}}}^{(2,2)}$ and $q_{\theta_{\mathrm{L}}}^{(2,2)}$ are computed from the model in Eq. (5.31). If V_{drop} has been experimentally measured with an input $V_{\mathrm{exp}} = 1$, a similar result should be obtained from a simulation with $V_{\mathrm{sim}} = 2$, as indicated by Eq. (5.39). Finally, Fig. 5.10 shows that the simulation fits with the experimental FRF. Moreover, the spatial distributions of the currents around the resonances approximate the mode shapes of a clamped plate. This validates the analogous network topology and confirms that the proposed finite difference scheme is able to reproduce the dynamic behavior of a plate.

5.4 Models for piezoelectric coupling to a 2D network

The coupled behavior of a square piezoelectric plate is defined from the 3D linear theory of piezoelectricity. A similar model is used for a square piezoelectric laminate made of a combination of piezoelectric and purely elastic layers. From this global model it can be drawn an electrical circuit defining the two-dimensional piezoelectric coupling. This new building block allows coupling the finite difference model to its analogous electrical

network. A discrete electromechanical unit cell can thus be defined and then eventually refined under a more accurate macro unit cell.

5.4.1 Square piezoelectric plate

As presented in Chap. 2, the 3D linear piezoelectricity [68] for a transverse isotropic PZT ceramic polarized in the direction '3' can be expressed as

$$\begin{bmatrix} \varepsilon_1 \\ \varepsilon_2 \\ \varepsilon_3 \\ \varepsilon_4 \\ \varepsilon_5 \\ \varepsilon_6 \\ D_1 \\ D_2 \\ D_3 \end{bmatrix} = \left[\begin{array}{cccccc|ccc} s_{11}^E & s_{12}^E & s_{13}^E & 0 & 0 & 0 & 0 & 0 & d_{31} \\ s_{12}^E & s_{11}^E & s_{13}^E & 0 & 0 & 0 & 0 & 0 & d_{31} \\ s_{13}^E & s_{13}^E & s_{33}^E & 0 & 0 & 0 & 0 & 0 & d_{33} \\ 0 & 0 & 0 & s_{44}^E & 0 & 0 & 0 & d_{15} & 0 \\ 0 & 0 & 0 & 0 & s_{44}^E & 0 & d_{15} & 0 & 0 \\ 0 & 0 & 0 & 0 & 0 & s_{66}^E & 0 & 0 & 0 \\ \hline 0 & 0 & 0 & 0 & d_{15} & 0 & \epsilon_{11}^\sigma & 0 & 0 \\ 0 & 0 & 0 & d_{15} & 0 & 0 & 0 & \epsilon_{11}^\sigma & 0 \\ d_{31} & d_{31} & d_{33} & 0 & 0 & 0 & 0 & 0 & \epsilon_{33}^\sigma \end{array}\right] \begin{bmatrix} \sigma_1 \\ \sigma_2 \\ \sigma_3 \\ \sigma_4 \\ \sigma_5 \\ \sigma_6 \\ E_1 \\ E_2 \\ E_3 \end{bmatrix}. \tag{5.43}$$

Regarding a thin piezoelectric plate whose thickness corresponds to the direction of polarization, a classical hypothesis is to consider that the electric field is zero along the principal directions [69], i.e. $E_1 = E_2 = 0$. The plane stress hypothesis $\sigma_3 = 0$ then leads to the reduced matrix

$$\begin{bmatrix} \varepsilon_1 \\ \varepsilon_2 \\ \varepsilon_4 \\ \varepsilon_5 \\ \varepsilon_6 \\ D_3 \end{bmatrix} = \begin{bmatrix} s_{11}^E & s_{12}^E & 0 & 0 & 0 & d_{31} \\ s_{12}^E & s_{11}^E & 0 & 0 & 0 & d_{31} \\ 0 & 0 & s_{44}^E & 0 & 0 & 0 \\ 0 & 0 & 0 & s_{44}^E & 0 & 0 \\ 0 & 0 & 0 & 0 & s_{66}^E & 0 \\ d_{31} & d_{31} & 0 & 0 & 0 & \epsilon_{33}^\sigma \end{bmatrix} \begin{bmatrix} \sigma_1 \\ \sigma_2 \\ \sigma_4 \\ \sigma_5 \\ \sigma_6 \\ E_3 \end{bmatrix}. \tag{5.44}$$

Consequently, it is found that

$$\begin{array}{l} \varepsilon_1 + \varepsilon_2 = (s_{11}^E + s_{12}^E)(\sigma_1 + \sigma_2) + 2d_{31}E_3 \\ D_3 = d_{31}(\sigma_1 + \sigma_2) + \epsilon_{33}^\sigma E_3 \end{array}. \tag{5.45}$$

From the definition of the material constants s_{11}^E and s_{12}^E [68, 69], we get $s_{11}^E + s_{12}^E = (1 - \nu_\mathrm{p})/Y_\mathrm{p}^E$, where ν_p is the Poisson's ratio of the piezoelectric material and $Y_\mathrm{p}^E = 1/s_{11}^E$ is its Young's modulus when the transverse electric field is equal to zero ($E_3 = 0$). Equation (5.45) can then be reorganized into

$$\begin{array}{l} \sigma_1 + \sigma_2 = \dfrac{Y_\mathrm{p}^E}{1-\nu_\mathrm{p}}(\varepsilon_1 + \varepsilon_2) - d_{31}\dfrac{2Y_\mathrm{p}^E}{1-\nu_\mathrm{p}}E_3 \\ D_3 = d_{31}\dfrac{Y_\mathrm{p}^E}{1-\nu_\mathrm{p}}(\varepsilon_1 + \varepsilon_2) + \epsilon_{33}^{\varepsilon^\star}E_3 \end{array}, \tag{5.46}$$

where

$$\epsilon_{33}^{\varepsilon^\star} = \epsilon_{33}^\sigma\left(1 - \frac{2}{1-\nu_\mathrm{p}}\frac{d_{31}^2}{s_{11}^E\epsilon_{33}^\sigma}\right) \tag{5.47}$$

is the equivalent permittivity of a piezoelectric plate which is blocked along its principal directions, i.e. $\varepsilon_1 = \varepsilon_2 = 0$.

For a plate subjected to bending motion, the strains ε_1 and ε_2 can be expressed as

$$\varepsilon_1 = -z\frac{\partial \theta_x}{\partial x} \quad \text{and} \quad \varepsilon_2 = -z\frac{\partial \theta_y}{\partial y} \ , \tag{5.48}$$

where x and y refer to the principal directions '1' and '2', and z refers to the transverse direction '3'. Considering the plate theory [136] for a square unit cell of side l_p, the bending moments M_x and M_y that has been defined in Eq. (5.8) are related to the stresses σ_1 and σ_2 through

$$M_x = l_\mathrm{p} \int_z \sigma_1 z dz \quad \text{and} \quad M_y = l_\mathrm{p} \int_z \sigma_2 z dz \ . \tag{5.49}$$

Furthermore, the total electric charge q_p and the voltage V_p between the two electrodes of the piezoelectric element are defined as

$$q_\mathrm{p} = -\int_x \int_y D_3 dx dy \quad \text{and} \quad E_3 = -\frac{V_\mathrm{p}}{h_\mathrm{p}} \ , \tag{5.50}$$

where h_p is the thickness of the piezoelectric plate. If the piezoelectric plate is at a distance λ from the mid-surface and is sufficiently thin, i.e. $\lambda \gg h_\mathrm{p}$ so that $\int_{\lambda-h_\mathrm{p}/2}^{\lambda+h_\mathrm{p}/2} z dz/h_\mathrm{p} \approx \lambda$, Eq. (5.46) gives

$$\begin{aligned} M_x + M_y &= -\frac{Y_\mathrm{p}^E I_\mathrm{p}}{1-\nu_\mathrm{p}} \left(\frac{\partial \theta_x}{\partial x} + \frac{\partial \theta_y}{\partial y} \right) + \lambda l_\mathrm{p} d_{31} \frac{2Y_\mathrm{p}^E}{1-\nu_\mathrm{p}} V_\mathrm{p} \\ q_\mathrm{p} &= \lambda l_\mathrm{p} d_{31} \frac{Y_\mathrm{p}^E}{1-\nu_\mathrm{p}} (\overline{\Delta\theta}_x + \overline{\Delta\theta}_y) + \epsilon_{33}^{\varepsilon\star} \frac{l_\mathrm{p}^2}{h_\mathrm{p}} V_\mathrm{p} \end{aligned} \ , \tag{5.51}$$

with $\overline{\Delta\theta}_x = \frac{1}{l_\mathrm{p}} \int_0^{l_\mathrm{p}} \Delta\theta_x(y) dy$ and $\overline{\Delta\theta}_y = \frac{1}{l_\mathrm{p}} \int_0^{l_\mathrm{p}} \Delta\theta_y(x) dx$ representing average differences of the angles at opposite sides, and $I_\mathrm{p} = l_\mathrm{p} \int_{\lambda-h_\mathrm{p}/2}^{\lambda+h_\mathrm{p}/2} z^2 dz$, the second moment of area. Recall that the sum of the bending moment is related to the variable M defined in Eq. (5.2) through

$$M_\mathrm{p} = -\frac{1}{1+\nu} \left(M_x + M_y \right). \tag{5.52}$$

So, Eq. (5.51) is equivalent to

$$\begin{aligned} M_\mathrm{p} &= l_\mathrm{p} D_\mathrm{p}^E \left(\frac{\partial \theta_x}{\partial x} + \frac{\partial \theta_y}{\partial y} \right) - \frac{2e_\mathrm{p}}{1-\nu_\mathrm{p}^2} V_\mathrm{p} \\ q_\mathrm{p} &= \frac{e_\mathrm{p}}{1-\nu_\mathrm{p}} (\overline{\Delta\theta}_x + \overline{\Delta\theta}_y) + C_\mathrm{p}^\varepsilon V_\mathrm{p} \end{aligned} \ , \tag{5.53}$$

where $D_\mathrm{p}^E = \dfrac{Y_\mathrm{p}^E I_\mathrm{p}}{(1-\nu_\mathrm{p}^2) l_\mathrm{p}}$ is the short-circuited bending stiffness, $C_\mathrm{p}^\varepsilon = \epsilon_{33}^{\varepsilon\star} \dfrac{l_\mathrm{p}^2}{h_\mathrm{p}}$ is the blocked piezoelectric capacitance and $e_\mathrm{p} = \lambda l_\mathrm{p} d_{31} Y_\mathrm{p}^E$ is the coupling coefficient. It is noticed that Eq. (5.53) does not offer a symmetrical reciprocity [74], i.e. the global coefficients related to

the piezoelectric coupling are not the same for the mechanical and electrical contributions. To model the coupling with a passive circuit involving a transformer as in Chaps. 3 and 4, the symmetry condition is yet required. Equation (5.53) can then be written as

$$\begin{aligned} M_\mathrm{p} &= l_\mathrm{p} D_\mathrm{p}^E \left(\frac{\partial \theta_x}{\partial x} + \frac{\partial \theta_y}{\partial y} \right) - \sqrt{2(1+\nu_\mathrm{p})} \frac{e_\mathrm{p}}{1-\nu_\mathrm{p}^2} \left[\sqrt{\frac{2}{1+\nu_\mathrm{p}}} V_\mathrm{p} \right] \\ \left[\sqrt{\frac{2}{1+\nu_\mathrm{p}}} q_\mathrm{p} \right] &= \sqrt{2(1+\nu_\mathrm{p})} \frac{e_\mathrm{p}}{1-\nu_\mathrm{p}^2} (\overline{\Delta\theta}_x + \overline{\Delta\theta}_y) + C_\mathrm{p}^\varepsilon \left[\sqrt{\frac{2}{1+\nu_\mathrm{p}}} V_\mathrm{p} \right] \end{aligned} , \tag{5.54}$$

which is equivalent to

$$\begin{aligned} M_\mathrm{p} &= l_\mathrm{p} D_\mathrm{p}^E \left(\frac{\partial \theta_x}{\partial x} + \frac{\partial \theta_y}{\partial y} \right) - e_\mathrm{p}^\star V_\mathrm{p}^\star \\ q_\mathrm{p}^\star &= e_\mathrm{p}^\star \left(\overline{\Delta\theta}_x + \overline{\Delta\theta}_y \right) + C_\mathrm{p}^\varepsilon V_\mathrm{p}^\star \end{aligned} , \tag{5.55}$$

where $e_\mathrm{p}^\star = \dfrac{\sqrt{2(1+\nu_\mathrm{p})}}{1-\nu_\mathrm{p}^2} e_\mathrm{p}$, $q_\mathrm{p}^\star = \sqrt{\dfrac{2}{1+\nu_\mathrm{p}}} q_\mathrm{p}$ and $V_\mathrm{p}^\star = \sqrt{\dfrac{2}{1+\nu_\mathrm{p}}} V_\mathrm{p}$.

5.4.2 Global model for a square piezoelectric laminate

A piezoelectric laminate is made of a superposition of piezoelectric and purely elastic layers. A simple laminate is represented in Fig. 5.11, where a square piezoelectric patch of side l_p and thickness h_p covers an elastic structure of side a and thickness h_s. If we consider that the piezoelectric laminate can be approximated by a homogeneous piezoelectric medium, a similar form as in Eq. (5.55) can be used to describe the piezoelectric coupling in the whole laminate:

$$\begin{aligned} M &= a D^E \left(\frac{\partial \theta_x}{\partial x} + \frac{\partial \theta_y}{\partial y} \right) - e_\theta V_{\theta_\mathrm{I}} \\ q_{\theta_\mathrm{I}} &= e_\theta \left(\overline{\Delta\theta}_x + \overline{\Delta\theta}_y \right) + C^\varepsilon V_{\theta_\mathrm{I}} \end{aligned} . \tag{5.56}$$

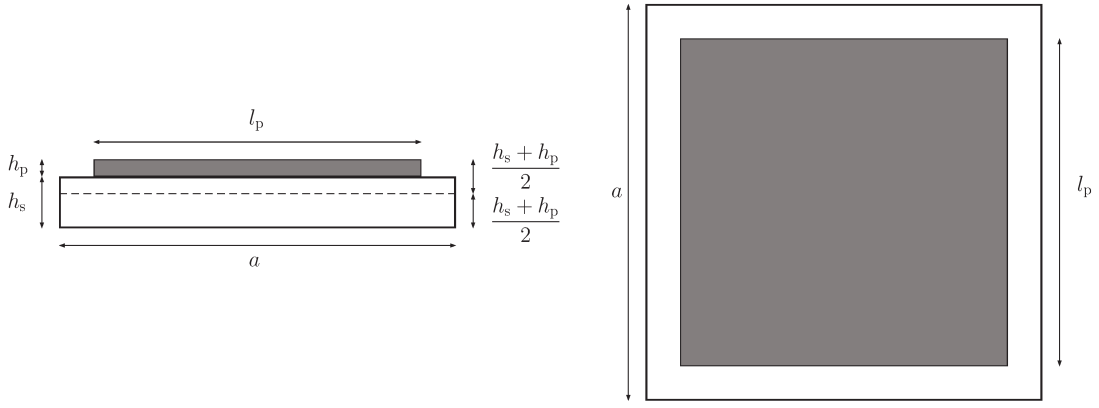

Figure 5.11: Square piezoelectric laminate with a single piezoelectric patch.

If the Poisson's ratio of the elastic structure ν_s is close to the one of the piezoelectric patch, the global bending stiffness of the laminate D^E is defined from

$$\frac{1}{D^E} = \frac{\left(1-\nu_\mathrm{s}^2\right) l_\mathrm{p}}{Y_\mathrm{s} I_\mathrm{s} + Y_\mathrm{p}^E I_\mathrm{p}} + \frac{\left(1-\nu_\mathrm{s}^2\right)(a-l_\mathrm{p})}{Y_\mathrm{s} I_\mathrm{s}}, \tag{5.57}$$

which corresponds to a series of two bending stiffness elements, one for the segment with piezoelectric material and one for the segments without piezoelectric material. I_s and I_p are the second moments of area for the elastic and piezoelectric plates, respectively. When considering that the Young's moduli of both material have close values and that the piezoelectric plate covers most of the elastic surface ($l_\mathrm{p} \approx a$), the mid-surface is around a position $(h_\mathrm{s}+h_\mathrm{p})/2$ from the free surface of the piezoelectric patch, as represented in Fig. 5.11. Consequently, the second moments of area can be approximated by

$$\begin{aligned} I_\mathrm{p} &= l_\mathrm{p} \int_{\frac{h_\mathrm{s}-h_\mathrm{p}}{2}}^{\frac{h_\mathrm{s}+h_\mathrm{p}}{2}} z^2 dz = l_\mathrm{p} \frac{(h_\mathrm{s}+h_\mathrm{p})^3 - (h_\mathrm{s}-h_\mathrm{p})^3}{24} \\ \text{and} \quad I_\mathrm{s} &= a \int_{-\frac{h_\mathrm{s}+h_\mathrm{p}}{2}}^{\frac{h_\mathrm{s}-h_\mathrm{p}}{2}} z^2 dz = a \frac{(h_\mathrm{s}-h_\mathrm{p})^3 + (h_\mathrm{s}+h_\mathrm{p})^3}{24} \end{aligned} . \tag{5.58}$$

The global coupling coefficient e_θ could be eventually obtained from 3D calculations [18, 71] but it has been remarked that the bonding layer between the main structure and the patches has generally a non-negligible influence. A more direct method to get the actual value for e_θ is to compare the short- and open-circuited responses of the whole piezoelectric structure. A lack of precise modeling of the bonding layer leads us to use the latter approach in the following comparisons with experimental results. The same conclusions arise for the determination of the blocked capacitance C^ε which would require a precise 3D modeling. This can be avoided by direct measurement of the piezoelectric capacitance when preventing transverse displacement of the mechanical structure.

5.4.3 Discrete electromechanical unit cell

The square piezoelectric laminate in Fig. 5.11 defines the unit cell of a system based on a periodic array of piezoelectric patches covering an elastic plate. When considering large wavelength compared to the length a of a unit cell,

$$\begin{aligned} \frac{\partial \theta_x}{\partial x} &\approx \frac{\theta_\mathrm{R} - \theta_\mathrm{L}}{a} \quad , \quad \frac{\partial \theta_y}{\partial y} \approx \frac{\theta_\mathrm{T} - \theta_\mathrm{B}}{a} \\ \overline{\Delta\theta}_x &\approx \theta_\mathrm{R} - \theta_\mathrm{L} \quad , \quad \overline{\Delta\theta}_y \approx \theta_\mathrm{T} - \theta_\mathrm{B} \end{aligned} , \tag{5.59}$$

where θ_R, θ_L, θ_T and θ_B are the angles on the 4 sides of the unit cell (right, left, top and bottom sides respectively). So, Eq. (5.56) is written as

$$\begin{aligned} M_\mathrm{I} &= D^E \left(\theta_\mathrm{R} - \theta_\mathrm{L} + \theta_\mathrm{T} - \theta_\mathrm{B}\right) - e_\theta V_{\theta_\mathrm{I}} \\ q_{\theta_\mathrm{I}} &= e_\theta \left(\theta_\mathrm{R} - \theta_\mathrm{L} + \theta_\mathrm{T} - \theta_\mathrm{B}\right) + C^\varepsilon V_{\theta_\mathrm{I}} \end{aligned} , \tag{5.60}$$

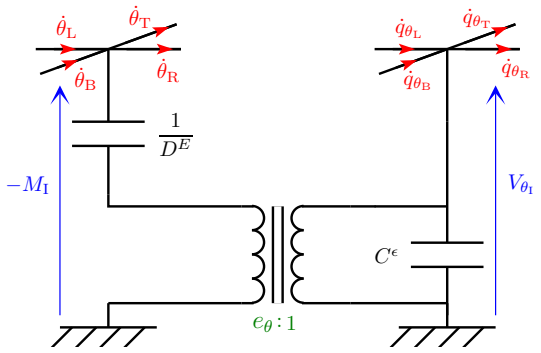

Figure 5.12: Model of the piezoelectric coupling for a square piezoelectric laminate.

which is equivalent to

$$\begin{aligned} -M_{\mathrm{I}} &= \frac{D^E}{\mathrm{j}\omega}\left(\dot{\theta}_{\mathrm{L}} - \dot{\theta}_{\mathrm{R}} + \dot{\theta}_{\mathrm{B}} - \dot{\theta}_{\mathrm{T}}\right) + e_{\theta} V_{\theta_{\mathrm{I}}} \\ V_{\theta_{\mathrm{I}}} &= \frac{1}{\mathrm{j}\omega C^{\varepsilon}}\left[\dot{q}_{\theta_{\mathrm{I}}} + e_{\theta}\left(\dot{\theta}_{\mathrm{L}} - \dot{\theta}_{\mathrm{R}} + \dot{\theta}_{\mathrm{B}} - \dot{\theta}_{\mathrm{T}}\right)\right] \end{aligned} . \tag{5.61}$$

Note that M_{I} has the same form as in Eq. (5.5) when the piezoelectric coupling coefficient e_{θ} is equal to zero. With $\dot{q}_{\theta_{\mathrm{I}}} = \dot{q}_{\theta_{\mathrm{L}}} - \dot{q}_{\theta_{\mathrm{R}}} + \dot{q}_{\theta_{\mathrm{B}}} - \dot{q}_{\theta_{\mathrm{T}}}$, Eq. (5.61) can be represented by the electrical circuit in Fig. 5.12. This corresponds to a 2D extension of the model used to represent the unit cell subjected to one-dimensional bending motion in Chap. 4.

The proposed 2D model offers a way to couple a square plate unit cell to it analogous electrical network. Indeed, the circuit in Fig. 5.12 can be inserted between the unit cell involving mechanical variables as in Fig. 5.2 and its electrical counterpart as in Fig. 5.3. In the end, we get a discrete electromechanical unit cell represented by an electrical circuit involving four external ports per side, i.e. 16 ports in total. The whole set of discrete equations defining the electromechanical unit cell is written down, the internal variables are then eliminated and the system of equations is solved for the side force and voltage variables as linear combinations of the displacement and electric charge variables. We obtain a 16×16 "dynamic stiffness matrix" of the coupled system under the form

$$\boldsymbol{F}_{\boldsymbol{c}}^{\mathrm{e}} = \boldsymbol{D}_{\boldsymbol{c}}^{\mathrm{e}} \boldsymbol{q}_{\boldsymbol{c}}^{\mathrm{e}} \tag{5.62}$$

Here, the force and displacement vectors are

$$\boldsymbol{F}_{\boldsymbol{c}}^{\mathrm{e}} = \begin{bmatrix} \boldsymbol{F}_{\mathrm{B}}^{\mathrm{e}} & \boldsymbol{F}_{\mathrm{L}}^{\mathrm{e}} & \boldsymbol{F}_{\mathrm{R}}^{\mathrm{e}} & \boldsymbol{F}_{\mathrm{T}}^{\mathrm{e}} \end{bmatrix}^T \quad \text{and} \quad \boldsymbol{q}_{\boldsymbol{c}}^{\mathrm{e}} = \begin{bmatrix} \boldsymbol{q}_{\mathrm{B}}^{\mathrm{e}} & \boldsymbol{q}_{\mathrm{L}}^{\mathrm{e}} & \boldsymbol{q}_{\mathrm{R}}^{\mathrm{e}} & \boldsymbol{q}_{\mathrm{T}}^{\mathrm{e}} \end{bmatrix}^T \tag{5.63}$$

where

$$\begin{aligned} \boldsymbol{F}_{\mathrm{B}}^{\mathrm{e}} &= \begin{bmatrix} -Q_{\mathrm{B}} & -M_{\mathrm{B}} & V_{w\mathrm{B}} & V_{\theta\mathrm{B}} \end{bmatrix}^T \\ \boldsymbol{F}_{\mathrm{L}}^{\mathrm{e}} &= \begin{bmatrix} -Q_{\mathrm{L}} & -M_{\mathrm{L}} & V_{w\mathrm{L}} & V_{\theta\mathrm{L}} \end{bmatrix}^T \\ \boldsymbol{F}_{\mathrm{R}} &= \begin{bmatrix} Q_{\mathrm{R}} & M_{\mathrm{R}} & -V_{w\mathrm{R}} & -V_{\theta\mathrm{R}} \end{bmatrix}^T \\ \boldsymbol{F}_{\mathrm{T}}^{\mathrm{e}} &= \begin{bmatrix} Q_{\mathrm{T}} & M_{\mathrm{T}} & -V_{w\mathrm{T}} & -V_{\theta\mathrm{T}} \end{bmatrix}^T \end{aligned} \quad \text{and} \quad \begin{aligned} \boldsymbol{q}_{\mathrm{B}}^{\mathrm{e}} &= \begin{bmatrix} W_{\mathrm{B}} & \theta_{\mathrm{B}} & q_{w\mathrm{B}} & q_{\theta\mathrm{B}} \end{bmatrix}^T \\ \boldsymbol{q}_{\mathrm{L}}^{\mathrm{e}} &= \begin{bmatrix} W_{\mathrm{L}} & \theta_{\mathrm{L}} & q_{w\mathrm{L}} & q_{\theta\mathrm{L}} \end{bmatrix}^T \\ \boldsymbol{q}_{\mathrm{R}}^{\mathrm{e}} &= \begin{bmatrix} W_{\mathrm{R}} & \theta_{\mathrm{R}} & q_{w\mathrm{R}} & q_{\theta\mathrm{R}} \end{bmatrix}^T \\ \boldsymbol{q}_{\mathrm{T}}^{\mathrm{e}} &= \begin{bmatrix} W_{\mathrm{T}} & \theta_{\mathrm{T}} & q_{w\mathrm{T}} & q_{\theta\mathrm{T}} \end{bmatrix}^T . \end{aligned} \tag{5.64}$$

The closed-form expression of $\boldsymbol{D}_{\boldsymbol{c}}^{\mathrm{e}}$ is not given in this document because the high number of symbolic equations results in a large symbolic matrix which cannot be written compactly. In any case, by following the same method as what has been presented in Sec. 5.2 with an assembly of element matrices, the model in Eq. (5.62) allows the simulation of a discretized plate coupled to its analogous electrical network.

5.4.4 Macro unit cell

Similarly to what has been observed in Chaps. 3 and 4, a discrete model based on a large wavelength assumption is not reliable when the considered wavelength approaches the length of the unit cell. In order to maintain a large wavelength condition, one could propose to increase the number of unit cell. However, when considering a practical system, the number of unit cells is usually defined from the choice of the piezoelectric array. A solution is to define a macro unit cell where the mechanical part is refined but the number of unit cells for the electrical network is kept constant. This solution is represented in Fig. 5.13(a) when the unit cell in Fig. 5.11 is divided in four identical sub-cells. The four piezoelectric patches are connected in parallel and the ratio of piezoelectric material is not modified. This means that the global constants D^E, C^ε and e_θ appearing in Eq. (5.60) are still the same for the macro unit cell. Also, from the definition of the global constants, the bending stiffness D^E is the same for the macro unit cell and for the sub-cells but as the coupling coefficient e_θ is proportional to the side of the square cells, it is divided by two when considering four sub-cells. The piezoelectric coupling in the macro unit cell in Fig. 5.13(a) can thus be represented by the electrical circuit in Fig. 5.14. In fact, this new circuit is made of four times the circuit in Fig. 5.12, around a single global capacitance C^ε.

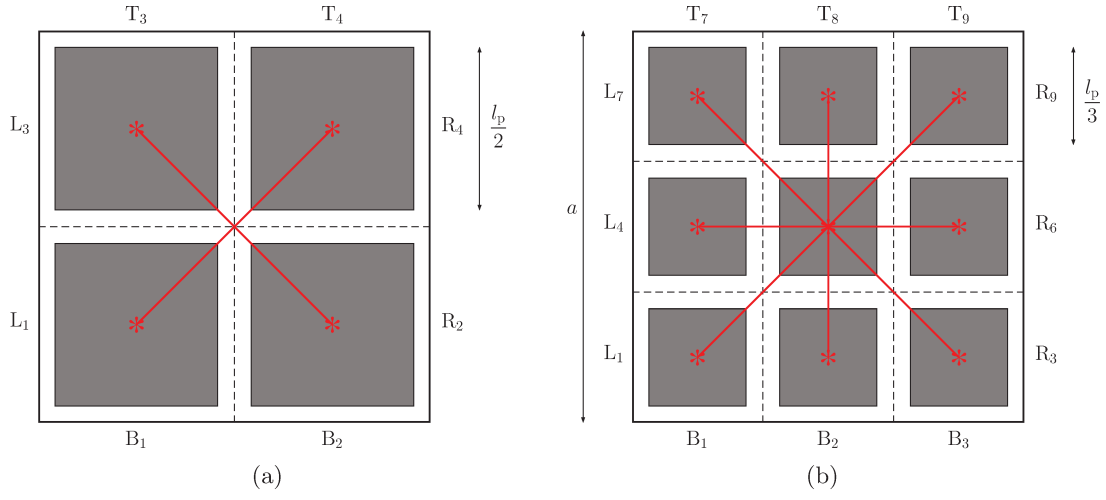

Figure 5.13: Macro unit cells: (a) With 4 sub-cells. (b) With 9 sub-cells.

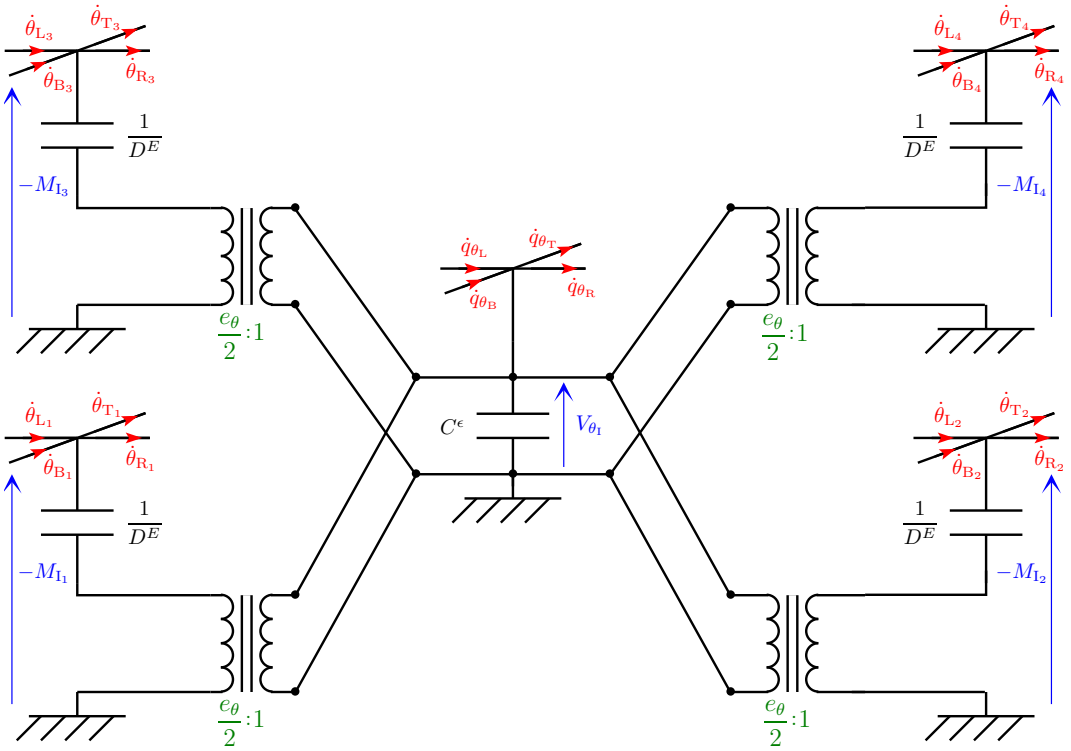

Figure 5.14: Model of the piezoelectric coupling for a macro unit cell with 4 sub-cells.

The numbering of the electrical variables refers to Fig. 5.13(a), where the side coordinates are written explicitly. In the end, we would get a macro unit cell with a number of mechanical variables that has been doubled. The element matrix $\boldsymbol{D}_{\boldsymbol{c}}^{\mathrm{e}}$ in Eq. (5.62) would thus be a 24×24 matrix, which can be obtained with a symbolic solver.

Depending on the considered wavelength, the macro unit cell in Fig. 5.13(a) may still require a finer mesh to generate a suitable approximation of the mechanical domain. An improvement is to use 9 sub-cells instead of 4, which leads to the macro unit cell represented in Fig. 5.13(b). A similar electrical circuit as in Fig. 5.14 could be drawn with 9 transformers connected to a single capacitor. From the whole set of equations defining the electrical unit cell and the 9 mechanical sub-cells, a 32×32 element matrix $\boldsymbol{D}_{\boldsymbol{c}}^{\mathrm{e}}$ is obtained. The force vectors on the sides of the macro unit cell are thus

$$\begin{aligned}
\boldsymbol{F}_{\mathrm{B}}^{\mathrm{e}} &= \begin{bmatrix} -Q_{\mathrm{B}_1} & -M_{\mathrm{B}_1} & -Q_{\mathrm{B}_2} & -M_{\mathrm{B}_2} & -Q_{\mathrm{B}_3} & -M_{\mathrm{B}_3} & V_{w\mathrm{B}} & V_{\theta\mathrm{B}} \end{bmatrix}^T \\
\boldsymbol{F}_{\mathrm{L}}^{\mathrm{e}} &= \begin{bmatrix} -Q_{\mathrm{L}_1} & -M_{\mathrm{L}_1} & -Q_{\mathrm{L}_4} & -M_{\mathrm{L}_4} & -Q_{\mathrm{L}_7} & -M_{\mathrm{L}_7} & V_{w\mathrm{L}} & V_{\theta\mathrm{L}} \end{bmatrix}^T \\
\boldsymbol{F}_{\mathrm{R}}^{\mathrm{e}} &= \begin{bmatrix} Q_{\mathrm{R}_3} & M_{\mathrm{R}_3} & Q_{\mathrm{R}_6} & M_{\mathrm{R}_6} & Q_{\mathrm{R}_9} & M_{\mathrm{R}_9} & -V_{w\mathrm{R}} & -V_{\theta\mathrm{R}} \end{bmatrix}^T \\
\boldsymbol{F}_{\mathrm{T}}^{\mathrm{e}} &= \begin{bmatrix} Q_{\mathrm{T}_7} & M_{\mathrm{T}_7} & Q_{\mathrm{T}_8} & M_{\mathrm{T}_8} & Q_{\mathrm{T}_9} & M_{\mathrm{T}_9} & -V_{w\mathrm{T}} & -V_{\theta\mathrm{T}} \end{bmatrix}^T
\end{aligned} \tag{5.65}$$

and the displacement vectors are

$$\begin{aligned}
\boldsymbol{q}^{\mathrm{e}}_{\mathrm{B}} &= \left[\begin{array}{cccccccc} W_{\mathrm{B}_1} & \theta_{\mathrm{B}_1} & W_{\mathrm{B}_2} & \theta_{\mathrm{B}_2} & W_{\mathrm{B}_3} & \theta_{\mathrm{B}_3} & q_{w\mathrm{B}} & q_{\theta\mathrm{B}} \end{array}\right]^T \\
\boldsymbol{q}^{\mathrm{e}}_{\mathrm{L}} &= \left[\begin{array}{cccccccc} W_{\mathrm{L}_1} & \theta_{\mathrm{L}_1} & W_{\mathrm{L}_4} & \theta_{\mathrm{L}_4} & W_{\mathrm{L}_7} & \theta_{\mathrm{L}_7} & q_{w\mathrm{L}} & q_{\theta\mathrm{L}} \end{array}\right]^T \\
\boldsymbol{q}^{\mathrm{e}}_{\mathrm{R}} &= \left[\begin{array}{cccccccc} W_{\mathrm{R}_3} & \theta_{\mathrm{R}_3} & W_{\mathrm{R}_6} & \theta_{\mathrm{R}_6} & W_{\mathrm{R}_9} & \theta_{\mathrm{R}_9} & q_{w\mathrm{R}} & q_{\theta\mathrm{R}} \end{array}\right]^T \\
\boldsymbol{q}^{\mathrm{e}}_{\mathrm{T}} &= \left[\begin{array}{cccccccc} W_{\mathrm{T}_7} & \theta_{\mathrm{T}_7} & W_{\mathrm{T}_8} & \theta_{\mathrm{T}_8} & W_{\mathrm{T}_9} & \theta_{\mathrm{T}_9} & q_{w\mathrm{T}} & q_{\theta\mathrm{T}} \end{array}\right]^T
\end{aligned} , \tag{5.66}$$

where the numbering refers to Fig. 5.13(b). This model based on a 32×32 element "dynamic stiffness matrix" is finally the one that is implemented in the following comparisons with experimental results.

5.5 Experiments on plate damping

Once the design of an analogous electrical network is validated, it can be dedicated to the damping of a plate. The network built in Sec. 5.3 is coupled to a clamped plate through an array of piezoelectric patches. When electrical modes match their mechanical analogues, they strongly influence the dynamic response of the plate. The tuning of the electrical network is then optimized by adjusting the inductance and resistance values. In the end, a significant vibration reduction is observed over a broad frequency range.

5.5.1 Clamped plate

The mechanical structure to control is a clamped aluminum plate, whose dimensions and material properties are listed in Table 5.1. The plate thus corresponds to a set of 5×4 identical squares of side 80 mm. The clamping frame is made of square aluminum bars reinforced with steel angle channels, as seen in Figs. 5.15(a) and 5.15(b). Two rows of bolts are equally tightened with a torque wrench to ensure zero deflection and zero slope boundary conditions [137, 138]. A white noise excitation is generated from a shaker between the square unit cells (2,1) and (2,2) and the transverse velocity field is measured

	Plate (Aluminum 1050)	Patches (PZT-5H)
Length (mm)	$l_x = 400$	$l_{\mathrm{p}} = 72.4$
Width (mm)	$l_y = 320$	$l_{\mathrm{p}} = 72.4$
Thickness (mm)	$h_{\mathrm{s}} = 1.9$	$h_{\mathrm{p}} = 0.27$
Density (kg/m^3)	$\rho_{\mathrm{s}} = 2700$	$\rho_{\mathrm{p}} = 7800$
Young's modulus (GPa)	$Y_{\mathrm{s}} = 69$	$1/s^E_{11} = 62$
Charge constant (pC/N)	-	$d_{31} = -320$
Permittivity (nF/m)	-	$\epsilon^\sigma_{33} = 33.6$

Table 5.1: Dimensions and material properties for the plate and for the piezoelectric patches.

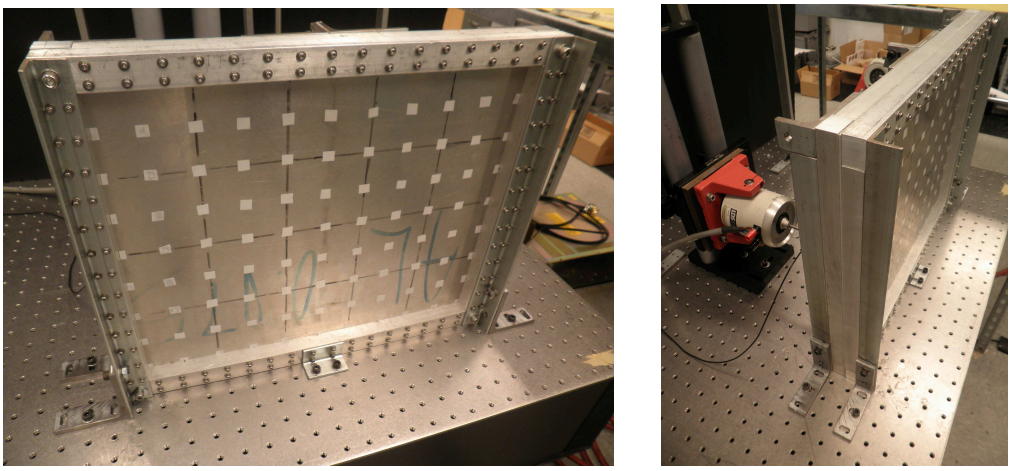

(a) (b)

Figure 5.15: Clamped aluminum plate: (a) Front of the plate with reflective tape for velocity measurement with a laser vibrometer. (b) Shaker exciting the back of the plate.

with a scanning laser vibrometer. The input force, around 0.1 N, is measured with a force sensor placed between the shaker and the plate. The force signal is then processed together with the velocity signal to compute the velocity FRFs.

Note that the considered bolted frame offers an adequate approximation of clamped boundary conditions up to 500 Hz. Above this frequency, the two rows of bolts still lead to a satisfactory clamping but the frame and its connections to the table are not stiff enough, which generates undesired low-frequency frame modes. The velocity FRFs are thus measured from 50 Hz to 500 Hz. The measurement point for the velocity corresponds to the center of the unit cell (2,2), as seen in Fig. 5.8. The velocity FRF in Fig. 5.16 shows four resonances over the considered frequency range. Actually, the 4^{th} resonance is the result of a combination of the 4^{th} and 5^{th} modes that exhibit close natural frequencies.

The finite difference model in Eq. (5.31) is implemented with 15×12 unit cells in order to ensure more than 10 unit cells per wavelength for the first five plate modes. The center of the unit cell (5,5) in the model corresponds to the center of the square (2,2), which had first been defined for a plate divided into 5×4 identical squares. The displacement at the center of the unit cell (5,5) is computed from the displacement and angle on its left side as

$$W_{\text{I}}^{(5,5)} = W_{\text{L}}^{(5,5)} + \frac{a}{2}\theta_{\text{L}}^{(5,5)}. \tag{5.67}$$

We note the non-negligible effect of the mass $m_{\text{add}} = 7.6$ g of the element which is added between the force sensor and the plate for connecting one to the other. Consequently, there is a difference between the simulated force F_{sim} acting on the plate and the force F_{exp} measured by the force sensor. If F_{exp} is the force applied by the force sensor to the

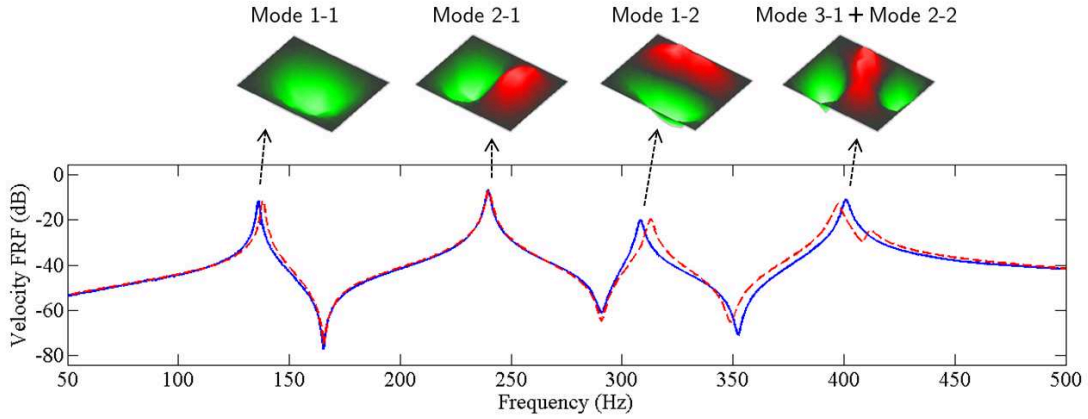

Figure 5.16: Experimental operating deflection shapes with respect to the velocity FRF - (—) experimental FRF, (– –) simulated FRF computed with 15×12 unit cells.

mass m_{add} and F_{sim} is the force applied to the plate

$$F_{\text{exp}} - F_{\text{sim}} = -\omega^2 m_{\text{add}} W_{\text{L}}^{(5,5)}. \tag{5.68}$$

Consequently, if $W_{\text{I}}^{(5,5)}$ has first been computed with $F_{\text{sim}} = 1$, it has to be divided by $1 - \omega^2 m_{\text{add}} W_{\text{L}}^{(5,5)}$ to find the actual FRF taking into account the added mass. Then, in order to consider structural damping, we combine a viscous damping applied to the transverse displacement and a viscous damping applied to the stiffness. This corresponds to the use of an equivalent complex density as $\rho(1 - 4.0\text{j}/\omega)$ and an equivalent complex Young's modulus as $Y(1 + 3.3 \times 10^{-6}\text{j}\omega)$, whose damping coefficients were determined experimentally. This damping model with the proposed numerical values offers a good correlation between experiments and simulations for the maxima of the velocity FRF below 500 Hz. Indeed, it is observed in Fig. 5.16 that the numerical results are in good agreement with the experimental ones. The main difference remains in the fact that the 4^{th} and 5^{th} modes can be distinguished on the simulated FRF. Yet, we note that refining the mesh does not clearly improve the correlation because it cannot overcome the bias introduced by the non-ideal clamped boundary conditions in the experiments.

5.5.2 Array of piezoelectric patches

The aluminum plate is covered with an array of 20 square PZT-5H patches, whose dimensions and properties are given in Table 5.1. As done by Anton et al. [62], the patches are glued onto the plate by using a vacuum bagging process, which allows reducing the thickness of the bonding layer. We chose the 3M DP460 two-part epoxy adhesive for its high shear strength and its adequate working life. The epoxy adhesive is applied on one side of the piezoelectric patches before their positioning onto the plate. The plate is then

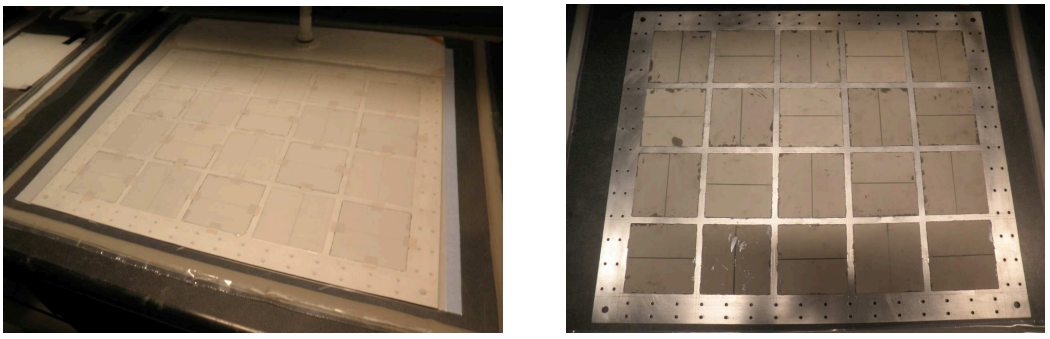

(a) (b)

Figure 5.17: Vacuum bonding process: (a) Plate in the vacuum bag. (b) Plate covered with piezoelectric patches after vacuum bonding.

placed in the vacuum bag shown in Fig. 5.17(a). After 24 hours, we obtain the functional piezoelectric plate in Fig. 5.17(b), which can be inserted into its clamping frame. The addition of piezoelectric patches does not strongly influence the modal distribution of the plate because both stiffness and mass are increased. With short-circuited patches, the natural frequency of the first mode is actually decreased by 2 % because the increase of the mass is the more significant. Furthermore, we can evaluate the difference in terms of natural frequencies when the patches are short- or open-circuited. As a reference, the first mode of the plate is around 140 Hz with open-circuited patches and this frequency is decreased by 3.5 % once the patches are short-circuited. From this result, the global coupling coefficient defined in Eq. (5.60) has been evaluated as $e_\theta = 1.4 \times 10^{-3}$ N·m/V.

With the vacuum bagging process, the bonding layer is actually so thin that we get a direct contact between the plate and at least one corner of the piezoelectric patches, which creates a short-circuit even with a "nonconductive" adhesive. The plate and its clamping frame are thus defined as the ground of the electrical circuit when considering the coupling to an electrical network. The network made of 5×4 unit cells is coupled to the plate through the piezoelectric capacitance C^ε offered by the patches. Consequently, no external capacitors are required. The piezoelectric capacitance is evaluated by direct measurement on the patches at the corners of the clamped plate. There, the boundary conditions naturally constrain the transverse displacement and it is found that the capacitance is $C^\varepsilon = 340$ nF. According to the discrete network topology obtained for a clamped plate, the patches on the corners do not play any role. Only 16 of the 20 patches are thus connected to the electrical network for the present application. The resulting coupled system is presented in Fig. 5.18, which shows the clamped plate and its analogous electrical network.

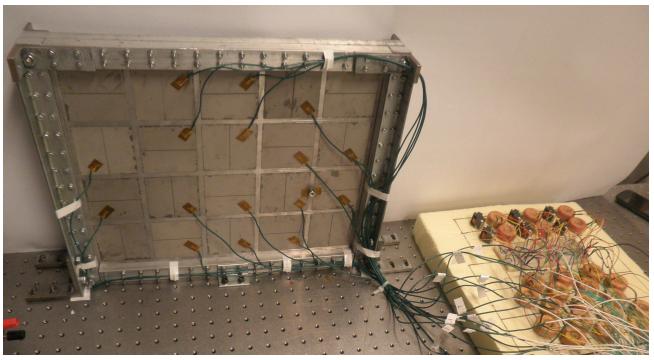

Figure 5.18: Clamped aluminum plate covered with piezoelectric patches connected to the multi-resonant network.

5.5.3 Multimodal coupling

Once the network is engaged, Fig. 5.19 shows that the coupling provides a strong modification of the modal behavior of the plate. For those measurements, the value of the 6 inductors is still equal to 0.9 H. Actually, this value has been chosen to satisfy the modal coupling condition

$$\frac{1}{\hat{a}^2}\frac{1}{LC^{\varepsilon}} = \frac{1}{a^2}\frac{D^E}{m}, \tag{5.69}$$

which is an extension of Eq. (5.29) to a case involving piezoelectric coupling. With this modal coupling condition, the modal properties of the plate and its analogous electrical network would be the same with an infinite number of unit cell. This is not the case for practical applications, but still, the inductance is tuned for optimal damping around at least the first mode of the plate. At 140 Hz and 230 Hz, we can easily observe in Fig. 5.19 local minima surrounded by two local maxima. This is a characteristic of an underdamped tuned mass control, which is here generated by the multi-resonant, spatially-distributed network. This confirms that the piezoelectric coupling of a 2D mechanical structure to

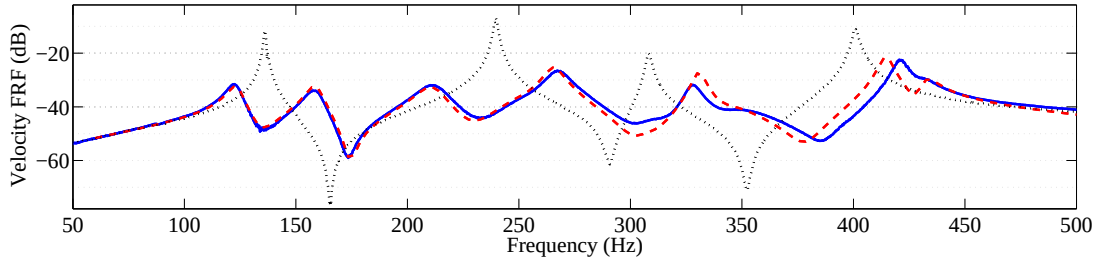

Figure 5.19: Effect of the coupling to the network on the velocity FRF of the plate - $(\cdots)$ experimental FRF with short-circuited patches, (—) experimental FRF with the electrical network tuned to $L = 0.9$ H and $R_s^+ = 0\ \Omega$, $(--)$ simulated FRF with the electrical network tuned to $L = 0.9$ H and $R_s^+ = 0\ \Omega$.

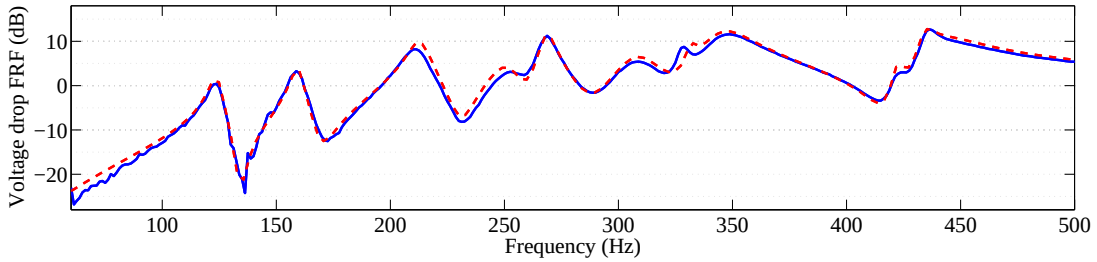

Figure 5.20: Voltage frequency response function - (—) experimental FRF with the electrical network tuned to $L = 0.9$ H and $R_s^+ = 0\ \Omega$, (– –) simulated FRF with the electrical network tuned to $L = 0.9$ H and $R_s^+ = 0\ \Omega$.

its electrical analogue leads to a passive control that acts as a multimodal tuned mass damping, similarly to what has been implemented for the control of 1D structures in Chaps. 3 and 4.

It is remarked that the vibration reduction is also significant for the highest modes. However, the network does not offer a tuning that is optimized for all the modes simultaneously. The exact analogue of a continuous structure cannot be obtained with a set of discrete electrical components. Therefore, our discrete network only offers an approximation of the continuous plate behavior at low frequency. The lower electrical resonances thus occur at frequencies that are close to the corresponding mechanical resonances but for higher modes the frequency error becomes non-negligible. Nevertheless, it is possible to more closely match the resonances of the plate with the same network topology by increasing the number of electrical unit cells.

The comparison between the experimental results and those coming from the model developed in Sec. 5.4 shows an adequate correlation in Fig. 5.19. Still, we note a better correlation for the lowest frequency range, which is due to two main reasons. First, even if the considered model involves macro unit cell giving 15×12 sub-cells for the plate, it is still a discrete model that is close to its limits for the highest modes. Then, the approximation of perfect clamped boundary conditions with the actual setup becomes questionable when approaching 500 Hz. A second solution to validate the numerical model and verify the tuning of the network is to proceed to electrical measurements. As has been performed in Sec. 5.3, FRFs of the network can be obtained from a voltage excitation and a measurement of the voltage drop across an inductor. The piezoelectric coupling between the network and the plate considerably influences the electrical FRF presented in Fig. 5.20. Indeed, when compared to Fig. 5.10, we see a completely different response even if the excitation and measurement points are the same. Note the clear antiresonance around 140 Hz that characterize the first mode of the plate and thus shows that the network is correctly tuned. In the end, the simulation of the electrical FRF is very reliable, which definitely validates

the proposed model based on two-dimensional coupling to an analogous network.

5.5.4 Tuning of the electrical network

The network can be tuned in different ways depending on the considered application. For example, if a control is required at one specific frequency which is near a mechanical resonance, the inductors can be adjusted in order to place the corresponding electrical resonance at the target frequency. This generates an antiresonance, as seen in Fig. 5.19 around the first mode of the plate. Then, the internal damping in the components must be minimized in order to increase the depth of the antiresonance.

On the other hand, a control over a broader frequency range requires the introduction of additional damping in the network. Indeed, it is shown in Fig. 5.21 that 180 Ω resistors in series with the 6 inductors flatten the FRF. Note that the addition of resistance does not necessarily increase the number of components as it can be taken into account when designing the inductors. A vibration reduction around 25 dB is obtained for the first two modes. Yet, the comparison between Figs. 5.19 and 5.21 shows that the introduction of resistors mainly affects the lowest modes. Again, this is due to the fact that the discrete electrical network yields inaccurate tuning at higher frequencies.

With the discrete network, a solution for a vibration reduction over a broader frequency range is to detune the first modes to better tune higher modes. This strategy is presented in Fig. 5.22, where the previous case involving a network with 0.9 H inductors and 180 Ω series resistors is compared to a second case with 0.7 H inductors and the same 180 Ω resistors. The second inductance value was obtained from a $\mathcal{H}_\infty$ optimization, which minimizes the maximum of the velocity FRF over the 50 Hz to 500 Hz frequency range:

$$\mathcal{H}_\infty = \min_L \left(\max_f \left[\mathrm{FRF}(f, L) \right] \right), \quad \text{where} \quad f \in [50 \text{ Hz}, 500 \text{ Hz}]. \tag{5.70}$$

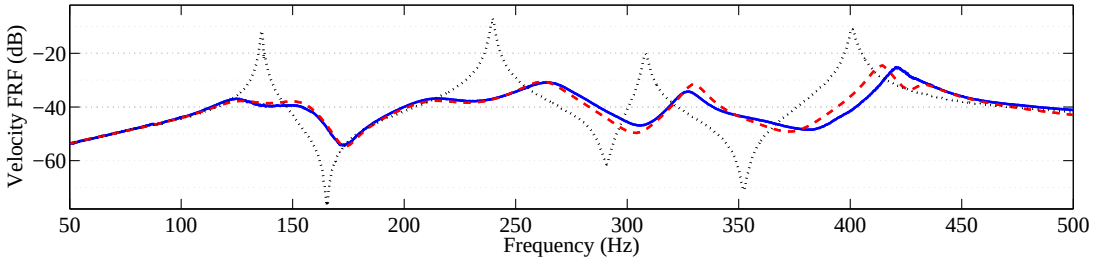

Figure 5.21: Effect of the multimodal control on the velocity FRF of the plate - (⋯) experimental FRF with short-circuited patches, (—) experimental FRF with the electrical network tuned to $L = 0.9$ H and $R_s^+ = 180$ Ω, (−−) simulated FRF with the electrical network tuned to $L = 0.9$ H and $R_s^+ = 180$ Ω.

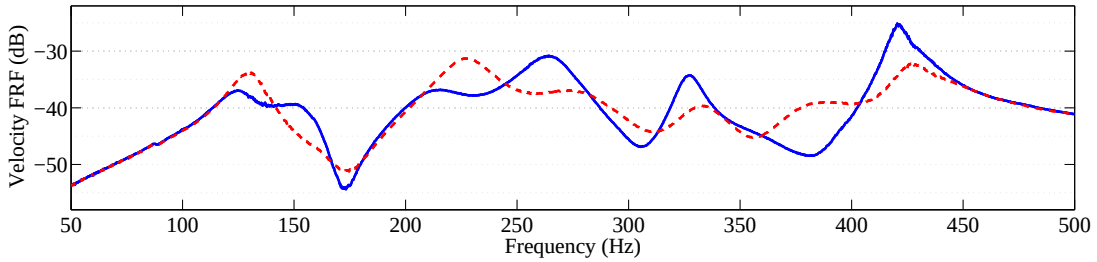

Figure 5.22: Broadband tuning of the network - (—) experimental FRF with the electrical network tuned to $L = 0.9$ H and $R_s^+ = 180\ \Omega$, (– –) experimental FRF with the electrical network tuned to $L = 0.7$ H and $R_s^+ = 180\ \Omega$.

By decreasing the inductance, the electrical resonances move to higher frequencies. In this case, we remark that the second electrical resonance is moved from a frequency below the second mechanical resonance to a frequency above it. Even if the modification of the tuning is not beneficial for the first mode, the maximum of the amplitude over the frequency range of interest is minimized. The decrease of the inductance moves the highest electrical resonances closer to their mechanical analogues, which clearly reduces the amplitude of the FRF around its upper frequency range. In the end, the vibration reduction is above 20 dB for the first five modes of the plate when compared to the short-circuited case. This shows that the analogous coupling offers an efficient broadband control, even with a coarse discretization of the electrical network.

5.6 Robustness of the control strategy

The robustness of the damping solution is evaluated by introducing a uniform variation of the electrical components. Then, local defects are added experimentally in order to observe the effect on control performance. For the same purpose, an alteration of the electrical or mechanical boundary conditions is finally considered. The damping performance is decreased but the vibration reduction remains significant when compared to the uncontrolled case.

5.6.1 Uniform detuning of the electrical network

A first observation related to the robustness of the strategy can be introduced by considering the difference between the natural frequencies of the plate and those of the electrical controller. Recall that the analogue network is discrete, so it cannot perfectly match several mechanical resonances simultaneously. The natural frequencies are compared in Table 5.2 when L is set to 0.7 H. It is seen that the $\mathcal{H}_\infty$ optimization over the

Table 5.2: Comparison of mechanical and electrical natural frequencies with $L = 0.7$ H.

	Mode 1-1	Mode 2-1	Mode 1-2	Mode 3-1	Mode 2-2
Clamped plate	138 Hz	242 Hz	315 Hz	409 Hz	411 Hz
Electrical network	163 Hz	270 Hz	309 Hz	374 Hz	424 Hz

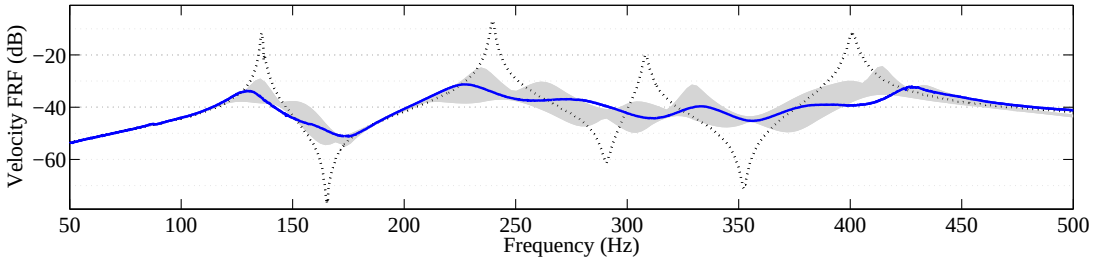

Figure 5.23: Sensitivity of the velocity FRF with respect to an inductance variation - (· · ·) experimental FRF with short-circuited patches, (—) experimental FRF with the analogous network tuned to $L = 0.7$ H and $R_s^+ = 180\ \Omega$, ( ) simulated frequency response envelope with a ±30% variation on L.

50 Hz to 500 Hz frequency range gives a positioning of the electrical natural frequencies that differs up to 18 % from the mechanical ones. Thus, an imprecise tuning of an electrical resonance can still lead to a 20 dB reduction of its mechanical counterpart, as observed in Figs. 5.21 and 5.22. This can be explained by the fact that the optimal electrical network is highly dissipative. Indeed, it has been seen in Fig. 5.10 that a resistance $R_s^+ = 180\ \Omega$ induces a relatively "flat" electrical FRF. This makes the control more robust, as it becomes less sensitive to electrical tuning variations.

The performance loss due to a detuning of the electrical parameters is evaluated by introducing a variation of the inductance L around its optimal value. A variation of the piezoelectric capacitance could also be analyzed but it would lead to similar conclusions. Furthermore, a variation of the resistance R_s^+ is not considered because it is observed that its influence is relatively low, which extends results obtained for a single resonant shunt [2, 46]. A ±30% uniform variation of L is considered, so that the electrical unit cells have a same inductance all over the network, but this inductance varies between 0.49 H and 0.91 H. This range is introduced in the electromechanical model that has been validated in Figs. 5.19, 5.20 and 5.21. By extracting the highest and lowest amplitudes computed at each frequency point, we get the simulated frequency response envelope presented in Fig. 5.23. The optimal FRF should always stay inside the frequency response envelope

because its inductance corresponds to the center of the range of variation. The fact that the experimental FRF can sometimes leave the envelope in Fig. 5.23 is simply due to slight deviations between model and experiment, according to what has been observed in Fig. 5.21. In any case, a $\pm 30\%$ variation on L induces a loss of 7 dB on the $\mathcal{H}_\infty$ criterion. This loss of performance is non-negligible but it still maintains a vibration reduction above 85% with respect to the maximum amplitude of the uncontrolled velocity FRF.

5.6.2 Local defect in a mechanical or an electrical unit cell

Local modifications of the electromechanical system can also affect the control performance. For example, a local damage can appear on the mechanical structure, which would modify the mass or the stiffness of one specific unit cell. On the other hand, the degradation of an electrical component might alter the modal properties of the entire network. A first experiment considers an addition of 50 grams through 3 lumped masses attached to the clamped plate, as seen in Fig. 5.24(a). Those lumped masses double the mass of one of the twenty 80×80 mm^2 mechanical unit cells. This added mass moves the plate resonances to lower frequencies (5% for the 1$^{\text{st}}$ resonance, 8% for the 2$^{\text{nd}}$ resonance), which detunes the control system. Considering mode 1-1 and mode 2-1 in Table 5.2, the gap between the mechanical and electrical frequencies was already significant before the addition of a local defect. Afterward, the gap is even larger, which accounts for the 3 dB loss that appears below 250 Hz in Fig. 5.25. On the other hand, we note that the local mass addition is beneficial above 250 Hz because it better tunes the resonance distribution for the highest modes.

In the electrical domain, the equivalent of a mass addition is an inductance increase on the same unit cell. Thus, one inductance of the network is doubled to implement the

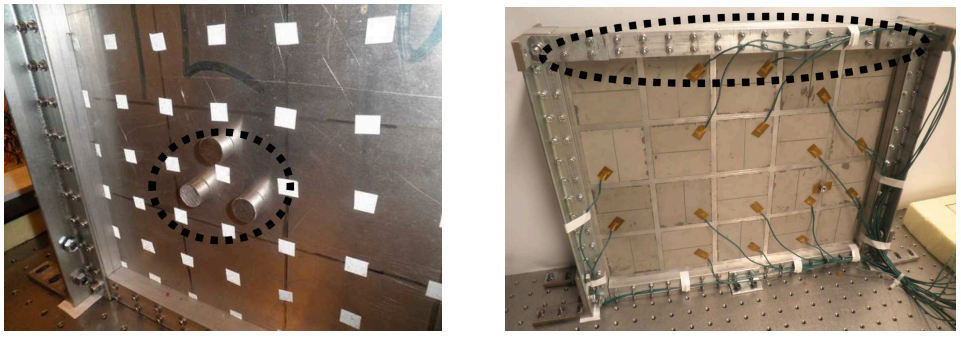

(a) (b)

Figure 5.24: Structural modifications of the clamped plate: (a) Addition of lumped masses. (b) Loose bolts on the upper bar of the frame.

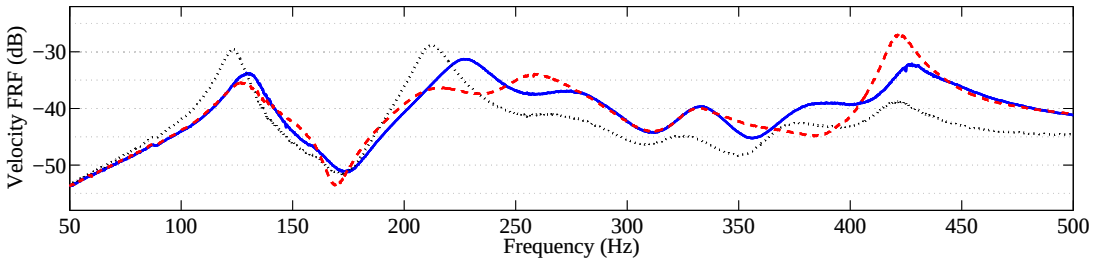

Figure 5.25: Influence of local defects - (—) optimal FRF with $L = 0.7$ H and $R_s^+ = 180\ \Omega$, $(\cdots)$ with a doubled mass in one mechanical unit cell, $(--)$ with a doubled inductance in one electrical unit cell.

counterpart of the previous experiment. This local defect moves the electrical resonances to lower frequencies. Consequently, the last FRF shown in Fig. 5.25 evolves in opposition to what has been observed after the modification of the mechanical structure: the tuning of the electrical network is improved for the modes 1-1 and 2-1 but the performance is decreased above 250 Hz. Actually, the performance loss is mainly due to the mode 3-1, which exhibits a 5 dB increase of the velocity around 420 Hz.

5.6.3 Modifications of the boundary conditions

A second set of experiments focuses on modifications of the mechanical or electrical boundary conditions. An alteration of plate boundary conditions is first considered by removing the bolts all along the upper bar of the clamping frame, which is highlighted in Fig. 5.24(b). The rotations and transverse displacements are no longer blocked on the upper side of the plate. This modifies the mechanical modes, especially their distribution over the frequency range. The stiffness reduction shifts the resonances to lower frequencies, as with the mass addition. Consequently, it is observed in Fig. 5.26 similar results to what has been presented Fig. 5.25 when looking at the performance loss around the first two modes. We note a 3 dB loss compared to the optimal FRF. The analysis above 250 Hz is less obvious because of the strong modification of the mechanical modal distribution. In any case, we remark that a significant alteration of the mechanical boundary conditions does not defeat the control strategy.

The electrical equivalent of the stiffness reduction along the upper boundary is approximated by short-circuiting the upper line of piezoelectric patches. Similarly to what appears after an increase of the inductance, the electrical resonances move to lower frequencies. This better tunes the control of the first two modes as seen in Fig. 5.26. Nevertheless, the evolution of the FRF is limited compared to the previous case involving the inductance

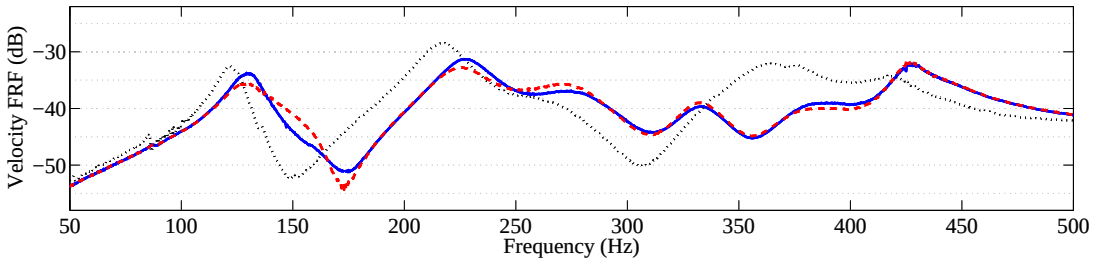

Figure 5.26: Influence of boundary conditions - (—) optimal FRF with $L = 0.7$ H and $R_s^+ = 180\ \Omega$, $(\cdots)$ with no bolts on the upper bar of the frame, $(--)$ with the upper line of piezoelectric patches which is short-circuited.

modification. This observation is clear above 250 Hz, where the short-circuits on the upper line of piezoelectric patches are almost ineffective. A reason is that the clamped-plate strain distribution induces a significant charge cancellation on those outer patches, especially when the wavelength approaches the size of the unit cell. In the end, the proposed modification of a network boundary does not significantly alter the control performance.

5.7 Conclusions

A distributed control strategy has been implemented by means of an interconnected array of piezoelectric patches. The interconnection is made through an electrical network analogous to the structure of interest. For a square plate unit cell, we show that a finite difference method applied to the Kirchhoff-Love theory gives a discrete model that can be converted into its direct electrical analogue. The analogues of clamped or simply-supported boundary conditions only require open- or short-circuited electrical ports on the edges of the network. Yet, free boundary conditions are more difficult to implement with the proposed topology. In any case, the electrical network can be modeled from an assembly of element matrices that are built from the constitutive discrete equations of an electrical unit cell. The analogous network is validated through a modal analysis procedure similar to what is normally performed with a mechanical structure. Electrical plate-like mode shapes are observed experimentally when looking at the distribution of the electrical current and the numerical simulations of the network are in good agreement with the experimental results.

The passive electrical network is coupled to a clamped plate and a significant modification of the mechanical response is observed. To the best of our knowledge, this work presents the first experimental coupling of a plate to an analogous electrical network. Depending on the application, a suitable tuning of the electrical network can then optimize

the vibration reduction around one specific frequency or over a broad frequency range. When tuned to minimize the velocity amplitude over a 50 Hz to 500 Hz frequency range, the resulting broadband vibration reduction validates the interest of the control strategy. Coupled models based on 2D electromechanical unit cells are also validated from the experiments. We note that the frequency range of interest influences the choice of a suitable macro unit cell, which is more refined for the mechanical domain than for the electrical domain.

Structural and electrical modifications are introduced in order to quantify the performance loss due to inaccurate tuning of the electromechanical system. The results obtained with the present setup give some guidelines concerning the robustness of a control solution based on analogous coupling. First, it is observed that a discrete network involving less than 5 unit cells per wavelength can still lead to a broadband vibration reduction above 20 dB. Second, a $\pm 30\%$ uniform variation of the network inductance induces a loss of 7 dB, which maintains most of the control performance. Local defects are introduced by doubling the mass or the inductance of one unit cell. Boundaries are also modified by removing the bolts or short-circuiting the patches on the upper side of the plate. In any case, the FRF rises by less than 5 dB over the considered frequency range. It is thus shown that the proposed control involving the discrete analogue of a plate is relatively robust when considering an alteration of the mechanical structure or a detuning of the electrical network. This conclusion offers future prospects concerning the implementation of such control solutions into industrial applications.

Chapter 6

Conclusions

6.1 Summary

The material presented in this thesis was partially published in journal papers and conference proceedings that are listed in Appendix C. The present document has been organized into four main chapters of increasing complexity. Indeed, coupled systems involving a single mechanical degree of freedom are first considered in Chap. 2, while Chaps. 3 and 4 deal with 1D structures as rods and beams. Finally, Chap. 5 extends the analysis to 2D plate structures. All of those chapters give theoretical and experimental results related to structural vibration damping by coupling to an analogous electrical network. Here, the results are summarized by highlighting three main lines of research that complement one another: the design of an electrical analogue, the use of the transfer matrix method and the damping of vibration with an interconnected array of piezoelectric patches.

6.1.1 Design of analogous electrical networks

Electrical analogues of rod, beam and plate structures have been defined from a finite difference method applied to their constitutive equations of motion. It is found a discrete mechanical model, which is converted to the electrical domain through the direct electromechanical analogy. Point masses are equivalent to inductors and springs gives capacitors. When considering structures subjected to transverse motion, transformers also appear as the analogues of mechanical levers. Homogeneous structures lead to the definition of periodic electrical networks, which can be divided into identical unit cells. Each unit cell is ruled by the same constitutive equations that are organized into transfer matrices for both one-dimensional networks. For the two-dimensional network, we rather define the equivalent of a dynamic stiffness matrix satisfying classical assembly methods. Consequently, electrical frequency response functions are computed for any choice of the

electrical components that can easily include parasitic effects as internal damping. To this end, equivalent electrical models are given for passive inductors and transformers. The practical design of both magnetic components is also described to allow the implementation of suitable electrical analogues. From those guidelines, it has been possible to build a 2D electrical network approximating the behavior of a clamped plate. Finally, the main original contributions related to the design of analogous electrical networks are summarized through the following points:

- Design of passive inductors for resonant piezoelectric shunts or analogous networks;
- Design of passive transformers for the beam and plate electrical analogues;
- New 2D electrical network representing the analogue of a plate;
- Numerical model of the proposed 2D electrical network;
- Experimental implementation and validation of the plate electrical analogue.

6.1.2 Transfer matrix method applied to eletromechanical waveguides

Along Chaps. 3 and 4, a transfer matrix method has been applied to rods and beams that are coupled to their electrical analogues through a periodic array of piezoelectric patches. We thus deal with a real electromechanical waveguide, which requires a combination of both mechanical and electrical variables in the state vectors of the transfer matrix formulation. In the proposed models, the electrical network is always discrete but the mechanical part of the unit cells can be either discretized, homogenized or represented by a finite element model. The Riccati transfer matrix method allows computing frequency response functions of a complete electromechanical structure made of several unit cells. Combined with an analysis of the propagation constants, it then becomes possible to compare the different models. It is noticed that the fully homogenized model is usually enough when focusing on a frequency range where the analogous control is effective. When the wavelength approaches the length of the unit cell, the discrete network is too coarse to approximate the dispersion relation of the continuous mechanical structure. This also shows that such a control strategy cannot be directly combined with a band gap attenuation offered by the periodic distribution of the piezoelectric patches. Finally, one can list the main original contributions concerning the application of the transfer matrix method to problems involving coupled waveguides:

- 1D transfer matrix models involving piezoelectric coupling to an electrical analogue;
- Analysis of electromechanical propagation constants subjected to analogous coupling;

- Comparison of discrete models, fully or piecewise homogenized models and finite element models over different frequency ranges.

6.1.3 Vibration damping through interconnected piezoelectric patches

The modeling of interconnected arrays of piezoelectric patches has been simplified by focusing on a purely electrical representation of the coupled problems. The equivalent electrical circuit is based on the direct electromechanical analogy (or velocity-current analogy), which allows representing the piezoelectric coupling with an electrical transformer. On both sides of this transformer, we note two similar topologies that directly validate the analogy between the mechanical structure to control and the considered electrical network. With piezoelectric transducers, the direct electromechanical analogy is the only one that offers such a unification of both domains, which questions the choice of the indirect analogy (or force-current analogy) in most of the previous works focusing on analogous piezoelectric networks. In any case, the unified electrical circuit is based on discrete models for both the mechanical and electrical media. For better accuracy, the continuity of the mechanical structure has been recovered with homogenized models or approximated with refined meshes. Yet, the electrical network is always kept discrete in order to be compatible with practical applications where the number of piezoelectric patches is generally limited. The resulting semi-continuous models then represent suitable tools for the design of a control system involving a coupling to an analogous network. This is proved by the proposed experimental setups focusing on rod, beam and plate structures that validate the electromechanical models. Actually, it is even possible to observe how the piezoelectric coupling influences the electrical frequency response of the networks. Experimentally, this gives a way to verify the tuning of the electrical components. Once the considered electrical network is correctly tuned, it is observed significant reduction of the structural vibration amplitude over a broad frequency range. This definitely validates the interest of piezoelectric analogous networks for multimodal vibration damping. Furthermore, it has been shown that this strategy is relatively robust as it tolerates defects in the mechanical or electrical domains. To conclude about vibration damping through analogous piezoelectric network, the main original contributions are:

- Discrete electrical circuits to model 1D or 2D electromechanical unit cells;
- Numerical models involving discrete piezoelectric networks;
- Experimental coupling of a rod, a beam and a plate to analogous electrical networks;
- Analysis of electrical frequency responses to verify the tuning of the passive networks;

- Experimental validation of the multimodal damping induced by analogous coupling for the control of a rod, a beam and a plate;
- Experimental evaluation of the robustness of the plate control.

6.2 Outlook

Regarding the design of analogous electrical networks, a natural perspective is the optimization of the size of the electrical components. A method has been proposed in Chap. 2 to design suitable passive inductors. Yet, this method focuses on single resonant shunts, which does not apply directly to a multi-resonant network made of several inductors and transformers. It is still possible to employ the proposed electromechanical models to determine the current flowing through the magnetic components for a specific amplitude and frequency range of the excitation. An optimal sizing of the electrical network would then allow comparing the mass of the structure to control to the total mass of magnetic material. This mass ratio most likely depends on the number of unit cells. Actually, it has been shown that the required inductance decreases with an increase of the number of unit cells but no direct conclusions can be drawn concerning the total mass of magnetic material since the number of components is increased. Energy considerations may be used to quantify the needs in terms of magnetic material when the number of unit cells tends to infinity. This might validate the analogous control strategy within the scope of small scale or meta-material applications, which could rely on autonomous 3D printing of miniature electrical components.

Other prospects concern the transfer matrix models developed in Chaps. 3 and 4. They can be used to quantify the sensibility to any variation of mechanical of electrical parameters. Uncertainties could also be introduced in the electrical components to compare the robustness of various control strategies. Furthermore, phase and attenuation constants have been drawn for comparing the discrete and homogenized models. The effect of the analogous coupling has been illustrated but a more accurate analysis of the propagation constants is still required. Understand how they are influenced by the tuning of the electrical network may lead to an optimization of the energy transfer over a broader frequency range. Then, the analysis of propagation constants could be extended to the two-dimensional case of a square plate unit cell coupled to its analogous electrical network. The 1D Wave Finite Element model might also be enriched to include 3D mechanical contributions or a 2D electrical network. In the end, the mechanical part of the macro unit cells proposed in Chap. 5 could be replaced by a finite element model in order to break the restriction on the minimum wavelength.

Concerning vibration damping with analogous piezoelectric network, one of the main

outlooks concerns the definition of an optimal resistance. It has been shown that damping occurs in the passive components through numerous parasitic contributions. All of them can be introduced into the proposed electromechanical models and a numerical optimization gives a value for additional resistors. However, it might be useful to get an approximation of the optimal resistance values and positioning prior complete modeling of the coupled system. About the electrical boundary conditions, an adequate implementation of the analogue of free boundary conditions is still under consideration for the 2D electrical network presented in Chap. 5. "Dynamic" boundary conditions, i.e. neither free nor blocked, are also considered in order to ensure better compatibility with more realistic cases. The aim at extending the analogous piezoelectric control to real structures also leads to reconsider the interest of the periodic layout. Actually, since we do not benefit from any band gap phenomenon, no periodicity is required as long as the analogy between the mechanical structure and the electrical network is maintained. A new experimental setup involving a plate and a 2D analogous network with more unit cells compared to the setup in Chap. 5 will allow to evaluate eventual aperiodicity as well as new electrical boundary conditions. The performance of the control will then be compared to other passive strategies involving a purely resistive network or viscoelastic materials. Finally, the use of electrical analogues will be extended to nonlinear vibrations by designing multi-resonant electrical networks approximating the nonlinearity of the structure to control. This must offer a passive multimodal controller for non-linear systems.

Bibliography

[1] J. P. Den Hartog, *Mechanical Vibrations*. McGraw-Hill, 1940.

[2] N. W. Hagood and A. H. von Flotow, "Damping of structural vibrations with piezoelectric materials and passive electrical networks," *Journal of Sound and Vibration*, vol. 146, no. 2, pp. 243–268, 1991.

[3] S. O. R. Moheimani, A. J. Fleming, and S. Behrens, "On the feedback structure of wideband piezoelectric shunt damping systems," *Smart Materials and Structures*, vol. 12, no. 1, p. 49, 2003.

[4] O. Thorp, M. Ruzzene, and A. Baz, "Attenuation and localization of wave propagation in rods with periodic shunted piezoelectric patches," *Smart Materials and Structures*, vol. 10, no. 5, p. 979, 2001.

[5] O. Thorp, M. Ruzzene, and A. Baz, "Attenuation of wave propagation in fluid-loaded shells with periodic shunted piezoelectric rings," *Smart Materials and Structures*, vol. 14, no. 4, p. 594, 2005.

[6] A. Spadoni, M. Ruzzene, and K. A. Cunefare, "Vibration and wave propagation control of plates with periodic arrays of shunted piezoelectric patches," *Journal of Intelligent Material Systems and Structures*, vol. 20, no. 8, pp. 979–990, 2009.

[7] A. J. Fleming, S. Behrens, and S. O. R. Moheimani, "Reducing the inductance requirements of piezoelectric shunt damping systems," *Smart Materials and Structures*, vol. 12, no. 1, p. 57, 2003.

[8] J. J. Hollkamp, "Multimodal passive vibration suppression with piezoelectric materials and resonant shunts," *Journal of Intelligent Material Systems and Structures*, vol. 5, no. 1, pp. 49–57, 1994.

[9] U. Andreaus and M. Porfiri, "Effect of electrical uncertainties on resonant piezoelectric shunting," *Journal of Intelligent Material Systems and Structures*, vol. 18, no. 5, pp. 477–485, 2007.

[10] S.-Y. Wu, "Method for multiple mode piezoelectric shunting with single PZT transducer for vibration control," *Journal of Intelligent Material Systems and Structures*, vol. 9, no. 12, pp. 991–998, 1998.

[11] S. Behrens, S. O. R. Moheimani, and A. J. Fleming, "Multiple mode current flowing passive piezoelectric shunt controller," *Journal of Sound and Vibration*, vol. 266, no. 5, pp. 929–942, 2003.

[12] F. dell'Isola and S. Vidoli, "Continuum modelling of piezoelectromechanical truss beams: an application to vibration damping," *Archive of Applied Mechanics*, vol. 68, no. 1, pp. 1–19, 1998.

[13] F. dell'Isola and S. Vidoli, "Damping of bending waves in truss beams by electrical transmission lines with PZT actuators," *Archive of Applied Mechanics*, vol. 68, no. 9, pp. 626–636, 1998.

[14] I. Giorgio, L. Galantucci, A. Della Corte, and D. Del Vescovo, "Piezo-electromechanical smart materials with distributed arrays of piezoelectric transducers: current and upcoming applications," *International Journal of Applied Electromagnetics and Mechanics*, vol. 47, no. 4, pp. 1051–1084, 2015.

[15] C. Maurini, "Electromechanical coupling of distributed piezoelectric transducers for passive damping of structural vibrations: comparison of network configurations," Master's thesis, Virginia Polytechnic Institute and State University, 2002.

[16] M. Porfiri, *Performances of passive electric networks and piezoelectric transducers for beam vibration control*. PhD thesis, Sapienza - Università di Roma and Université de Toulon, 2005.

[17] C. Maurini, F. dell'Isola, and D. Del Vescovo, "Comparison of piezoelectronic networks acting as distributed vibration absorbers," *Mechanical Systems and Signal Processing*, vol. 18, no. 5, pp. 124–1271, 2004.

[18] C. Maurini, *Piezoelectric composites for distributed passive electric control: beam modelling, modal analysis, and experimental implementation*. PhD thesis, Université Pierre et Marie Curie - Paris VI and Sapienza - Università di Roma, 2005.

[19] F. dell'Isola, M. Porfiri, and S. Vidoli, "Piezo-electromechanical (PEM) structures: passive vibration control using distributed piezoelectric transducers," *Comptes Rendus Mécanique*, vol. 331, no. 1, pp. 69–76, 2003.

[20] S. Alessandroni, F. dell'Isola, and M. Porfiri, "A revival of electric analogs for vibrating mechanical systems aimed to their efficient control by PZT actuators," *International Journal of Solids and Structures*, vol. 39, no. 20, pp. 5295–5324, 2002.

[21] M. Porfiri, F. dell'Isola, and F. M. Frattale Mascioli, "Circuit analog of a beam and its application to multimodal vibration damping, using piezoelectric transducers," *International Journal of Circuit Theory and Applications*, vol. 32, no. 4, pp. 167–198, 2004.

[22] U. Andreaus, F. dell'Isola, and M. Porfiri, "Piezoelectric passive distributed controllers for beam flexural vibrations," *Journal of Vibration and Control*, vol. 10, no. 5, pp. 625–659, 2004.

[23] S. Alessandroni, U. Andreaus, F. dell'Isola, and M. Porfiri, "Piezo-electromechanical (PEM) Kirchhoff-Love plates," *European Journal of Mechanics - A/Solids*, vol. 23, no. 4, pp. 689–702, 2004.

[24] S. Alessandroni, U. Andreaus, F. dell'Isola, and M. Porfiri, "A passive electric controller for multimodal vibrations of thin plates," *Computers & Structures*, vol. 83, no. 15-16, pp. 1236–1250, 2005.

[25] T. Valis, A. H. von Flotow, and N. W. Hagood, "An acoustic-electromagnetic piezoelectric waveguide coupler," *Journal of Sound and Vibration*, vol. 178, no. 5, pp. 669–680, 1994.

[26] F. dell'Isola, C. Maurini, and M. Porfiri, "Passive damping of beam vibrations through distributed electric networks and piezoelectric transducers: prototype design and experimental validation," *Smart Materials and Structures*, vol. 13, no. 2, p. 299, 2004.

[27] M. Panella, M. Paschero, and F. M. Frattale Mascioli, "Optimised RC-active synthesis of PEM networks," *Electronics Letters*, vol. 41, no. 19, pp. 1041–1043, 2005.

[28] M. Paschero, *Modeling and synthesis of circuits analogue of generalized ondulatory phenomena gyroscopically coupled*. PhD thesis, Sapienza - Università di Roma, 2007.

[29] M. Paschero, M. Panella, and F. M. Frattale Mascioli, "Stability analysis of optimal PEM networks," *Electronics Letters*, vol. 42, no. 17, pp. 961–962, 2006.

[30] R. H. MacNeal, *The solution of partial differential equations by means of electrical networks*. PhD thesis, 1949.

[31] V. Bush, "Structural analysis by electric circuit analogies," *Journal of the Franklin Institute*, vol. 217, no. 3, pp. 289–329, 1934.

[32] G. Kron, "Tensorial analysis and equivalent circuits of elastic structures," *Journal of the Franklin Institute*, vol. 238, no. 6, pp. 399–442, 1944.

[33] G. Carter and G. Kron, "Network analyzer solution of the equivalent circuits for elastic structures," *Journal of the Franklin Institute*, vol. 238, no. 6, pp. 443–452, 1944.

[34] G. Kron, "Numerical solution of ordinary and partial differential equations by means of equivalent circuits," *Journal of Applied Physics*, vol. 16, no. 3, pp. 172–186, 1945.

[35] G. Kron, "Electric circuit models of partial differential equations," *Electrical Engineering*, vol. 67, no. 7, pp. 672–684, 1948.

[36] R. Barnoski and C. Freberg, "Passive-element analog circuits for three-dimensional elasticity," *Journal of Engineering for Industry*, vol. 88, no. 1, pp. 8–16, 1966.

[37] S. U. Benscoter and R. H. MacNeal, "Introduction to electrical-circuit analogies for beam analysis," tech. rep., NACA, 1952.

[38] S. U. Benscoter and R. H. MacNeal, "Equivalent-plate theory for a straight multicell wing," tech. rep., NACA, 1952.

[39] R. H. MacNeal, "Electrical analogies for stiffened shells with flexible rings," tech. rep., NACA, 1954.

[40] R. H. MacNeal, "The solution of aeroelastic problems by means of electrical analogies," *Journal of the Aeronautical Sciences*, vol. 18, no. 12, pp. 777–789, 1951.

[41] K. Liu and J. Liu, "The damped dynamic vibration absorbers: revisited and new result," *Journal of Sound and Vibration*, vol. 284, no. 3, pp. 1181–1189, 2005.

[42] R. L. Forward, "Electronic damping of vibrations in optical structures," *Applied Optics*, vol. 18, no. 5, pp. 690–697, 1979.

[43] O. Thomas, J. Ducarne, and J.-F. Deü, "Performance of piezoelectric shunts for vibration reduction," *Smart Materials and Structures*, vol. 21, no. 1, p. 015008, 2012.

[44] F. Bachmann, R. de Oliveira, A. Sigg, V. Schnyder, T. Delpero, R. Jaehne, A. E. Bergamini, V. Michaud, and P. Ermanni, "Passive damping of composite blades using embedded piezoelectric modules or shape memory alloy wires: a comparative study," *Smart Materials and Structures*, vol. 21, no. 7, p. 075027, 2012.

[45] T. Delpero, *Design of adaptive structures with piezoelectric materials*. PhD thesis, Eidgenössische Technische Hochschule - ETH Zürich, 2014.

[46] L. Airoldi and M. Ruzzene, "Wave propagation control in beams through periodic multi-branch shunts," *Journal of Intelligent Material Systems and Structures*, vol. 22, no. 14, pp. 1567–1579, 2011.

[47] B. Mokrani, R. Bastaits, M. Horodinca, I. Romanescu, I. Burda, R. Viguié, and A. Preumont, "Parallel piezoelectric shunt damping of rotationally periodic structures," *Advances in Materials Science and Engineering*, vol. 2015, 2015.

[48] G. Wang, S. Chen, and J. Wen, "Low-frequency locally resonant band gaps induced by arrays of resonant shunts with Antoniou's circuit: experimental investigation on beams," *Smart Materials and Structures*, vol. 20, no. 1, p. 015026, 2011.

[49] L. Airoldi and M. Ruzzene, "Design of tunable acoustic metamaterials through periodic arrays of resonant shunted piezos," *New Journal of Physics*, vol. 13, no. 11, p. 113010, 2011.

[50] F. Casadei, M. Ruzzene, L. Dozio, and K. A. Cunefare, "Broadband vibration control through periodic arrays of resonant shunts: experimental investigation on plates," *Smart Materials and Structures*, vol. 19, no. 1, p. 015002, 2010.

[51] S. Chen, G. Wang, J. Wen, and X. Wen, "Wave propagation and attenuation in plates with periodic arrays of shunted piezo-patches," *Journal of Sound and Vibration*, vol. 332, no. 6, pp. 1520–1532, 2013.

[52] C. W. T. McLyman, *Transformer and Inductor Design Handbook*. CRC Press, 2004.

[53] B. Multon, "Composants passifs de l'électronique de puissance (magnétiques et capacitifs)." 2015.

[54] Epcos, *Ferrites and accessories. General - Definitions*, 2006.

[55] W. Voigt, *Lehrbuch der kristallphysik (mit Ausschluss der Kristalloptik)*. BG Teubner, 1910.

[56] H. Kawai, "The piezoelectricity of poly (vinylidene fluoride)," *Japanese Journal of Applied Physics*, vol. 8, no. 7, p. 975, 1969.

[57] G. M. Sessler, "Piezoelectricity in polyvinylidenefluoride," *The Journal of the Acoustical Society of America*, vol. 70, no. 6, pp. 1596–1608, 1981.

[58] H. S. Nalwa, *Ferroelectric polymers: chemistry: physics, and applications*. CRC Press, 1995.

[59] D. Guyomar, A. Badel, E. Lefeuvre, and C. Richard, "Toward energy harvesting using active materials and conversion improvement by nonlinear processing," *IEEE Transactions on Ultrasonics, Ferroelectrics, and Frequency Control*, vol. 52, no. 4, pp. 584–595, 2005.

[60] E. Lefeuvre, A. Badel, C. Richard, and D. Guyomar, "Piezoelectric energy harvesting device optimization by synchronous electric charge extraction," *Journal of Intelligent Material Systems and Structures*, vol. 16, no. 10, pp. 865–876, 2005.

[61] E. Lefeuvre, A. Badel, C. Richard, L. Petit, and D. Guyomar, "A comparison between several vibration-powered piezoelectric generators for standalone systems," *Sensors and Actuators A: Physical*, vol. 126, no. 2, pp. 405–416, 2006.

[62] S. R. Anton, A. Erturk, and D. J. Inman, "Multifunctional self-charging structures using piezoceramics and thin-film batteries," *Smart Materials and Structures*, vol. 19, no. 11, p. 115021, 2010.

[63] A. Erturk and D. J. Inman, *Piezoelectric energy harvesting*. John Wiley & Sons, 2011.

[64] R. Alkhatib and M. Golnaraghi, "Active structural vibration control: a review," *Shock and Vibration Digest*, vol. 35, no. 5, p. 367, 2003.

[65] A. Singh, D. J. Pines, and A. Baz, "Active/passive reduction of vibration of periodic one-dimensional structures using piezoelectric actuators," *Smart Materials and Structures*, vol. 13, no. 4, p. 698, 2004.

[66] G. Gatti, M. Brennan, and P. Gardonio, "Active vibration control of a beam using piezoelectric actuators," tech. rep., ISVR, 2005.

[67] M. Yuan, H. Ji, J. Qiu, and T. Ma, "Active control of sound transmission through a stiffened panel using a hybrid control strategy," *Journal of Intelligent Material Systems and Structures*, vol. 23, no. 7, pp. 791–803, 2012.

[68] ANSI/IEEE, "IEEE standard on piezoelectricity," *ANSI/IEEE Std 176-1987*, 1988.

[69] E. Balmes and A. Deraemaeker, *Modeling structures with piezoelectric materials*, 2013.

[70] O. Thomas, J.-F. Deü, and J. Ducarne, "Vibrations of an elastic structure with shunted piezoelectric patches: efficient finite element formulation and electromechanical coupling coefficients," *International Journal for Numerical Methods in Engineering*, vol. 80, no. 2, pp. 235–268, 2009.

[71] C. Maurini, J. Pouget, and F. dell'Isola, "Extension of the Euler-Bernoulli model of piezoelectric laminates to include 3D effects via a mixed approach," *Computers & Structures*, vol. 84, no. 22-23, pp. 1438–1458, 2006.

[72] Y. S. Cho, Y. Pak, C. S. Han, and S. K. Ha, "Five-port equivalent electric circuit of piezoelectric bimorph beam," *Sensors and Actuators A: Physical*, vol. 84, no. 1–2, pp. 140–148, 2000.

[73] R. P. Paganelli, A. Romani, A. Golfarelli, M. Magi, E. Sangiorgi, and M. Tartagni, "Modeling and characterization of piezoelectric transducers by means of scattering parameters. Part I: Theory," *Sensors and Actuators A: Physical*, vol. 160, no. 1-2, pp. 9–18, 2010.

[74] A. Bloch, "Electromechanical analogies and their use for the analysis of mechanical and electromechanical systems," *Journal of the Institution of Electrical Engineers - Part I: General*, vol. 92, no. 52, pp. 157–169, 1945.

[75] F. A. Firestone, "A new analogy between mechanical and electrical systems," *The Journal of the Acoustical Society of America*, vol. 4, no. 3, pp. 249–267, 1933.

[76] M. Berardengo, O. Thomas, C. Giraud-Audine, and S. Manzoni, "Improved resistive shunt by means of negative capacitance: new circuit, performances and multi-mode control," *Smart Materials and Structures*, vol. 25, no. 7, p. 075033, 2016.

[77] P. Soltani, G. Kerschen, G. Tondreau, and A. Deraemaeker, "Piezoelectric vibration damping using resonant shunt circuits: an exact solution," *Smart Materials and Structures*, vol. 23, no. 12, p. 125014, 2014.

[78] J. Ducarne, O. Thomas, and J.-F. Deü, "Placement and dimension optimization of shunted piezoelectric patches for vibration reduction," *Journal of Sound and Vibration*, vol. 331, no. 14, pp. 3286–3303, 2012.

[79] J. Ducarne, *Modeling and optimisation of non-linear vibration damping by switch shunting of piezoelectric elements*. PhD thesis, Conservatoire national des arts et métiers - Cnam, 2009.

[80] A. Sénéchal, *Optimization of shunted piezoelectric patches for vibration reduction of complex structures : application to a turbojet fan blade*. PhD thesis, Conservatoire national des arts et métiers - Cnam, 2011.

[81] Agilent-Technologies, *Agilent Impedance Measurement Handbook, A guide to measurement technology and techniques*, 4^{th} edition ed., 2009.

[82] D. J. Mead, "Wave propagation in continuous periodic structures: research contribution from southampton, 1964-1995," *Journal of Sound and Vibration*, vol. 190, no. 3, pp. 495–524, 1996.

[83] L. Brillouin, *Wave propagation in periodic structures*. McGraw-Hill, 1946.

[84] L. L. Beranek, *Acoustics*. McGraw-Hill, 1954.

[85] W. Zhou, Y. Wu, and L. Zuo, "Vibration and wave propagation attenuation for metamaterials by periodic piezoelectric arrays with high-order resonant circuit shunts," *Smart Materials and Structures*, vol. 24, no. 6, p. 065021, 2015.

[86] S. Chen and G. Wang, "Wave propagation in beams with anti-symmetric piezoelectric shunting arrays," *Chinese Physics B*, vol. 25, no. 3, p. 034301, 2016.

[87] T. Y. Wu and K. W. Wang, "Periodic isolator design enhancement via vibration confinement through eigenvector assignment and piezoelectric circuitry," *Journal of Vibration and Control*, vol. 13, no. 7, pp. 989–1006, 2007.

[88] G. Wang, J. Wang, S. Chen, and J. Wen, "Vibration attenuations induced by periodic arrays of piezoelectric patches connected by enhanced resonant shunting circuits," *Smart Materials and Structures*, vol. 20, no. 12, p. 125019, 2011.

[89] H. Zhang, J. Wen, S. Chen, G. Wang, and X. Wen, "Flexural wave band-gaps in phononic metamaterial beam with hybrid shunting circuits," *Chinese Physics B*, vol. 24, no. 3, p. 036201, 2015.

[90] M. Collet, K. A. Cunefare, and M. N. Ichchou, "Wave motion optimization in periodically distributed shunted piezocomposite beam structures," *Journal of Intelligent Material Systems and Structures*, vol. 20, no. 7, pp. 787–808, 2009.

[91] B. S. Beck, K. A. Cunefare, M. Ruzzene, and M. Collet, "Experimental analysis of a cantilever beam with a shunted piezoelectric periodic array," *Journal of Intelligent Material Systems and Structures*, vol. 22, no. 11, pp. 1177–1187, 2011.

[92] H. Yu, K. W. Wang, and J. Zhang, "Piezoelectric networking with enhanced electromechanical coupling for vibration delocalization of mistuned periodic structures - theory and experiment," *Journal of Sound and Vibration*, vol. 295, no. 1–2, pp. 246–265, 2006.

[93] L. Li, P. Deng, and Y. Fan, "Dynamic characteristics of a cyclic-periodic structure with a piezoelectric network," *Chinese Journal of Aeronautics*, vol. 28, no. 5, pp. 1426–1437, 2015.

[94] S. Vidoli and F. dell'Isola, "Modal coupling in one-dimensional electromechanical structured continua," *Acta Mechanica*, vol. 141, no. 1-2, pp. 37–50, 2000.

[95] R. Batra, F. dell'Isola, S. Vidoli, and D. Vigilante, "Multimode vibration suppression with passive two-terminal distributed network incorporating piezoceramic transducers," *International Journal of Solids and Structures*, vol. 42, no. 11-12, pp. 3115–3132, 2005.

[96] M. Porfiri, F. dell'Isola, and E. Santini, "Modeling and design of passive electric networks interconnecting piezoelectric transducers for distributed vibration control," *International Journal of Applied Electromagnetics and Mechanics*, vol. 21, no. 2, pp. 69–87, 2005.

[97] M. Kader, M. Lenczner, and Z. Mrcarica, "Distributed control based on distributed electronic circuits: application to vibration control," *Microelectronics Reliability*, vol. 41, no. 11, pp. 1857–1866, 2001.

[98] M. Panella and G. Martinelli, "RC distributed circuits for vibration damping in piezo-electromechanical beams," *IEEE Transactions on Circuits and Systems II: Express Briefs*, vol. 52, no. 8, pp. 486–490, 2005.

[99] P. Bisegna, G. Caruso, and F. Maceri, "Optimized electric networks for vibration damping of piezoactuated beams," *Journal of Sound and Vibration*, vol. 289, no. 4–5, pp. 908–937, 2006.

[100] A. E. Bergamini, M. Zündel, E. A. Flores Parra, T. Delpero, M. Ruzzene, and P. Ermanni, "Hybrid dispersive media with controllable wave propagation: A new take on smart materials," *Journal of Applied Physics*, vol. 118, no. 15, p. 154310, 2015.

[101] Y. Lu and J. Tang, "Electromechanical tailoring of structure with periodic piezoelectric circuitry," *Journal of Sound and Vibration*, vol. 331, no. 14, pp. 3371–3385, 2012.

[102] S. Chen, J. Wen, G. Wang, D. Yu, and X. Wen, "Improved modeling of rods with periodic arrays of shunted piezoelectric patches," *Journal of Intelligent Material Systems and Structures*, vol. 23, no. 14, pp. 1613–1621, 2012.

[103] N. Stephen, "On the riccati transfer matrix method for repetitive structures," *Mechanics Research Communications*, vol. 37, no. 7, pp. 663–665, 2010.

[104] R. S. Langley, N. S. Bardell, and P. M. Loasby, "The optimal design of near-periodic structures to minimize vibration transmission and stress levels," *Journal of Sound and Vibration*, vol. 207, no. 5, pp. 627–646, 1997.

[105] D. Cardella, P. Celli, and S. Gonella, "Manipulating waves by distilling frequencies: a tunable shunt-enabled rainbow trap," *Smart Materials and Structures*, vol. 25, no. 8, p. 085017, 2016.

[106] B. R. Mace, D. Duhamel, M. J. Brennan, and L. Hinke, "Finite element prediction of wave motion in structural waveguides," *The Journal of the Acoustical Society of America*, vol. 117, no. 5, pp. 2835–2843, 2005.

[107] D. Duhamel, B. R. Mace, and M. J. Brennan, "Finite element analysis of the vibrations of waveguides and periodic structures," tech. rep., ISVR, 2003.

[108] T. L. Huang, M. N. Ichchou, O. A. Bareille, M. Collet, and M. Ouisse, "Traveling wave control in thin-walled structures through shunted piezoelectric patches," *Mechanical Systems and Signal Processing*, vol. 39, no. 1–2, pp. 59–79, 2013.

[109] L. Yan, *Broadband vibration control using nonlinearly interfaced piezoelectric elements*. PhD thesis, Institut National des Sciences Appliquées de Lyon - INSA Lyon, 2013.

[110] M. Lallart, L. Yan, C. Richard, and D. Guyomar, "Damping of periodic bending structures featuring nonlinearly interfaced piezoelectric elements," *Journal of Vibration and Control*, vol. 22, no. 18, pp. 3930–3941, 2016.

[111] B. Bao, D. Guyomar, and M. Lallart, "Vibration reduction for smart periodic structures via periodic piezoelectric arrays with nonlinear interleaved-switched electronic networks," *Mechanical Systems and Signal Processing*, vol. 82, pp. 230–259, 2017.

[112] L. Yan, B. Bao, D. Guyomar, and M. Lallart, "Periodic structure with interconnected nonlinear electrical networks," *Journal of Intelligent Material Systems and Structures*, p. 1045389X16649448, 2016.

[113] P. Celli and S. Gonella, "Tunable directivity in metamaterials with reconfigurable cell symmetry," *Applied Physics Letters*, vol. 106, no. 9, p. 091905, 2015.

[114] A. Chen, F. Li, and Y. Wang, "Localization of flexural waves in a disordered periodic piezoelectric beam," *Journal of Sound and Vibration*, vol. 304, no. 3–5, pp. 863–874, 2007.

[115] M. S. Rao and S. Narayanan, "Active control of wave propagation in multi-span beams using distributed piezoelectric actuators and sensors," *Smart Materials and Structures*, vol. 16, no. 6, p. 2577, 2007.

[116] L. Ding, H. Zhu, and T. Yin, "Wave propagation in a periodic elastic-piezoelectric axial-bending coupled beam," *Journal of Sound and Vibration*, vol. 332, no. 24, pp. 6377–6388, 2013.

[117] S. Vidoli, *Structures and Control: Integrated Continuum Models*. PhD thesis, Sapienza - Università di Roma, 2000.

[118] F. Casadei, L. Dozio, M. Ruzzene, and K. A. Cunefare, "Periodic shunted arrays for the control of noise radiation in an enclosure," *Journal of Sound and Vibration*, vol. 329, no. 18, pp. 3632–3646, 2010.

[119] F. Casadei, T. Delpero, A. E. Bergamini, P. Ermanni, and M. Ruzzene, "Piezoelectric resonator arrays for tunable acoustic waveguides and metamaterials," *Journal of Applied Physics*, vol. 112, no. 6, p. 064902, 2012.

[120] L. Dai, S. Jiang, Z. Lian, H. Hu, and X. Chen, "Locally resonant band gaps achieved by equal frequency shunting circuits of piezoelectric rings in a periodic circular plate," *Journal of Sound and Vibration*, vol. 337, pp. 150–160, 2015.

[121] H. Zhang, J. Wen, Y. Xiao, G. Wang, and X. Wen, "Sound transmission loss of metamaterial thin plates with periodic subwavelength arrays of shunted piezoelectric patches," *Journal of Sound and Vibration*, vol. 343, pp. 104–120, 2015.

[122] M. Collet, M. Ouisse, M. N. Ichchou, and R. Ohayon, "Semi-active optimization of 2D wave dispersion into shunted piezo-composite systems for controlling acoustic interaction," *Smart Materials and Structures*, vol. 21, no. 9, p. 094002, 2012.

[123] B. S. Beck, *Negative capacitance shunting of piezoelectric patches for vibration control of continuous systems*. PhD thesis, Georgia Institute of Technology, 2012.

[124] F. Casadei, B. S. Beck, K. A. Cunefare, and M. Ruzzene, "Vibration control of plates through hybrid configurations of periodic piezoelectric shunts," *Journal of Intelligent Material Systems and Structures*, vol. 23, no. 10, pp. 1169–1177, 2012.

[125] F. Tateo, M. Collet, M. Ouisse, and K. A. Cunefare, "Design variables for optimizing adaptive metacomposite made of shunted piezoelectric patches distribution," *Journal of Vibration and Control*, 2014.

[126] M. Collet, M. Ouisse, and F. Tateo, "Adaptive metacomposites for vibroacoustic control applications," *IEEE Sensors Journal*, vol. 14, no. 7, pp. 2145–2152, 2014.

[127] F. Tateo, M. Collet, M. Ouisse, M. N. Ichchou, K. A. Cunefare, and P. Abbe, "Experimental characterization of a bi-dimensional array of negative capacitance

piezo-patches for vibroacoustic control," *Journal of Intelligent Material Systems and Structures*, vol. 26, no. 8, pp. 952–964, 2015.

[128] S. Vidoli and F. dell'Isola, "Vibration control in plates by uniformly distributed PZT actuators interconnected via electric networks," *European Journal of Mechanics - A/Solids*, vol. 20, no. 3, pp. 435–456, 2001.

[129] I. Giorgio, A. Culla, and D. Del Vescovo, "Multimode vibration control using several piezoelectric transducers shunted with a multiterminal network," *Archive of Applied Mechanics*, vol. 79, no. 9, pp. 859–879, 2008.

[130] I. Giorgio, *Multimode Collocated Vibration Control with Multiple Piezoelectric Transducers*. PhD thesis, Sapienza - Università di Roma, 2008.

[131] S. Alessandroni, "Electrical analogs for plate equations and their applications in mechanical vibration suppression by P.Z.T. actuators," Master's thesis, Virginia Polytechnic Institute and State University, 2000.

[132] M. Berardengo, A. Cigada, S. Manzoni, and M. Vanali, "Vibration control by means of piezoelectric actuators shunted with LR impedances: performance and robustness analysis," *Shock and Vibration*, vol. 2015, 2015.

[133] J. A. B. Gripp, L. C. S. Góes, O. Heuss, and F. Scinocca, "An adaptive piezoelectric vibration absorber enhanced by a negative capacitance applied to a shell structure," *Smart Materials and Structures*, vol. 24, no. 12, p. 125017, 2015.

[134] G. Rosi, J. Pouget, and F. dell'Isola, "Control of sound radiation and transmission by a piezoelectric plate with an optimized resistive electrode," *European Journal of Mechanics - A/Solids*, vol. 29, no. 5, pp. 859–870, 2010.

[135] G. Rosi, *Control of sound radiation and transmission by means of passive piezoelectric networks : modelling, optimization and experimental implementation*. PhD thesis, Université Pierre et Marie Curie - Paris VI, 2010.

[136] S. P. Timoshenko, *Theory of plates and shells*. McGraw-Hill, 1940.

[137] U. Aridogan, I. Basdogan, and A. Erturk, "Analytical modeling and experimental validation of a structurally integrated piezoelectric energy harvester on a thin plate," *Smart Materials and Structures*, vol. 23, no. 4, p. 045039, 2014.

[138] U. Aridogan, I. Basdogan, and A. Erturk, "Multiple patch-based broadband piezoelectric energy harvesting on plate-based structures," *Journal of Intelligent Material Systems and Structures*, vol. 25, no. 14, pp. 1664–1680, 2014.

Appendices

Appendix A

Optimization of the resonant shunt

The objective of this appendix is to define optimum values for the resonant shunt frequency ω_e and the damping factor ξ_e, in order to minimize the maximum of the modulus $|H(\omega)|$ that has been defined in Sec. 2.3. Recall that

$$|H(\omega)|^2 = \frac{A_0 + A_2\xi_e^2}{B_0 + B_2\xi_e^2}, \tag{A.1}$$

where

$$\begin{aligned} A_0 &= \left[1 - \frac{\omega^2}{\omega_e^2}\right]^2, \quad A_2 = 4\frac{\omega^2}{\omega_e^2}, \quad B_2 = 4\frac{\omega^2}{\omega_e^2}\left[1 - \frac{\omega^2}{\omega_O^2}\right]^2 \\ \text{and} \quad B_0 &= \left[\frac{\omega_S^2}{\omega_O^2} - \left(\frac{1}{\omega_O^2} + \frac{1}{\omega_e^2}\right)\omega^2 + \frac{\omega^4}{\omega_O^2\omega_e^2}\right]^2 \end{aligned}. \tag{A.2}$$

Then, it is remarked that there exist two points P and Q, whose respective ordinates $|H(\omega_-)|$ and $|H(\omega_+)|$ do not depend on the damping factor [2, 41, 43]. Those two fixed points are shown in Fig A.1. They represent the approximate positioning of the two local maxima of the function $|H(\omega)|$ after optimization of ω_e and ξ_e. A first step thus consist in finding the value for ω_e that leads to $|H(\omega_-)| = |H(\omega_+)|$. The angular frequencies ω_-

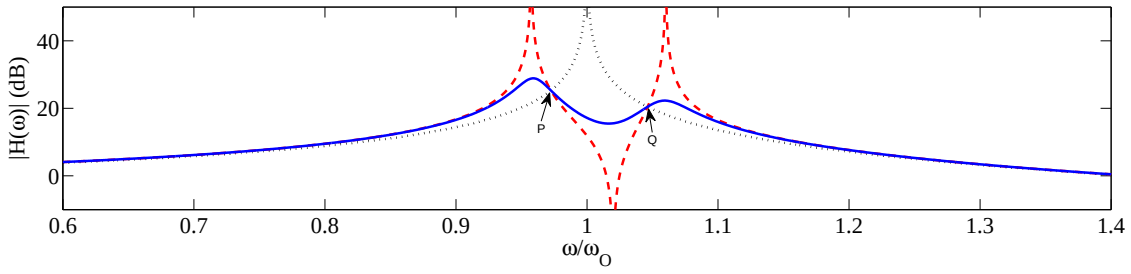

Figure A.1: Modulus of the transfer function $H(\omega)$ - $(\cdots)$ with $\xi_e \to +\infty$, (- -) with $\omega_e = 1.02 \times \omega_O$ and $\xi_e = 0$, (—) with $\omega_e = 1.02 \times \omega_O$ and $\xi_e = \sqrt{\frac{3}{8}\frac{k_c}{2}}$.

and ω_+ are the abscissas of the fixed point, therefore they satisfy

$$|H(\omega_\pm)|^2_{\xi_e=0} = |H(\omega_\pm)|^2_{\xi_e\to+\infty}, \quad \text{which gives} \quad \frac{A_0}{B_0} = \frac{A_2}{B_2}. \tag{A.3}$$

Equation (A.3) can also be written $A_0B_2 - A_2B_0 = 0$, so that Eq. (A.2) gives

$$\left[1 - \left(1 + \frac{\omega_O^2}{\omega_e^2}\right)\Omega + \frac{\omega_O^2}{\omega_e^2}\Omega^2\right]^2 - \left[\frac{\omega_S^2}{\omega_O^2} - \left(1 + \frac{\omega_O^2}{\omega_e^2}\right)\Omega + \frac{\omega_O^2}{\omega_e^2}\Omega^2\right]^2 = 0, \tag{A.4}$$

where $\Omega = \omega_\pm^2/\omega_O^2$. Equation (A.4) is factorized into

$$\left[1 + \frac{\omega_S^2}{\omega_O^2} - 2\left(1 + \frac{\omega_O^2}{\omega_e^2}\right)\Omega + 2\frac{\omega_O^2}{\omega_e^2}\Omega^2\right]\left[1 - \frac{\omega_S^2}{\omega_O^2}\right] = 0, \tag{A.5}$$

that is equivalent to

$$\omega_e^2\left(1 + \frac{\omega_S^2}{\omega_O^2}\right) - 2\left(\omega_e^2 + \omega_O^2\right)\Omega + 2\omega_O^2\Omega^2 = 0. \tag{A.6}$$

The solution of this quadratic equation is

$$\Omega = \frac{-b \pm \sqrt{\Delta}}{2a}, \tag{A.7}$$

where $\Delta = b^2 - 4ac$, $a = 2\omega_O^2$, $b = -2\left(\omega_e^2 + \omega_O^2\right)$, and $c = \omega_e^2\left(1 + \frac{\omega_S^2}{\omega_O^2}\right)$. Finally,

$$\omega_\pm^2 = \frac{1}{2}\left(\omega_e^2 + \omega_O^2 \pm \sqrt{\omega_e^4 + \omega_O^4 - 2\omega_S^2\omega_e^2}\right), \tag{A.8}$$

which defines the square of the angular frequencies corresponding to both fixed points of the function $|H(\omega)|$. The amplitude at those fixed point is obtained from the open-circuit case, which simplifies the expression in Eq. (A.1) as

$$|H(\omega)|^2_{\xi_e\to+\infty} = \frac{A_2}{B_2} = \left[1 - \frac{\omega^2}{\omega_O^2}\right]^{-2} \tag{A.9}$$

From, Eqs. (A.8) and (A.9), note that

$$|H(\omega_+)|^2_{\xi_e\to+\infty} = |H(\omega_-)|^2_{\xi_e\to+\infty} \quad \text{when} \quad \omega_e = \omega_O. \tag{A.10}$$

Therefore, for any ξ_e,

$$\omega_e = \omega_O \quad \text{gives} \quad |H(\omega_+)| = |H(\omega_-)|, \tag{A.11}$$

because ω_- and ω_+ are the abscissas of the two fixed points that keep the same ordinates for any damping factor. With $\omega_e = \omega_O$, Eqs. (A.1) and (A.8) gives

$$\omega_\pm^2 = \omega_O^2\left[1 \pm \frac{1}{\sqrt{2}}\sqrt{1 - \frac{\omega_S^2}{\omega_O^2}}\right] \quad \text{and} \quad |H(\omega_+)| = |H(\omega_-)| = \sqrt{2}\frac{\sqrt{1+k_c^2}}{k_c} \approx \frac{\sqrt{2}}{k_c}. \tag{A.12}$$

The last approximation relies on the fact that the coupling coefficient k_c is usually around or below 0.1 for the considered applications involving thin piezoelectric patches. Then, we want to find two specific values of the damping factor, ξ_e^- and ξ_e^+, that generate a local minimum at ω_- and ω_+, respectively. Following the method proposed by Liu [41] and according to the definition of the present parameters,

$$(1+k_c^2)(\xi_e^{\pm})^2 = \frac{3\mu\sqrt{2\mu}}{8(\sqrt{2\mu}\pm\mu)(1-\mu)} \quad \text{where} \quad \mu = \frac{k_c^2}{1+k_c^2}. \tag{A.13}$$

Equation (A.13) leads to

$$(\xi_e^{\pm})^2 = \frac{3}{4}\frac{k_c^2}{2(1+k_c^2)\pm\sqrt{2}k_c\sqrt{1+k_c^2}}, \tag{A.14}$$

which can be approximated by a single damping factor

$$\xi_e^{\pm} \approx \sqrt{\frac{3}{8}}k_c. \tag{A.15}$$

In the end, the optimal values of parameters ω_e and ξ_e that minimize the function $|H(\omega)|$ are approximated by

$$\omega_e = \omega_O \quad \text{and} \quad \xi_e = \sqrt{\frac{3}{8}}k_c. \tag{A.16}$$

Appendix B

Element matrices for the 1D finite element model

According to Thomas et al. [70], the stiffness matrix $\boldsymbol{K_m}$, the mass matrix $\boldsymbol{M_m}$ and the coupling matrix $\boldsymbol{K_c}$ result from the assembly of the following element matrices $\boldsymbol{K}^{\mathrm{e}}_{\boldsymbol{m}}$, $\boldsymbol{M}^{\mathrm{e}}_{\boldsymbol{m}}$ and $\boldsymbol{K}^{\mathrm{e}}_{\boldsymbol{c}}$. For a unit cell which is symmetric with respect to its neutral axis, bending and extensional motions are decoupled. The element stiffness matrix is then written as

$$\boldsymbol{K}^{\mathrm{e}}_{\boldsymbol{m}} = \frac{A}{L_{\mathrm{e}}}\begin{bmatrix} 1 & 0 & 0 & -1 & 0 & 0 \\ 0 & 0 & 0 & 0 & 0 & 0 \\ 0 & 0 & 0 & 0 & 0 & 0 \\ -1 & 0 & 0 & 1 & 0 & 0 \\ 0 & 0 & 0 & 0 & 0 & 0 \\ 0 & 0 & 0 & 0 & 0 & 0 \end{bmatrix} + \frac{D}{L_{\mathrm{e}}^3}\begin{bmatrix} 0 & 0 & 0 & 0 & 0 & 0 \\ 0 & 12 & 6L_{\mathrm{e}} & 0 & -12 & 6L_{\mathrm{e}} \\ 0 & 6L_{\mathrm{e}} & 4L_{\mathrm{e}}^2 & 0 & -6L_{\mathrm{e}} & 2L_{\mathrm{e}}^2 \\ 0 & 0 & 0 & 0 & 0 & 0 \\ 0 & -12 & -6L_{\mathrm{e}} & 0 & 12 & -6L_{\mathrm{e}} \\ 0 & 6L_{\mathrm{e}} & 2L_{\mathrm{e}}^2 & 0 & -6L_{\mathrm{e}} & 4L_{\mathrm{e}}^2 \end{bmatrix}, \quad \text{(B.1)}$$

where L_{e} is the length of the element. Along the 's' segment $A = Y_{\mathrm{s}}S_{\mathrm{s}}$ and $D = Y_{\mathrm{s}}I_{\mathrm{s}}$, and along the 'sp' segment $A = Y_s S_s + 2Y_{\mathrm{p}}^E S_p$ and $D = Y_{\mathrm{s}}I_{\mathrm{s}} + 2Y_{\mathrm{p}}^E I_{\mathrm{p}}$. When neglecting the rotational inertia, the element mass matrix is

$$\boldsymbol{M}^{\mathrm{e}}_{\boldsymbol{m}} = \frac{\lambda L_{\mathrm{e}}}{420}\begin{bmatrix} 140 & 0 & 0 & 70 & 0 & 0 \\ 0 & 156 & 22L_{\mathrm{e}} & 0 & 54 & -13L_{\mathrm{e}} \\ 0 & 22L_{\mathrm{e}} & 4L_{\mathrm{e}}^2 & 0 & 13L_{\mathrm{e}} & -3L_{\mathrm{e}}^2 \\ 70 & 0 & 0 & 140 & 0 & 0 \\ 0 & 54 & 13L_{\mathrm{e}} & 0 & 156 & -22L_{\mathrm{e}} \\ 0 & -13L_{\mathrm{e}} & -3L_{\mathrm{e}}^2 & 0 & -22L_{\mathrm{e}} & 4L_{\mathrm{e}}^2 \end{bmatrix}, \quad \text{(B.2)}$$

where $\lambda = \rho_{\mathrm{s}}S_{\mathrm{s}}$ along the 's' segment and $\lambda = \rho_{\mathrm{s}}S_{\mathrm{s}} + 2\rho_{\mathrm{p}}S_{\mathrm{p}}$ along the 'sp' segment. Finally, for extensional motion

$$\boldsymbol{K}^{\mathrm{e}}_{\boldsymbol{c}} = e_{\mathrm{sp}}\begin{bmatrix} -1 & 0 & 0 & 1 & 0 & 0 \end{bmatrix} \quad \text{(B.3)}$$

and for bending motion

$$\boldsymbol{K}^{\mathrm{e}}_{\boldsymbol{c}} = e_{\mathrm{sp}}\begin{bmatrix} 0 & 0 & 1 & 0 & 0 & -1 \end{bmatrix}. \quad \text{(B.4)}$$

Appendix C

Publications

C.1 Journal papers

- B. Lossouarn, M. Aucejo, and J.-F. Deü, "Multimodal coupling of periodic lattices and application to rod vibration damping with a piezoelectric network," *Smart Materials and Structures*, vol. 24, no. 4, p. 045018, 2015.
- B. Lossouarn, J.-F. Deü, and M. Aucejo, "Multimodal vibration damping of a beam with a periodic array of piezoelectric patches connected to a passive electrical network," *Smart Materials and Structures*, vol. 24, no. 11, p. 115037, 2015.
- B. Lossouarn, J.-F. Deü, M. Aucejo, and K. A. Cunefare, "Multimodal vibration damping of a plate by piezoelectric coupling to its analogous electrical network," accepted for publication in *Smart Materials and Structures*
- B. Lossouarn, M. Aucejo, J.-F. Deü, and K. A. Cunefare, "Design of a passive electrical analogue for piezoelectric damping of a plate," submitted to *Sensors & Actuators: A. Physical*

C.2 Conference proceedings

- B. Lossouarn, J.-F. Deü, and M. Aucejo, "Wave propagation in coupled periodic lattices and application to vibration attenuation through a piezoelectric network," *Proceedings of the 26th International Conference on Noise and Vibration Engineering*, ISMA 2014, Leuven (Belgium), September 15-17, 2014.
- B. Lossouarn, M. Aucejo, and J.-F. Deü, "Multimodal vibration damping through a periodic array of piezoelectric patches connected to a passive network," *Proceedings*

of the SPIE Smart Structures/NDE 2015, San Diego, California (USA), March 8-12, 2015.

- J.-F. Deü, B. Lossouarn, and M. Aucejo, "Comparison of electromechanical transfer matrix models for passive damping involving an array of shunted piezoelectric patches," *Proceedings of the 22nd ICSV Congress on Sound and Vibration*, Florence (Italy), July 12-16, 2015.

- B. Lossouarn, M. Aucejo, J.-F. Deü, and K. A. Cunefare, "Multimodal damping of a plate with a passive piezoelectric network," *Proceedings of the 34th IMAC Conference and Exposition on Structural Dynamics*, Orlando, Florida (USA), January 25-28, 2016.

- B. Lossouarn, O. Thierry, M. Aucejo, and J.-F. Deü, "Comparison of passive inductor designs for piezoelectric shunt damping," *Proceedings of the SPIE Smart Structures/NDE 2016*, Las Vegas, Nevada (USA), March 20-24, 2016.

- B. Lossouarn, K. A. Cunefare, M. Aucejo, and J.-F. Deü, "Robustness of a multimodal piezoelectric damping involving the electrical analogue of a plate," *Proceedings of the SPIE Smart Structures/NDE 2016*, Las Vegas, Nevada (USA), March 20-24, 2016.

- B. Lossouarn, M. Aucejo, J.-F. Deü, and K. A. Cunefare, "Amortissement multimodal par couplage piézoélectrique à un analogue électrique passif," *20th Symposium Vibrations, Shocks and Noise, VISHNO 2016*, Le Mans (France), April 11-15, 2016.

- B. Lossouarn, M. Aucejo, and J.-F. Deü, "Transverse wave propagation in a one-dimensional structure coupled to its electrical analogue: comparison of transfer matrix models," *7th ECCOMAS Congress on Computational Methods in Applied Sciences and Engineering*, Hersonissos, Crete (Greece), June 5-10, 2016.